NICKEL MINERALISATION IN THE JAMESTOWN OPHIOLITE, BARBERTON GREENSTONE BELT, SOUTH AFRICA

BY

NATHANIEL CHABANGU

Dissertation submitted in fulfilment of the requirements for the degree of

Master of Science

in the

Faculty of Science

Department of Geology

University of the Free State

Bloemfontein, South Africa

2015

Supervisor: Professor Marian Tredoux

Declaration

I, Nathaniel Chabangu declare that this thesis and the work presented in it are my own and have been generated by me as the result of my own original research.

I confirm that:

1. This work was done wholly or mainly while in candidature for a research degree at the University of the Free State, Bloemfontein

2. Where any part of this thesis has previously been submitted for a degree or any other qualification at the University or any other institution, this has been clearly stated

3. Where I have consulted the published work of others, this is always clearly attributed

4. Where I have quoted from the work of others, the source is always given. With the exception of such quotations, this thesis is entirely my own work

5. I have acknowledged all main sources I have consulted for help

6. Where the thesis is based on work done by myself jointly with others, I have made clear exactly what was done by others and what I have contributed myself

Signed:

Date:

Abstract

The Bon Accord oxide deposit was found in the Bon Accord farm in Barberton, Mpumalanga Province, South Africa. It represented a remarkable deposit that was hosted within highly serpentinised meta-peridotites of the Onverwacht Group of the Barberton Supergroup in the Barberton Greenstone Belt. The aims of this research are to investigate methods that can be applied in modelling the characteristics of the nickel oxide mineralisation in the deposit, as well as establish parameters that can be used to find similar deposits. A variety of analytical techniques (Appendix A) were used to investigate the samples.

The ultramafic rocks of the Bon Accord nickel oxide deposit are highly deficient in sulphur but have unusually high nickel mineralisation (NiO ~36%) and comprise unusually high nickel-rich mineral assemblages. The nearly chondritic average ratios $(Gd/Yb)_N \approx 1$, and $Al_2O_3/TiO_2 \approx 17$ of the in Bon Accord nickel oxide body are similarities shared with komatiites, and may be thought to represent a possible link between the two rock suites and their processes of formation. Bon Accord oxide and its altered host rocks are characterised by slightly enriched light rare earth elements and flat heavy rare earth elements in both chondrite and primitive mantle normalised plots. The formation model tends to correlate with mantle thermal plume activities possibly induced by either subduction of cold lithosphere or by lithosphere subduction in a back arc environment. Such environments are suitable for the production of the observed crustal characteristics seen in the Bon Accord host rocks and also present a possible mechanism for the exposure at surface of what would have been a dense nickel-rich mass.

The density of Bon Accord oxide deposit requires that the mantle thermal plume(s) responsible for transportation, must have been large with sufficient energy, and high temperatures >1800°C to accommodate and maintain such a process without losing all the material and energy during

ascent. The occurrence of material which is highly enriched chalcogenic elements (As and Sb) but sulphur deficient led to the formation of unknown mineral phases serve which could serve as an indication of favourable environmental properties to form the nickel enrichment. While the relatively flat PGE patterns with a Pd negative anomaly and low Pd/Ir ratios (<1), low Ni/Cu and Pd/Ir and relatively enriched Pd/Pt ratios in the nickel sulphide host rock samples imply formation in an environment that contained some sulphur phases that were replaced by late stage sulphur deficient processes, similar to those observed in komatiites. Enrichment could have been from activities associated with post-magmatic, low-temperature hydrothermal oxidation of primary magmatic sulphide phases and the associated sulphur loss which possibly led to significant upgrading of the originally already concentrated nickel mineralisation.

The variable magnetic susceptibility measurements observed in the Bon Accord oxide and host rock samples were influenced by temperature, grain size and chemical composition. Bon Accord oxide samples are mainly characterised by ferromagnetic materials with relatively large positive values and susceptibility readings in excess of 2000. Bon Accord host rocks are characteristic of both diamagnetic and paramagnetic properties with readings recorded almost <100. The high magnetic properties of Bon Accord oxide samples probablymare due to the abundant occurrence of Ni- magnetite trevorite.

Table of Contents

List of Figures

List of Tables

List of abbreviations (*All inusual abbreviations used in the text which follows are defined in the list below.)*

Abbreviations	**Meaning**
ANL	African Nickel Limited
Bon	Bonaccordite
Bun	Bunsenite
BGB	Barberton Greenstone Belt
Cal	Calcite
Cc	Chalcocite
Ccp	Chalcopyrite
Chl	Chlorite
Cpx	Clinopyroxenes
END	Element not detected by analytical technique
Gsp	Gaspeite
Gt	Goethite
Hbl	Hornblende
Hem	Hematite
ICP-MS	Inductively coupled plasma mass spectrometry
ICP-OES	Inductively coupled plasma optical emission spectrometry
Ilm	Ilmenite
IPGE	Most refractory PGE, i.e. Os, Ir and Ru
Leu	Leucoxene
Lieb	Liebenbergite
Lm	Limonite
Min	Magnetite
Mrt	Millerite
Mus	Muscovite
NA	Not analysed in this study
NiCr	Nichromite
Nmt	Nimite
Npt	Népouite
Ol	Olivine
Opq	Opaque
Opx	Orthopyroxene
Pn	Pentlandite
Po	Pyrrhotite
PPGE	Less refractory PGE, i.e. Pd, Pt and Rh
Py	Pyrite
Pxn	Pyroxene
Qtz	Quartz
Srp	Serpentine
Spl	Spinel
Sul	Sulphide
Tlc	Talc
Trv	Trevorite
Trem	Tremolite
Wil	Willemseite

Chapter 1- Introduction

1.1. Overview of the Barberton greenstone belt geology

South Africa hosts a variety of world class mineral deposits and the Barberton Greenstone Belt (BGB) found in the Mpumalanga Province (Fig 1.1), represents one of the oldest gold deposits formed during the Archean Eon. The rocks represent > 3.0 Ga a greenschist facies belt which might contain remnants of ancient oceanic crust (de Wit et al, 1987). The BGB is a strongly folded, ENE-trending (Fig 1.2), mid-Archean (3.6 - 3.1 Ga), volcano-sedimentary remnant, entirely surrounded by a variety of granitoids, Brandl et al, (2006).

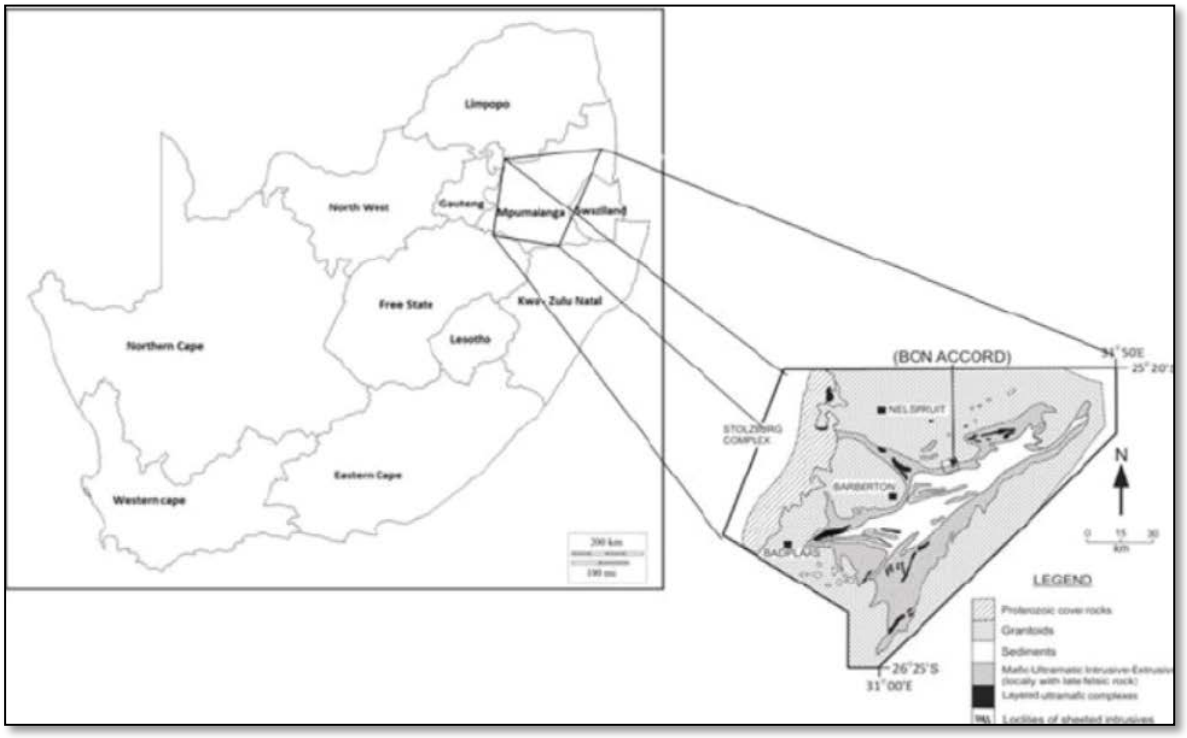

Figure 1.1. Map of South Africa showing study area (Barberton) in Mpumalanga Province (South Africa map was modified after d-maps and the BGB insert was adapted from Tredoux et al, 1989).

The greenstone belt is interlayered with granitic sheets which have an overall shallow southerly dip (de Wit, 1991). These rocks have been subdivided according to their stratigraphical sequences: Barberton Supergroup and the Jamestown Ophiolite Complex (JOC).

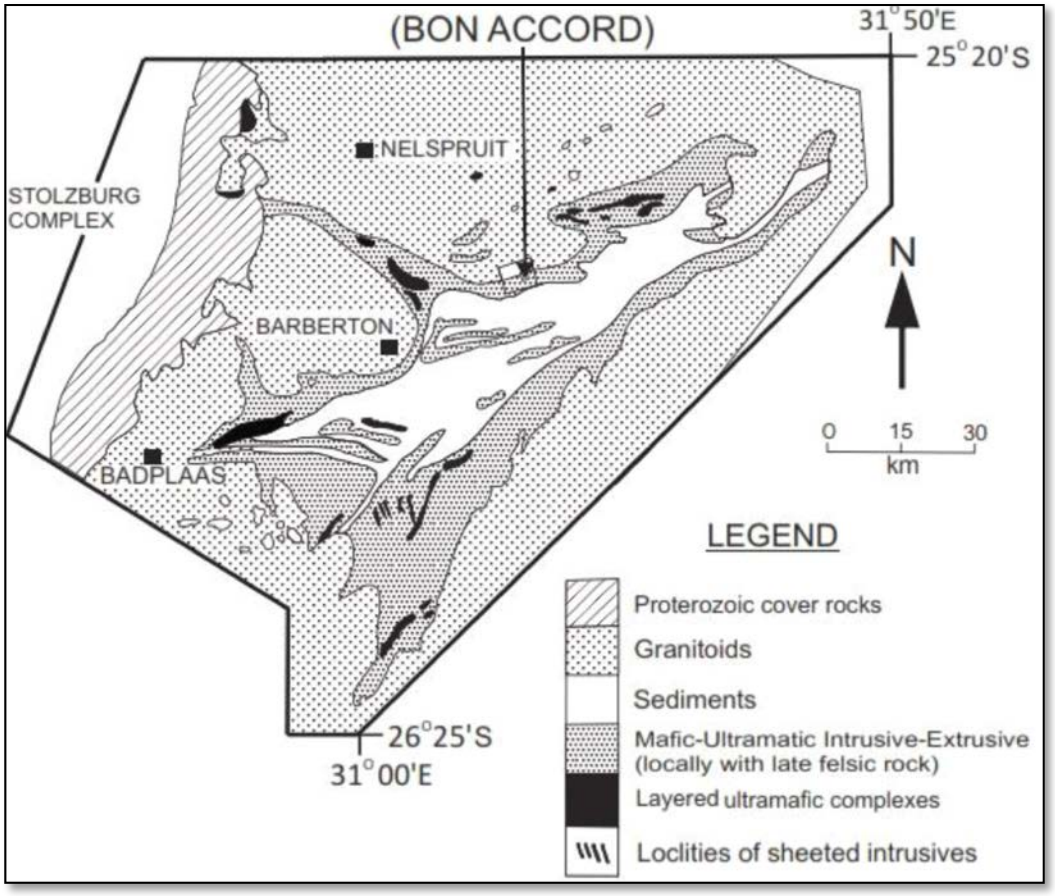

Figure 1.2. Map of Barberton Greenstone Belt (BGB) (adapted after Tredoux et al, 1989).

1.2. The Barberton Supergroup

The Barberton Supergroup is divided into three lithostratigraphic groups (Fig 1.3). The groups from oldest to the youngest are: Onverwacht Group, Fig Tree Group and Moodies Group.

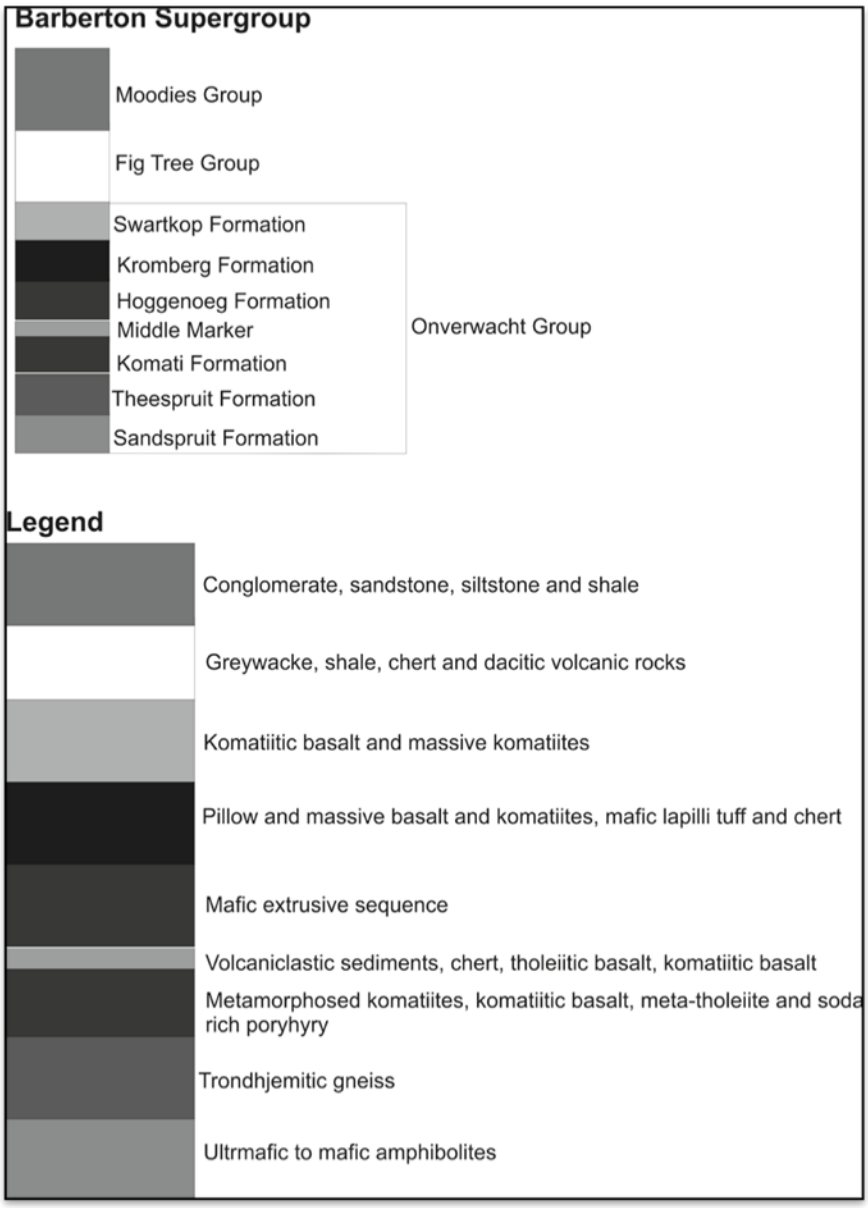

<u>Figure 1.3.</u> Lithostratigraphic Sequence of Barberton Supergroup (not to scale).

The Onverwacht Group comprises ultramafic to mafic volcanic rocks and is made up of southern and central parts which are fairly understood, and a northern part which is not clearly understood (Brandl et al, 2006). The southern part has been divided into six Formations (Sandspruit, Theespruit, Komati, Hooggenoeg, Kromberg and Mendon Formations) with only the top four

Formations thought to represent an intact sequence of up to 10 km in thickness (Brandl et al, 2006). According to Brandl et al (2006) the material in the north of the Theespruit pluton has yielded a minimum age of 3.45 Ga and the Theespruit Formation represents an allochthonous basal mélange. A maximum age of 3.47 Ga has been reported for the Komati Formation as determined for two interflow sediments, one more or less situated at the same stratigraphic level as the Soda Porphyry and the overlying Middle Marker (Brandl et al, 2006).

The Middle Marker is contained in the base of the Hooggenoeg Formation and comprises cherts, limestones and shale, the Middle Marker probably represents a fundamental break in deposition (Truswell, 1977). The Hooggenoeg Formation has yielded maximum ages of 3.47 – 3.41 Ga (Robin-Popieul et al, 2012). The preliminary palaeomagnetic work conducted shows that the Komati and Hooggenoeg Formations' poles coincide thus implying they must have formed part of the same convergent plate volcanic arc processes with temporally rapid and spatially focused emplacement (Brandl et al, 2006). However, not much work has been done to determine the volcanic setting of the Kromberg Formation but, it might represent the distal part of a volcanic sequence erupted from a volcanic centre located on the west limb of the Onverwacht Anticline (Brandl et al, 2006). The possible depositional environment for the Onverwacht Group was in some type of mid-oceanic ridge (MOR) environment because the rocks of this group are associated with extensive sea-floor type metamorphism, metasomatism and black-smoker type mineralisation (de Wit, 1991). The second oldest group making up the Barberton Supergroup, the Fig Tree Group, comprise mainly greywacke, shale, chert and dacitic volcanic rocks and consists of a southern shallow water facies and a northern deep water facies separated by the Inyoka fault (Brandl et al, 2006). This group has been subdivided into three formations in the northern terrane: from oldest to youngest; (a) Sheba Formation comprising turbiditic lithic greywacke and

shale, (b) Belvue Formation comprising shale, siltstone, greywacke, chert and coarse volcaniclastic rocks and altered komatiitic lava capped by a black chert near the top and (c) Schoongezict Formation comprising coarse felsic, volcaniclastic sandstone, conglomerate, breccia, mudstone and shale (Brandl et al, 2006).

Later two additional formations were defined in the northern terrane: (1) Ulundi Formation which consists of iron rich shales and chert and (2) Bien Venue Formation consisting of aluminous quartz muscovite schist (Brandl et al, 2006). The quartz muscovite schist is derived from a sequence of quartz dacitic to rhyodacitic volcaniclastic protoliths dated at 3.26-3.29 Ga together with subordinate banded chert, phyllite and chlorite schist. The two facies determined for the Fig Tree group have yielded ages of 3.26 to 3.23 Ga and 3.22 Ga for the southern and northern facies respectively.

The youngest group completing the stratigraphy of the Barberton Supergroup, the Moodies Group comprises conglomerate, sandstone, siltstone and shale and has been divided into three formations (older Cluthas Formation overlain by Joe's Luck Formation and on top is the younger Baviaanskop Formation). This group represents an upward fining cycle and the base of the Moodies Group is made up of coarse conglomeratic quartzose sandstone, siltstone and shale (Brandl et al, 2006). The deposition of the Moodies Group commenced at about 3.22 Ga and deposition ceased at about 3.11 Ga (Brandl et al, 2006). According to de Wit (1991), the Fig Tree and Moodies Groups were deposited in similar depositional environments, a foredeep or foreland basin due to the synorogenic sedimentation during and following the obduction of the Onverwacht Group northwards across the continental crust. Recent work has shown that the Fig Tree and Moodies Groups might have been deposited in separate basins at different times which

were later juxtaposed in response to major crustal shortening and possibly extensional collapse (de Wit, 1991). This is supported by noting that the lowermost sequences of both these groups represent sediments deposited in basins which initially formed along complex subduction related plate boundaries and which only later evolved into foreland depositories along and within collisional environments (de Wit, 1991).

1.3. Tectonic evolution

Various theories regarding the actual tectonic evolution of the Barberton Supergroup have been proposed. The Barberton volcanic and sedimentary rocks span ca. 400 million years of discontinuous accumulation and are intruded by contemporaneous to younger sills and dykes ranging in composition from ultramafic to felsic (de Wit et al, 2011). According to Brandl et al (2006) the early ultramafic to mafic Onverwacht Group volcanics formed in oceanic extensional environment(s), island arc or oceanic plateau settings. The Komati Formation is said to represent an ancient mid-ocean ridge spreading centre consisting of a sheeted dyke complex with its associated overlying pillow lavas, presently in the right way up position as reported by de Wit 1987a in Brandl et al (2006). Thus Brandl et al (2006) have proposed that the rocks of the Onverwacht Group represent a vertically rotated volcanic sequence similar to the extrusive part of an oceanic plateau. As the extrusive pile thickened during the deposition of the Onverwacht Group, shallow marine conditions were attained by means of isostacy (Brandl et al, 2006). The newly formed rocks of the Onverwacht Group between 3.45 and 3.41 Ga were delaminated (D1) at an intra-oceanic subduction like environment onto an active arc like terrane (Brandl et al, 2006). The above mentioned events resulted in the conclusion of the calc-alkaline magmatism of

the trondhjemite suite and buck ridge porphyry and allied volcanics (Brandl et al, 2006). Between 3.25 and 3.20 Ga there was a second period of intra-arc, NW directed thrusting (D2) which affected both the Barberton and ancient gneiss complexes, the vertical rotation of the BGB, collisional suturing, emplacement of the tonalitic suite of intrusions and amalgamation of the BGB and ancient gneiss complexes have all been attributed to this second period (D2) of widespread convergent tectonism (Brandl et al, 2006). Brandl et al, (2006) also noted that the transcurrent shearing D3 followed the D2 event.

1.4. Geology in the vicinity of Bon Accord (BA)

The BA Ni-oxide deposit (Fig 1.4) occurs on the farm Bon Accord, but currently only a mined out void remains. According to the interpretation of de Wit and co-workers, BA is hosted within the Jamestown Ophiolite Complex (JOC) of the Onverwacht Group (see discussion below). The BA nickel oxide deposit formed a lens close to the contact with a tightly folded band of Moodies Group quartzite (de Waal, 1978) and the meta-peridotites of the JOC, and it was underlain by a metamorphosed succession of E-W striking mafic and felsic schists as well as cherty and ultramafic materials of the Theespruit Formation.

The metamorphic grade has been interpreted to represent an upper greenschist facies with evidence of retrograde metamorphism to lower temperature assemblages. The northern portion of the Bon Accord farm is underlain by tonalite gneiss assemblages while the southern portion of the farm is characterised by the occurrence of massive talc bearing serpentinites and talc schist (as seen at Scotia Talc Mine).

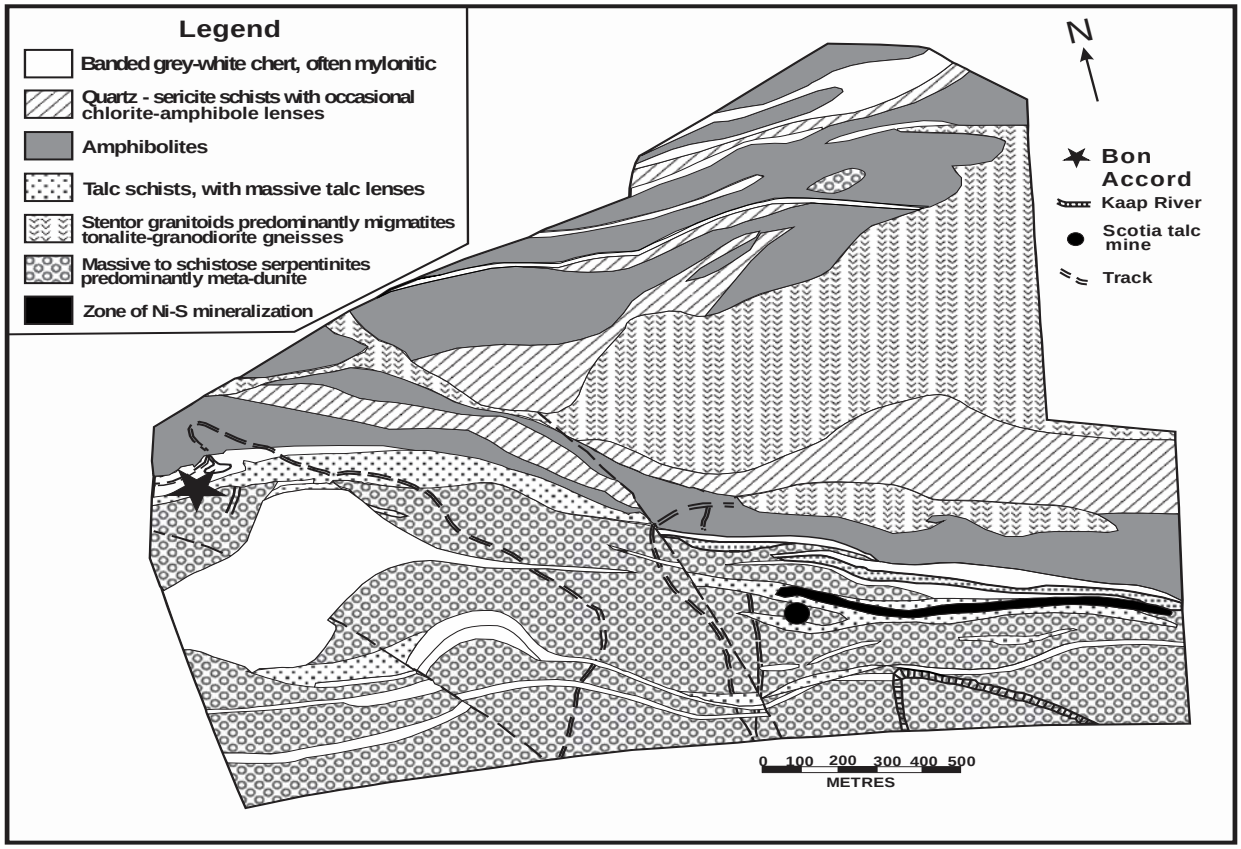

<u>Figure 1.4.</u> Geological map around the BA occurrence, showing both the BA oxide deposit and Scotia Talc mine (Adapted from Tredoux et al, 1989). Latitude. 25° 40' 0S, Longitude. 31° 10' 0E.

On the western portion of Scotia Talc Mine, the upper chert horizon interfingers with a nickeleferous magnetite-chlorite rock (Keenan, 1986). The high magnetite content (up to 70%) in these rocks led Keenan (1986) to suggest that maybe the mineralogy of this magnetite chlorite rock may be similar to that of BA nickel deposit. The rocks of the lowermost Tjakastad subgroup have been interpreted as part of a thick (≈17 km) continuous volcanic sequence (Onverwacht Group), dominated by ultramafic lavas, while the rocks of the upper unit (Geluk Subgroup) hosts mafic and felsic lavas (de Wit and Tredoux, 1988). The reconstruction of the section through the BGB suggests that the fundamental part of this section consists of a lower (rare earth elements-

REE depleted) peridotitic tectonite zone (Tredoux et al, 1989). This zone is then overlain by a zone which consists of a complex array of magma chambers and conduits (in part sheeted), which in turn intrude and are covered by a substantial carapace of pillow lavas and thin cherts (Tredoux et al, 1989). The JOC is defined by the mafic-ultramafic rocks of the BGB, and it forms a pseudo-stratigraphy comparable to that of Phanerozoic ophiolites (de Wit et al, 1987). The JOC consists of a high temperature tectono-metamorphic peridotite overlain by an intrusive-extrusive igneous section, which is in turn capped by a chert-shale sequence (de Wit et al, 1987). Within single intrusive units in this complex there is a complete range from komatiitic to tholeiitic compositions. The BA nickel sulphide mineralisation is located on the Bon Accord farm south east of the BA nickel oxide deposit (currently owned by African Nickel). This sulphide deposit is enriched in fuchsite and chromian spinel in the quartz-muscovite schists. The Mineralisation occurs in rocks of the lower Tjakastad subgroup within a cherty succession near a contact with altered ultramafic assemblages (Keenan, 1986). Keenan, 1986 also noted that the silicified host rocks and sheared sulphide bearing komatiites or alternatively the nickel sulphide from the komatiites may have been preferentially accumulated in semi-consolidated inter-flow cherty material.

1.5. Brief history of the mining history of the BA oxide body

The first discovery of the BA nickel oxide deposit was made (by a mining inspector) in the 1920s, and it was described as a mixture of nickel silicate and magnetite. The initial attraction of this deposit was due to the extreme NiO assays (≈36%) obtained from massive material in the centre of the body (Fig 1.5); however, due to lack of technological know-how at the time of the

initial discovery, the smelting of this enriched nickel ore could not be acchieved and the deposit was then abandoned. It was rediscovered in the 1970s, during a regional nickel exploration program by Eland Resources Limited.

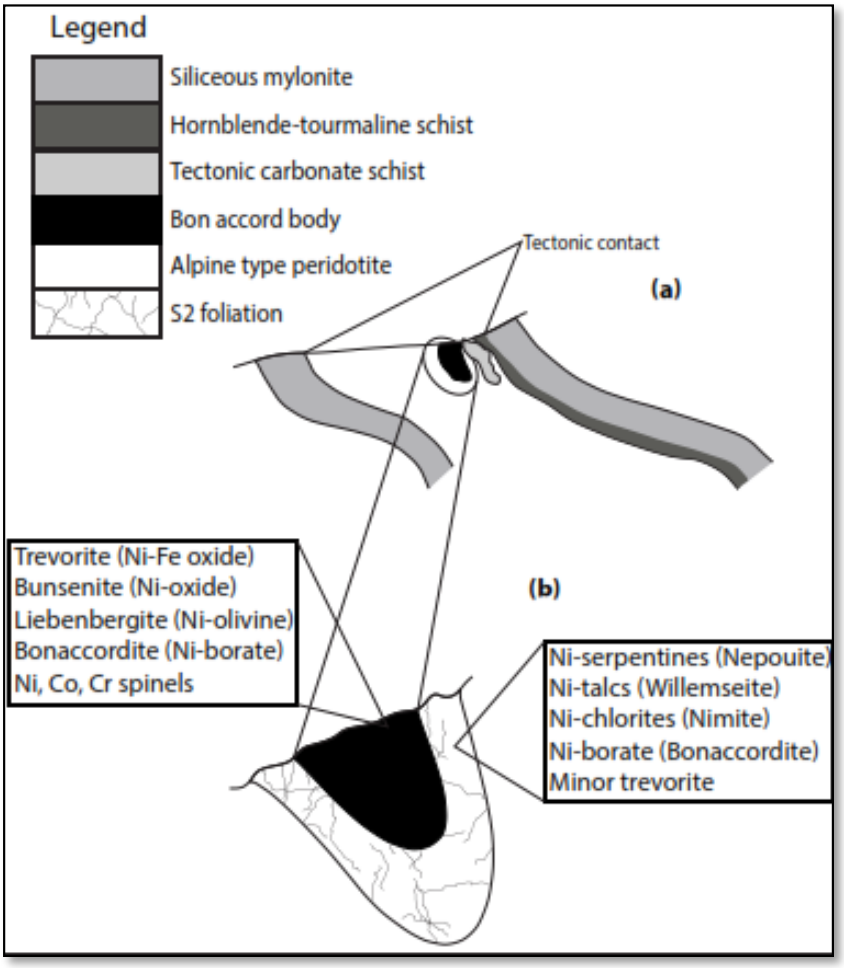

Figure 1.5. (a) Schematic section across the BA occurrence and its host rocks (not to scale). (b) Expanded section of the BA ore body, showing simplified distribution of the nickel minerals with respect to the overprinted D_2 schistosity, not to scale (Adapted from Tredoux et al, 1989).

Due to the BA oxide deposit forming as a small tabular body at the contact between the Moodies quartzite and serpentinised ultramafics of the JOC, it made the study of the origin and mutual relationship between the two assemblages (Moodies quartzite and serpentinised ultramafics of

the JOC) extremely difficult (de Waal, 1978). During a study conducted by de Waal (1969), a variety of nickel rich minerals were identified, which he identified as, nickel rich talc (willemseite), nickel-rich chlorite (nimite), reevesite, as well as violarite and millerite, prior to the discovery of these minerals a nickel rich talc mineral (trevorite) was first reported by Major Tudor Gruffydd Trevor in the 1920s (Mindat.org, 2013).

The exotic nature of the BA nickel oxide deposit led de Waal (1969), to describe associations between different mineral assemblages namely: (a) willemseite-nimite-ferroan trevorite-reevesite-millerite-violarite-goethite and (b) Ni-trevorite, Ni-olivine, Ni-serpentine, ludwigite-Bunsenite-violarite-millerite-gaspeite-nimite. In the process of describing different mineral assemblages several new minerals were identified: cochromite – cobalt rich spinel, nichromite – nickel and chromium-rich spinel, ferroan trevorite (de Waal, 1969), nimite – nickel-rich chlorite, willemseite, a nickel-rich talc and liebenbergite, a nickel-rich silicate. The rare and exotic nature of the mineral assemblages formed the beginning of exploration of BA oxide deposit's possible origin. During the process of classifying BA nickel oxide deposit's origin, de Waal (1978) and Tredoux et al, (1989) proposed the origin models discussed below. Unfortunately most of the ore was removed during prospecting and mining activities such that in-situ investigations of the different assemblages were not possible (de Waal, 1973).

1.6. Observational constraints made by de Waal (1978 and Tredoux et al (1989):

The mechanisms of formation for the BA oxide deposit have been subject of major debate and controversy since its first discovery in the 1920s. This debate resulted in the offering of a variety

of mechanisms of formation. Any proposed mechanism of formation will have to account for the following:

- The position of the Bon Accord oxide deposit within an extensive sheet of coarse-grained ultramafic rocks.
- The association of Bon Accord with hornblende-tourmaline schist along its upper margin.
- The size and apparent rootless nature of the Bon Accord oxide deposit.
- The characteristic sharp contact between the fine and coarse textured rocks of the Moodies group and the JOC.
- The exceptionally high Ni contents of the ore and its unusual mineralogy.
- The similar compositions of chrome-spinels of Bon Accord oxide deposit and those of other local peridotites.
- The constant bi-modal grouping of the chemistry and isotopic ratios on Bon Accord samples, which appear to reflect the control of two distinct mineral assemblages.
- The PGE geochemistry, which is not only extraordinary in absolute concentrations of these elements as well as trends displayed between two distinct groups (group A-enriched in Sb, Ni and Fe and group B-enriched in As and LREE from previous studies).
- The unusual trace element geochemistry, including the very low sulphur and copper contents.

- The strong similarity between the Pb-Pb and Sm-Nd-isotopic data of Bon Accord oxide deposit and those of mafic-ultramafic rocks at other localities in the greenstone belt.

1.7 Models proposed for the formation of the Bon Accord body:

1.7.1. The proposed palaeo-meteorite (de Waal, 1978)

The most likely mechanism of origin for the BA Ni-oxide deposit as proposed by de Waal (1978), suggests that a nickel-iron meteorite could have reacted with and was oxidised by a peridotitic komatiite-type magma and therefore this mode of origin could be used to explain the features observed in the BA nickel oxide deposit.

In this model, it is envisaged that during the extrusion of the Onverwacht lavas ≈3.5 Ga ago, a nickel-iron meteorite (with iron content ≈ 50%) was engulfed by komatiitic magma. The oxidation of the metal phase and introduction of silicates and boron occurred during the initial reaction with the magma and later reaction with the crystalline komatiites during a complex history of metamorphism. The high temperature minerals: trevorite, liebenbergite, bonaccordite and Bunsenite observed in the deposit were formed during the process of impact. de Waal (1978) also noted that the preservation of the original structure was due to the above-mentioned reactions occurring below the liquidus temperature of the impactor and that the reworked meteorite was finally placed in its present position. It was also noted that the time of nepoutisation of the liebenbergite was rather difficult to assess, but that the formation of willemseite and nimite was due to the shearing effects on the contact of the competent quartzite and incompetent serpentinite. Accordingly the shearing affected the palaeometeoritic material in

an inverse proportion to its trevorite content (competency) and may also be responsible for the orbicular structures found in one of the rocks. It was also noted that during this time a minor redistribution of nickel occurred to form five different types of rocks: I) a massive trevorite-népouite rock, II) a sheared trevorite-willemseite rock, III) a schistose ferroan trevorite-magnesian willemseite-nimite rock, IV) a mixed magnesian willemseite-chlorite-nickeloan magnetite schist and V) a nickeloan talc-chlorite magnetite schist away from the main body.

1.7.2. Crustal models (Tredoux et al, 1989)

The following models were proposed to shed light on the unique nickel occurrence in the BA oxide deposit, without invoking a meteorite precursor. Tredoux et al (1989) proposed their models to try and resolve whether the extreme nickel and PGE enrichment of BA oxide deposit happened in the mantle (i.e. before being emplaced in the crust) or whether this enrichment resulted from secondary redistribution of disseminated values in the crustal environment.

1.7.2.1. Formation due to secondary alteration of a massive Ni-sulphide ore body.

Formation by this mechanism should be similar to those described in association with the Archean komatiitic flows at Kambalda (Tredoux et al, 1989). However field relationships raised potential concerns when looking at this model especially when taking into account the model of deep mantle origin of ultramafic rocks proposed by de Wit et al, (1987) in the vicinity of Bon Accord. These concerns were due to the fact that the Kambalda massive Ni – Cu ores are always associated with komatiitic flows and feeders to these komatiitic flows, while the underlying dunites carry only weakly disseminated sulphides. The de Wit et al (1987) model would imply that the BA nickel oxide deposit host rocks, represent deep level ophiolitic peridotites, stratigraphically placed below the komatiites and dunites (mentioned above) thus making it

almost impossible to host massive ore bodies. Furthermore, Tredoux et al (1989) noted that there is no mineralogical evidence in any of the BA oxide samples suggesting replacement of pre-existing sulphide minerals by the current oxide minerals.

1.7.2.2. Formation due to alteration of a chromite pod often associated with the lowermost peridotites of ophiolites.

Deposits of this nature are normally associated with the lowermost peridotites of ophiolites (Tredoux et al, 1989), where (in the case of Bon Accord oxide deposit) the chromite could have been replaced by trevorite to form the nickel-rich mineralogy. Based on the petrographical information of the BA oxide deposit, this type of formation mechanism would certainly seem to suit the formation mechanism for the BA oxide deposit, and if the de Wit et al (1987) model is applicable to surrounding ultramafic rocks then the geological setting would also be in support of such a model. However, Tredoux et al (1989) noted that this model is not fully convincing, because the expected PGE patterns of chromite pods of ophiolites, which show negative trends (i.e. enrichment of the IPGE relative to the PPGE), do not match those of the BA nickel oxide deposit.

1.7.2.3. Formation caused by serpentinisation during mid-ocean ridge type metamorphism.

The mechanism of formation by serpentinisation during mid-ocean ridge type metamorphism was only considered after it was established that the rocks of the JOC underwent extensive hydration and serpentinisation following their formation (Tredoux et al, 1989). These two processes (hydration and serpentinisation) could be called upon to explain the association of Bunsenite with serpentinised liebenbergite following observations made by (Dick, 1974) that awaruite forms during serpentinisation of olivine. However, the petrography indicates that the

liebenbergite-bunsenite assemblage pre-dates the formation of népouite from liebenbergite (Tredoux et al, 1989), which precludes the possibility of bunsenite being formed due to the serpentinisation of Ni-olivine.

1.7.2.4. Formation due to dynamo- thermal metamorphism during granite emplacement.

Evidence supporting late metamorphic events of greenschist-amphibolite facies grade and associated deformation are recorded along the margins of the greenstone belt (Tredoux et al., 1989). Association of BA nickel oxide deposit and tourmaline-hornblende schist and presence of a borate mineral (bonaccordite) in BA oxide deposit serve as an indication of metasomatism. Fluids which could have served as sources for the boron could have been derived from the nearby syntectonic granitoids plutons (de Wit et al., 1987).

The elevated radiogenic Pb and disturbances of the Sm/Nd isotopic systematics in the group B samples (also enriched in As and LREE) can be explained by the higher fluid/rock ratios in the more schistose margin of the body. However, the ages indicated for the BA nickel oxide body by the U-Pb and Sm-Nd systems do not show a major resetting at 3 Ga (the intrusion age of the adjacent Stentor pluton (Tredoux et al, 1989).

1.7.2.5. Hydrothermal/volcanic-exhalative model.

Tredoux et al (1989) proposed that ores of this origin generally have distinctly different fields of Ni/Fe ratios unlike those observed in BA oxide deposit. Some of the geochemistry (Co>5000ppm, Cu<100ppm) does not correspond well with that observed in hydrothermal/volcanic-exhalative ores. These ores are generally characterised by depletions in siderophiles and enriched in chalcophiles (Co<300ppm, Cu>1000ppm) and have S~9% and the

PGEs trends and concentrations in these hydrothermal/volcanic-exhalative ores are characterised by the apparent depletions in Os, Ir and Ru relative to Pt and Pd.

1.7.2.6. Core formation and its implications for BA.

Tredoux et al (1989) proposed a model that envisages the BA nickel oxide deposit as already concentrated into a massive, Ni-PGE enriched form in the asthenospheric mantle prior to its emplacement into what was then lithospheric mantle. Due to the extreme nickel enrichment, absence of sulphides and lack of evidence suggesting that the BA nickel oxide deposit never had sulphide mineralogy, it was then concluded the BA nickel oxide deposit originally was a metallic mass. However, they rejected the palaeometeoric origin proposed by de Waal (1978), because of mineralogical similarities, e.g. of chromites, between the BA nickel oxide body and the host ultramafics. Tredoux et al (1989) proposed that the BA nickel oxide deposit might have originated from a metal-enriched mass which formed in the lower mantle during inefficient separation of Fe-Ni alloy from the proto-mantle. Thus they envisaged the proto BA nickel oxide deposit to have been an alloy that separated out from host silicates at depth either (a) in the residual lower mantle after initial core event formation or (b) from material which accreted and did not sink, after the main core event formation. This model requires that the alloy-silicate separation never reach completion, so that the Fe-Ni metal remains intimately associated with the host silicates. Therefore silicates containing little amounts of metal could rise with upwelling plumes that are generated near the D" layer. The metallic ‘xenolith’ would then be progressively oxidised as it becomes exposed to increasingly less reducing conditions in the upper mantle.

1.7.3. The asthenosphere model (Wildau, 2012)

The work conducted by Wildau (2012), was mainly based on investigating microscopic phases in the BA nickel oxide deposit and possible formation mechanisms for the studied mineral assemblages were also proposed. This study suggested that two processes could be responsible for the formation of the BA nickel oxide body. (1) A magmatic high-temperature formation and (2) A hydrothermal low-temperature formation. Wildau (2012) proposed that the cochromite/nichromite and liebenbergite formed the primary assemblage during a magmatic high temperature process, while the liebenbergite became altered to népouite and further to willemseite during hydrothermal alteration. Furthermore Wildau (2012) reported a variety of unidentified minerals, only reported as unknown #1 to unknown #8. Wildau (2012) concluded that the Ge-enriched generation of unknown #1b / unknown #1c / trevorite / ferroan trevorite / nickeloan magnetite formed as by-products. Nimite is said to have formed during these processes, Ge-depleted generation of unknown #1b / unknown #1c / trevorite / ferroan trevorite / nickeloan magnetite formed under hydrothermal conditions, together with bonaccordite and the second generation of bunsenite. The sulphides, sulphosalts and pure Sb and Cu formed at least during the formation of the Ge-depleted trevorite.

1.8. Motivation of this study

The BA nickel oxide body represented a unique Ni-oxide deposit, which was surrounded by nickel sulphide (African Nickel Limited) and talc (Scotia Talc Mine) deposits in close proximity. The BA nickel oxide deposit appears to be the only deposit of its type found in the world, since its occurrence seems to be confined to the Bon Accord farm in Barberton, Mpumalanga. The

debate on the origin of the BA nickel oxide deposit resulted in researchers proposing different mechanisms of formation, ranging from association with a meteorite impact to deep earth origin (magmatic high-temperature formation). A major open question remains the connection, if any, between the BA nickel oxide body and the adjacent zone of sulphide mineralisation.

The research reported on in this dissertation was largely based on investigating the nickel oxide mineralisation of the BA nickel oxide body itself and uncovering the uniqueness of this exotic deposit. The distinctive nature of BA nickel oxide deposit is such that the mineral enrichment apparently is confined to a small area and the extent of the deposit as measured in the field at about 10x8x2m, but the possibility of other similar pods may exist, but are just not on outcrop at the current erosion levels.

The study aimed to provide clear methods and mechanisms which can be applied in modelling the characteristics of the nickel mineralisation in the BA nickel oxide body type deposit. Another aim was to establish parameters that can be applied in similar localities to find similar deposits. The aforementioned aims will be established through a variety of investigations and analyses which will measure and record the mineralogical and chemical characteristics of the BA nickel oxide deposit. This study also attempted to delineate any correlations and/or disassociations to previously proposed models with current findings. Accurate determination of these parameters would establish a precedent for future work on similar deposits.

The study area therefore was confined to the BA nickel oxide deposit and surrounding nickel sulphide and talc deposits due to lack of sufficient quality samples and the aims of the research were largely and specifically based on uncovering the cause(s) that resulted in the uniqueness of the NiO rich BA nickel oxide deposit.

1.9. Research questions and goals

1) To establish the relationship between the possible geochemistry of deep mantle materials and the BA oxide deposit (looking at currently existing mineralogy and geochemistry data).

2) To re-evaluate previously proposed models for the formation of the BA body in the light of the current new data.

3) To establish, if at all possible, whether there is any relationship between the nickel-oxide rich BA deposit and the surrounding low-grade sulphide rocks.

PLEASE NOTE THE FOLLOWING IMPORTANT POINT:

In the text that follows, Bon Accord oxide has been abbreviated to BA oxide or BA nickel oxide. Please note that BA oxide and BA nickel oxide refer to the same deposit thus have been used interchangeably in the text that follows. The stratiform sulphide layer will be referred to as the BA sulphide.

Chapter 2 - Research methodology

A summary of samples investigated in this study is given in Table 2.1. A more comprehensive description of the different analytical techniques used and their functions can be found in Appendix A.

Table 2.1. Samples with their place of origin and method of investigation (✓= analytical technique used and ✖ = analytical technique not used)

Sample ID	Origin	Sample description	OM	XRF	SEM	EMPA	ICP-MS	ICP-OES	SUS
NC-A to NC-G	Collected at site	Bon Accord Ni-oxide host rocks	✓	✓	✓	✓	✓	✖	✓
NC-H to NC-K	Donations	Bon Accord oxide ore rocks	✓	✓	✓	✓	✓	✖	✓
NC-L	Collected at site	Scotia Talc Mine	✓	✓	✓	✓	✖	✖	✖
NC-MA and NC-NA	Collected by supervisor	Kraubath alpine ophiolite, Austria	✓	✓	✓	✓	✓	✖	✖
UFS	African Nickel Ltd	Bon Accord Ni-sulphide host rocks	✖	✖	✖	✖	✓	✓	✖

OM = Optical microscopy, XRF = X-ray fluorescence, SEM = Scanning electron microscopy, EMPA = Electron microprobe analysis, ICP-MS = Inductively coupled plasma mass spectroscopy, ICP-OES = Inductively coupled plasma optical emission spectroscop,y and SUS = magnetic susceptibility.

2.1. Sampling

A total of twenty samples were involved in this study at various localities (Table 2.1). The samples were collected and sourced in different locations (Table 2.1 and Fig 2.1) and underwent

specific and different investigations and analyses. Out of the twenty studied samples, only ten samples (NCA-NCG and NCH-NCK) underwent through the whole range of investigations and analyses with the exception of ICP-OES investigations (Table 2.1).

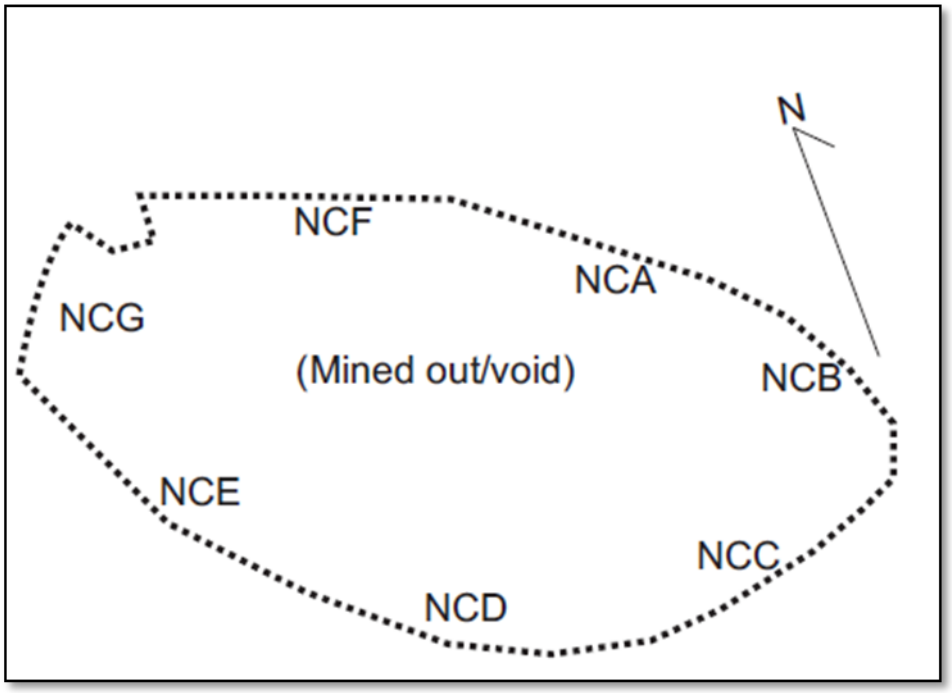

Figure 2.1. Pit outline with the respective areas where host rock samples NCA-NCG were collected in the exploration pit left in the field (not to scale: the long diameter of the pit is ~5 m).

The Kraubath samples were included in this research for comparison purposes, as they are considered to represent a *de facto* ophiolite (Malitch et al, 2003). The Kraubath dunite–harzburgite massif, the largest mantle relict in the Eastern Alps, is situated within the Austrian Province of Styria. It has been interpreted as part of a dismembered Precambrian to Early Paleozoic ophiolite sequence, strongly deformed and metamorphosed, which forms part of the Speik Complex (Malitch et al, 2003). The BA oxide body host rocks have been described as ocean floor that has since been obducted onto the continental crust. Therefore comparisons

between the Kraubath samples and BA oxide host rock samples provided a good opportunity to investigate this interpretation.

2.2. Susceptibility measurements

Susceptibility measurements were obtained for all of the BA oxide deposit samples (NCH to NCK) and all the host rocks (NCA to NCG), using a KT-6 hand held magnetic susceptibility meter with an effective resolution of 1 x 10^{-5} χ (the SI unit for magnetic susceptibility). To get a better understanding of how susceptibility measurements are reported, there are certain parameters that need to be defined:

The intrinsic magnetic susceptibility of a material (χ, gauss oe-1 cm-3) is defined as χ, =J/H, where χ, is the magnetic susceptibility, J is the magnetisation and H is the applied magnetic field strength (Rathore and Heinz, 1980). To obtain measurements the hand held KT-6 meter was placed on a flat face of the sample to be measured for a few seconds. Once the meter was removed, the true magnetic susceptibility measurements of the sample were displayed on the screen in SI units.

2.3. Geochemical analysis

The samples that underwent geochemical analyses were coarse crushed to average grain size 5-10cm, and then split into two samples. The one part of the split was crushed using a Retsch KG 5657 Haan BB100 jaw crusher composed of breaking jaws and wearing plates made up of tungsten carbide. After crushing the samples were milled using a Siebtechnik swing mill using a steel carbide bowl. This sample preparation technique was for the production of pellets and fused beads for XRF analysis. Half of the other part of the split was used for the preparation of thin sections, using a slab saw. The remaining material was kept in the archive as reference material.

2.3.1. Mineral chemistry

2.3.1.1. Optical microscopic analysis

The analyses carried out using the optical microscope were conducted on two types of sections. (1) A 30µm thick slice of rock attached to a glass slide using epoxy-resin embedding medium (standard petrographic thin section) and (2) Circular polished sections. The sections were optically investigated in transmitted and reflected light using an Olympus BX 51 binocular microscope at the Geology Department, University of the Free State (see Appendix A, Fig. 2). Photomicrographs were taken using the Altra Soft Imaging System 20 camera mounted on the optical microscope.

2.3.1.2. Scanning electron microscope (SEM)

The Joel JSM 6610 scanning electron microscope at the Geology Department, University of the Free State (Fig. 2.2) was used to do both semi-quantitative and quantitative work. SEM analyses were conducted on BA oxide deposit samples, BA oxide deposit host rocks, NC-L and Kraubath samples, with the main focus largely on the Ni-rich phases observed in the BA oxide deposit. Both thin and polished sections were used for analyses. Sample preparation is of paramount importance when working with the SEM, so prior to placing the samples in the SEM, the samples had to be prepared by carbon coating them (to prevent sample charging). Upon completion of the carbon coating process, the samples were then fixed in the sample holder of the SEM. Once fixed, only the polished sections were stuck with carbon tape to prevent electrical charging to avoid negatively impacting the measurements and mapping authenticity. The SEM was used as an aid in the identification of rare mineral phases and it was preferred due to its

application of non-destructive analyses on solid surfaces, therefore aiding in sample preservation.

Figure 2.2. The Joel JSM 6610 scanning electron microscope at the Geology Department, University of the Free State.

2.3.1.3. Electron microprobe analysis (EMPA)

The Joel JSM 5410 EMPA (Appendix A, Fig. 4) at the Geology Department at the University of Johannesburg was used to determine the samples' chemical data. Thin and polished sections were used, both types of sections were carbon coated prior to being mounted on the sample holder. The EMPA functions in a similar manner to the SEM, in that it is a non-destructive analytical tool; it operates under the following principles: to obtain results from the SEM, a solid sample material needs to be bombarded by an accelerated and focused electron beam.

The EMPA was used for the analysis of individual mineral phases and also to quantify the elemental concentrations in each mineral phase that was analysed. The individual mineral phases were identified and analysed in rock samples as listed in Table 2.1.

2.4 Whole rock geochemistry

2.4.1. X-ray fluorescence (XRF)

The PANalytical WD-XRF Axios spectrometer at the Geology Department, University of the Free State was utilised for the investigation and analyses of major and trace elements (Fig. 2.3). The XRF is however a destructive tool but it was still used to gain whole rock geochemical data.

Figure 2.3. The PANalytical WD-XRF Axios spectrometer, Geology Department, University of the Free State.

Due to the delicate nature of the host rock samples, it was imperative to firstly remove the weathered surfaces (mainly on the BA host rocks) on the rock samples to provide fresh material.

The rocks were then crushed and milled to produce a homogenised powder. The milled powder was weighed using a Precisa BJ 6100D balance and then dried in an oven furnace at temperatures of 110ºC for 24 hours. After 24 hours it was weighed again to determine the surface water lost. It was then roasted for a further 4 hours at 1000ºC and weighed again to determine the loss on ignition (LOI) which represents water bound in the minerals. From the roasted powder fused beads were produced for the analysis of major elements and pellets were used for the analyses of trace elements. The unusual chemistry of BA oxide samples meant that the production of fused beads could not be prepared and processed by the normal methods used for fusion beads preparation for major element analysis by XRF.

Major elements fused beads of the BA oxide samples were produced in the following "unconventional" manner: a mixture of 1.5g Li-metaborate and Li-tetraborate (fluxes) together with 0.21g of milled sample plus 0.7g SiO_2 and 0.02g of sodium nitrate were mixed, thus adding up to 2.43g in total. From this mixture, fused beads were then prepared for major element analysis. The major elements that were analysed include: SiO_2, Al_2O_3, Fe_2O_3, MnO, MgO, CaO, NaO, K_2O, TiO_2, P_2O_5, CoO and NiO.

Pellets were pressed from 8g of crushed and milled sample mixed with 3g of Hoechst wax, the mixture was then shaken in the Griffin flask shaker for ±5 minutes. After mixing in the Griffin flask shaker the homogenised powder was then compressed into pellets for the analysis of trace elements. All the studied samples were analysed for major and trace elements by XRF with the exception of the UFS samples. Trace elements that were analysed include: Sc, V, Cr, Co, Ni, Cu, Zn, As, Br, Rb, Sr, Y, Zr, Nb, Mo, Ag, Cd, Sn, Sb, Ba, Tl, Pb, Th and U.

2.4.2. Inductively coupled plasma- mass spectrometry (ICP-MS)

The ICP-MS (Fig. 2.4) represents a destructive analytical method but it has an advantage in that it produces accurate results for trace elements due to its inherent sensitivity capabilities.

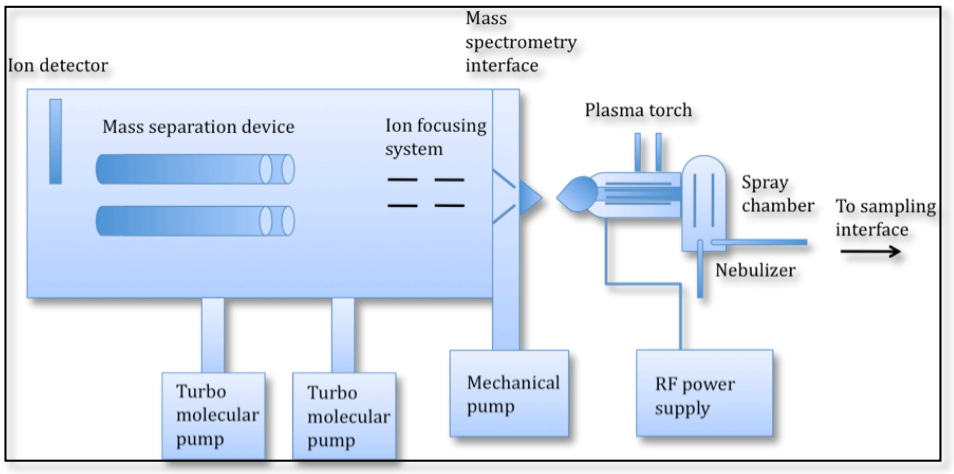

Figure 2.4. Schematic depicting the basic components of an ICP-MS system (connexions, 2010).

This method uses liquid or solid samples but for this research liquid samples were used during analyses. The multi-collector ICP-MS at the University of Cape Town, Department of Geological Sciences was used. The following trace elements. Sc, V, Cr, Co, Ni, Cu, Zn, As, Br, Rb, Sr, Y, Zr, Nb, Mo, Ag, Cd, Sn, Sb, Ba, Tl, Pb, Th and U in BA host and BA oxide samples.

Chapter 3 – Mineralogy results

Full descriptions of the individual thin sections together with their specific abundances and photomicrographic evidence in each of the samples are given in Appendix B. This chapter will discuss summaries of the general characteristics (both physical and microscopic descriptions) of minerals in each sample together with all the various mineral associations in different environments. For an explanation of the sample names and the provenance of the samples see Table 2.1.

3.1. Optical mineralogy

3.1.1. A summary of major mineralogy

The BA host rocks, Kraubath samples and ANL nickel sulphide samples, contained common minerals are similar to those normally expected and found in ultramafic rocks (such as peridotites, komatiites etc.). The common minerals noted in the above mentioned rock types have been divided into different groups: silicates, oxides, hydroxides and sulphides, and are listed in Table 3.1.

The minerals listed in Table 3.1 are the major components of the rocks in the vicinity of the BA oxide mineralisation, as well as the mafic-ultramafic samples from the Kraubath massif in the Austrian Alps. The samples NC-L and the all the ANL samples are representative of the stratiform sulphide layer near the BA oxide deposit, and are therefore highly enriched in sulphide minerals.

Table 3.1. Common mineral groups observed in the studied thin sections.

Silicates	Oxides	Hydroxides	Sulphides
Amphibole	Hematite	Goethite	Chalcocite
Chlorite	Ilmenite		Chalcopyrite
Olivine	Leucoxene		Gersdorffite
Pyroxene	Magnetite		Pentlandite
Quartz			Pyrite
Serpentine			Pyrrhotite
Talc			

- ***Silicates minerals***

Chlorite [$(Mg, Fe, Al)_3 (Si, Al)_4O_{10}(OH)$]

The chlorite is an anisotropic mineral, characterised by prismatic crystals (Fig. 3.1a). Under transmitted light it is light yellow with weak pleochroism. In some cases it is distinguished by its apparent "micro-folding" structures and higher than normal relief and it is mainly interwoven with talc, a clear genetical link between these two mineral species.

Talc [$Mg_3Si_4O_{10} (OH)_2$]

The talc (Fig. 3.1b) represents an anisotropic phase and occurs as kinked grains. In transmitted light it is colourless to slightly yellowish green with very weak pleochroism. The crystals always

occur as clustered cumulates. The kinked grains could be an indication of micro-folding in the vicinity of the BA host rocks.

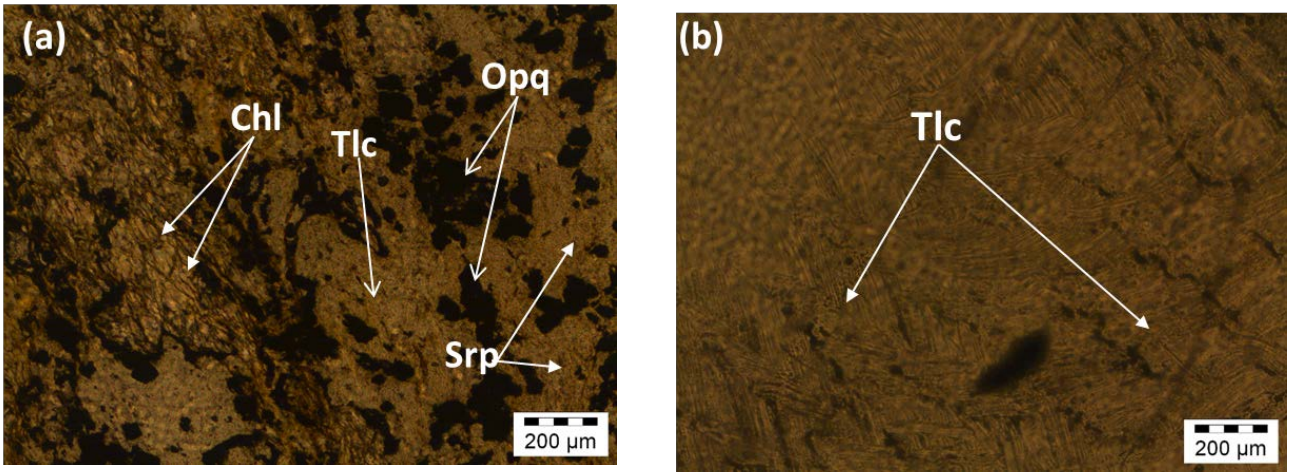

Figure 3.1. (a) Different mineral assemblages with little amounts of serpentine (with typical needle like appearance) embedded within the talc in the host rocks. Talc-chlorite-spinel assemblage in transmitted light under crossed nicols – Sample NC-B and (b) Talc flakes exhibiting chevron texture (possibly indicative of micro-folding), in transmitted light – Sample NC-A. Photomicrographs taken using the Olympus BX 51

Serpentine [$Mg_3Si_2O_5(OH)_4$]

The serpentine is an isotropic mineral phase characterised by lath shaped (Fig. 3.2a) intergrown crystals. In transmitted light it is colourless to pale yellowish green without pleochroism.

Quartz [SiO_2]

Quartz (Fig. 3.2b) is an anisotropic mineral exhibiting xenomorphic grain shapes, under transmitted light quartz appears colourless without any pleochroism and shows typical greyish interference colours under crossed polarisers. The quartz in BA host rocks characteristically occurs as singular inequigranular grains associated with opaque minerals.

- ***Oxides and hydroxides minerals***

Magnetite [$Fe^{2+}Fe^{3+}{}_2O_4$]

Magnetite is an isotropic mineral, black in colour without pleochroism under transmitted light. It is whitish grey under reflected light and occurs in close association with the sulphide minerals (pyrite and chalcopyrite) however only in small proportions and often seen as single grains.

Hematite [Fe_2O_3]

Hematite is isotropic and in transmitted light it exhibits blood red colours without any pleochroism. It does not change colour in reflected light and mostly occurs as veins or infilling veins (Appendix B, NCE and NCF) and has no apparent grains visible both in transmitted and reflected light.

Ilmenite [$FeTiO_3$]

- Ilmenite is isotropic in nature and characteristic of the skeletal texture in some of the sections studied (Appendix B, NCD). The ilmenite always appears closely associated with the mineral magnetite in all cases where ilmenite was observed, a characteristic attributed to alteration.

- ***Sulphides minerals***

Pyrite [FeS]

Pyrite is an isotropic phase, occurring as minute and at times cubic grains always associated with magnetite and at times chalcopyrite. It displays yellowish colours in reflected light.

Chalcopyrite [$CuFeS_2$]

Chalcopyrite is an isotropic phase. When viewed under reflected light it occurs as minute yellowish grains embedded within the oxide minerals. It largely occurs as irregular grains with large variation in size, from minute to slightly large and mostly associated with magnetite.agnetite.

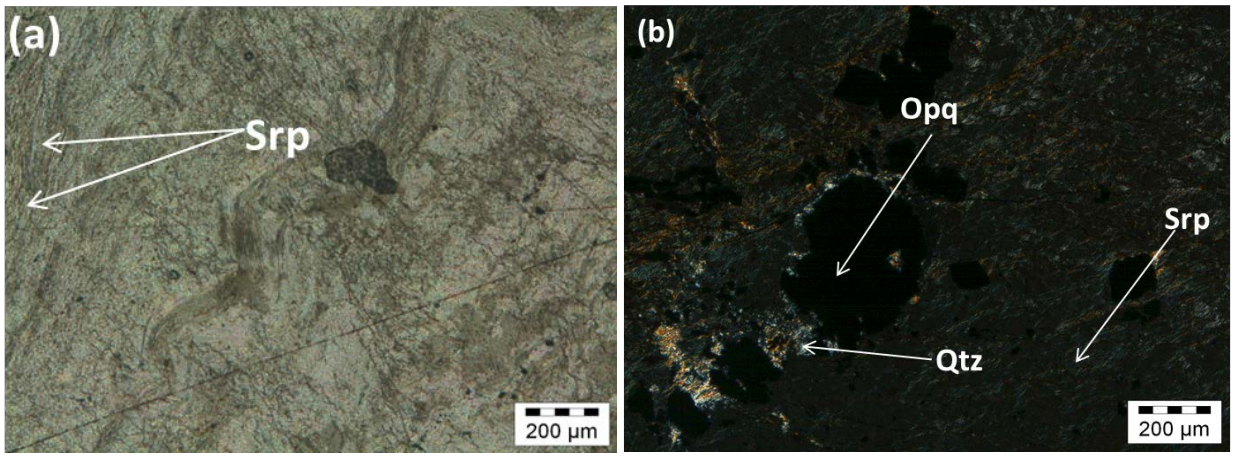

<u>Figure 3.2.</u> Minor amounts of serpentine and quartz occurrence, (a) Serpentine grains in a talc matrix. Kinky textured band filled with talc running across the thin section, in plane polarised view - Sample NC-C and (b) Largely serpentine with some quartz grains hosting the isotropic spinel under crossed nicols. Isotropic minerals appear as scatter granules and seem to be deforming from the rim towards the core, viewed under crossed nicols Sample - NC-F. Photomicrographs taken using the Olympus BX 51 petrographic microscope.

<u>3.1.2. Unusual Ni-rich minerals</u>

The unusual Ni-rich minerals are only observed in the BA oxide samples, these minerals are similar to those noted in table 3.1, except these minerals are highly Ni-rich. The most abundant mineral phases are the talc (willemseite), chlorite (nimite), spinel (trevorite) – see Table 3.2. For mineralogical descriptions and exact chemical formulas the reader is referred to de Waal (1969,

1970a, 1970b, 1972 and 1978, and de Waal and Calk (1973)). The most abundant mineral phases in the BA pod are willemseite (talc), nimite (chlorite) and trevorite (spinel), while the accessories are largely represented by millerite, liebenbergite and serpentines occur scattered.

Table 3.2. Unusual minerals observed in the Bon Accord oxide deposit thin sections.

Silicates	Oxides	Sulphides
Liebenbergite	Bunsenite	Millerite
Népouite	Hematite	Bravoite
Nimite	Trevorite	
Willemseite		

3.2. Summarised general descriptions of different rock types studied

3.2.1 Schistosed peridotite rocks in the immediate vicinity of the Bon Accord oxide body.

(Photomicrographs together with their full descriptions are given in Appendix B.)

The BA host rocks (NCA - NCG) are dominated by talc, minor chlorite, oxides, hydroxides and serpentine group minerals and remnant minute grains of chromite. There are very minute (see appendix D) occurrences of millerite embedded within the oxide minerals and most of these minerals are extremely altered. The grain shapes range from subhedral to completely anhedral. The main texture is characterised by a combination of subhedral and anhedral grains(see samples NCA, NCB, NCC, NCF and NCG in Appendix B), but samples NC-C and NC-G show

occurrences of micro-folding in the oxide minerals where the talc interstices are filled by oxide minerals (hematite, magnetite and/or goethite) (see Appendix B).

3.2.2. The Bon Accord Ni-oxide body. ***(Photomicrographs together with their full descriptions are given in Appendix B.)***

The unusual and rare minerals, talc (willemseite), chlorite (nimite), olivine (liebenbergite), serpentine (népouite), and trevorite (Table 3.2 and Appendix B) observed in the BA oxide samples (NCH - NCK) represent Ni-rich equivalents of the silicates seen in the surrounding (host) rocks. Also observed were nickeloan magnetite, minor ilmenite and limonite and minute sulphide minerals. The grain sizes in the thin sections vary, from large (mm) to small (µm) scale. The abundance of oxide minerals ranges between ±25-45%, while the willemseite, the most dominant silicate, can be as much as ± 35-50%. In some cases the willemseite occurs as irregular flakes and fibers, while the nimite occurs as prismatic crystals and the népouite occurs as fibrous masses characterised by anhedral to subhedral grains. For descriptions of the optical properties of these minerals, see Appendix B.

3.2.3. The Bon Accord Ni-sulphide layer. ***(Photomicrographs together with their full descriptions are given in Appendix B.)***

3.2.3.1 Scotia Talc Mine sample

Sample NC-L is largely dominated by sulphide minerals (pyrite, chalcopyrite and pentlandite), together with some quartz and talc occurring as the next most dominant phases. Little amounts of chlorite were also noted and appear pronounced in this section mainly because of its characteristic greenish colour and platy appearance.

Chlorite occurs mostly mimicking a micro-folding pattern and found embedded within these chlorite patterns are opaque (sulphide) grains. The percentage of the opaque minerals is ± 55% while the next dominant phase (quartz) is ± 25%. This sample is characterised by subhedral to anhedral sulphide and quartz crystals with a porphyritic texture, in a groundmass of talc and chlorite (see appendix B, sample NCL).

3.2.3.2 African Nickel Limited (ANL) samples

These samples come from exploration drill cores and are composed of a variety of mineral assemblages: olivine, pyroxene, weathered chlorites, sulphide minerals (pyrrhotite, pentlandite and pyrite) quartz and serpentine minerals. The olivine (largely dominated by the Mg-rich end member - forsterite) is characterised by fractured phenocrysts as well as its typical granular nature, with compositions ranging between 5-15%. Also, noted was the abundance of massive and stubby prismatic pyroxene crystals. The chlorite occurs weathered in varying degrees, with sample UFS 38e exhibiting the most intense alteration with visible replacement characteristic patterns.

3.2.4. Mafic-ultramafic rocks of Kraubath ophiolite, Austria. (Photomicrographs together with their full descriptions are given in Appendix B.)

Sample NC-MA is dominated by olivine phenocrysts, while the pyroxene occurs as the second most dominant phase. Furthermore, the fractured olivine phenocrysts with alteration occurring along the fracture planes together with cumulate textures are very characteristic in this sample. The olivine percentage was noted at ± 60%. Sample NC-NA is characterised by long prismatic and fibrous crystals and generally shows two directions of cleavage in a hand specimen. It is

largely dominated by the amphiboles, with their percentages measured at ±50%. The occurrence of quartz is characterised by typical infilling of veins running across the sample.

3.3. Summary descriptions of mineralogy under the microscope.

For detailed hand specimen descriptions together with mineral modal percentages, rock types and thin section textures, see Appendix B.

3.3.1. Mineralogical description of the Bon Accord weathered peridotitic host rocks

3.3.1.1 NC-A (talc schist)

NC-A is fine grained with a characteristic anhedral texture. Talc constitute the major component of the thin section followed by blood red opaque minerals (ideally hematite and mostly occurs as infilling veins and cracks). In some instances the talc occurs in veins, while some of the blood red opaque minerals appear strictly confined veins in this section. In some cases, the mineral leucoxene can be seen and it is characterised by its skeletal appearance while its presence is attributed to formation as a result of alteration of the opaque minerals.

3.3.1.2 NC-B (serpentinised talc schist)

Sample NC-B is comprises a dominant talc phase characterised by its subhedral prismatic and almost tabular form. The normally first order interference colours of talc are now in the third order range and its alteration intensity varies throughout the entire section, also, noted under reflected light were bright minute yellowish grains representing sulphide minerals.

3.3.1.3 NC-C (quartz-containing talc schist)

Sample NC-C, is fine grained with visibly irregular grains in the hand specimen. The thin section is characterised by a kinking (chevron) pattern (possibly representing micro-folding structures), and dominated by the groundmass of talc. Serpentines occur as fibrous needle like crystals while the occurrence of chlorite is due to the replacement of previously existing pyroxene and/or other mafic minerals. The opaque minerals appear to be altered and/or replaced to form minute goethite and under reflected light yellowish grains were observed. This section is mainly dominated by anhedral to subhedral crystals with an allotriomorphic texture. There is a clear intergrowth between the talc and opaque minerals as they both follow the same "stream flow" pattern (possible micro-folding)

3.3.1.4 NC-D (talc schist)

The hand specimen is visibly characterised by oxidation colours (Appendix B, Table 4) like most of BA host samples, it has a soapy feel, with a medium grained texture. This sample mainly shows the skeletal texture of the Fe-oxide minerals (common in ilmenite and leucoxene, see Appendix B, Fig 4). The talc mineral series occurs as a dominant groundmass and all the visible hematite now occurs as accessory amounts, due to alteration to form goethite and possibly leucoxene.

3.3.1.5 NC-E (serpentinised talc schist)

Sample NC-E represents a medium grained hand specimen with an aphanitic to porphyritic texture. The physical properties of the hand specimen are characterised by soapy texture as a result of the serpentines, clay minerals, chlorites and talc within the sample. Under optical microscopy investigations, the dominant phases are talc and opaque minerals with minor chlorite

and serpentine. There appears to be replacement and/or alteration of the opaque minerals and the crystals range from subhedral to anhedral in nature.

3.3.1.6 NC-F (serpentinised talc schist)

The dominant phases are talc and opaque minerals (largely the hematite-goethite assemblages). When viewed under the optical microscope, this sample is characterised by subhedral crystals with a hypidiomorphic texture. Some hematite occurs in small patches and under reflected light the replacement of the opaque minerals is much more pronounced and shows dominant yellowish-whitish creamy grains.

3.3.1.7 NC-G (quartz-containing talc schist)

NC-G is characterised by kinking (possible micro-folding structures) structure patterns of talc and oxides (Appendix B, Fig 7). Opaque minerals are largely dominant and therefore occur as the major phases. The groundmass is characteristic of altered talc occurring only in small amounts. Under reflected light, minute yellowish grains (sulphide phases) were observed, these minute yellowish grains occur embedded within the opaque mineral assemblages. Anhedral crystals with a characteristic allotriomorphic-porphyritic texture are a characteristic feature of this sample. The characteristic combination texture is associated with the resultant alteration processes.

3.3.3. Mineralogical description of the Bon accord oxide ultramafic rocks

3.3.3.1 NC-H (ultramafic rock)

This thin section is dominated by a slightly altered/deformed groundmass of prismatic crystals of talc with a poikilitic texture. Chlorite occurs in close association with talc and formed after talc

alteration. Under reflected light the opaque mineral grains seem to have been packed or stacked together to give them a specifically distinctive shape/pattern. These opaque minerals (magnetite and/or trevorite) exhibit a cubic crystal pattern and appear to be replaced therefore resulting in the appearance of ilmenite from the alteration of Fe-oxides and spinel minerals.

The serpentine occurs as acicular fibers embedded within the talc and most of the serpentine minerals are growing and/or inter-growing with the talc. The secondary mineral goethite formed after the alteration of the hematite which now occurs as a minor phase. Major occurrence of blood red opaque minerals (ideally hematite) is confined to veins running across the section.

There are yellowish-whitish grains representing sulphide minerals (millerite, NiS) embedded within the opaque mineral (spinels) grains. Minute grains (approximately 2%) of liebenbergite occur enclosed within the oxide/spinel minerals. The hypidiomorphic texture with subhedral crystals represents the main dominant crystal shapes in this sample, a phenomenon also described by (Tyrrell, 1975), where it was noted that, in cases where subhedral grains are dominating, hypidiomorphic texture can be observed.

3.3.3.2 NC-J (ultramafic rock)

This thin section is dominated by a groundmass of flaky and tabular talc crystals. The crystals range from anhedral to subhedral with a characteristic porphyritic-poikilitic texture. The opaque minerals (trevorite, minor limonite and ilmenite and mainly pseudomorphous goethite) occur as the second dominant phase and the pseudomorphous goethite formed after the alteration of magnetite and hematite which are now present in trace amounts. The occurrence of goethite is much more pronounced as compared to the occurrence of magnetite and hematite. Visibly, fresh hematite is confined to the veins while the serpentine mineral grains occur embedded within the

talc. In some cases the talc and chlorite appear to share a very close possibly genetic relationship as they appear to be inter-growing with each other. The opaque crystals show a cubic crystal form, some of these opaque minerals display replacement by secondary ilmenite, leucoxene and goethite. The replacement seems to be occurring from the core to the rim of the mineral grains. Embedded inside the opaque minerals are yellowish-whitish grains representing sulphide minerals (mainly the millerite mineral series) resulting from a late stage geologic process associated with the envisaged hydrothermal activities in the deposit.

3.3.3.3 NC-K (ultramafic rock)

A highly altered groundmass of talc is clearly visible and pronounced, but the opaque minerals constitute ±75% and serpentine inclusion minerals occur as acicular grains. The intense alteration resulted in very minimal visibility of talc. The chlorite occurs closely associated with talc, while serpentine occurrence is very limited. Embedded inside the opaque minerals are yellowish grains, which are less pronounced, when compared to those in sections NC-H and NC-J. Sample NC-K represents a hybrid of textures, from allotriomorphic and porphyritic to hypidiomorphic texture.

Below is a list of the unusual Ni-rich minerals found in samples NC-H, NC-J and NC-K:

- ***Silicate minerals***

Willemseite [$(Ni, Mg)_3 Si_4O_{10}(OH)_2$]

Willemseite occurs as the major constituent in the BA oxide samples (Fig. 3.3a) and it is only confined to the BA deposit. It represents an anisotropic mineral phase, and when observed in transmitted light, it is usually colourless with characteristic weak pink and green pleochroic

colours (Fig 3.3a and b). In instances where the willemseite has a slightly higher iron content it indicates higher than normal interference colours, a clear contrast to the first order coloured népouite minerals (Fig 3.3c). In some cases the willemseite occurs as irregular flakes and fibers and embedded within are clusters of minute opaque grains.

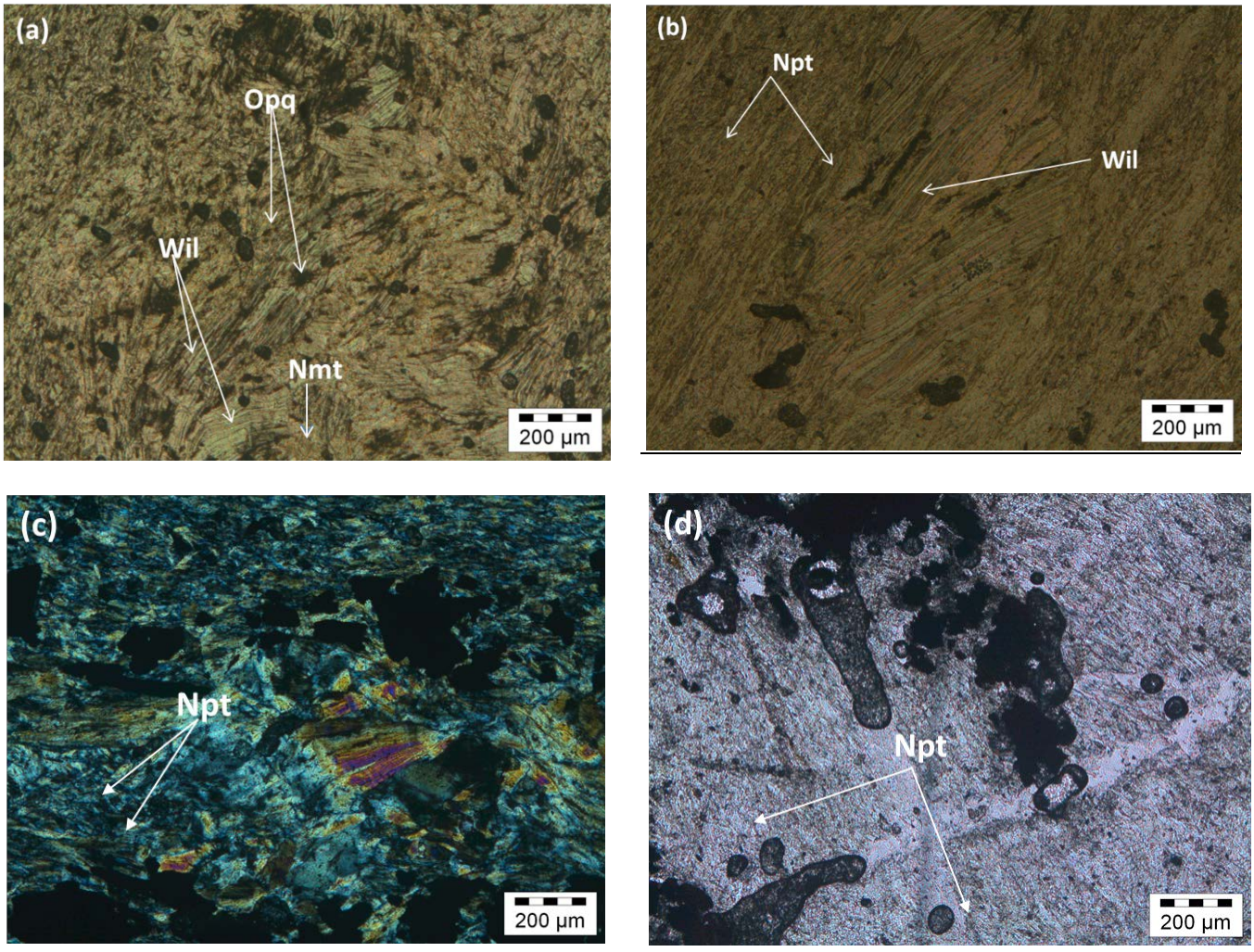

<u>Figure 3.3.</u> (a) Small nimite crystals embedded in flaky willemseite minerals. Willemseite-nimite assemblage under transmitted light - Sample NCH (b) Large népouite crystals embedded within the willemseite, in plane polarised light - Sample NCH (c) Népouite grains enclosed within the willemseite groundmass. High birefringent talc crystals, with népouite embedded within the dominate willemseite minerals. Close association of the népouite-trevorite assemblage observed in transmitted light under crossed nicols - Sample NCJ and (d) Népouite embedded within the willemseite in plane polarised light - sample NC-K. Photomicrographs taken with the Olympus BX 51 petrographic microscope.

Népouite [*$Ni_3 Si_2 O_5 (OH)_4$]***

Népouite is an anisotropic mineral characterised by flaky to prismatic grains (Fig. 3.3b, Fig. 3.3c, Fig 3.3d and Fig. 3.4a). In transmitted light it exhibits different colours, ranging from colourless with no pleochroism to slightly pink-green with greenish pleochroism however, in most of the thin sections, it appears as colourless grains without any distinct pleochroic properties. Népouite appears to be more dominantly visible in sections that contain opaque minerals more abundantly as compared to the nimite and/or willemseite minerals.

Nimite [*$Ni_5Al\ (Si_3Al)\ O_{10}\ (OH)_8$]***

The nimite represents an anisotropic mineral with flaky and prismatic crystals (3.4b and d). It displays a variety of colours under transmitted light, from slightly green without any pleochroism, light yellow with weak pleochroism and yellowish green to clear green with pleochroism. In instances where it usually occurs mostly embedded within the willemseite, it further illustrates the genetically close relationship between these mineral species. The nimite is also characterised by minor kinking patterns similar to those observed in the secondary chlorite phase of BA host rock samples

Liebenbergit**e [**$(Ni, Mg)_2SiO_4$**]**

Liebenbergite is an anisotropic mineral phase, and under transmitted light it exhibits colourless to pale yellowish colours without any pleochroism. Liebenbergite is characterised by infilling of the interstices between the trevorite grains, however was later replaced by secondary willemseite and népouite assemblages, thus further illustrating the close relationship and association between the liebenbergite with the willemseite and népouite (Fig. 3.4c).

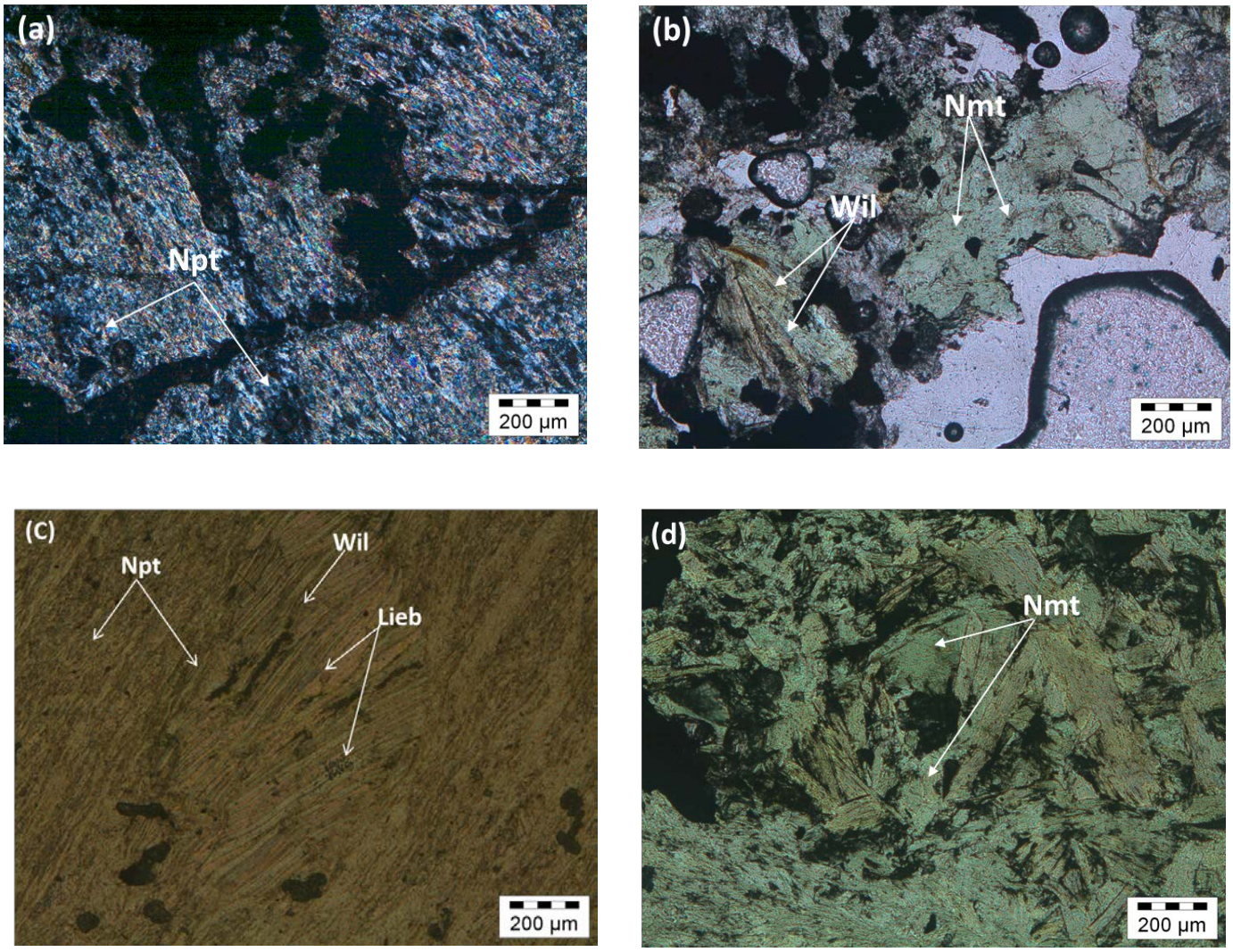

Figure 3.4. (a) Népouite embedded within willemseite under crossed nicols – sample NCK; (b) Groundmass of nimite and willemseite – sample NCK; (c) Minute liebenbergite altering to secondary willemseite – sample NCH and (d) Irregularly formed nimite in association with willemseite, under plane polarised light – sample NCJ. Photomicrographs taken using the Olympus BX 51 petrographic microscope.

- ***Oxides and hydroxides***

Trevorite [Ni Fe O_4]

Trevorite is an isotropic mineral phase and mainly observed as hypidiomorphic lath shaped grains. In transmitted light it occurs as greyish black grains. Under reflected light it displays

whitish cream colours (Fig. 3.5a). In almost all the thin sections studied the trevorite occurs as accumulated crystals however in some cases it occurs as singular grains and when observed in plane polarised light it appears to have some association with the népouite phase (characterised by the first order interference colours).

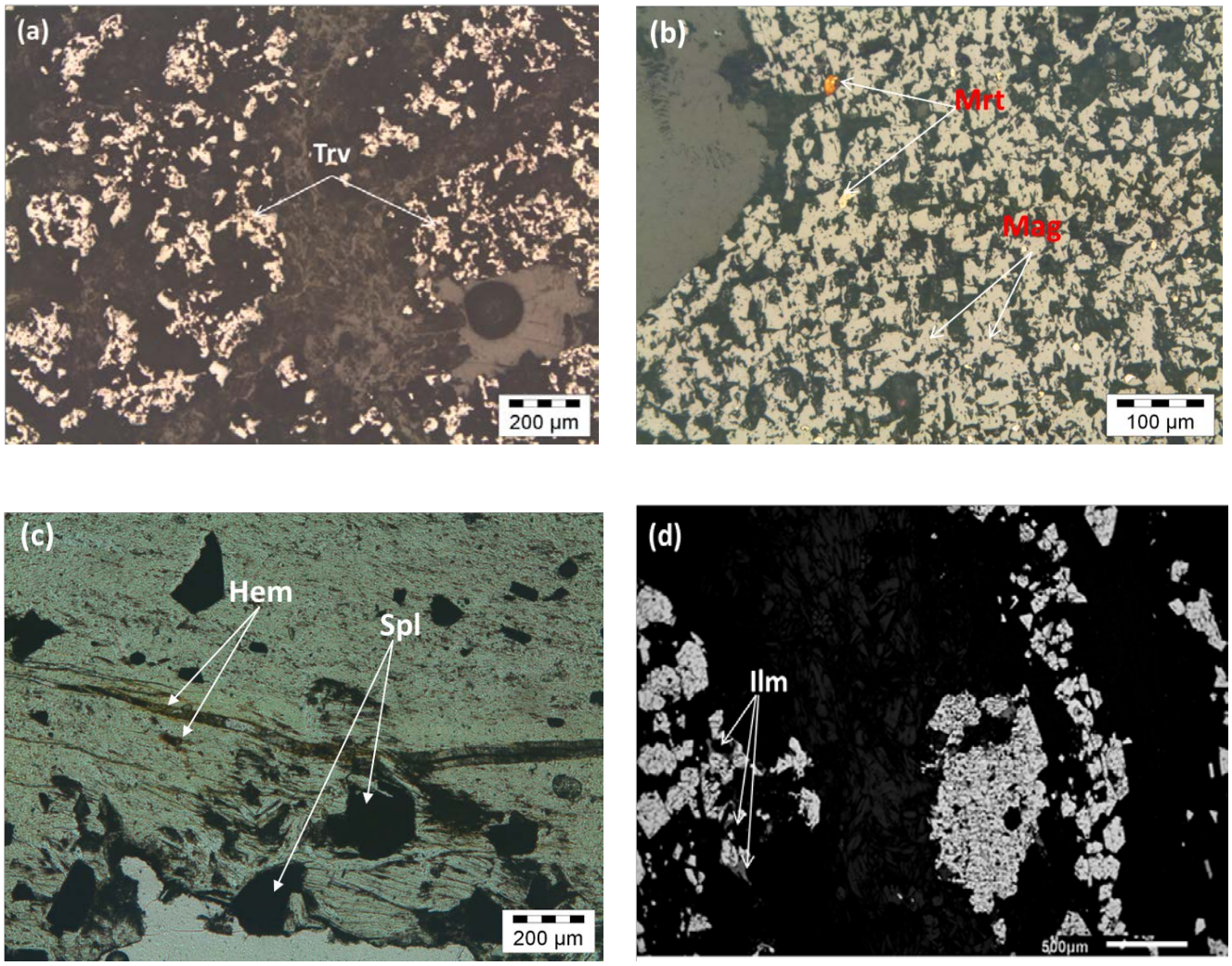

Figure 3.5. (a) Irregular trevorite grains with the associated deformation cause by the envisaged deformation event in the vicinity of Bon Accord oxide deposit, view under reflected light. (b) Close association of the millerite and magnetite in a magnetite-trevorite-millerite assemblage, view under reflected light. (c) Hematite and the associated alteration product, goethite, view in plane polarised light and (d) Ilmenite (dark grey, occurring as deformed grains) characterised by the skeletal texture, occurring in association with magnetite, in an ilmenite-magnetite-trevorite-millerite assemblage, view in reflected light. Photomicrograph taken using the Olympus BX 51 petrographic microscope.

Magnetite [$Fe^{2+}Fe^{3+}_2O_4$]

Magnetite is an isotropic mineral phase, it is black without pleochroism when observed under transmitted light. Under reflected light it is whitish grey (Fig. 3.5b). It occurs in close association with the trevorite however only in small proportions and it is often seen as single grains and at times appears to be replacing the trevorite.

Hematite [Fe_2O_3]

Hematite is anisotropic mineral and in transmitted light it exhibits blood red colours without any pleochroism. Its colour does not change in reflected light and it mostly occurs as veins running across the matrix of the willemseite (Fig. 3.5c) and has no apparent grains visible both in transmitted and reflected light.

Ilmenite [$FeTiO_3$]

Ilmenite is anisotropic in nature and it is characterised by the skeletal texture in some of the studied sections (fig 3.5d). In reflected light it is grey in colour and occurs as inequigranular grains (Fig. 3.5d) and it always appears closely associated with the minerals trevorite/magnetite in all cases where it was observed, a characteristic that can be attributed to the alteration of trevorite/magnetite to form ilmenite.

Sulphides minerals

Millerite [*NiS*]

Millerite is an isotropic mineral phase and it is very difficult to distinguish in transmitted light. Under reflected light, it occurs as minute yellowish gold grains embedded within the oxide

minerals (Fig 3.5, 3.6 and Appendix B, Fig 9). The millerite grains are mainly minute and spherical in nature and are embedded within the trevorite.

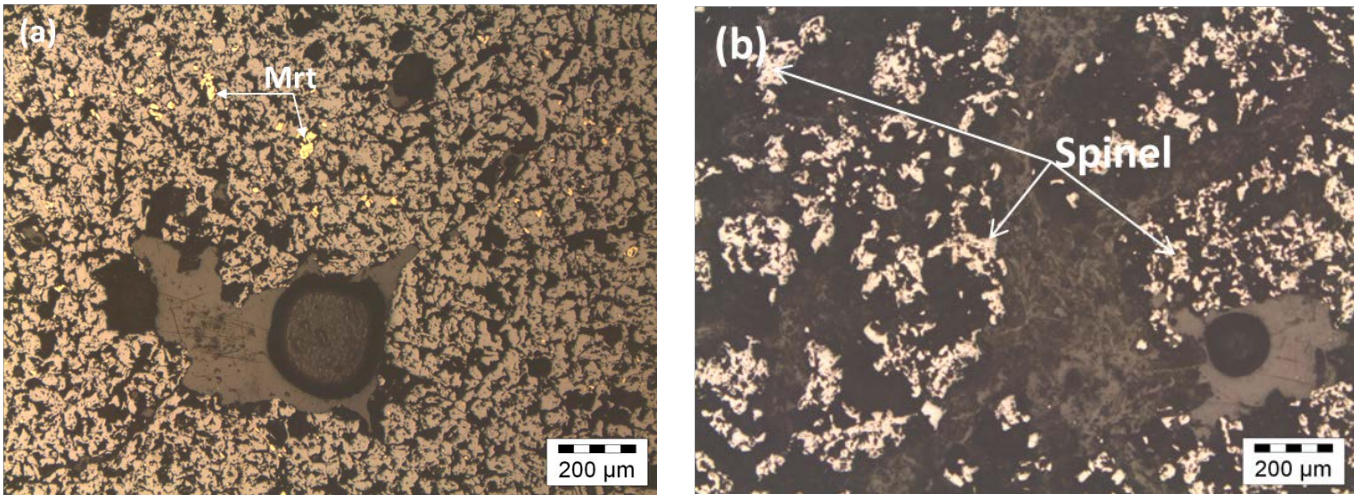

Figure 3.6. (a) Inclusions of millerite grains inside the irregular to columnar shaped opaque minerals – Sample NC-J and (b) Sulphide grains embedded within the massive opaque minerals with a hypidiomorphic texture – Sample NC-K. Photomicrographs taken using the Olympus BX 51 petrographic microscope.

3.3.4. Mineralogical description of the Bon Accord stratiform sulphide layer samples

3.3.4.1 NC-L (quartz-rich chlorite schist)

NC-L is dominated by opaque minerals, with quartz and talc as the next dominant phases. The noted chlorite stands out mainly because of its characteristic greenish colour and platy appearance. Also, visible in this sample is the apparent minor to moderate alteration of the talc and chlorite phases. The occurrence of chlorite suggests the involvement of a hydrothermal component during the alteration process, also noted by Holmes, (1930). Chlorite occurs mimicking a flow pattern and found within this chlorite flow pattern are some opaque grains attributed to a late stage enrichment event. The flow pattern of chlorite is indicative of a banded texture, most probably caused by dynamo-metamorphism subsequent to ore deposition (Bastin,

1957). This thin section is characterised by subhedral to anhedral crystals with a porphyritic texture, where the large opaque crystals are in a groundmass of talc and chlorite.

3.3.4.2 UFS 39a (serpentinised ultramafic rock)

UFS 39a shows medium alteration, and is highly rich in serpentine minerals and characterised by typical colourless to pale yellowish pale green colours in the hand specimen. Serpentine minerals are typically subhedral in their crystal form and inter-growing with the opaque minerals. When observed under crossed nicols, serpentine is highly birefringent (thus lacking its typical low birefringent colours), possibly due to the accommodation of elements like Fe, Mn, Zn and Ni into its lattice while the calcite together with tremolite appears in close association with the dominant serpentine mineral series.

3.3.4.3 UFS 39b (pyroxene-chlorite schist)

This sample is extremely altered and opaque mineral dominated, other phases present are pyroxenes, flaky muscovite in little amounts as well as weathered chlorite in parts. The opaque minerals are largely confined to the veins. The dominant opaque minerals make up 40 wt% of the minerals observed, while the pyroxene minerals account for 30 wt% of the minerals and the other minor phases make up the rest of the 30 wt%.

3.3.4.4 UFS 16c (quartz-rich chlorite schist)

The quartz chlorite schist is highly altered, characterised by large occurrences of quartz, chlorite and relatively minor opaque minerals. Also, visible under the microscope, were small flaky muscovite grains, however successfully distinguishing the muscovite grains from the quartz grains in plane polarised light is almost impossible as they occur embedded within the calcite,

however; the muscovite appears to have a slightly higher dominant relief. The growth of the opaque minerals appears to have been confined to the conduits in the sample. The quartz percentage was noted to be as much as 40 wt% while the chlorite percentage was noted to be just less than that of the quartz at 30 wt%.

3.3.4.5 UFS 4CS2 (mineralised chert (sulphide chert zone))

Sample UFS 4CS2 is highly weathered and comprised of remnant pyroxene and olivine minerals. Major phases are quartz and opaque minerals, while highly altered minute plagioclase relics and chlorite minerals are also visible, the plagioclase is largely altered to form the chlorite minerals. The opaque minerals are indicative of mainly growing within the veins of the sample, a clear indication of late fluids along the conduits which provided pathways for mineralisation.

3.3.4.6 UFS 38e (pyroxene quartzo-feldsphatic schist)

UFS 38e represents an altered sample, mainly comprised of pyroxene and minute olivine relics, which are now largely represented by the mineral chlorite. Little amounts of chlorite occur as highly weathered phases with characteristics replacement textures. The pyroxene mineral series makes up 45 wt% of the mineral assemblages.

Silicates minerals

Chlorite [$(Mg,Fe,Al)_3$ $(Si,Al)_4O_{10}(OH)$]

The chlorite is an anisotropic mineral, characterised by flaky and prismatic crystals. Under transmitted light it is dark green with strong yellowish green pleochroism colours. It is also characterised by flowing patterns and overgrown (replacement texture) by the opaque minerals (Fig. 3.7a).

Clinopyroxene [(Ca, Mg, Fe, Al)$_2$ (Si, Al)$_2$ O$_6$]

Clinopyroxene is anisotropic mineral in transmitted light. It exhibits pale brownish green and greenish pleochroism, with well pronounced cleavage. The clinopyroxene also shows replacement into chlorite minerals (Fig. 3.7b). The clinopyroxene and chlorite appears to indicate a close relationship that is further characterised by micro-folding patterns, especially in sample UFS 38e.

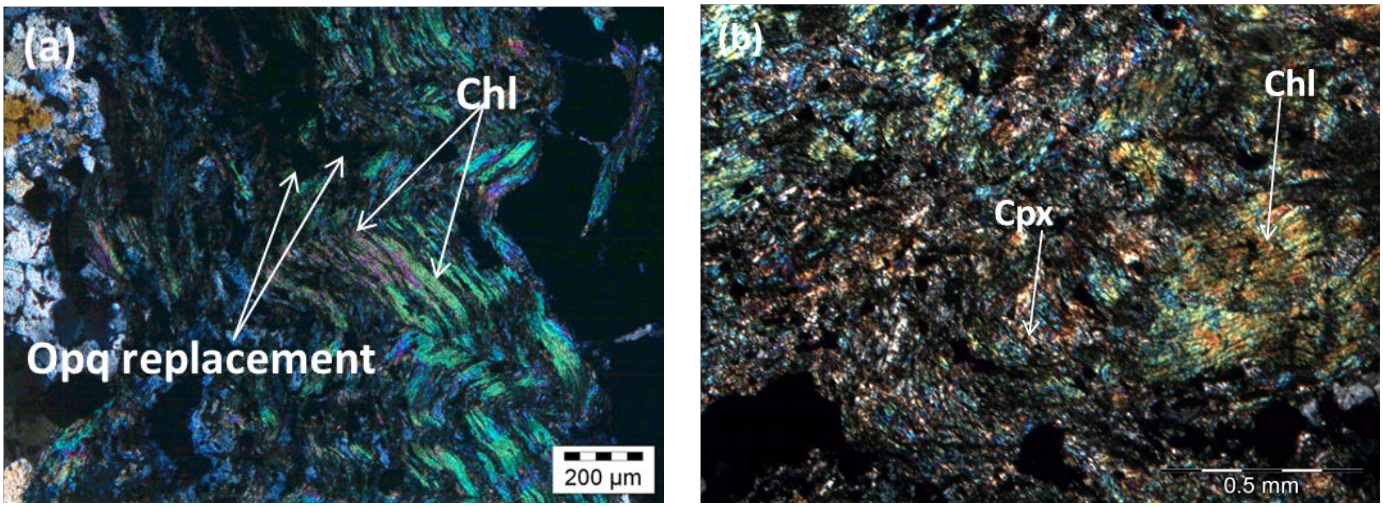

Figure 3.7. Chlorite-clinopyroxene and minor quartz mineral assemblage, from Scotia talc mine, photomicrographs taken using the Olympus BX 51 petrographic microscope. (a) Characteristic chlorite showing "chevron" growth patterns and replacement texture by opaque minerals - Sample NC-L and (b) Clinopyroxenes with minor irregular quartz grains in the surrounding areas– Sample UFS 38e

(Actinolite)-Tremolite [Ca$_2$(Mg, Fe)$_5$Si$_8$O$_{22}$(OH)$_2$]

Tremolite occurs as an anisotropic mineral with prismatic crystals (typical of its elongated appearance) and characterised by colourless to high interference colours (Fig. 3.8c), the iron largely attributed to the actinolite end member caused higher than normal interference colours in the tremolite. The typical 124 degree intersecting cleavage is not fully visible as it is masked by the intense alteration to its precursor pyroxene.

Muscovite [$KAl_2(AlSiO_3O_{10})(OH)_2$]

Muscovite occurs characteristically as small flaky crystals embedded inside the calcite crystals and largely characterised by high birefringent colours (Fig.3.8a-b). Distinguishing muscovite from quartz is almost impossible under normal plane polarised light due to their similar characteristics in this view, muscovite was successfully identified under crossed nicols.

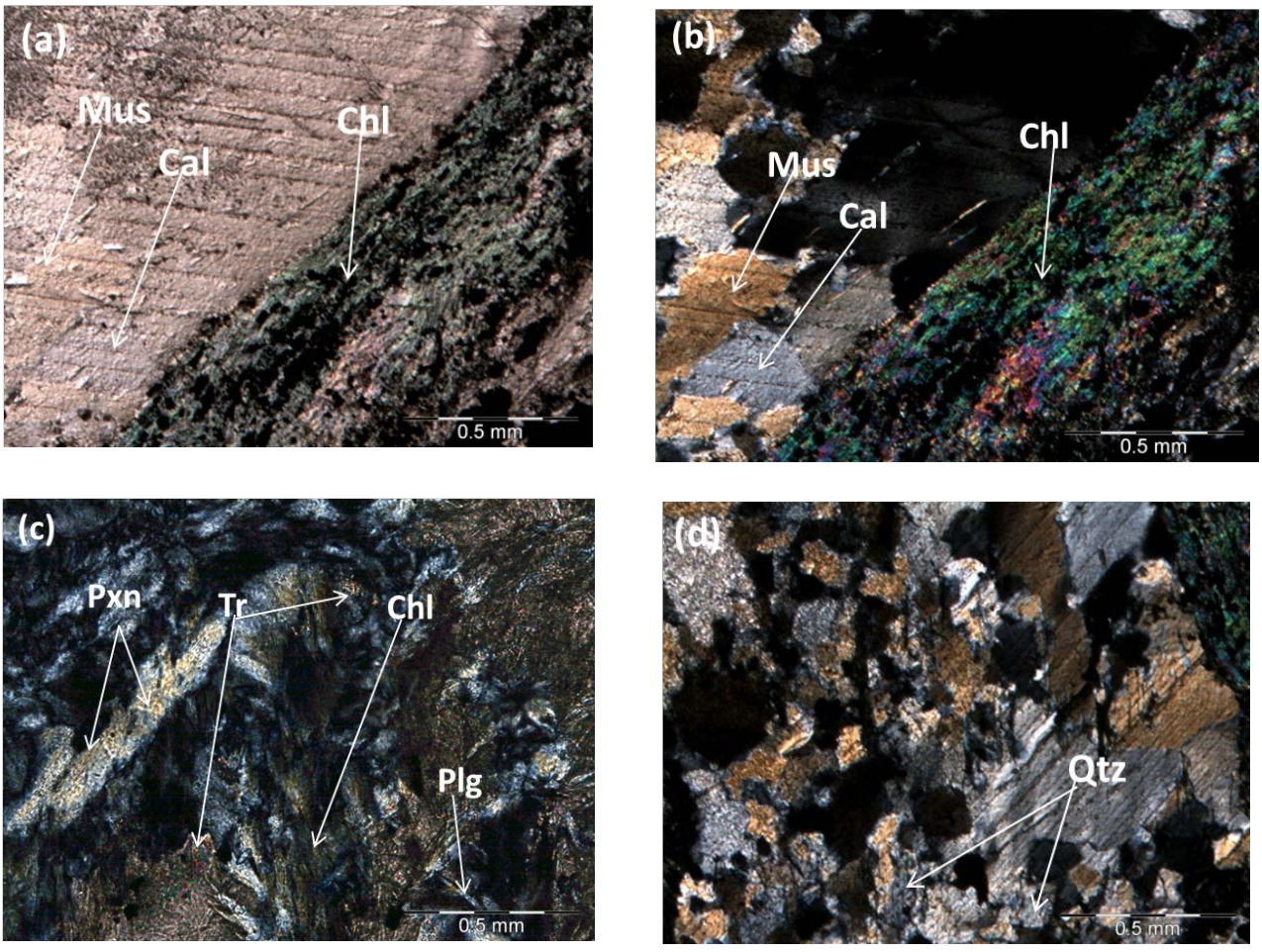

<u>Figure 3.8.</u> Different mineral accumulations with their typical characteristics. (a) Chlorite-calcite-muscovite mineral assemblages of the African Nickel in plane polarised light – Sample UFS 16C, (b) Faint brown muscovite in association with the mineral calcite under transmitted light – Sample UFS-16C, (c) Only little amounts of plagioclase remain and pyroxene (mostly relics) as they form tremolite, chlorite and serpentine products – Sample UFS-39a and (d) Quartz occurring as irregular grains with minor association to the opaque mineral phases – Sample UFS-39a. Photomicrographs taken using the Olympus BX 51 petrographic microscope.

Quartz [SiO_2]

Quartz is an anisotropic mineral exhibiting xenomorphic grain shapes (Fig. 3.8d). Under transmitted light, it is colourless without any pleochroism. In some cases it occurs as irregular grains surrounding tremolite and muscovite together with calcite in some instances.

Carbonates minerals

Calcite [$CaCO_3$]

The calcite exhibits a prismatic structure in short prisms with impure faint brownish colours under plane polarised light, with typical change in relief with changes to the plane of view on the stage.

Sulphides minerals

Chalcocite [Cu2S]

Chalcocite represents an isotropic mineral phase, and when viewed in reflected light, it displays bright blue colours and largely occurs as irregular sulphide grains intimately associated with the pyrite and pentlandite (Appendix B, Fig. 16d).

Pyrite [FeS_2]

Pyrite represents an isotropic mineral phase, occurring as massive and irregular sulphide grains (Fig. 3.9). When viewed in reflected light, it displays yellowish colours and seemingly appears to be concentrated within the vein structures of the sample, an indication of fluid flow in zones of weaknesses during mineralisation.

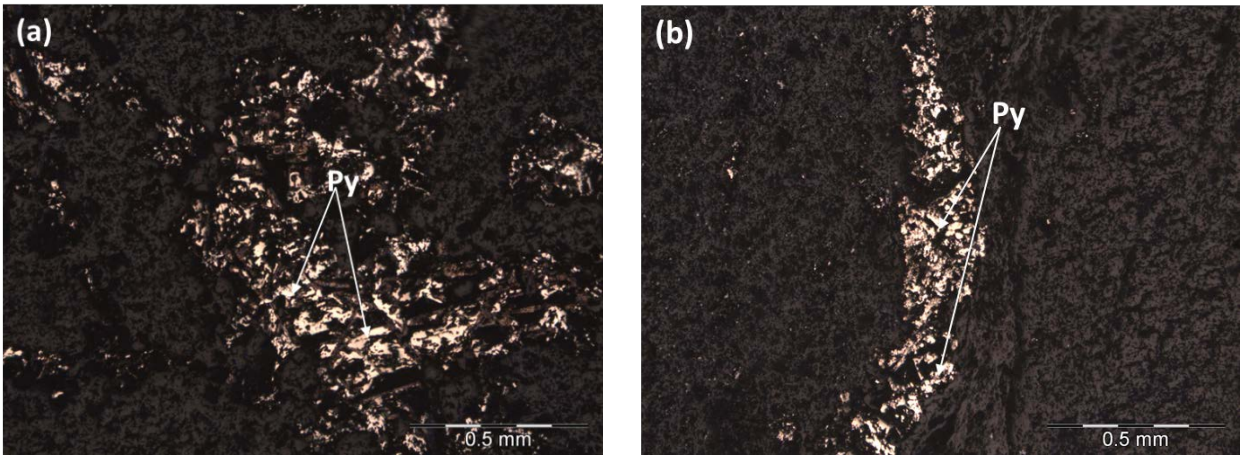

Figure 3.9. Sulphide group minerals comprising pyrite in sample UFS-4CS2. (a) Pyrite with distinct alteration zone (bottom left), in a willemseite matrix and (b) Pyrite infilling one of the veins acting as conduits for fluid migration in a willemseite matrix. Photomicrographs taken using the Olympus BX 51 petrographic microscope.

Pentlandite [$(Fe, Ni)_9S_8$]

Pentlandite occurs as an isotropic mineral phase and when viewed under reflected light, it is characterised by its typical yellow brown colours and occurs as irregular grains (Appendix B, Fig 16b).

Pyrrhotite [Fe_7S_8]

Pyrrhotite is an isotropic mineral phase and characterised by pinkish brown colours (Appendix B, Fig 16b). Pyrrhotite occurs as irregular grains without any specific grain shape but in close association with the pentlandite and other sulphides.

Gersdorffite [NiAsS]

Gersdorffite is an isotropic mineral phase typified by its euhedral grains and an indication of hydrothermal activity in the region. The Gersdorffite occurs as an accessory phase found

embedded within some pentlandite grains in sample NCL and since it occurs in accessory amounts, it was quantified through the application of the electron microprobe analysis.

3.3.5. Mineralogical description of the Kraubath ophiolite rocks

3.3.5.1 NC-MA (olivine-rich ultramafic rock)

It is characterised by the dominant phenocrysts of olivine. The opaque phase occurs as the second dominant phase and with less than 10 wt% pyroxenes. Fractured olivine phenocrysts with alteration along the fracture planes together with cumulate textures are very common features in this thin section.

3.3.5.2 NC-NA (amphibolite)

It is characterised by long prismatic crystals of pyroxene, while the amphiboles generally shows two directions of foliation in the hand specimen. Under the optical microscope it appears to be largely dominated by the groundmass of amphiboles (hornblende) and an indication of late stage enrichment of quartz rich fluids probably after deposition had ceased is supported by the occurrence of quartz as vein infillings. Sample NC-NA is characterised by the allotriomorphic texture.

Silicate minerals

Olivine $(Mg,Fe)_2SiO_4$

Olivine is an anisotropic mineral and brownish green when viewed under transmitted light with greenish pleochroism. It occurs as dominant well developed clustered phenocrysts in sample NC-MA and typically exhibits cumulate textures (Fig. 3.10).

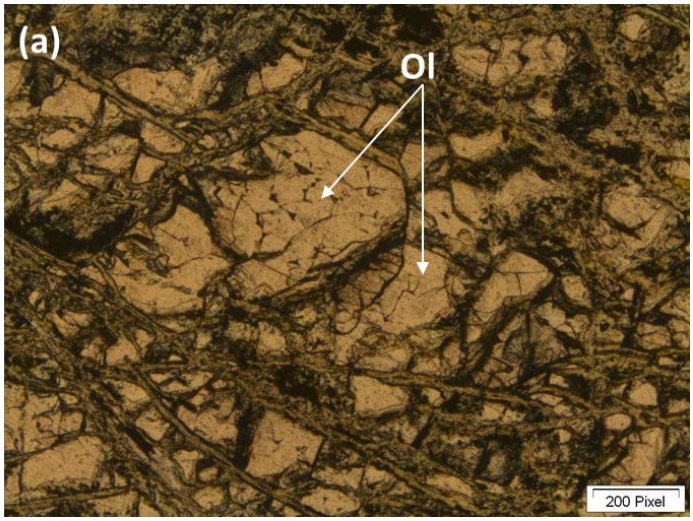

Figure 3.10.Olivine phenocrysts with alteration along the fracture planes, sample NC-MA. Photomicrographs taken using the Olympus BX 51 petrographic microscope.

Clinopyroxene $(Ca, Mg, Fe, Al)_2 (Si, Al)_2 O_6$

Clinopyroxene (Fig. 3.11a) is an anisotropic mineral when viewed under transmitted light, exhibiting pale brownish green and pinkish green pleochroism, with well pronounced cleavage.

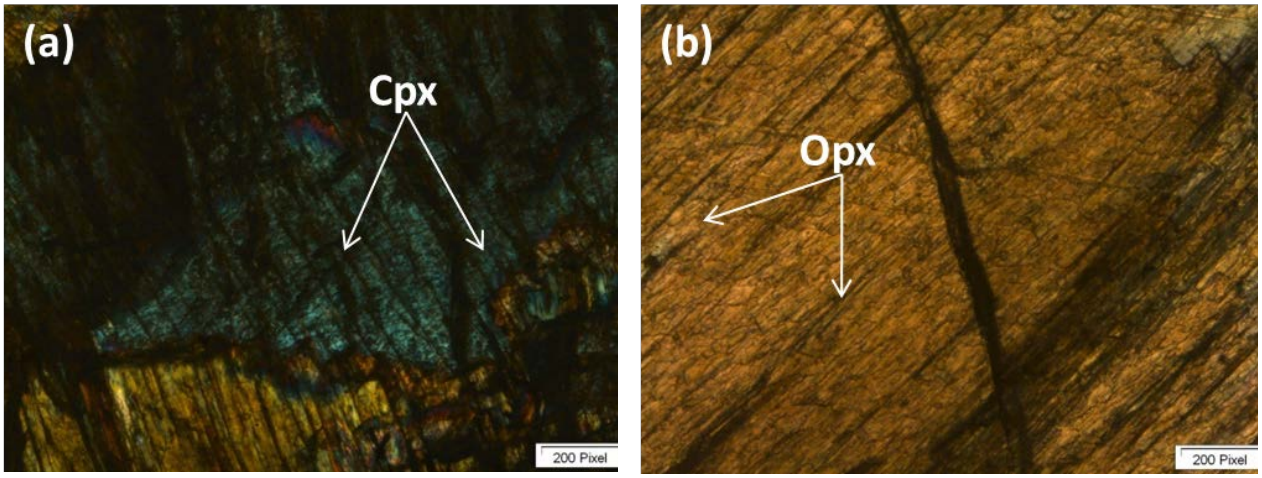

Figure 3.11. (a) Anhedral phenocrysts of clinopyroxene showing characteristic high birefringent colours under crossed nicols- Sample NC-NA and (b) Orthopyroxene exhibiting the characteristic 90° cleavage- Sample NC-NA. Photomicrographs taken using the Olympus BX 51 petrographic microscope.

Orthopyroxene (Mg, Fe) SiO_3

Orthopyroxene (Fig. 3.11b) is an anisotropic mineral with relatively high relief, and it is pale brownish green with slightly greenish-pink pleochroic colours under transmitted light.

Hornblende $(Ca,Na)_{2-3}(Mg,Fe^{+2},Fe^{+3},Al)_5Si_6(Si,Al)_2O_{22}(OH)_2$

Hornblende is anisotropic mineral and it is typically yellowish green to brown under transmitted light. It is pleochroic and shows shades of green and brown. The hornblende occurs as columnar and prismatic crystals (Fig. 3.12).

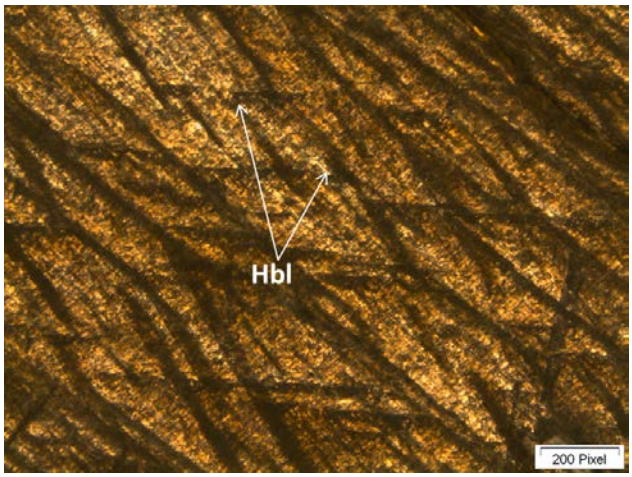

Figure 3.12. Hornblende showing its characteristic cleavage and simple twinning in plane polarised light – sample NC-NA.

3.4. SEM results

Detailed SEM data is provided in Appendix C on the CD in the pocket inside the back cover. Tables 3.3 and 3.4 below, are a summary of the distribution of major elements as well as important trace elements in all BA oxide and host rocks together with Kraubath and Scotia Talc samples.

Table 3.3. Summary of selected SEM data of silicates and oxides of all BA host and NCH and NCJ samples investigated using the Joel JSM 6610 scanning electron microscope at the University of Free State, Geology Department. Element concentrations in wt%

	MgO	Al_2O_3	SiO_2	TiO_2	Cr_2O_3	FeO	NiO	K_2O	CaO	MnO	CoO	S	Cl	As	Total	Comments
NCA #1*	24.83	8.94	22.42	7.90	0.53	31.83	0.41	END	END	END	END	END	END	END	100.02	Clinochlore
NCA #2	34.98	15.1	36.85	2.04	0.42	7.04	0.46	END	END	END	END	END	END	END	96.89	Clinochlore
NCA #3	12.73	4.82	9.65	END	14.21	54.5	0.32	END	END	END	END	END	END	END	96.23	Clinochlore
NCB #1	34.35	16.29	37.30	END	2.54	6.71	END	END	END	END	END	END	END	END	97.19	Chlorite
NCB #5	36.01	15.84	38.67	END	0.67	7.84	END	END	END	END	END	END	END	END	99.02	Chlorite
NCB #19*	END	0.59	0.79	END	18.29	79.33	0.71	END	END	END	END	END	END	END	100	Spinel
NCB #13	0.43	0.47	0.56	END	4.75	92.07	0.83	END	END	END	END	END	END	END	99.11	Magnetite
NCB #14	END	END	END	END	4.57	91.33	0.52	END	END	END	END	END	END	END	96.42	Magnetite
NCB #16	0.40	END	0.71	67.15	END	30.12	END	END	END	0.90	END	END	END	END	99.28	Ilmenite
NCB #17*	0.34	END	END	54.82	END	43.33	END	END	END	1.51	END	END	END	END	99,99	Ilmenite
NCC #1	2.86	1.17	3.45	60.1	END	33.04	END	END	END	1.02	END	END	END	END	101.6	Ilmenite
NCC #2	0.55	0.45	1.16	69.81	0.66	25.44	END	END	END	0.5	END	END	END	END	98.57	Ilmenite
NCC #16*	21.55	7.87	24.64	30.51	0.45	14.99	END	END	END	END	END	END	END	END	100	Chlorite
NCC #11*	24.28	END	69.78	END	END	3.05	END	1.74	END	END	END	END	1.14	END	100	Talc
NCD #10	END	END	99.48	END	END	0.52	END	END	END	END	END	END	END	END	100	Quartz
NCD #11	0.55	0.10	98.70	END	END	0.64	END	END	END	END	END	END	END	END	100	Quartz
NCD #12	0.27	END	99.73	END	END	END	END	END	END	END	END	END	END	END	100	Quartz
NCD #24	18.76	1.04	29.64	END	0.99	52.45	0.17	END	END	END	END	END	END	END	103.1	Serpentine
NCD #1	END	END	END	END	1.12	97.52	0.23	END	END	END	END	END	END	END	98.87	Magnetite
NCD #2	0.27	END	END	END	0.85	97.07	0.32	END	END	END	END	END	END	END	98.24	Magnetite
NCE #3*	2.98	1.80	73.49	END	END	END	END	2.11	13.64	END	END	1.14	4.85	END	100	Unknown #11

Normalised data, for original data please see Appendix C, END = Element not detected. The low totals are as a result of the hydrous nature of the minerals found in these samples. To see the total loss on ignition (LOI) of these samples, please see the XRF data in Table 4.1 and Appendix C.

Table 3.3. Summary of selected SEM data of silicates and oxides of all BA host and NCH and NCJ samples. Element concentrations in wt%. Continued.

	MgO	Al_2O_3	SiO_2	TiO_2	Cr_2O_3	FeO	NiO	K_2O	CaO	MnO	CoO	S	Cl	As	Total	Comments
NCE #4*	13.19	END	57.32	END	END	END	END	END	4.20	END	END	3.01	22.28	END	100	Unknown #11
NCE #7	8.12	4.04	77.89	END	END	END	END	1.12	7.03	END	END	0.31	END	END	98.51	Unknown #12
NCE #8	2.99	2.63	83.12	END	END	END	END	1.37	9.65	END	END	END	0.16	END	99.91	Unknown #12
NCF #1	END	END	END	END	END	98.65	END	END	END	END	END	END	END	END	98.65	Magnetite
NCF #2	END	END	END	END	END	97.99	END	END	END	END	END	END	END	END	97.99	Magnetite
NCF #6	0.36	END	END	END	15.14	87.5	0.65	END	END	0.12	END	END	END	END	103.8	Chromian spinel
NCF #7	END	END	END	END	13.91	84.11	0.65	END	END	END	END	END	END	END	98.67	Chromian spinel
NCG #1	END	END	0.54	END	END	END	17.04	81.22	END	0.13	END	END	END	END	98.92	Chromian spinel
NCG #2	END	END	0.56	END	END	END	14.80	86.16	END	END	END	END	END	END	101.5	Chromian spinel
NCG #10	23.47	2.76	63.00	END	END	12.69	END	END	0.46	END	END	END	END	END	102.4	Talc
NCH #1*	0.28	1.25	1.44	END	END	79.07	17.27	END	END	END	END	END	END	END	99.31	Trevorite
NCH #3	0.35	0.74	1.46	0.15	END	79.76	16.34	END	END	END	END	END	END	END	98.80	Trevorite
NCH #4*	0.11	0.33	0.37	0,19	END	80.80	16.20	END	END	END	END	END	END	END	98.92	Trevorite
NCH #11	5.01	END	67.45	END	END	4.14	26.67	END	END	END	END	END	END	0.50	103.3	Willemseite
NCH #12*	9.33	0.05	58.13	END	END	4.09	27.59	END	END	END	0.55	0.26	END	END	100	Willemseite
NCJ #16*	2.23	2.45	7.26	END	END	14.01	60.00	END	END	END	5.61	0.69	2.98	2.62	97.86	Garnierite
NCJ #17*	0.32	END	19.55	END	END	10.10	60.93	END	END	END	5.24	0.47	2.18	0.6	99.39	Garnierite

Normalised data, for original data please see Appendix C, END = Element not detected. The low totals are as a result of the hydrous nature of the minerals found in these samples. To see the total loss on ignition (LOI) of these samples, please see the XRF data in Table 4.1 and Appendix C.

NC-A

NC-A, is enriched in a variety of minerals particularly the Fe-Mg end-member chlorite group minerals (Table 3.3). The chamosite is the most dominant phase compared to other chlorite end members (clinochlore). The chamosite is relatively enriched in Ti and Cr as seen in NCA#1 and #3 respectively (Table 3.3) and correspond to decreasing Mg content.

NC-B

There is abundant occurrence of hematite with the more pseudomorphous goethite, followed by the clinochlore mineral phase as well as minor chromite spinel. The oxides (mainly hematite/goethite and magnetite) occur in the groundmass of the surrounding chlorite minerals (Fig. 3.13a). In some cases the oxide minerals (NCB #13, #14 and #19) contain Cr, a process normally associated with substitution, as reported by (Sack and Ghiorso, 1991). The occurrence of relatively high Cr in the host rocks could possibly represent origin of magnetite (especially NCB) that is associated with mafic-ultramafic igneous intrusives.

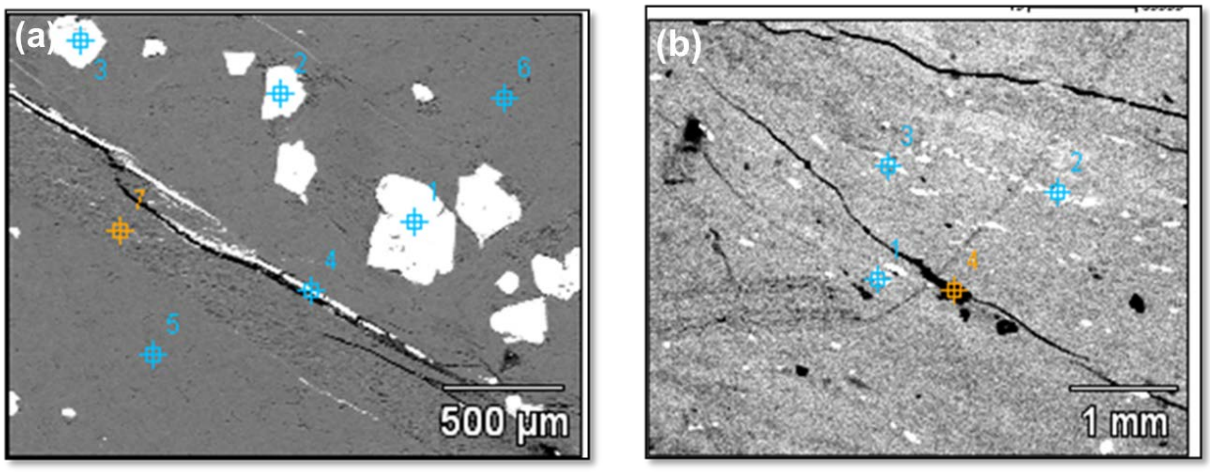

Figure 3.13. SEM back-scattered electron images of the Bon Accord host rocks (a) NCB and (b) NCC

NCC

All the analysed points are shown in Fig 3. 13b, the presence of ilmenite is characterised by minor Mg and Si contents while the chlorite contain some Ti (Table 3.3, NCC #16). Talc shows higher than normal SiO_2 concentrations as seen in NCC #11, Table 3.3 and Appendix B.

NC-D

The occurrence of almost pure quartz grains (Table 3.3, NCD #10, #11 and #12) could possibly be evidence of a chilled margin, which resulted in the preservation of the quartz crystal during formation in the envisaged metamorphic processes. Talc (together with the opaque minerals) is still the dominant mineral phase and the opaque minerals are largely made up of the magnetite mineral (Table 3.3, NCD #1 and 2), and two chlorite end members chamosite and clinochlore (Appendix B, NCD) occur. The chemical composition of the two clinochlore grains analysed is almost identical, while the chamosite has lower Al but higher Fe in comparison and the chamosite is unusually high in Cl (Appendix B, NCD #22).

NC-E

NCE shows occurrence of some unusual minerals and these minerals have been marked as unknowns (Table 3.3 NCE, unknown #11 and #12). Unknown #11 has higher than normal Cl it seems to be in the same class as rondorfite ($Ca_8Mg\ (SiO_4)_4Cl_2$), however the higher SiO_2 (maximum of 59.17 wt%) and relatively lower CaO (minimum of 3.53 wt%, Appendix B, NCE) means it is unlikely to be rondorfite, but very likely that it could possibly represent a mineral in the same family as rondorfite. Unknown #12 (Table 3.3, NCE) seems to be a remnant of plagioclase of some kind but as with unknown #11, high SiO_2, slightly high MgO and low K_2O and CaO as well as lack of any visible plagioclase in thin section possibly due to deformation makes it almost impossible to accurately confirm plagioclase as its precursor.

NC-F

NC-F is highly enriched in chlorite and contains minor pseudomorphous hematite (Fig. 3.14a). NCF also contains some chromian spinels (Table 3.3 NCF #6 and #7), with high Fe content, which is characteristics of Fe diffusion from serpentinised solution(s) during the decomposition of the spinel. The pseudomorphous magnetite/hematite series is the dominant mineral phase, with little amounts of Cr (Table 3.3) while talc occurs as the second most dominant phase (Appendix B, NCF). Points NCF #1 and 2 contain almost pure magnetite/hematite series without any significant impurities, probably as a result of minor ions (Mg, Al and Si) diffusing out during decomposition of the spinels.

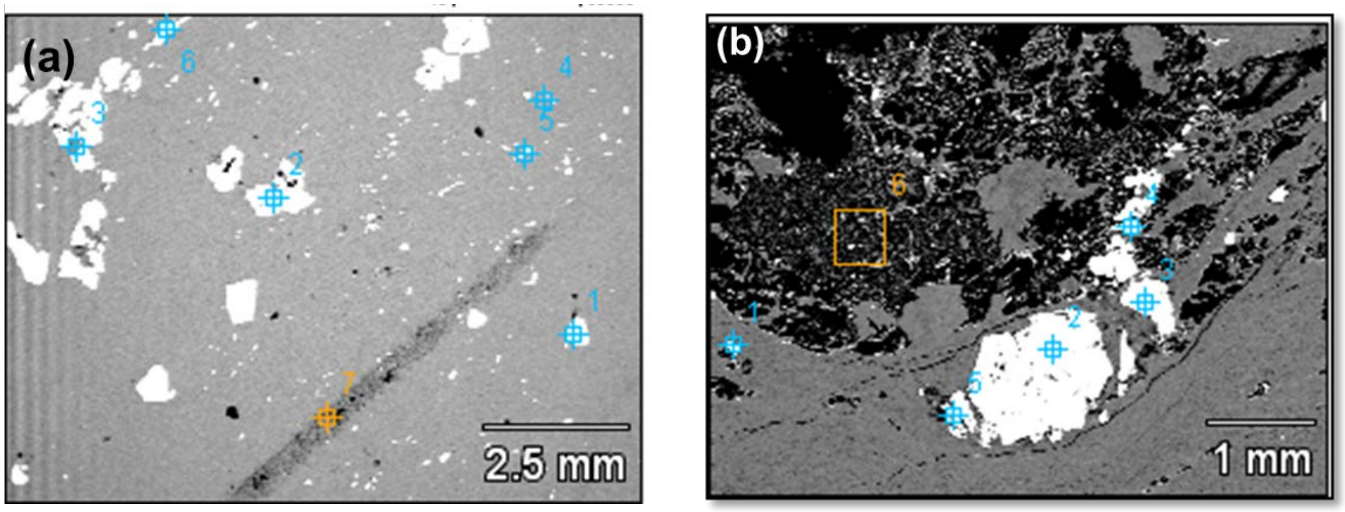

Figure 3.14. (a) BSE image illustrating talc-chlorite-magnetite assemblage in sample NCF and (b) Replacement texture characterising the interaction of the oxide minerals with serpentinised solutions and associated alteration, sample

NC-G

Mineralogy of NCG is indicative of intense oxide minerals (chromian spinel) alteration (Fig 3.14b) by serpentinised solutions and it appears as though the serpentinised solutions are acting

to concentrate talc (Fig 3.14b and NCG #10 in Table 3.3). There is also occurrence of a K-feldspar phase in this sample (Appendix B NCG #8), mainly surrounded by deformed talc and spinel minerals.

NC-H

Trevorite together with chlorite and willemseite are the main components of NCH (Table 3.3). The willemseite has relatively moderate Fe concentration with a recorded FeO maximum of ≈4 wt%, with negligible S and As (Table 3.3 and Appendix B, respectively). The trevorite still has remnant ions (such as Mg, Al and Si) from its precursor prior to alteration (NCH #1, 3 and 4 in Table 3.3).

NC-J

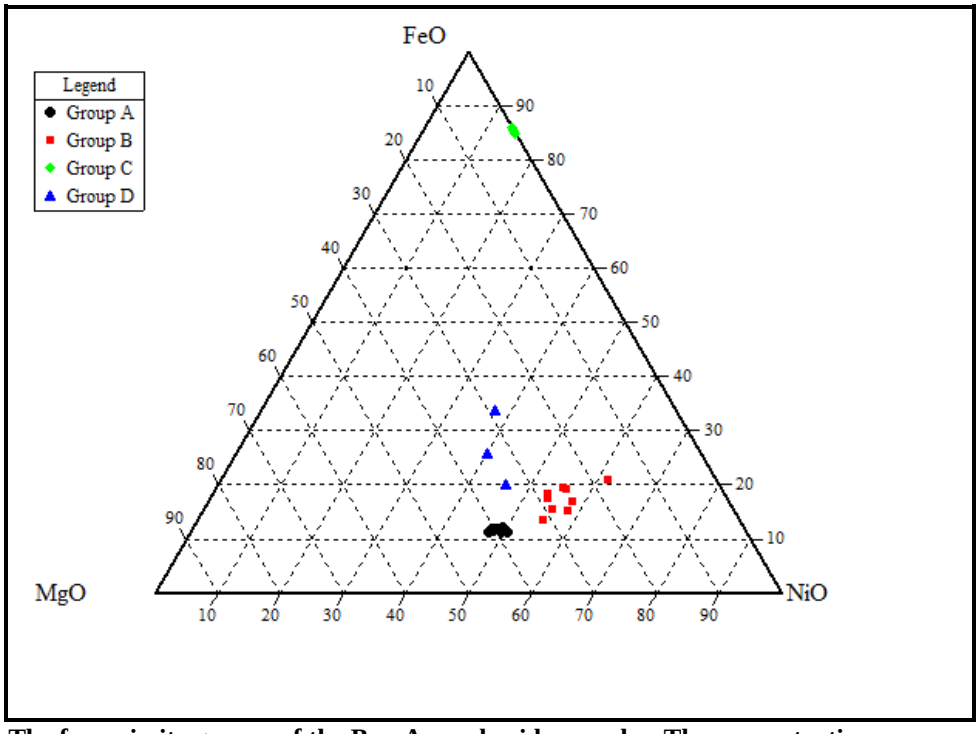

Figure 3.15. The four nimite groups of the Bon Accord oxide samples. The concentrations were normalised to 100 wt%.

Sample NCJ is characterised by four different nimite groups (Fig 3.15). Group A mainly contains low FeO, moderate NiO and MgO, group B has low FeO but slightly higher concentration of NiO and moderate MgO, group C has high FeO with low NiO and MgO concentrations whereas group D has moderate FeO, NiO and MgO concentrations. Groups A and B appear to almost concentrate in similar positions on the ternary diagram (Fig 3.15).

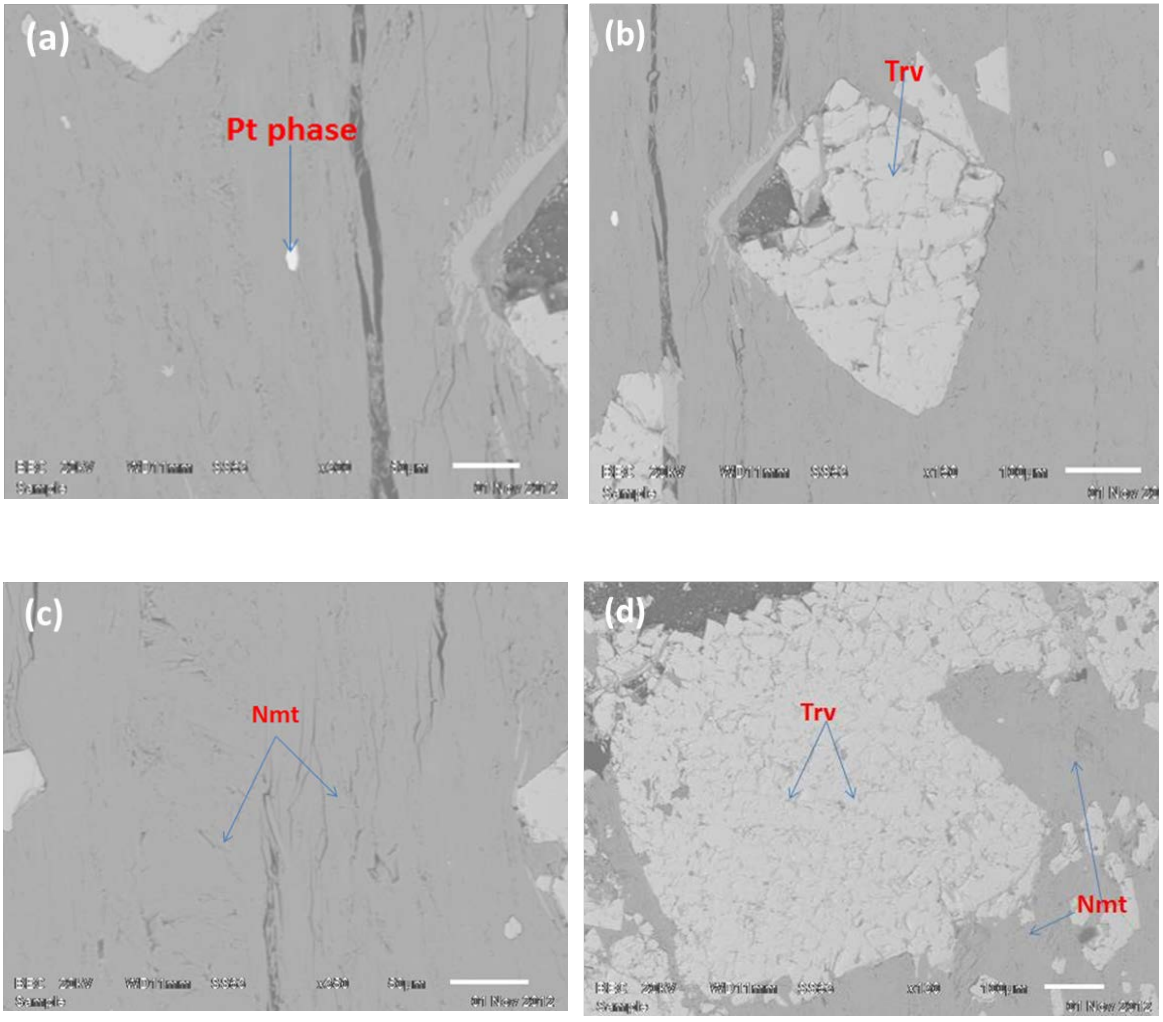

<u>Figure 3.16.</u> Back-scattered electron images of sample NCJ taken using the SEM. (a) Minute Pt phase in the nimite. Scale is 50µm, (b) Large trevorite grain, with slight alteration on the rim. Scale is 100 µm, (c) Nimite infilling the trevorite interstices. Scale is 50µm and (d) Small trevorite grains clustered into one massive grain and nimite infilling the trevorite interstices. Scale is 100 µm

There is also the appearance of a Ni-Mg silicate phase, probably garnierite however the typically expected Mg-Fe substitution resulted in unusually extensive substitution of Mg by Fe, thus leaving behind a relatively Fe-rich garnierite end member and little to no Mg end members (Table 3.3, NCJ #1 and #17 and Appendix B).

The apparent Fe-rich olivine end member fayalite, is within the trevorite in a talc matrix. There is a close but genetically unrelated relationship between Pt-phase together with the dominant trevorite and nimite phase (Fig. 3.16a). The occurrence of trevorite is characterised by two distinct grain sizes: massive singular grains as seen in Fig 3.16b, and as small clustered grains Fig 3.16d together with the associated weathering/alteration from the rim towards the center and nimite is filling the interstices between the trevorite (Fig 3.16c and d).

NC-K

The results in Table 3.4, indicate a high concentration of a NiAs mineral phase.

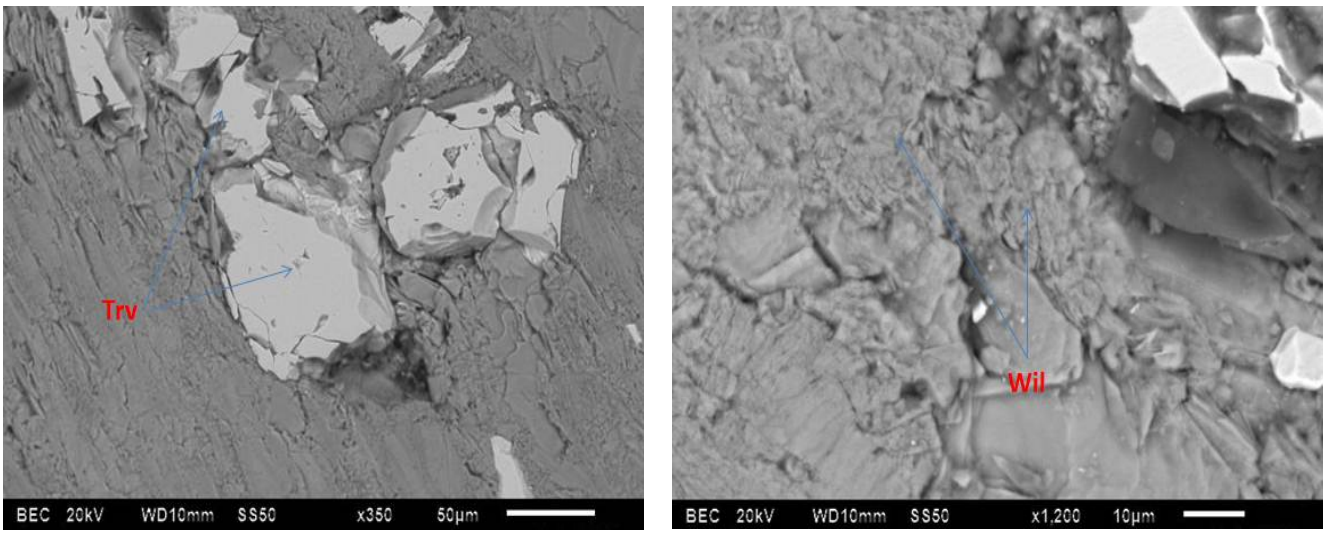

Figure 3.17. The association of the trevorite, arsenic and willemseite phases, the back-scattered images taken by the SEM

The NiAs phase occurs as very minute grains embedded within the trevorite, highlighting its close relationship with the trevorite. The occurrence of the As phases in association with the trevorite-willemseite assemblages can be seen in Fig. 3.17. However the As phases are only confined to certain parts of the section and they are also characterised by minor occurrence of Sb (Table 4, NCK #22).

NC-L

Sample NC-L is sulphide rich and has Ni-rich pyrite as observed in NCL #4 in Appendix C, chlorite is also visible and shows an association with sulphur (Table 3.4, NCL #15). The abundant sulphide minerals noted are the pyrite end member as well as some pentlandite (NiFeS in Appendix C).

NC-MA

Table 3.4, shows high enrichment of two phases (olivine and nickel rich pyrite). The olivine end member found in this sample is the Mg rich forsterite and the pyrite is represented by the nickeloan pyrite, bravoite (Table 3.4, NCMA #1 and Appendix C respectively).

NC-NA

NC-NA is highly enriched in Mg and Cr (Table 3.4). The high concentrations of Mg are as a direct result of the high amphiboles and pyroxenes in the NCNA sample. The amphibole, pyroxene (Appendix C) and chromite mineral (Table 3.4, NCNA #1 and 2) phases are directly characterised by the high Cr concentrations observed. The Cr-rich phase in some cases appears strictly confined to the amphibole alteration fracture planes (Fig. 3.18).

Table 3.4. **Summary of SEM data of all the samples investigated using the Joel JSM 6610 scanning electron microscope continued**

	MgO	Al_2O_3	SiO_2	TiO_2	Cr_2O_3	FeO	NiO	K_2O	MnO	S	As	Sb	V_2O_5	Total	Comments
NCK #22	END	END	END	END	END	8.97	60.09	END	END	END	29.79	2.02	END	100.87	Nickeline
NCK #18	0.35	END	END	59.95	END	END	39.85	1.93	1.81	END	END	END	END	103.89	Ilmenite
NCK #19	0.86	0.72	1.09	56.21	END	END	37.07	1.74	1.07	END	END	END	END	98.77	Ilmenite
NCL #15	8.91	20.53	23.63	END	2.61	32.25	4.20	END	0.61	3.58	END	END	END	96.32	Chlorite
NCMA #1	43.55	END	42.22	END	END	14.22	END	END	END	END	END	END	END	99.99	Olivine
NCNA #1	5.15	1.93	3.42	2.31	51.48	34.63	END	END	1.08	END	END	END	END	100.00	Chromite
NCNA #2	2.14	2.04	1.02	2.14	47.58	39.43	END	END	0.79	END	END	END	1.36	96.50	Chromite

END = Element not detected

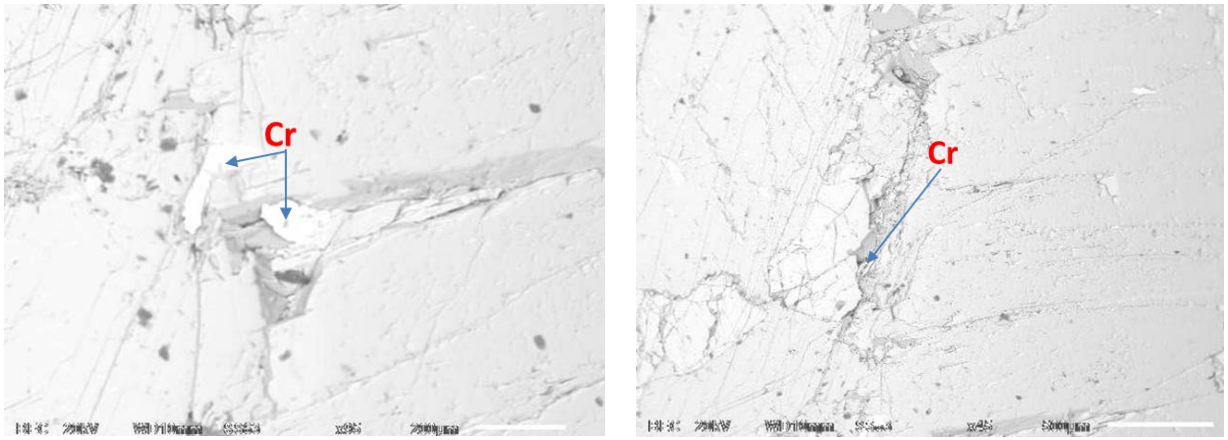

Figure 3.18. **Chromite phase confined within the alteration fractures of the amphiboles. Sample NCNA**

The occurrence of the Cr-rich phase cross-cutting the amphibole represents late stage enrichment in the Cr phase and thus resulted in the post formation association of the amphiboles and the Cr-rich phase.

3.5. EMPA results

Analyses on the electron microprobe were only conducted on the BA oxide, Scotia Talc mine and Kraubath samples. The electron microprobe analyses data revealed the occurrence of unknown phases (Table 3.5) which were first described by Wildau 2012 and new minerals which have not been described before and were also referred to as unknowns in this research.

Table 3.5. Part trace element data obtained from the Joel JSM 5410 EMPA

NCH	As	Co	Fe	Ni	Sb	S	Total	Comment
1	0.2	2.12	3.99	63.77	END	32.49	102.58	Bravoite
2	0.76	1.74	4.44	62.83	END	32.11	101.89	Bravoite
3	0.56	1.55	3.48	63.7	END	32.04	101.32	Bravoite
4	41.39	0.23	4.3	49.93	1.3	0.4	97.55	Unknown #5
5	43.47	0.36	4.28	50.53	0.93	0.1	99.66	Unknown #5
NCK								
5*	0.25	END	5.33	29.65	64.4	END	99.98	Unknown #4
6*	0.77	END	10.19	31.04	57.39	END	100.02	Unknown #4
7*	0.74	END	7.92	31.96	58.92	END	100	Unknown #4
8*	0.55	END	43.84	25.25	29.77	END	100	Unknown #10
9*	0.16	END	61.98	22.02	15.47	END	100.01	Unknown #10
NCL								
1	END	END	28.03	38.69	END	33.32	100.13	Pentlandite
2	0.09	0.14	46.17	0.1	END	53.36	99.89	Pyrite
3	0.01	END	27.44	38.94	END	33.31	99.79	Pentlandite
4	45.06	0.56	1.18	34.84	1.02	19.52	102.37	Gersdorffite

*** = Normalised, Original data attached as Appendix C, *END* = *Element not detected***

NC-H

The part analysis in NC-H, also indicates the occurrence of minor Co in association with the sulphide minerals (Table 3.5, NCH, #1-3). This part analysis is also characterised by As and Ni rich minerals, unknown #5 (Table 3.5, NCH #4 and #5).

NC-J

There is unusual occurrence of the remnant mineral apatite (Table 3.6, NCJ #1). This part of the sample is dominated by Fe and Ni, largely from the spinel mineral group. The concentration of Mg, Al and Si is indicative of the presence of chlorite (nimite), which occurs as the next dominant mineral phase after the trevorite.

NC-K

Sample NC-K is dominantly trevorite with minor talc assemblages (Table 3.5, NCK points 1-3 and 4 respectively). The trevorite appears to illustrate different Fe enrichment mechanisms and/or factors, in areas where trevorite is slightly depleted in Fe, it is enriched in Ni and the Fe:Ni ratio is from 3 to 4. Elemental concentrations representing new unknown minerals species were identified by the current study (Table 3.5, NCK points 8-9).

The chemical composition of the new mineral species is similar to that described by Wildau, (2012) with the exception only noted in the number of cations present. The new unknown species identified has been named as unknown #10. The unidentified phases occur in the altered planes and rims of the trevorite phase (Fig. 3.19), therefore revealing a close association of the unknown phases with trevorite.

NC-L

NCL is dominated by the sulphides mineral phases (Table 3.5, NCL points 1-4) and the sulphide mineralisation is associated with nickel and arsenic mineralisation. The sulphur

occurs more abundantly as compared to the iron, where both sulphur and iron occur. The dominant sulphide mineral phases comprising, pyrite, Gersdorffite type minerals and pentlandite are clearly documented.

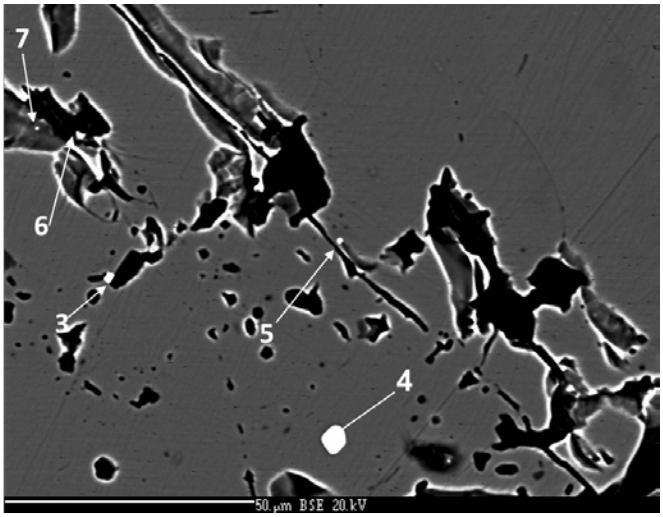

Figure 3.19. BSE image of sample NCK showing the occurrence of unknown phases in altered and rims of the mineral trevorite

Table 3.6. Selected major element data obtained from the Joel JSM 5410 EMPA

*** = Normalised, Original data attached as Appendix C, *END = Element not detected***

NCK	MgO	SiO_2	FeO	Al_2O_3	TiO_2	CoO	NiO	As_2O_3	Cr_2O_3	P_2O_5	CaO	Total	Phase
1*	0.01	0.12	69.35	END	END	0.34	23.57	6.24	END	END	END	99.63	Trevorite
2*	0.01	0.03	81.18	END	END	0.41	18.04	END	END	END	END	99.67	Trevorite
3*	0.03	0.46	79.88	END	END	0.37	18.41	0.03	END	END	END	99.18	Trevorite
4*	10.48	55.79	1.85	END	END	0.36	31.39	END	END	END	END	99.87	Talc
NCJ													
1	0.63	END	END	END	END	END	0.61	END	END	41.33	57.14	99.71	Apatite
NCMA													
1	44.5	40.21	14.11	END	END	END	0.14	END	END	END	END	98.96	Olivine
2	44.93	45.76	8.86	END	END	END	0.18	END	END	END	END	99.73	Olivine
3	45.19	39.96	14.28	END	END	END	0.14	END	END	END	END	99.57	Olivine
NCNA													
1	5.83	END	29.84	15.00	0.48	END	END	END	48.22	END	END	99.36	Chromite

NC-MA

Sample NC-MA represents an olivine rich phase, the MgO content is the very similar in all three points analysed (Table 3.6, NCMA points 1-3). The MgO and FeO show a slight indirect relationship, where MgO increases with decreasing FeO and only negligible traces of NiO were noted. The Mg-rich forsterite is the olivine end member represented by all three points as depicted in Table 3.6, while the substitutional relationship between Fe and Mg should also be noted, as it could have played a role in the final outcome of the olivine composition.

NC-NA

The part of NC-NA analysed indicates high enrichment in a Cr-phase, most likely chromite (see Table 3.6, NCNA).

3.6. Mineral chemistry and geochemistry

The mineral chemistry and geochemistry section will discuss a few selected minerals from each sample that were analysed. For full and comprehensive mineral and geochemistry analyses data (each mineral maximum, minimum, average, standard deviation wt% values and coefficient of variation), please see Appendix C.

3.6.1. Host rocks

3.6.1.1. NCA

Chlorites

A total of three chlorite mineral grains were analysed, the Al_2O_3 in this sample vary in concentration with a minimum of 4. 82 wt%, maximum of 15.10 wt% and averaging 9.36

wt%, with a variance of 56.06 % (Table 3.7). MgO is also characterised by a relatively large variance of 47.54%, with a minimum of 12.73 wt%, maximum of 34.98 wt% at an average of 23.45 wt%. SiO_2 also shows a wide range in its concentration with a minimum of 9.65 wt%, maximum of 36.85 wt% at an average of 22.31 wt% and with a variance of 61.38 wt%. The TiO_2 is not too varied largely due to the low concentration, the TiO_2 has a minimum of 2.04 wt%, with a maximum of 7.20 wt% and averaging 4.62 wt% with a variance of 78.98 wt%.

Table 3.7. Summary of SEM data of chlorite in NC-A (n=3) wt%

	MgO	**Al_2O_3**	**SiO_2**	**TiO_2**	**Cr_2O_3**	**FeO**	**NiO**
Max	34,98	15,10	36,85	7,20	14,21	54,50	0,46
Min	12,73	4,82	9,65	2,04	0,42	7,04	0,32
Mean	23,45	9,36	22,31	4,62	5,05	31,12	0,40
STDEV	11,15	5,25	13,70	3,65	7,93	23,74	0,07
CoV	47,54	56,06	61,38	78,98	156,93	76,27	17,89

The Cr_2O_3 is remarkably varied and this variation is indicated by the large coefficient of variation recorded at 156.93 wt%, and a minimum of 0.42 wt%, a maximum of 14.21 wt% with an average of 7.93 wt%. FeO has a maximum of 54.50 wt%, minimum of 7.04 wt%, averaging 31.12 wt% and the NiO shows the lowest coefficient of variation, measured at 17.89 wt%.

3.6.1.2. NCB

Talc

In total five talc grains were analysed on the SEM. The SiO_2 has a maximum of 36.79 wt%, minimum of 34.08 wt% and an average of 35.58 wt%. K_2O occurs in very low concentrations (Table 3.8) and was only observed in the two grains out of the five analysed grains (Appendix C).

Table 3.8. **Summary of SEM data of talc NC-B (n=5) wt%**

	MgO	Al_2O_3	SiO_2	K_2O	Cr_2O_3	MnO	FeO	NiO	V_2O_5
Max	36,79	16,29	41,20	0,14	2,54	0,10	8,95	0,51	0,30
Min	34,08	15,37	35,20	0,10	0,67	0,10	5,88	0,51	0,30
Mean	35,58	15,73	38,61	0,12	1,69	0,10	7,38	0,51	0,30
STDEV	1,29	0,36	2,46	0,03	0,74	END	1,15	END	END
CoV	0,04	0,02	0,06	0,28	0,44	END	0,16	END	END

END = Element not detected

There appears to be a solid solution substitution between the Cr and Fe, however even with this seemingly close association, the averages between Cr and Fe are very different and were measured at 1.69 wt% and 7.38 wt% respectively. Only trace amounts of NiO were observed in the one grain out of the five grains analysed.

3.6.1.3. NCC

Ilmenite

Table 3.9. **Summary of SEM data of ilmenite in NC-C (n=3) wt%**

	MgO	Al_2O_3	SiO_2	Cr_2O_3	MnO	FeO	NiO	TiO_2
Max	4.27	1.23	5.29	0.66	1.02	33.04	0.33	69.81
Min	0.55	0.45	1.16	0.55	0.28	25.44	0.33	60.10
Mean	2.56	0.95	3.30	0.61	0.60	27.98	0.33	64.34
STDEV	1.88	0.43	2.07	0.07	0.38	4.38	END	4.97
CoV	0.73	0.45	0.63	0.12	0.63	0.16	END	0.08

END = Element not detected

A total of three ilmenite grains were analysed, the distribution of the major components of ilmenite do not seem to have any obvious variances. The TiO_2 has a maximum of 69.81 wt%, a minimum of 60.10 wt% with an average of 64.34 wt% and variation of 8%. Similarly the FeO behaves in the same manner as the TiO_2 with a maximum of 33.04 wt%, minimum of 25.44 wt% averaging 27.98 wt% and variance of 16% (Table 3.9).

3.6.1.4. NCD

Quartz

A total of three quartz grains were analysed. Si recorded a maximum of 97 wt%, minimum of 94.26 wt% with an average of 95.36 wt%. The variation is nearly absent and was only recorded at 2% (Table 3.10). The accessory Fe and Mg are probably an indication of minor interaction with Mg and Fe carrying fluids at some stage in the cycle of the quartz.

Table 3.10. Summary of SEM data of quartz in NC-D (n=3) wt%

	O	Mg	Si	Fe
Max	4,90	0,53	97,00	0,61
Min	2,49	0,26	94,26	0,51
Mean	3,96	0,40	95,36	0,56
STDEV	1,29	0,19	1,45	0,07
CoV	0,33	0,48	0,02	0,13

END = Element not detected

Accessory amounts of Fe and Mg were also noted, however the low concentration of these elements (Mg and Fe) did not play any significant role in the final outcome of the quartz composition.

3.6.1.5. NCE

Unknown #11

In total, seven unknown #11 grains were analysed and these grains appear to have been some form of apatite (probably Ellestadite), however the higher than normal SiO_2 content also makes a compelling case for a quartz substituted component. The maximum SiO_2 is 87.48 wt%, with a minimum of 48.21 wt%, the CaO has a maximum of 21.94 wt%, a minimum of 3.53 wt% with an average of 12.49 wt%. This unknown phase is also rich in Cl in some grains but the variance also indicates that the Cl enrichment is not generally consistent (Table

3.11). The Cl has a maximum of 18.74 wt%, a minimum of 0.16 wt% averaging 8.19 wt% with a coefficient of variation recorded at 92%.

Table 3.11. Summary of SEM data of unknown #11 in NC-E (n=7) wt%

	MgO	Al_2O_3	SiO_2	FeO	K_2O	CaO	S	Cl	Pm	Mo
Max	11,09	4,04	87,48	1,17	4,32	21,94	2,53	18,74	1,16	0,63
Min	2,57	1,89	48,21	1,17	1,12	3,53	0,31	0,16	0,46	0,63
Mean	4,93	2,88	71,41	1,17	2,07	12,49	1,45	8,19	0,81	0,63
STDEV	3,32	0,86	15,31	END	1,21	6,27	0,81	7,51	0,49	END
CoV	0,67	0,30	0,21	END	0,58	0,50	0,56	0,92	0,61	END

END = Element not detected

3.6.1.6. NCF

Magnetite

A total of 5 magnetite grains were analysed, from the data (Table 3.12), it is very obvious that the magnetite composition does not vary much and therefore was not too influenced by external forces during and after formation, this is also quantified by the relatively low coefficient of variation recorded at 3% (Table 3.12). The FeO has a maximum of 98.65 wt%, a minimum of 91.45 wt% averaging 96.27 wt%. The accessory MgO, Al_2O_3 and SiO_2 were only noted in one of the five grains analysed (Appendix C).

Table 3.12. Summary of SEM data of magnetite in NC-F (n=5) wt%

	MgO	Al_2O_3	SiO_2	Cr_2O_3	FeO	NiO
Max	1,01	0,42	0,66	3,75	98,65	0,58
Min	1,01	0,42	0,66	1,94	91,45	0,58
Mean	1,01	0,42	0,66	2,81	96,27	0,58
STDEV	END	END	END	0,91	2,84	END
CoV	END	END	END	0,32	0,03	END

END = Element not detected

3.6.1.7. NCG

Chromite

A total of 3 chromite grains were analysed on the SEM (Table 3.13). The major constituent of the chromite, the Cr_2O_3 has a maximum of 56.15 wt%, a minimum of 14.80 wt% averaging 29.33 wt%. There is not much variance within the distribution of the Cr_2O_3 and the coefficient of variation was measured at 3%. Accessory Zn and Br were also noted but their concentrations are not of any significant value. Minor accessory amounts of SiO_2 were also noted and just like the Zn and Br, the low SiO_2 concentrations do not have any significant impact on the final outcome of the chromite composition.

Table 3.13. Summary of SEM data of chromite in NC-G (n=3) wt%

	MgO	**Al_2O_3**	**SiO_2**	**Cr_2O_3**	**MnO**	**FeO**	**NiO**	**ZnO**	***Br-L***
Max	0,65	1,32	0,56	56,15	1,48	86,16	1,33	0,92	0,74
Min	0,65	1,32	0,54	14,80	0,13	44,34	1,33	0,00	0,58
Mean	0,65	1,32	0,55	29,33	0,81	70,57	1,33	0,55	0,66
STDEV	END	END	0,02	23,25	0,96	22,85	END	0,48	0,11
CoV	END	END	0,03	0,79	1,19	0,32	END	0,88	0,17

END = Element not detected

3.6.1.8. NCH

Trevorite

Table 3.14. Summary of SEM data of trevorite in NC-H (n=8) wt%

	MgO	**Al_2O_3**	**SiO_2**	**FeO**	**NiO**	**TiO_2**	**Os**	**Ir**	**Tl**
Max	0,66	1,09	2,01	82,08	16,41	0,85	0,62	0,59	1,01
Min	0,10	0,30	0,34	68,91	14,62	0,15	0,27	0,23	1,01
Mean	0,27	0,71	0,98	77,78	15,49	0,38	0,45	0,41	1,01
STDEV	0,21	0,39	0,63	4,54	0,68	0,33	0,25	0,25	END
CoV	0,79	0,55	0,64	0,06	0,04	0,87	0,56	0,62	END

END = Element not detected

A total of eight trevorite grains were analysed, the distribution of the major components of trevorite were not too variable. The only relatively large variances were noted in accessories

such as TiO_2 and SiO_2 with variances recorded at 87% and 64% respectively (Table 3.14). The NiO had a maximum of 16.41 wt%, a minimum of 14.62 wt% and averaging 15.49 wt% while FeO had a maximum of 82.08 wt%, a minimum of 68.91 wt% and averaging 77.78 wt%. The variation for both major constituents (NiO and FeO) was recorded at 4% and 6% respectively. There is also minor isomorphous substitution of the Fe by the Ti.

Willemseite

Only two willemseite grains were analysed, the data (Table 3.15) was normalised, for the original data, see Appendix C. A relatively large variance was only noted in MgO with a coefficient of variation of 43% (Table 3.15). The maximum MgO was 9.33 wt%, with a minimum of 5.01 wt% and averaging 7.17 wt%. The SiO_2 had a maximum of 67.45 wt%, a minimum of 58.13 wt%, averaging 62.79 wt% and the coefficient of variation was 10%. The coefficient of variation NiO and FeO suggests similar behaviour (Table 3.15), the NiO had a maximum of 27.59 wt%, a minimum of 26.67 wt%, averaging 27.13 wt% and with a coefficient of variation of 2%. The FeO had a maximum of 4.14 wt%, a minimum of 4.09 wt% averaging 4.12 wt% with a coefficient of variation at 1% (Table 3.15).

Table 3.15. Summary of SEM data of willemseite in NC-H (n=2) normalised wt%

	MgO	Al2O3	SiO2	FeO	NiO	CoO	As	S
Max	9,33	0,05	67,45	4,14	27,59	0,55	0,50	0,26
Min	5,01	0,05	58,13	4,09	26,67	0,55	0,50	0,26
Mean	7,17	0,05	62,79	4,12	27,13	0,55	0,50	0,26
STDEV	3,05	END	6,59	0,03	0,65	END	END	END
CoV	0,43	END	0,10	0,01	0,02	END	END	END

END = Element not detected

3.6.1.9. NCJ

Nimite

Table 3.16. Summary of SEM data of nimite in NC-J (n=14) wt%

	MgO	Al_2O_3	SiO_2	Cr_2O_3	FeO	NiO	TiO_2	P_2O_5	CaO	CoO	Cl	Pt
	18,69	15,37	31,84	END	5,51	22,28	END	0,44	0,63	END	END	END
	19,42	16,27	33,88	END	5,24	22,45	END	END	0,14	END	END	END
	16,77	13,08	27,52	END	4,76	20,08	END	2,92	5,29	END	END	END
	18,13	14,59	30,52	0,54	13,60	21,34	END	END	0	END	END	END
	19,84	16,08	36,27	0,82	6,13	25,46	END	END	0,13	0,66	END	END
	18,76	14,89	33,32	0,50	5,34	23,95	END	END	0,03	0,71	END	END
	17,46	14,27	30,84	0,66	10,35	23,67	END	END	END	0,64	END	END
	4,81	3,52	10,14	END	12,90	45,58	END	END	END	2,64	2,52	END
	3,62	3,35	4,62	1,36	78,05	5,70	0,87	END	END	END	END	0,78
	19,84	15,84	34,63	0,54	5,73	26,26	END	END	END	END	END	END
	17,99	15,52	33,04	END	7,70	31,89	END	END	0,52	END	END	0,33
	19,14	15,44	33,75	END	5,61	23,50	END	END	END	END	END	0,1
	16,83	12,13	29,25	0,63	19,65	21,78	END	END	END	END	END	END
	9,89	6,56	16,11	END	11,97	35,64	END	END	1,22	END	END	END
Max	19,84	16,27	36,27	1,36	78,05	45,58	0,87	2,92	5,29	2,64	2,52	0,78
Min	3,62	3,35	4,62	0,50	4,76	5,70	0,87	0,44	0,00	0,64	2,52	0,10
Mean	15,80	12,64	27,55	0,72	13,75	24,97	0,87	1,68	0,99	1,16	2,52	0,40
STDEV	5,50	4,62	9,88	0,30	19,02	8,88	END	1,75	1,78	0,99	END	0,35
CoV	0,35	0,37	0,36	0,42	1,38	0,36	END	1,04	1,80	0,85	END	0,86

END = Element not detected

A total of 14 nimite grains were analysed. A large variance was noted in the FeO, with a maximum of 78.05 wt%, a minimum of 4.36 wt%, averaging 13.75 wt% with a coefficient of variation recorded at 138%. The coefficient of variation of the other major components such as MgO, Al_2O_3, SiO_2, and NiO was consistently the same (Table 3.16). MgO had a maximum of 19.84 wt%, a minimum of 3.62 wt%, averaging 15.80 wt% and with a coefficient of variation recorded at 35%. The Al_2O_3 had a maximum of 16.27 wt%, a minimum of 3.35 wt% averaging 12.64 wt% and with a coefficient of variation recorded at 37%. The SiO_2 had a maximum of 36.27 wt%, a minimum of 4.62 wt%, averaging 27.55 wt% and with a recorded coefficient of variation of 36%. The NiO had a maximum of 45.58 wt%, a minimum of 5.70 wt% averaging 24.97 wt% and with a recorded coefficient of variation of 36%.

3.6.1.9. NCK

Népouite

A total of three népouite grains were analysed. The SiO_2 had a maximum of 60.56 wt%, a minimum of 47.37 wt% averaging 53.87 wt% and with a coefficient of variation of 12%. The NiO had a maximum of 42.61 wt%, a minimum of 32.69 wt% averaging 36.63 wt% and with a recorded coefficient of variation of 14% (Table 3.17). The népouite has some accessory F noted in only one of the two grains analysed.

Table 3.17. Summary of SEM data of népouite in NC-K (n=3) wt%

	MgO	Al_2O_3	SiO_2	FeO	NiO	F	Cl
Max	6,11	0,51	60,56	7,10	42,61	9,76	0,38
Min	4,40	0,51	47,37	3,61	32,69	9,76	0,38
Mean	5,26	0,51	53,87	4,94	36,63	9,76	0,38
STDEV	1,21	END	6,60	1,88	5,27	END	END
CoV	0,23	END	0,12	0,38	0,14	END	END

END = Element not detected

Millerite

A total of three millerite grains were analysed. The major millerite constituents (Ni and S) show an identical coefficient of variation (Table 3.18), with some accessory As, Co and Fe phases also present. The Fe had a maximum of 4.44 wt%, a minimum of 3.48 wt% averaging 3.97 wt% and a coefficient of variation recorded at 12%, the Co had a maximum of 2.12 wt%, minimum of 1.55 wt% averaging 1.80 wt% with a coefficient of variation of 16% and As had a maximum of 0.76 wt%, minimum of 0.20 wt% averaging 0.51 wt% with a much higher coefficient of variation recorded at 56%.

Table 3.18. Summary of SEM data of millerite in NC-K (n=3) wt%

	As	Co	Fe	Ni	S
Max	0,76	2,12	4,44	63,77	32,49
Min	0,20	1,55	3,48	62,83	32,04
Mean	0,51	1,80	3,97	63,43	32,21
STDEV	0,28	0,29	0,48	0,52	0,24
CoV	0,56	0,16	0,12	0,01	0,01

END = Element not detected

The Ni had a maximum of 63.77 wt%, a minimum of 62.83 wt%, averaging 63.43 wt% and with a recorded coefficient of variation of 1% (Table 3.18). Another accessory element noted was the occurrence of As, however it was only noted in only three of the four analysed grains (Appendix C) and it shows a higher coefficient of variation of 56%.

3.6.1.10. NCL

Pyrite

A total of five pyrite grains were analysed. The largest variance was noted in grains with accessory Ni, with variation recorded at 86%, maximum of 2.27 wt%, minimum of 0.57 wt% and averaging 1.14 wt%. The S and Fe have an almost identical variation, recorded at 5 % and 4 % respectively. The S had a maximum of 56.43 wt%, a minimum of 50.05 wt% averaging 55.01 wt% the Fe had a maximum of 47.65 wt%, a minimum of 43.13 wt% and an average of 44.30 wt% (Table 3.19).

Table 3 19. Summary of SEM data of pyrite in NC-L (n=5) wt%

	S	Fe	Ni
Max	56,43	47,65	2,27
Min	50,05	43,13	0,57
Mean	55,01	44,30	1,14
STDEV	2,78	1,89	0,98
CoV	0,05	0,04	0,86

Pentlandite

A total of five pentlandite grains were analysed. The Fe had a maximum of 26.80 wt%, a minimum of 24.73 wt% averaging 26.25 wt% with a recorded coefficient of variation of 3%. The Ni had a maximum of 36.79 wt%, a minimum of 30.34 wt% averaging 34.83 wt% and a coefficient of variation of 7%.

Table 3.20. Summary of SEM data of pentlandite in NC-L (n=5) wt%

	S	Fe	Ni	Si
Max	44,97	26,80	36,79	0,13
Min	36,41	24,73	30,34	0,13
Mean	38,90	26,25	34,83	0,13
STDEV	3,44	0,86	2,58	END
CoV	0,09	0,03	0,07	END

END = Element not detected

Sulphur had the largest variation (9%) relative to the other elements (Fe and Ni), the maximum was 44.97 wt%, with a minimum of 36.41 wt% and an average of 38.90 wt% (Table 3.20). The Si was possibly replaced during the sulphide forming processes and therefore only represents insignificant accessory phases as noted in Table 3.20.

3.6.1.11. NCMA

Olivine

A total of three olivine grains were analysed. In the major constituents of olivine, the largest variance was observed in the FeO, where the coefficient of variation was recorded at 32 wt%, while the maximum was 14.28 wt% with a minimum of 7.48 wt% and averaging 11.96 wt% (Table 3.21). The SiO_2 showed the lowest variance with the coefficient of variation recorded at 2%, with a maximum of 40.21 wt%, a minimum of 38.62 wt% and averaging 39.60 wt%. The MgO had a maximum of 45.19 wt%, a minimum of 37.92 wt% averaging 42.54 wt% and with a recorded coefficient of variation of 9%.

Table 3 21. Summary of EMPA data of olivine in NC-MA (n=3) wt%

	MgO	SiO_2	MnO	FeO	NiO
Max	45,19	40,21	0,23	14,28	0,15
Min	37,92	38,62	0,11	7,48	0,14
Mean	42,54	39,60	0,18	11,96	0,14
STDEV	4,01	0,86	0,06	3,88	0,01
CoV	0,09	0,02	0,35	0,32	0,04

Accessory amounts of NiO were also observed, but the NiO had no impact on the final composition of the olivine and the distribution of the other elements within the olivine.

3.6.1.12. NCNA

Pyroxene

A total of nine pyroxene grains were analysed. There appears to have been an isomorphous solid state substitution between Cr and Fe and Cr was only noted in 3 of the 9 pyroxene grains. The Cr concentration range of 0.29 – 20.17 wt% has also resulted in a large variance, recorded at 154%.

Table 3 22. Summary of EMPA data of pyroxene in NC-NA (n=9) wt%

	MgO	Al_2O_3	SiO_2	Cr_2O_3	MnO	FeO
Max	37,87	1,35	68,12	20,17	0,26	17,95
Min	25,92	1,05	34,61	0,29	0,18	4,32
Mean	34,01	1,15	50,35	7,27	0,22	12,41
STDEV	4,83	0,13	8,62	11,18	0,06	3,66
CoV	0,14	0,11	0,17	1,54	0,26	0,30

The MgO had a maximum of 37.87 wt%, a minimum of 25.92 wt%, averaging 34.01 wt% and with a coefficient of variation of 14%. The SiO_2 had a maximum of 68.12 wt%, a minimum of 34.61 wt%, averaging 50.35 wt% and with a recorded coefficient of variation of 17%. The FeO had a maximum of 17.95 wt%, a minimum of 4.32 wt%, averaging 12.41

wt% and a coefficient of variation of 30% (Table 3.22). The occurrence of the accessory Al_2O_3 could be as a result of substitution between Al and Si, as it is not uncommon in amphiboles, however the occurrence of Al is minor and does not have any influence on the composition of the pyroxene.

3.7. Mineral comparison between samples and rock identification based on mineralogy

Comparison between minerals found in the rock samples were conducted on ternary diagrams, however only the major constituents (such as chlorite, serpentine, talc, sulphide species) were compared. For the full range of analyses with all the minerals that were investigated during the study, please see Appendix C. The talc grains from the BA host samples plot in different areas on the SiO_2+FeO+NiO ternary diagram and thus illustrates three different types of talc species (Fig 3.20). Group A has high SiO_2 (> 55 wt%) and very low FeO+NiO (<5 wt%), group B has moderate SiO_2 (≈45 wt%) and low FeO+NiO and group C has very high FeO+NiO (=>75 wt%) but low SiO_2 and MgO (Fig 3.20). The willemseite grains in the BA oxide samples all plot in the same area on the SiO_2+FeO+NiO ternary digram and do not show any significant compositional differences.

The chlorite distribution ternary diagram for both BA host and BA nickel oxide suite of rocks indicate that most of the chlorite grains plot in fairly the same position on the SiO_2+FeO+NiO+MgO+Al_2O_3 teranry diagram (Fig 3.21), with only minor (negligible) compositional differences. However there appears to be some outliers, one of the outliers has little to no SiO_2 and Al_2O_3 but high FeO+NiO+Mgo, while three of the outliers have SiO_2 content ranging between (20-25 wt%) and another three outliers have SiO_2 content between 55-60 wt% (Fig 3.21). The scattering trend (especially the outliers) is an indication of possible multiple events that acted on the original talc mineral species during formation but

were possibly not too different in composition, thus did not result in major compositional differences as would be expected with events variably different to the original talc composition.

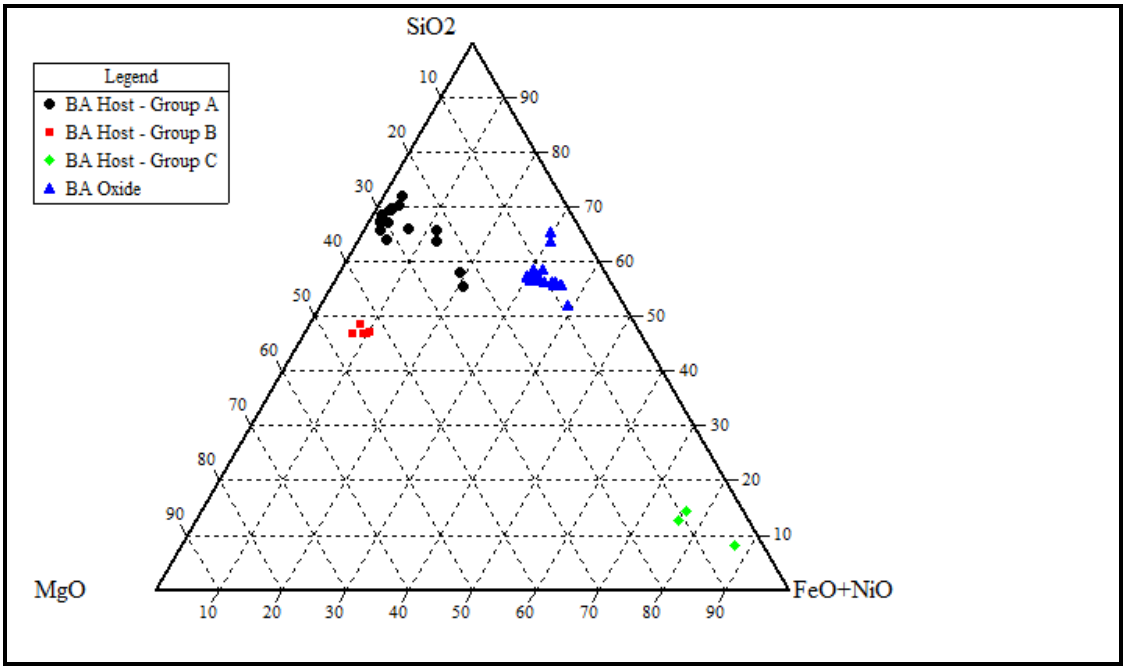

Figure 3.20. Talc composition represented by the SiO_2 + FeO+NiO + MgO ternary diagram, the concentrations were normalised to 100 wt%.

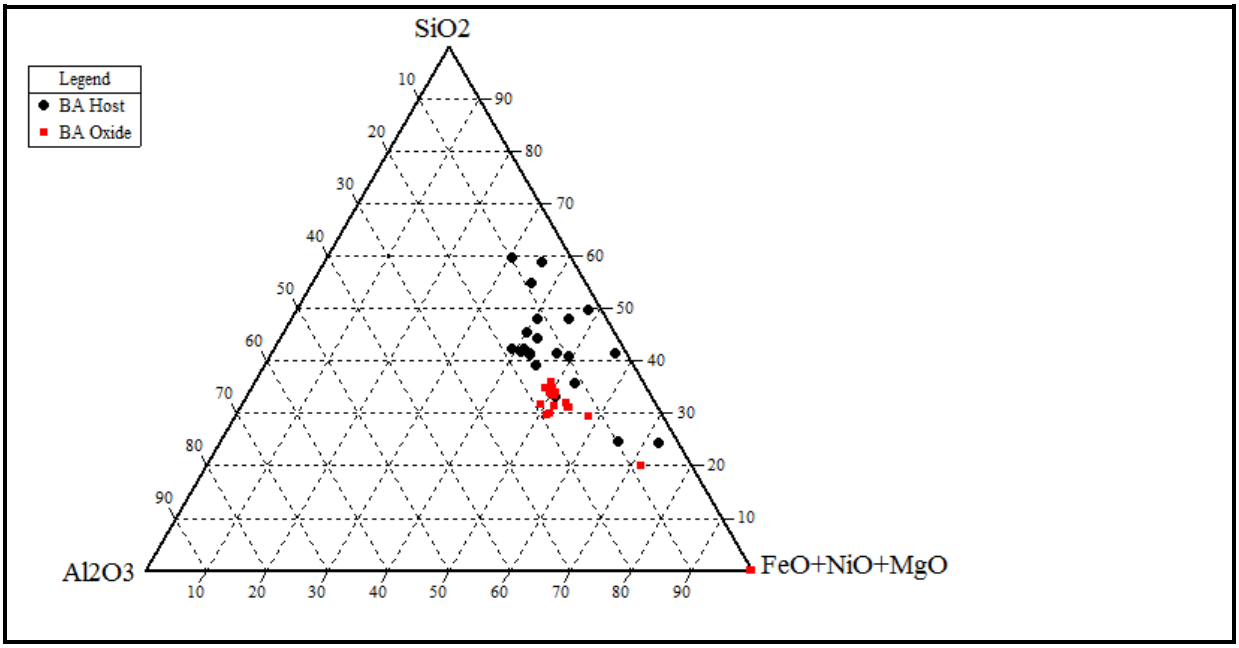

Figure 3 21. Fairly consistently distributed chlorite minerals in a SiO_2+FeO+NiO+MgO+Al_2O_3 ternary diagram, the concentrations were normalised to 100 wt%.

The BA host samples chlorites plotted on the FeO+NiO+MgO ternary diagram, show three different chlorite groups as seen in Fig 3.22. Group A has very low FeO (< 20 wt%) content and moderate MgO and NiO, group B has FeO content measured at ≈18 wt% on average and NiO measuring > 53 wt% on average, group C has very high FeO content (≈ 85 wt% on average) but very low MgO (<1 wt%).

The nimite of the BA nickel oxide samples also show three groups (Fig 3.22), all three nimite groups show very contrasting FeO+NiO+MgO compositions varied over a wide range. Group A nimite grains of the BA oxide samples have low FeO (≈ 10 – 12 wt%) and moderate MgO and NiO (47 – 52 wt%), group B has relatively low FeO content (13 -22 wt%) while the outliers have FeO ranging between ≈ 20 – 33 wt% characterised by almost constant MgO and NiO (≈ 40 – 52 wt%) and group C has high FeO (≈ 85 wt%) but low MgO and higher NiO concentrations.

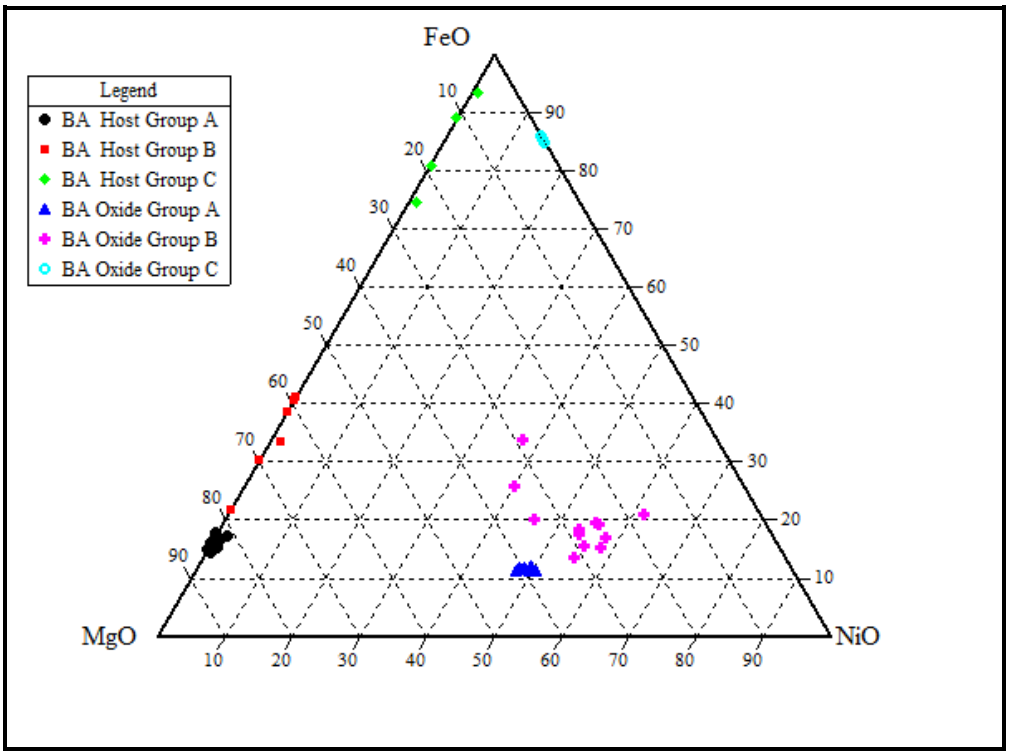

<u>Figure 3.22.</u> Different groups of chlorite minerals represented by a FeO+NiO+MgO ternary diagram, the concentrations were normalised to 100 wt%.

The BA host rocks show two different species of serpentine, although only two grains were analysed (Fig 3.23), therefore this should only be used as an example and should not be used to provide difinitive conclusions about the serpentine species of BA host rocks. For comparison purposes, one of the serpentine species has moderate SiO_2 (≈28 wt%) and high FeO+NiO (≈50 wt%), while the second species has high SiO_2 content (≈65 wt%) but very low FeO+NiO (<10 wt%). The népouite grains in the BA nickel oxide samples all plot in the same area and have a fairly consistent composition, moderate to high SiO_2 content (> 50 wt%), moderate FeO+NiO (38 – 45 wt%) and low MgO (< 10 wt%), with one of the serpentine grains showing very low MgO content (almost zero, Fig 3.23).

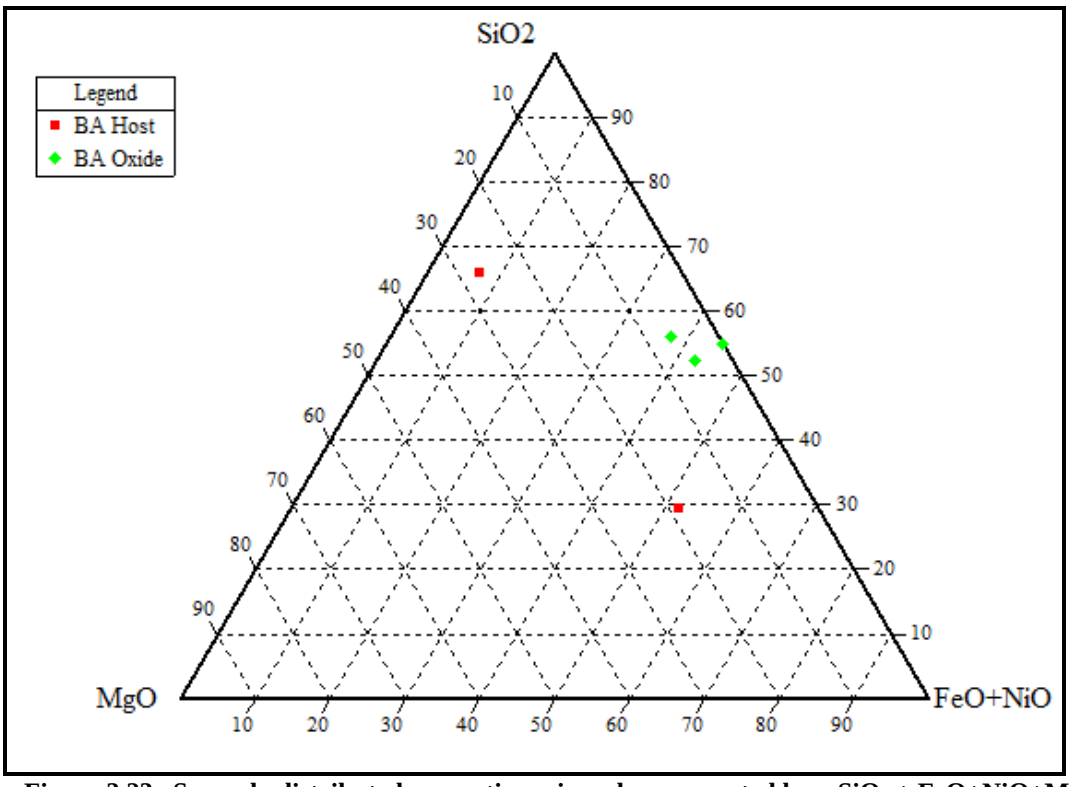

Figure 3.23. Sparsely distributed serpentine minerals represented by a SiO_2 + FeO+NiO+MgO ternary diagram, the concentrations were normalised to 100 wt%.

As with the BA host serpentine grains, the nepouite composition of the BA nickel oxide in Fig 3.23 should only be used for comparison purposes and not to draw definitive conclusions

due to the small grain (sample) population. The minimal number of nepouite grains analysed is noted as due to nepouite only representing the least of the major dominant minerals (willemseite and nimite) in the BA oxide samples. On the As+Ni+Fe ternary diagram (Fig 3.24), unknown #5 plots in the same position and it is relatively enriched in As (≈44 wt %) and highly enriched in Ni (≈95 wt %), while it is highly depleted in Fe. Unknowns #4 and #10 are both highly depleted in As but enriched in Ni and Fe respectively and are characterised by the nearly scattered patterns of the grains. Unknown #10 indicates a noticeable range in differences in both Fe and Ni concentration on the analysed grains, with the range between 62 – 73 wt% and 27 – 38 wt% respectively. Unknown #10 could not be plotted since only a single Pt-rich grain was noted and analysed, therefore could not be conclusively attributed to a specific phase.

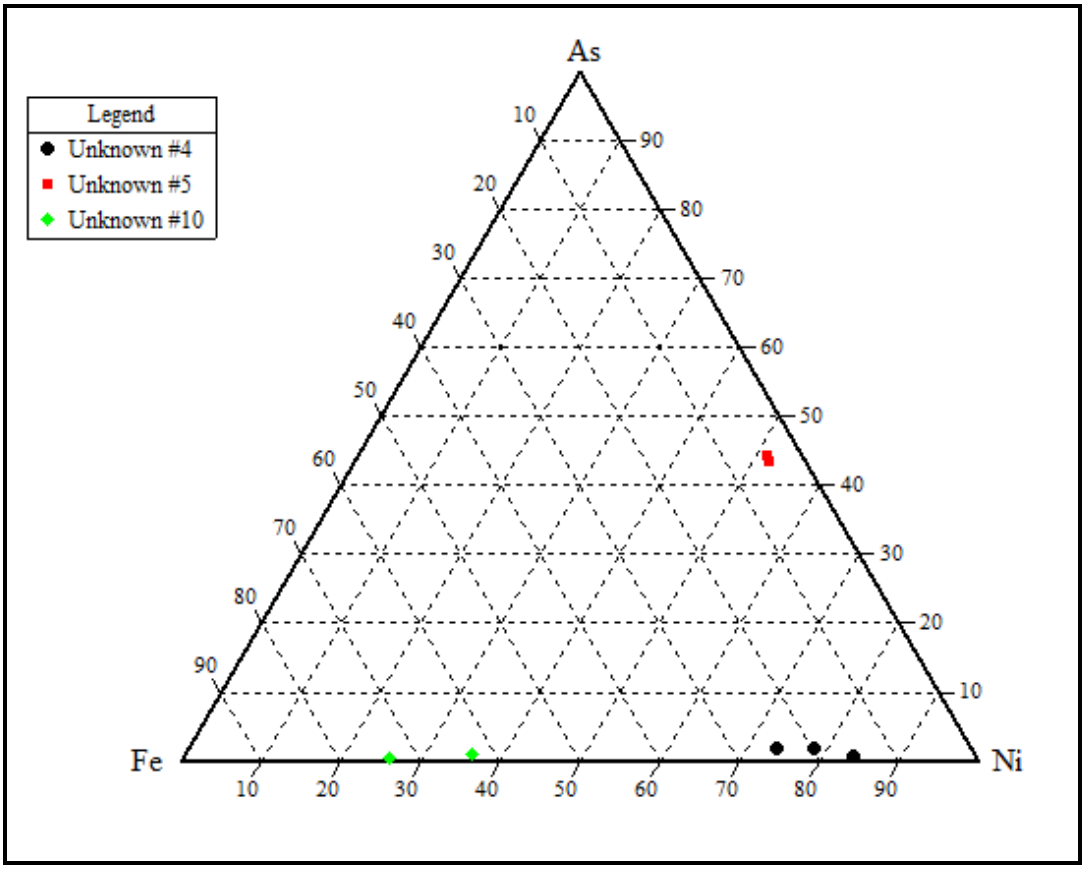

Figure 3.24. Distribution of the unknown minerals in a As + Ni + Fe ternary diagram, the concentrations were normalised to 100 wt%.

On the Ni+Fe+Sb ternary diagram (Fig 3.25) unknown #4 has very low Fe, moderate Ni and high Sb content, while unknown #10 appears to have relatively low Ni and moderate to high Fe concentrations with slightly low to moderate Sb ranging from 17 – 30 wt% (Fig 3.25). Unknown #5 is highly deficient in Fe but highly enriched in Sb and Ni ((Fig 3.25), a function of only plotting the one main constituents against accessory components.

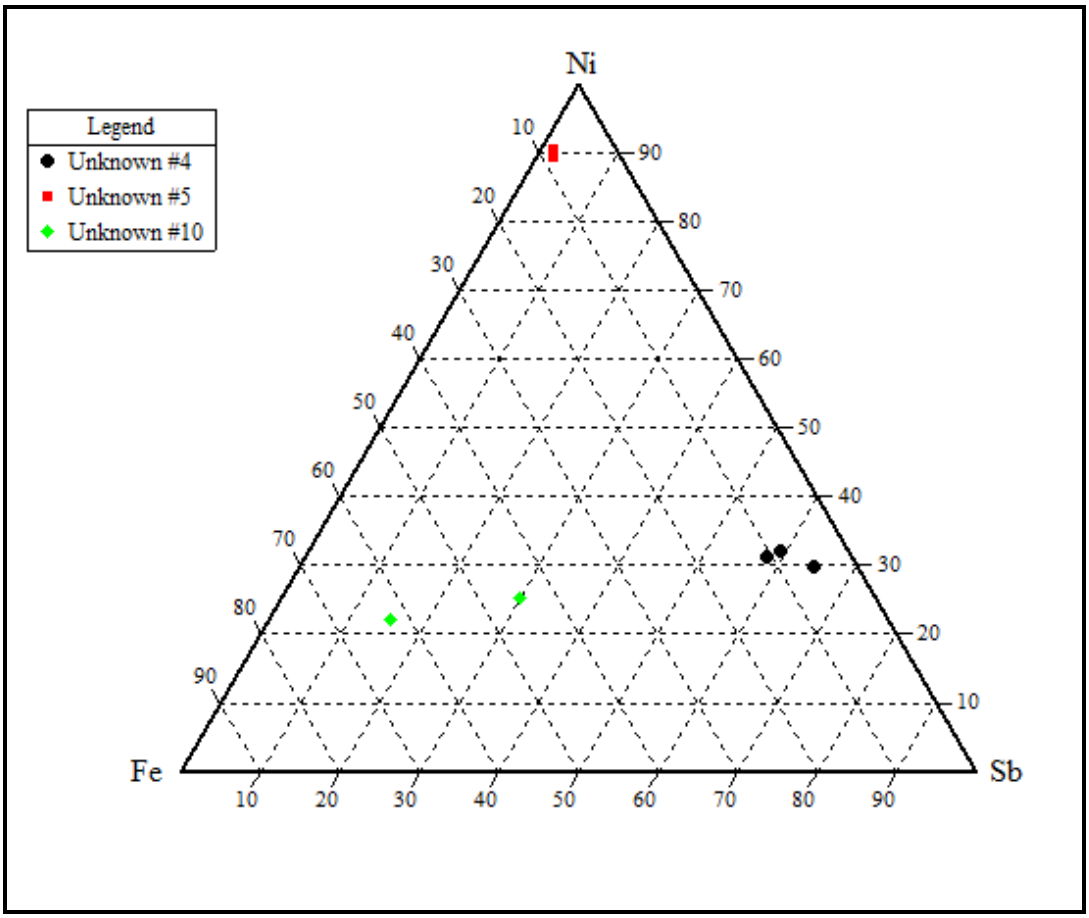

<u>Figure 3.25.</u> Distribution of the unknown minerals in a As + Ni + Fe ternary diagram, the concentrations were normalised to 100 wt%.

The sulphides in the Fe+Ni+S ternary diagram show varied concentrations, the nickel rich pyrite (bravoite) is highly deficient in Fe as expected due to the substitutional relationship between Ni and Fe in solid solution, while the normal pyrite is highly deficient in nickel but enriched in S as is expected in normal pyrite (Fig 2.26). The pentlandite averages ≈25 wt%

Fe with moderate Ni and S while the millerite indicates two different types of species (Fig 3.26). The one millerite species has high Fe (ranging from 44 – 60 wt%), with moderate Ni and slightly lower S content, while the second millerite species is characterised by low Fe (< 10 wt%), high Ni (> 55 wt%) and moderate S (ranging from ≈ 41 – 45 wt%). All the sulphides with the exception of the millerite analysed were from the NCL sample, while the millerite analyses are from the BA oxide samples.

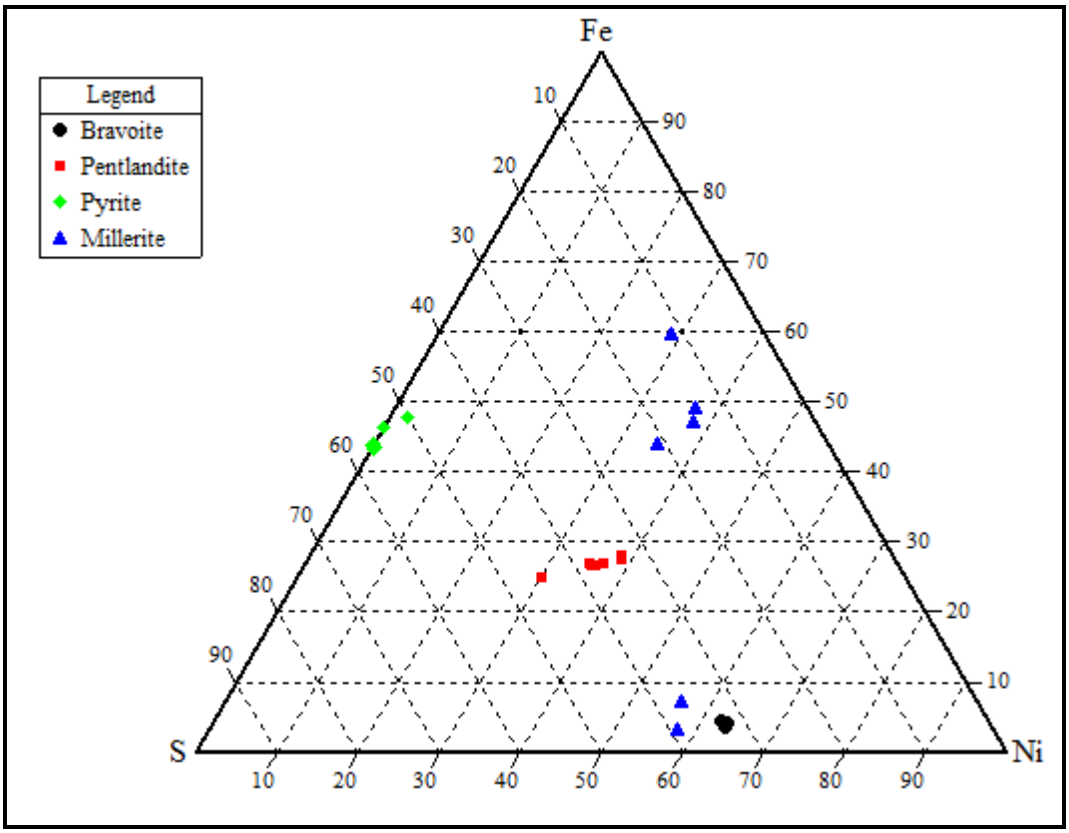

<u>Figure 3.26.</u> Distribution of the sulphide minerals in a Fe + Ni + S ternary diagram, concentrations all added to 100 wt%.

Typical mineral compositions of serpentinites that formed after peridotites comprise olivine, pyroxene, chromium spinel and plagioclase Evans and Girardeau (1988) therefore samples: NC-A and NC-D, were determined to represent a typical talc schist and are made up mainly of talc phases, with remnants of olivine, orthopyroxene (often representing an exsolution texture), clinopyroxene and chromian spinel in various proportions (Pereira et al, 2008) and

samples NC-B, NC-E and NC-F, all represent a serpentinised talc schist. Serpentinised talc schists are typically rich in the serpentine group minerals (chlinochlore, chamosite, some magnetite etc.), and talc as evidenced by the above mentioned samples. Also characteristic within these serpentinised talc schist is the occurrence of oxide minerals such as ilmenite, hematite (mainly pseudomorphous) and/or goethite, and some minor Cr-rich phases. Sample NC-C and NC-G represents a quartz talc schist that has not yet undergone complete serpentinisation.

Based on the work done by Eggins et al, (1998), where they concluded that peridotites are comprised of olivine, orthopyroxene, clinopyroxene, spinel and amphibole breakdown products, it is therefore within reason to suggest that BA host rocks, show similarities to precursor peridotite. Therefore, it is within this context that the mineralogy of BA host rocks and peridotites, have been found to be similar and thus resulted in the identification and classification of samples NC-A to NC-G as highly altered and modified peridotite that has now been altered to form different types of schists and their related mineral assemblages. However the deformation appears to be more pronounced in samples NC-A, NC-B, NC-D, NC-E and NC-F while samples NC-C and NC-G are not completely serpentinised. The mineralogical and elemental investigations made it possible to classify samples NC-H, NC-J and NC-K as representations of a suite of rocks enriched in siderophile elements with certain similarities to peridotite and komatiites and therefore have only been classified as ultramafic rocks.

Chapter 4 – Whole rock chemical results

Twenty samples were investigated using a variety of investigative techniques. The techniques employed were magnetic susceptibility, XRF, SEM, EMPA and ICP-MS (for sample origin refer to Table 2.1). All the analytical results are attached in Appendix C, and are summarised in this chapter.

4.1. XRF results

Table 4.1. Major elements results from the PANalytical WD-XRF Axios spectrometer at the Geology Department, University of the Free State, in wt%.

(wt%)	NCA	NCB	NCC	NCD	NCE	NCF	NCG	Avg	NCH	NCJ	NCK	Avg	NCL
SiO_2	36.23	29.66	60.32	54.24	51.74	33.88	54.78	45.84	26.28	51.11	21.91	33.10	44.62
Al_2O_3	17.83	11.25	1.69	2.89	3.1	9.75	3.03	7.08	1.28	2.16	1.46	1.63	8.05
Fe_2O_3	7.69	26.81	3.87	9.75	12.68	24.19	8.88	13.41	41.49	21.27	43.75	35.50	32.02
MnO	0.05	0.09	0.02	0.1	0.07	0.06	0.17	0.08	0.01	0.03	0.02	0.02	0.13
MgO	38.38	28.7	32.01	30.94	29.71	29.16	30.41	31.33	5.31	4.48	3.78	4.52	1.53
CaO	0.04	0.03	0.03	0.05	0.05	0.04	0.06	0.04	END	END	END	END	0.04
K_2O	END	END	END	END	END	END	END	END	END	END	END	END	1.98
TiO_2	0.82	0.43	0.08	0.12	0.15	0.44	0.13	0.31	0.1	0.11	0.08	0.10	0.29
P_2O_5	END	0.01	END	0.01	END	0.02	0.01	0.01	0.01	0.02	0.01	0.01	0.01
NiO	0.41	0.6	0.28	0.36	0.33	0.52	0.37	0.41	21.01	12.59	22.96	18.85	2.22
Cr_2O_3	0.28	1.42	0.15	0.31	0.31	0.88	0.22	0.51	0.1	1.69	0.02	0.60	2.54
LOI	0.37	0.19	0.16	0.84	1.38	0.27	3.30	0.93	1.94	6.00	4.05	4.00	7.36
Total	102.10	99.20	98.62	99.61	99.51	99.21	101.4	99.95	97.53	99.45	98.04	98.34	100.81

END = Element not detected

The major elements data contained in Table 4.1, illustrates relationships and variabilities that can be deduced for the major element constituents in the twenty studied rock samples. The variability is largely prominent in specific major elements (i.e. SiO_2, Al_2O_3, Fe_2O_3 and MgO) between BA host rocks and the nickel sulphide samples (comprising the ANL and NCL samples), the ANL samples are slightly enriched in comparison in the aforementioned major elements however, it is vital to note this is due to the different rock types as it is clearly seen in Table 4.1.

Table 4.1. Major elements results from the PANalytical WD-XRF Axios spectrometer at the Geology Department, University of the Free State and the ICP-OES, in wt%. Continued.

(wt%)	NCMA	NCNA	Avg	*UFS 16a	*UFS 38a	*UFS 39a	*UFS 16c	*UFS 4CS2	*UFS 39b	*UFS 38e	Avg
SiO_2	53,46	71,53	62,49	37,15	34,63	37,61	39,74	85,25	62,4	51,65	49,78
Al_2O_3	1,39	END	1,39	0,22	0,24	0,26	11,19	0,86	18,14	13,15	6,29
Fe_2O_3	13,03	5,23	9,13	5,29	3,78	6,64	13,91	3,02	11,75	20,29	9,24
MnO	0,20	0,10	0,15	0,14	0,05	0,22	0,13	0,03	0,01	0,03	0,09
MgO	7,89	14,27	11,08	44,88	33,52	37,65	1,28	0,40	0,57	0,18	16,93
CaO	0,03	0,37	0,20	0,39	0,04	0,01	0,03	0,13	0,34	0,06	0,14
Na_2O	END	END	END	0,1	0,01	END	0,16	0,02	1,07	0,56	0,32
K_2O	END	END	END	0,04	0,03	0,03	2,15	0,07	0,67	1,16	0,59
TiO_2	END	END	END	0,01	0,01	0,01	0,41	0,02	0,74	0,45	0,24
P_2O_5	END	END	END	0,07	0,02	0,02	0,03	0,02	0,04	0,01	0,03
NiO	0,19	0,09	0,14	0,43	0,40	0,50	2,17	2,59	2,30	1,35	1,39
Cr_2O_3	24,58	0,32	12,45	0,12	0,14	0,16	2,07	0,17	0,62	2,58	0,84
LOI	0,14	7,48	3,81	10,06	26,42	15,80	26,52	8.02	1,41	7,43	13,66
Total	100,90	99,39	100,20	98,89	99,3	98,92	99,77	100,60	100.00	98,90	99,48

END = Element not detected and *Analysed using ICP-OES.

The BA oxide samples have the lowest SiO_2 concentrations on average (33.10 wt%, normally expected in deep earth derived samples) when compared to all the other studied samples. The nickel sulphide and BA host samples show almost similar Al_2O_3 contents however both ANL and BA host rocks indicate very large variations within their Al_2O_3 levels when compared to the other samples. Generally the BA oxide and Kraubath rock samples have similar Al_2O_3 concentrations and represent the lowest Al_2O_3 concentration in all the samples. The BA oxide samples are much more enriched in Fe_2O_3 when compared to the other rock samples with the only exception noted in the Scotia Talc mine sample.

The BA host rocks together with certain ANL samples (UFS16a, UFS38a and UFS39a, Table 4.1) show similar MgO enrichment but with distinctly different MgO averages (Table 4.1),

while BA oxide samples all have MgO <6 wt%. The other remaining ANL samples (UFS 4CS2, UFS 39b, UFS 38e and UFS 16c) all have MgO <1 wt% on average, while 1.28 wt% of MgO, is solely accounted for by UFS 16c. As expected in mafic to ultramafic deposits the CaO, K_2O, P_2O_5 and TiO_2 concentrations are all <1 wt% in all the studied samples with the exception of sample NC-L where K_2O is 1.98 wt%, in some instances CaO was not detected as it was below the detection limit of 303.55ppm of the XRF. The BA oxide samples show high enrichment in NiO (18.55 wt% on average) when compared to all the studied samples, where the NiO content is <1 wt% on average (Bon Accord host and Kraubath samples, Table 4.1) with the exception of the ANL samples with 1.39 wt% on average and 2.22 wt% on average for the NCL sample.

All samples, with the exception of the Kraubath samples are highly depleted in Cr_2O_3, with Cr_2O_3 concentrations recorded at <1 wt% for the other samples (Bon Accord oxide, Bon Accord host and ANL samples), the only exception is noted in sample NCL with Cr_2O_3 concentrations recorded at 2.54 wt% on average. All samples with the exception of samples UFS 39b and NCL, are highly depleted in P and Na (Table 4.1).

The trace element data in Table 4.2, indicates enrichment in Co and relative enrichment in V in the BA host rocks, but with a very large range (V = 14 to 278 ppm and Co = 40 to 252 pm). Out of all detected trace elements, Mo is the least enriched in BA host rocks and has a range between 0.30 to 0.90 ppm.

Bon Accord oxide samples are enriched in Co and Cu and the enrichment range between both trace elements (Co and Cu), the variation was noted as a range (Co = 4839.34 – 8869.76 ppm and Cu = 385.89 – 795.11 ppm), compared to other elements within the same samples, while Sr ranging between 0.2 to 0.7 ppm is the least enriched in the BA nickel oxide samples.

Table 4.2. **Trace elements results from the PANalytical WD-XRF Axios spectrometer, in ppm.**

(ppm)	NCA	NCB	NCC	NCD	NCE	NCF	NCG	NCH	NCJ	NCK	NCL
Sc	39,25	67,9	2,17	18,2	17,72	43,75	15,62	END	73,67	END	61,64
V	173,9	270,7	14,03	60,52	58,65	187,3	34,34	37,03	336,98	0,85	438,6
Co	104,6	251,6	39,57	122,7	118,41	225,4	92,06	8869	8583	4839	491,1
Cu	8,16	19,25	7,2	9,13	8,76	26,17	4,98	795,11	525,9	385,9	117,3
Zn	54,61	71,25	28,09	30,03	24,29	49,14	27,76	59,07	60,83	24,66	96,97
As	5,04	45,55	13,58	19,1	14,09	21	18,64	107,1	171,1	27,99	1704
Br	2,63	4	2,23	3	2,41	3,94	3,16	3,6	3,48	2,42	1,44
Sr	0,95	0,57	0,16	1,45	1,18	0,72	1,73	0,7	0,3	0,18	20,01
Rb	0,31	0,42	END	1,65	0,99	END	1,04	END	0,51	END	41,83
Y	4,93	2,63	0,82	2,28	2,74	2,78	2,75	2,62	9,54	2,12	0,22
Zr	107,55	23,41	5,67	12,05	15,07	53,93	13,74	29,64	30,3	7,38	25,2
Nb	4,24	1,35	0,74	0,79	0,53	1,85	0,54	1,25	0,83	0,88	0,17
Mo	0,42	0,89	0,21	END	0,47	0,29	END	0,87	0,9	0,91	4,04
Ag	6,89	END	22,93	7,86	END	3,96	0,98	11,39	18,64	38,59	END
Cd	END	END	END	END	END	END	END	END	4,57	END	END
Sb	END	4,57	3,85	3,03	END	2,18	2,39	23,16	38,53	22,05	40,69
Ba	END	107,3	END	11,35	13,98	21,7	18,46	7,81	11,74	15	1821
Tl	3,04	4,52	1,07	2,12	1,42	3,64	1,9	2,78	0,69	2,35	3,56
Pb	END	1,96	END	0,74	END	1,93	END	END	END	END	19,39
Th	1,91	2,24	0,67	END	0,86	0,45	0,03	0,09	0,75	0,91	1,63
U	1,06	0,93	0,22	0,66	END	END	0,44	2,52	0,51	END	2,72

END = Element not detected

The two Kraubath samples (NCMA and NCNA) investigated show contrasting V, Co, Cu and Zn concentrations, with sample NCMA relatively enriched in Co, Cu, V and Zn compared to sample NCNA (Table 4.3). When comparing all the elements investigated in the Kraubath samples, it emerged that both samples (NCMA and NCNA) are variably enriched in V, Co, Cu and Zn, and depleted in the other trace elements (Table 4.3), Zr is the most depleted and was measured at 0.13 ppm in sample NCNA while it was not detected in sample NCMA.

Table 4 3. Trace elements results from the PANalytical WD-XRF Axios spectrometer.

(ppm)	NCMA	NCNA	NCL	UFS 16a*	UFS 38a*	UFS 39a*	UFS 16c*	UFS 4CS2*	UFS 39b*	UFS 38e*
Sc	21,83	15,07	61,64	2,9	2,2	2,7	51,6	6,5	36,1	28,3
V	3322	70,18	438,6	6,8	8,6	12,7	260,7	19,8	380,4	417,4
Co	258,8	80,11	491,1	70,9	66,9	54,7	250,1	228,3	311,1	781,5
Cu	143,9	26,09	117,3	124,9	65,9	128,2	200,3	86,4	1149	144,1
Zn	554,1	53,13	96,9	35,2	15,4	23,8	95,4	13,7	164,4	1328
As	0,22	END	1704	END	END	END	END	END	END	END
Br	1,27	0,31	1,44	END	END	END	END	END	END	END
Sr	1,4	0,48	20,01	5,3	1,3	0,8	52,5	3,7	142,7	260,6
Rb	1,72	0,7	41,83	0,4	END	0,3	50,9	0,9	32,1	77,2
Y	END	0,19	0,22	0,5	0,4	0,5	1,5	0,3	25,1	2,1
Zr	END	0,13	25,2	6,7	7,9	7,6	27,7	9,9	83	30,2
Nb	0,43	0,5	0,17	0,22	0,43	0,25	1,73	0,19	8,91	0,95
Mo	1,45	0,6	4,04	END	END	END	END	END	END	END
Ag	39,18	END	END	END	END	END	END	END	END	END
Sn	END	19,05	END	3,7	1,43	3,4	3,73	1,23	4,65	3,71
Sb	2,72	1,79	40,69	END	END	END	END	END	END	END
Ba	16,49	0,76	1821	3,3	1,7	3,4	1655	15,7	435,9	570,2
Tl	END	3,46	3,56	END	END	END	END	END	END	END
Pb	0,35	1,55	19,39	END	END	END	END	END	END	END
Th	1,16	0,82	1,63	0,04	0,05	0,06	0,43	0,05	1,53	0,13
U	END	0,91	2,72	0,02	0,01	0,01	0,12	0,01	0,41	0,09

END = Element not detected and *Analysed on the ICP-OES and ICP-MS

The As and Ba concentrations also provide contrasting comparisons, BA oxide samples contain the highest As concentrations followed by the BA host rocks, no As was detected in the ANL samples while the Kraubath samples contain the least As. The Ba is concentrated in

certain samples (NCL, UFS 16c and UFS 39b) of the nickel sulphide layer, while Ba in BA oxide samples appear to be slightly more enriched compared to BA host rocks and Ba was only detected in the one (NCMA) of the Kraubath samples.

Sample NC-L is relatively enriched in a few elements in varying proportions and this sample shows relatively high concentrations in V, Co, Cu, As and Ba. While the most depletion is noted in Nb, which measured at 0.17 ppm. The V, Co, Cu, As and Ba concentrations in sample NCL were measured as follows V = 438.6 ppm, Co = 491.1 ppm, Cu = 117.3 ppm, As = 1704 ppm and Ba = 1821 ppm. The ANL samples with the exception of samples (UFS 16c, UFS 38e and UFS 39b) are depleted in the entire trace element range.

The relatively enriched samples (UFS 16c, UFS 38e and UFS 39b) show relative enrichment in V, Co, Cu and Zn (Table 4.3). The enriched elements in sample UFS 16c were measured at V = 260.7 ppm, Co = 250.1 ppm and Cu = 200.3 ppm, while in sample UFS 38e, V = 417.4 ppm, Co = 781.5 ppm, Cu = 144.1 ppm and Zn = 1328 ppm and sample UFS 39b, V = 380.4 ppm, Co = 311.1 ppm, Cu = 1149 ppm and Zn = 164.4 ppm. Only a few trace elements were not detected during the investigation using the XRF; in the BA host rocks only Cd was not detected in all the samples, while in BA oxide samples only Pb was not detected in all the samples and Rb, Cd and Sc were only detected in sample NCJ. All the nickel sulphide samples did not contain As, Br, Mo, Ag, Tl, Sb and Pb since these elements were not detected during the XRF investigation (Table 4.3).

The light rare earth elements (LREE) are relatively enriched when compared to the heavy rare earth elements (HREE) with the exception of Eu in all the investigated samples (Table 4.4).

4.2. ICP-MS analysis results

ICP-MS was used to investigate the rare earth elements of BA host, BA oxide and ANL samples. At this point, only the tendencies of the data will be discussed; the REE plots and their implications are presented in the next chapter.

Table 4.4a. Rare earth element concentration data representing both light rare earth elements and heavy rare earth elements distributions in all the studied samples.

ppm	La	Ce	Pr	Nd	Sm	Eu	Gd	Tb	Dy	Ho	Er	Tm	Yb	Lu
NCA	3.98	9.85	1.23	5.07	0.93	0.07	0.60	0.07	0.42	0.09	0.32	0.06	0.45	0.08
NCB	0.67	0.88	0.17	0.75	0.19	0.04	0.22	0.04	0.26	0.06	0.18	0.03	0.22	0.04
NCC	0.70	1.45	0.19	0.78	0.16	0.03	0.14	0.02	0.16	0.03	0.10	0.02	0.10	0.02
NCD	2.61	6.02	0.90	3.80	0.70	0.11	0.50	0.07	0.38	0.07	0.21	0.03	0.20	0.03
NCE	1.34	2.65	0.40	1.67	0.35	0.06	0.31	0.05	0.30	0.06	0.18	0.03	0.18	0.03
NCF	1.57	2.80	0.41	1.76	0.40	0.06	0.42	0.06	0.42	0.09	0.29	0.05	0.37	0.06
NCG	1.83	4.84	0.52	2.11	0.43	0.09	0.38	0.06	0.38	0.07	0.22	0.03	0.23	0.04
NCH	0.40	0.98	0.13	0.67	0.28	0.02	0.46	0.09	0.73	0.17	0.59	0.10	0.76	0.12
NCJ	3.39	7.75	0.95	3.90	0.83	0.05	0.62	0.08	0.45	0.09	0.28	0.04	0.32	0.06
NCK	0.68	1.72	0.22	1.02	0.33	0.02	0.46	0.09	0.71	0.16	0.50	0.08	0.49	0.07
UFS 16a	0.15	0.32	0.04	0.14	0.06	0.03	0.05	0.01	0.06	0.01	0.03	0.01	0.03	END
UFS 38a	0.05	0.11	0.02	0.16	0.06	0.02	0.07	0.01	0.05	0.01	0.03	0.01	0.04	0.01
UFS 39a	0.13	0.26	0.04	0.17	0.08	0.02	0.06	0.01	0.05	0.02	0.03	0.01	0.04	0.01
UFS 16c	1.40	3.78	0.50	2.07	0.45	0.32	0.29	0.04	0.20	0.04	0.08	0.01	0.08	0.02
UFS 4CS2	0.04	0.09	0.01	0.08	0.04	0.01	0.06	0.01	0.05	0.01	0.03	0.01	0.04	0.01
UFS 39b	10.4	23.44	3.07	13.71	3.75	1.07	3.60	0.60	3.84	0.74	2.33	0.37	2.37	0.4
UFS 38e	0.23	0.51	0.08	0.36	0.15	0.20	0.21	0.04	0.27	0.06	0.18	0.03	0.22	0.04

Table 4.4b. Normalised rare earth element distributions in all the studied samples, continued. The REE data used for normalisation (reported by Lodders, 2003) in given at the bottom of the table.

Normalised	La	Ce	Pr	Nd	Sm	Eu	Gd	Tb	Dy	Ho	Er	Tm	Yb	Lu
NCA	17	16	13	11	6	1.2	3	1.9	1.8	1.6	2	2.5	2.8	3.3
NCB	3	1.5	2	2	1.3	0.7	1.1	1.1	1.1	1.1	1.1	1.3	1.35	1.7
NCC	3	2	2	2	1.1	0.6	0.7	0.6	0.7	0.5	0.6	0.8	0.6	0.8
NCD	11	10	10	8	5	2	3	2	1.6	1.25	1.3	1.25	1.2	1.25
NCE	6	4	4	4	2	1.1	2	1.4	1.3	1.1	1.1	1.25	1.1	1.25
NCF	7	5	4	4	3	1.1	2	1.7	1.8	1.6	1.8	2	2	2.5
NCG	8	8	6	5	3	1.6	2	1.7	1.6	1.25	1.4	1.3	1.4	1.7
NCH	2	1.5	1.4	1.5	2	0.4	2	2.5	3	3	4	4	5	5
NCJ	15	12	10	8	6	0.9	3	2	1.9	1.6	1.7	1.7	2	2.5
NCK	3	3	2	2.2	2	0.4	2	2.5	3	3	3	3	3	3
UFS 16a	0.6	0.5	0.4	0.3	0.4	0.6	0.2	0.28	0.3	0.2	0.2	0.4	0.2	END
UFS 38a	0.2	0.2	0.2	0.3	0.4	0.4	0.4	0.3	0.2	0.2	0.2	0.4	0.25	0.4
UFS 39a	0.6	0.4	0.4	0.4	0.6	0.4	0.3	0.3	0.2	0.4	0.2	0.4	0.25	0.4
UFS 16b	6	6	5	4	3	6	1.5	1.1	0.8	0.7	0.5	0.4	0.5	0.8
UFS 4CS2	0.2	0.1	0.1	0.2	0.3	0.2	0.3	0.3	0.2	0.2	0.2	0.4	0.25	0.4
UFS 39b	45	38	33	30	26	19	18	17	16	13	14	15	15	17
UFS 38e	1.0	0.8	0.9	0.8	1.0	4	1.1	1.1	1.1	1.1	1.1	1.25	1.35	1.7
Lodders 2003	0.232	0.621	0.093	0.457	0.145	0.055	0.198	0.036	0.238	0.056	0.162	0.024	0.163	0.024

END = Element not detected

The data in Table 4.4a were obtained by ICP–MS analyses. Normalisation was done using REE data values as reported by Lodders (2003). The following trends can be seen:

In the BA host rocks, samples NC-A and NC-D are slightly enriched in all the LREE (La - Sm) and samples NC-E, NC-F and NC-G all show almost identical LREE compositions. Samples NC-B and NC-C are highly LREE deficient, with NC-B being especially deficient in the LREE and NC-C in the HREE.

In the BA oxide, sample NC-H shows the highest enrichment in HREE but it is the most LREE deficient in all the BA oxide samples and Yb in NCH shows the highest normalised value of 5 in all BA oxide samples. NC-J is the most HREE depleted sample, but shows the highest LREE enrichment, La which has a normalised value at 15 is the most enriched LREE relative to the other LREE in the BA oxide samples.

The ANL samples are largely depleted in the REE (both LREE and HREE), with the exception of samples UFS 16b and UFS 39b. Sample UFS 39b is enriched in the entire REE range while sample UFS 16b is only relatively enriched when compared to the other depleted samples (Table 4.4). Rare earth element depletion is largely observed in sample UFS 4CS2, where Lu is the most enriched and Pr the most. Samples UFS 16a, UFS 38a and UFS 39a show distinctly similar HREE concentrations, the only major difference is noted in sample UFS 16a, where Lu was not detected (Table 4.4).

4.3. Element compositional variation diagrams illustrating the extent of chemical variation within the studied rock samples and their environments

The Harker diagrams below were plotted against MgO wt% due to its wide field of occurrence.

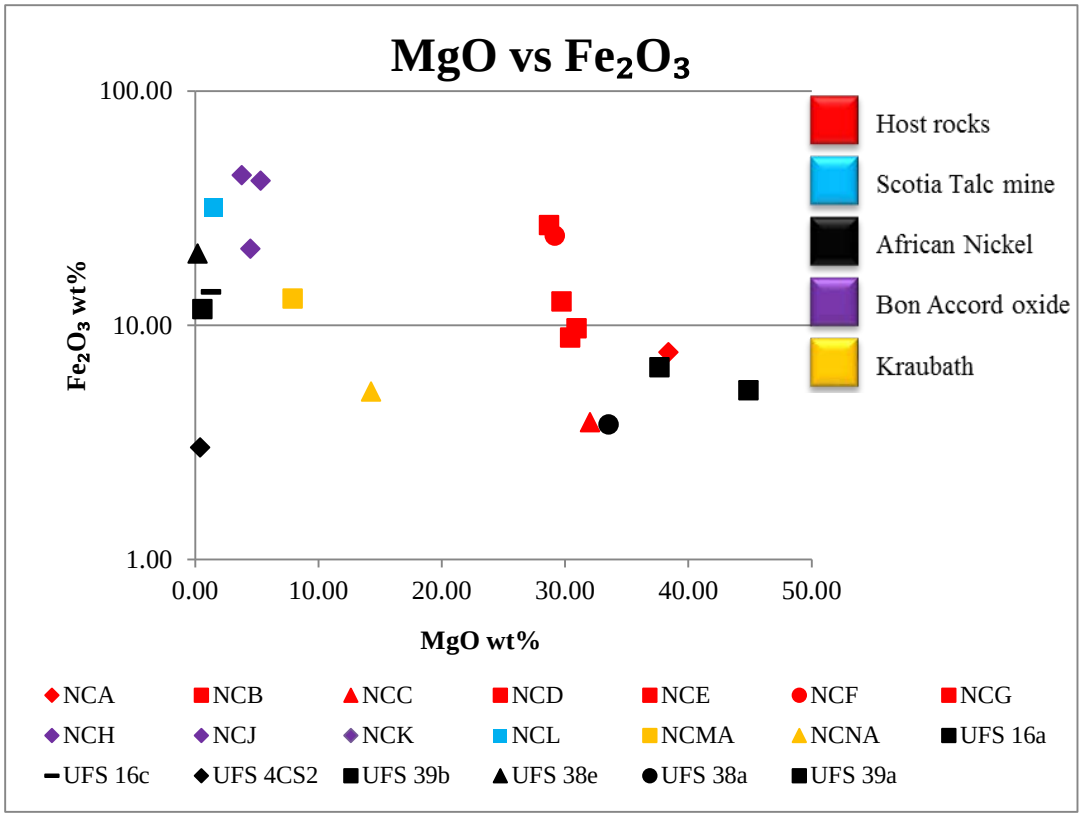

Figure 4.1. Harker diagram illustrating MgO vs Fe_2O_3 variations within the two rock suites.

Most of the studied rocks, with the exception of BA host and certain ANL samples (UFS 38e, UFS 39b, UFS 16c, UFS 4CS2), are all highly MgO deficient (Fig. 4.1). The BA oxide host rocks indicate an almost constant MgO concentration with increasing Fe_2O_3 content, while the MgO enrichment in the ANL samples (UFS 16a, UFS 38a and UFS 39a) range between 33–45 wt%. The Kraubath samples are relatively enriched in MgO (8-14 wt%) when compared to BA oxide samples. On average, the NiO mineralisation in BA oxide is at least >45 times compared to the NiO concentrations in the BA host rocks, while it is approximately >8 times more than that seen in the Scotia Talc mine sample, and approximately >13 times more when compared to the ANL samples and >188 times more in the Kraubath samples.

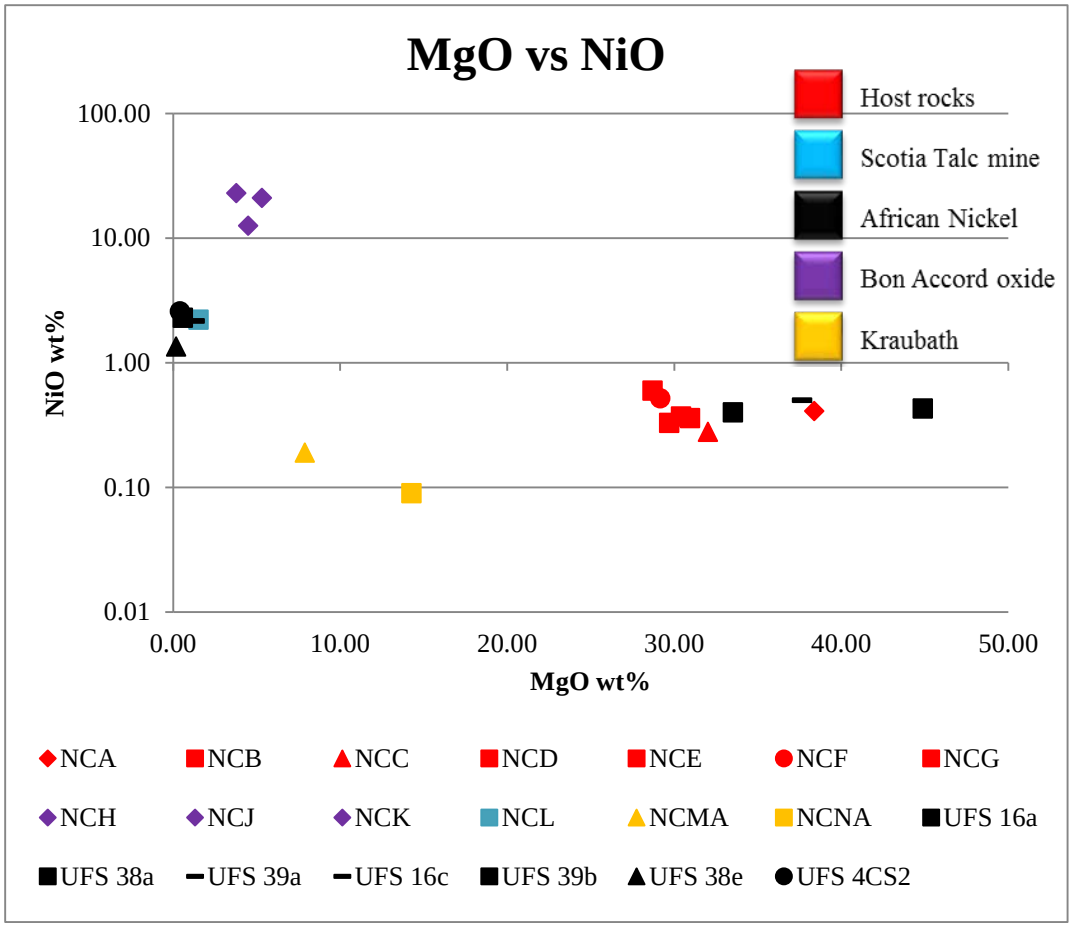

Figure 4.2. MgO vs NiO diagram indicating clustering of the two different rock types.

The MgO vs NiO plot show a contrasting relationship, especially between the ANL samples (representing nickel sulphide samples), the ANL samples show two relationships (Fig 4.2), group 1: an increase in NiO at very low MgO values and group 2: an increase in MgO at constant NiO values. The Kraubath samples show the lowest NiO concentration at any given MgO range, sample NCL plots in the same area as the group 1 samples of the ANL samples (containing ≈ 2 wt% NiO). Bon Accord host samples plot in the same area as the group 2 ANL samples (containing about ≈ 0.5 wt% NiO) and as expected, the BA oxide samples contain the highest NiO wt% content.

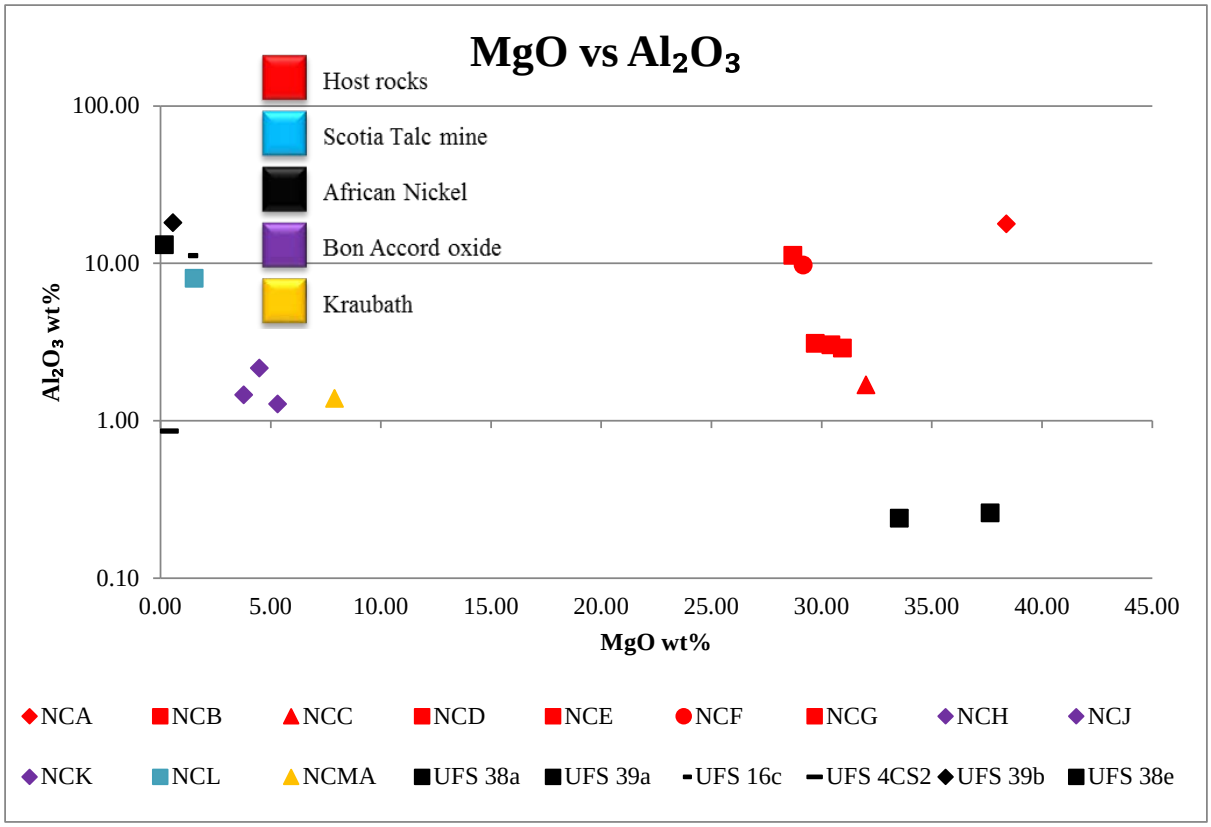

Figure 4.3. MgO vs Al_2O_3 variation diagram depicting differences in concentration levels.

Sample NC-NA did not plot in the MgO vs Al_2O_3 graph due its lack of Al, all the other samples generally illustrate a negative correlation trend (Fig. 4.3) with samples UFS 38a, UFS 39a and UFS 16a being the only exception; illustrating a consistent (flat) Al_2O_3 trend. Al_2O_3 is severely depleted in all samples except in samples NC-A, NC-B, NC-F, UFS 16c, UFS 38e and UFS 39b which are relatively enriched compared to the rest of the investigated samples. The ANL samples are again characterised by three groups, group 1: relatively enriched Al_2O_3 at very low MgO concentrations, sample NCL also plots with the group 1 ANL samples, group 2: severely depleted Al_2O_3 at higher MgO concentrations and group 3: only represented by one sample (UFS 4CS2), characterised by low Al_2O_3 and MgO contents (Fig 4.3). The BA oxide samples plot together with the one Kraubath sample (NCMA), these samples show high levels of Al_2O_3 depletion correlating to lower MgO concentrations.

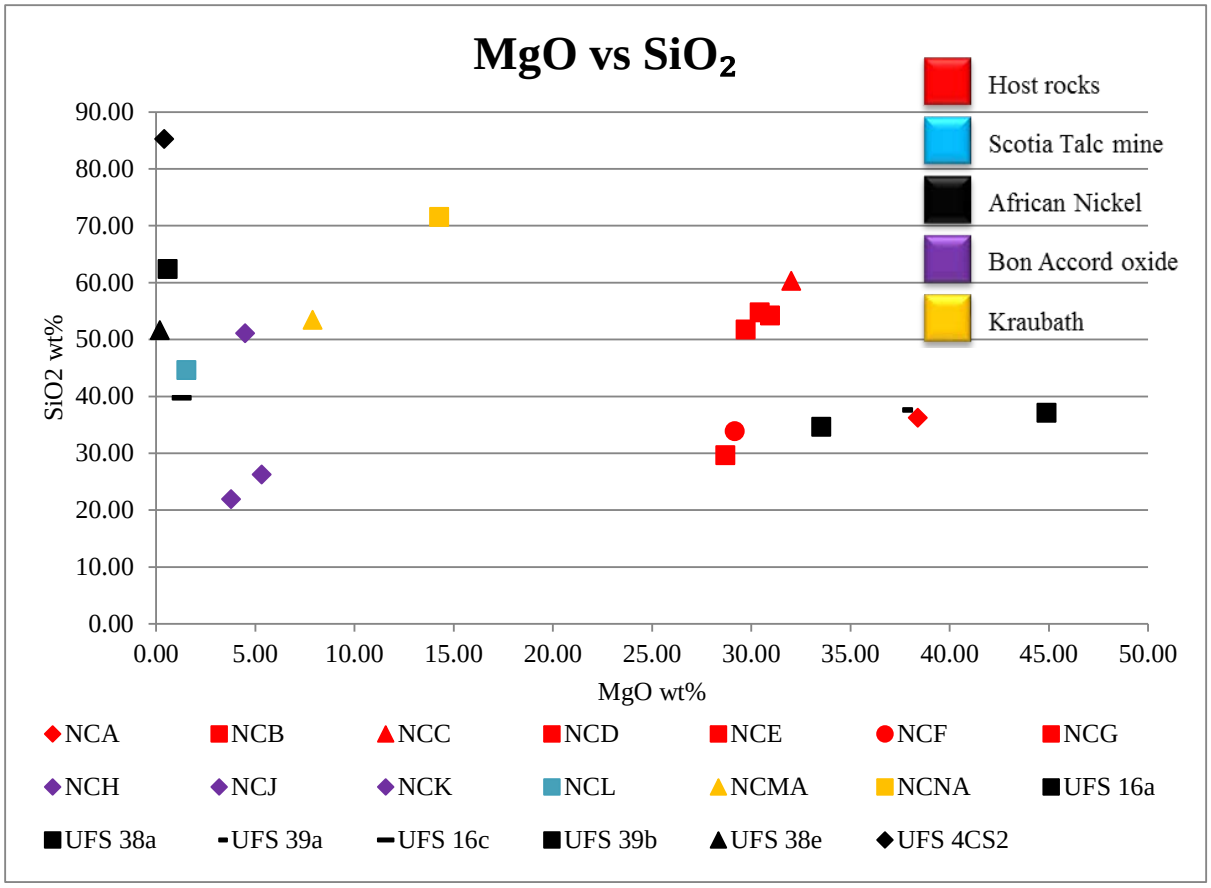

Figure 4.4. Diagram showing steady increase in SiO2 while MgO remains steadily unchanged.

The SiO_2 vs MgO trend displays an almost erratic distribution and BA host rocks are characterised by three groups. Group I has relatively moderate SiO_2 content (≈31 wt%) that correlates with moderate MgO content (≈27 wt%), group II has higher SiO_2 content (≈55 wt%) with slightly moderate MgO content (30 wt%) and group III (although only represented by one sample, NCA) has moderate MgO content (≈38 wt%) with moderate SiO_2 content (≈ 38 wt%). The BA oxide samples appear to be represented by two groups, group I has low SiO_2 content (≈25 wt%) with very low MgO content (≈5 wt%) and group II has very low Mg content (≈5 wt%) but higher SiO_2 content (≈50 wt%), sample NCL also plots in the same area as group II samples of the BA oxide samples (Fig 4.4). Bon Accord oxide and NCL samples are relatively depleted in Si, averaging ≈15% with depletion in MgO averaging 4%, Kraubath

samples are variably enriched in Si with an average of 29% and depleted in MgO with an average of 11%. The ANL samples are also characterised by two groups, group I has very low MgO content (≈0.5 wt%) with increasing SiO_2 content (a function typical of different rock types that are variably SiO_2 enriched) and group II has almost constant (flat) SiO_2 content with increasing MgO content.

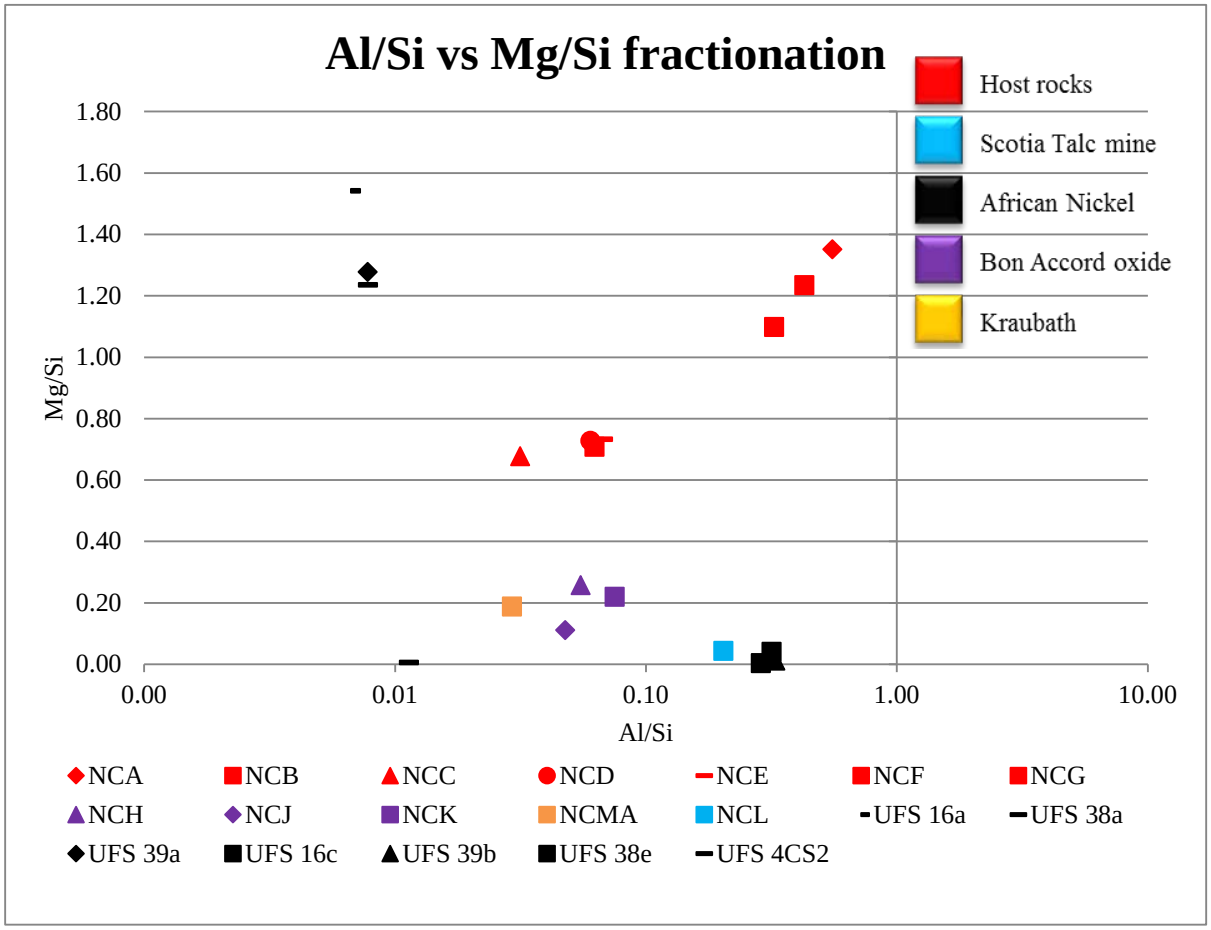

Figure 4.5. Ratio diagram illustrating the comparisons between Al, Mg and Si.

The BA oxide and its host samples indicate an apparent increase in Mg/Si with increasing Al/Si (though slightly less prevalent for BA oxide samples), although the concentration between the two rock suites (BA oxide and host) are different, their trend is typical for rocks accumulated during the early stages of the earth (cosmochemical fractionation trend). The

ANL samples with the exception of sample UFS 4CS2, occur in groups of two: group I (UFS 16a, 38a and 39a) relatively enriched in Al/Si and depleted in Mg/Si; while group II (UFS 16c, UFS 38e and UFS 39b) samples are depleted in Al/Si and enriched in Mg/Si and sample UFS 4CS2 shows extreme depletions in both ratios (Fig 4.5). Scotia Talc sample (NCL) occurs as an outlier enriched in Al/Si with low Mg/Si ratio.

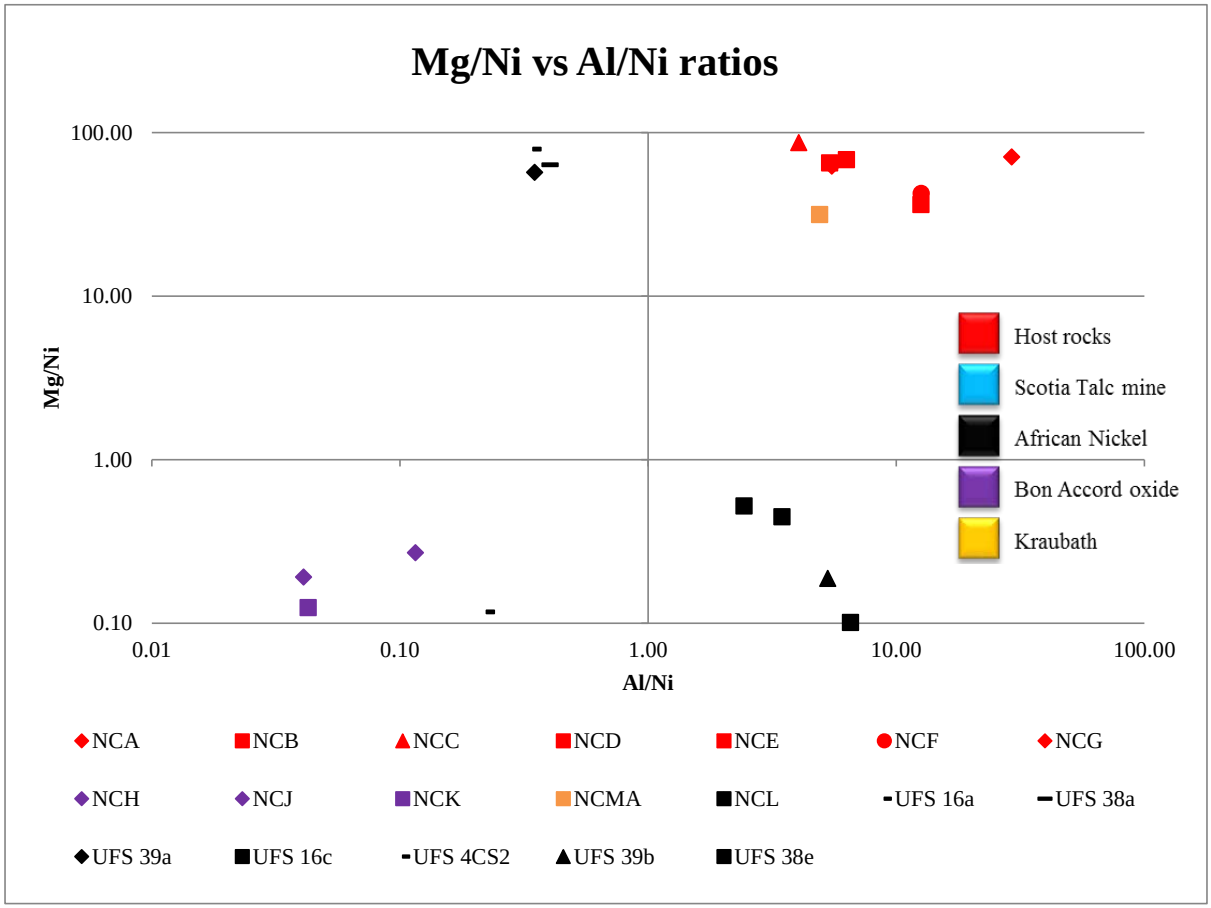

Figure 4 6. Illustration of the cosmochemical fractionation trend of Mg, Al and Ni. The elemental abundances are given in wt %.

Bon Accord host rocks together with sample NC-MA, are characterised by clustered trends (relatively enriched in Al/Ni) corresponding to elements occurring in almost equal proportions, (NC-C, NC-D, NC-E and NC-G, Fig. 4.6). Sample UFS 4CS2 together with BA oxide samples are highly depleted in both Mg/Ni and Al/Ni elemental ratios due to a source environment deficient in Al and Mg. The ANL samples show a very erratic behaviour due in

part to their variance in elemental compositions and occur as two groups, where group I has higher Mg/Ni ratios with lower Al/Ni ratios and group II has higher Al/Ni ratios with very low Mg/Ni ratios (Fig 4.6). Mg/Ni and Al/Ni ratios in the Scotia Talc mine sample (NCL) are almost constant (both Mg/Ni and Al/Ni ratios are very low).

Chapter 5 – Discussion

5.1. Introduction

The NiO mineralisation in BA oxide deposit has been a subject of controversy ever since its discovery; different mechanisms for its formation have been proposed (see Chapter 1), but due to the fact that only a few samples remain for investigations, it has been difficult to choose between the proposed models. A summary of current findings and research data are discussed below, together with suggestions of possible mechanisms that could be used to explain the unusual NiO mineralisation in the BA oxide deposit.

The mineralogical assemblages of BA host rocks (see the petrography data in Chapter 3 and Appendix B) have shown that the original host rocks surrounding the BA oxide body underwent metamorphism and/or metasomatism. Through the application of mineralogy and geochemistry, the author has concluded that the BA oxide host rocks form part of the Onverwacht Group (the Tjakastad Subgroup in particular). In particular, the chondrite deleted REE concentrations of these rocks suggest a connection.

Although the host rocks have been altered to metamorphic equivalents by the intrusion of nearby felsic volcanic rocks, the XRF data for the major elements (Table 4.1) indicate distinct differences in the elemental composition in all the rock types investigated. despite the alteration, the BA host rocks (NC-A to NC-G) still show evidence of initially originating from a relatively REE depleted zone (Table 4.4), which might indicate a depleted mantle derivation. The author accepts, however, that this interpretation is tenuous and controvertial.

5.2. Mineral paragenesis and relationships

A wide variety of mineral assemblages were noted and documented in the studied rock suites: it was established that BA oxide and host rock samples have similar mineralogical compositions (talc, chlorite, spinels, etc.) with the exception that the minerals in BA oxide samples are all rare Ni-rich end members. However, before detailing the relationships between the mineral assemblages it is vitally important to discuss the elemental compositions as noted in chapter 4, Appendix B and C.

The Cr-rich phase indicates preferential distribution of the chromium within the pseudomorphous magnetite and hematite/goethite series, and it (the chromium) is homogeneously distributed within what is now an accessory chromite phase (Appendix C, SEM - NCB, NCC, NCF and NCG). Minor substitution of Si by Ti resulting in a talc phase slightly enriched in Ti (Appendix C, SEM - NCE and NCG) is clearly illustrated; this behaviour is uncommon but has previously been noted by Knoche et al, (1998). Almost pure silicon grains were observed in NC-D (Appendix C, SEM), as entrapped or "locked in" as a secondary phase in the pseudomorphous magnetite and hematite assemblages, possibly during a period of super cooling, indicating very reduced conditions.

As previously mentioned the BA host rocks contain Ni-deficient mineral equivalents as those observed in the BA oxide samples as well as quartz. The ANL, Kraubath and Scotia talc mine samples contain the usual minerals; pyroxenes, olivine, quartz, magnetite, pyrite, tremolite, calcite, chlorite, talc, serpentine, muscovite, hornblende, magnetite and hematite albeit in varying degrees.

The rare Ni-rich minerals observed in the BA oxide samples as described by de Waal (1969, 1970a, 1970b, 1972 and 1978, and de Waal and Calk (1973)) are: willemseite, trevorite, nimite, népouite, liebenbergite, bunsenite, and very observed in most of the BA oxide

samples studied. More common minerals noted are: magnetite, ilmenite, leucoxene (minor), goethite, hematite, millerite, Sb-rich sperrylite, nickeline and two unknown phases. The occurrence of the Ni-rich end members of minerals like spinel (trevorite), talc (willemseite), olivine (liebenbergite) and serpentine (népouite) is highly unusual and only confined to the BA farm; this observation led Tredoux et al. (2010) to suggest that the BA oxide samples should be regarded as a new rock type, called jamestownite. A possible paragenetic sequence of the minerals studied in the BA oxide samples, suggested by Wildau (2012), is illustrated by Fig 5.1 below.

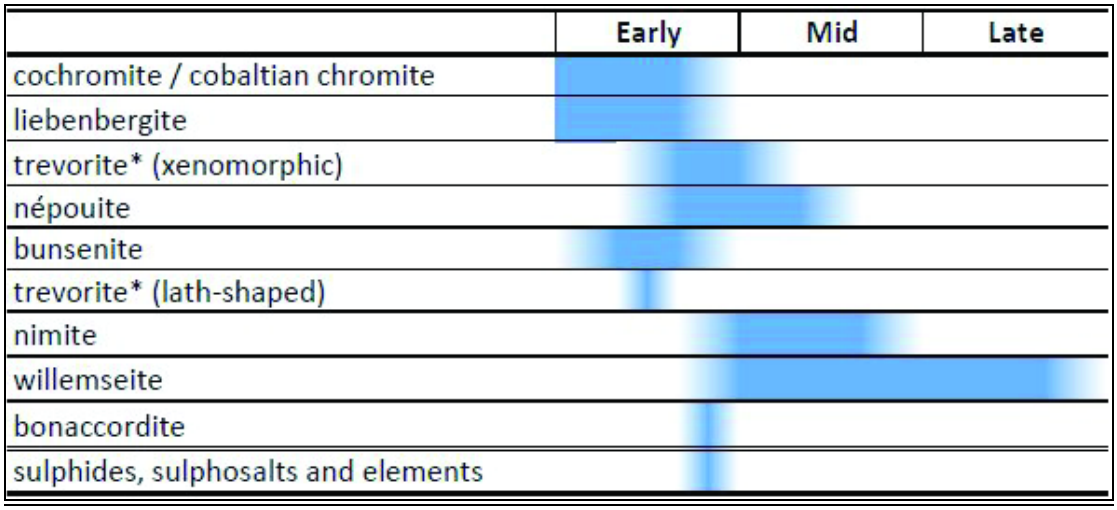

Figure 5.1. Paragenetic sequence of the observed minerals in the Bon Accord deposit. Fading colour marks the unknown start, respectively end of occurrence of a mineral. Early, mid and late indicate possible alteration events which led to the formation of alteration products (adapted after Wildau, 2012).

The BA oxide samples are characterised by the willemseite-népouite-nimite assemblages, where the willemseite and népouite are often found inter-grown and nimite occurs as an accessory phase. Embedded within the willemseite-népouite-nimite assemblages are millerite and hypidiomorphic and lath shaped grains of trevorite and nickeloan magnetite (Wildau, 2012).

A Pt-rich phase (sperrylite, Fig 3.15) was noted and found in association with the willemseite-népouite-nimite assemblages (Fig. 3.15). The occurrence of both the Fe and Mg chlorite end members is visible (Appendix C, SEM - NCA), with the Fe end member actually representing the chamosite phase, which is surrounded by the clinochlore. The Fe enrichment in the chlorite represents remnants of Fe (magnetite) before it was replaced by magnesium during recrystallisation accompanying the greenschist facies metamorphism.

While the liebenbergite occurs in very minute amounts, as relics within weathering products. According to Wildau (2012) there are two generations of trevorite: lath-shaped trevorite is associated with the liebenbergite remnants, and seem to have formed in place, since all relic liebenbergite phases, which occur together in one nodule go extinct at the same time. It is likely that each nodule used to be one whole liebenbergite grain which got altered. Therefore owing to the complex nature of the BA oxide deposit and its almost interchangeable relationship between the mineral assemblages, Wildau (2012) noted that, the lath-shaped trevorite formed as a by-product during alteration while the népouite altered to willemseite.

The mineral népouite had formed through the alteration of the mineral liebenbergite. The intergrowth between nimite and willemseite (Fig. 3.3b-c) was facilitated by their contemporaneous formation. The back scattered electron image (Fig 5.2), illustrates the inhomogeneous distribution of the Mg and Fe in chlorite and magnetite respectively.

Sample NC-J is largely dominated by a trevorite-nimite-willemseite assemblage; however the willemseite occurs as a minor phase infilling the trevorite interstices. Specific points in NC-J show a decrease in Fe and an increase in Ni while other points in NC-J indicate the inverse with ta Fe:Ni ratio approximating 3:1. This behaviour is due to the substitutional relationship between Ni and Fe in a solid solution series, NC-K is largely dominated by the mineral willemseite together with trevorite. Minor NiAs phases occur as minute grains embedded

within the spinel group minerals (mainly trevorite), therefore further highlighting the close relation of the trevorite and the As-phases in the BA oxide samples. The Ni-rich pyrite (bravoite end member species) observed in sample NC-L is an indication of a post Ni -rich fluid that resulted in pyrite mineralisation.

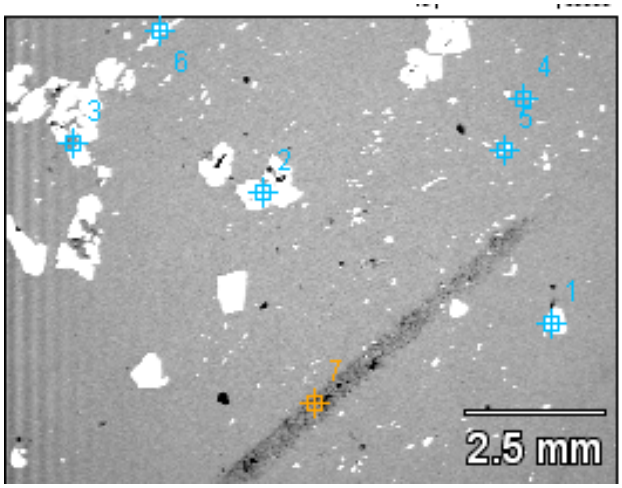

Figure 5.2. Back scattered electron image representing distribution of Mg and Fe mineral phases (numbered points represent spots analysed on the sample). Light spots (numbers 1 and 2) usually represent magnetite and dark spots (3-7) represent chlorite.

The chlorite also represents a late stage alteration process probably associated with the envisaged subsequent processes during the emplacement of BA oxide deposit.

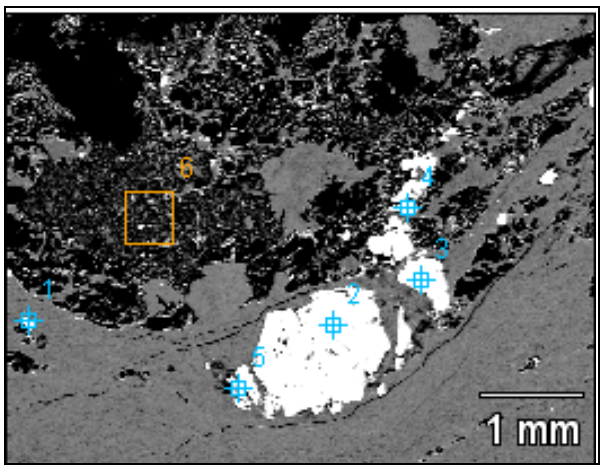

Figure 5.3. Replacement texture characterising the interaction of the magnetite with secondary silicate fluids.

Samples NC-L, NC-MA and NC-NA are largely dominated by the olivine, pyroxene, amphiboles, spinel mineral group and sulphide minerals together with nickel-rich pyrite, however in varying proportions. The olivine end member observed represents the Mg-rich forsterite. Bravoite (Ni-rich pyrite) occurs embedded in the pyroxene grains, indicative of a secondary enrichment fluid phase rich in nickel. The enrichment of the amphiboles and some pyroxenes contributed to the high Mg content observed, whereas the high Cr concentration is attributed to the amphibole, pyroxene and chromite mineral phases. Important to note is that in some cases the Cr substituted for the Fe and Mg and was partitioned into the pyroxene phases during the earliest stages of crystal fractionation.

In some instances sample NC-NA shows Al depletion, perhaps due to a melt originating from a partially molten sedimentary source. The chromite phase in some cases appears confined to the amphibole alteration fracture planes possibly illustrating pathways as the mechanism of enrichment. The unidentified antimony phases occur in close association with the trevorite and no further investigations were conducted on these phases since they did not form part of the scope of this research. Trevorite occurs as large irregular grains, while the Sb-phase occurs embedded within the trevorite mineral grains. The results in the unknown phase (Appendix C, EMPA -arranged data, NCH) indicate a high concentration of a NiAs mineral phase.

5.2.1. Mineral formation processes

Chlorite

The nickel enrichment in the chlorite of the BA host rocks formed as a result of dehydration and interaction with nickel rich fluids. The initial nickel enrichment of the Ni-carrying fluids occurred in the lower mantle but the final nickel enrichment occurred close to and/or on the

surface associated with the transport during ascent. The chlorite is a function of a hydrothermal activity and/or a deuteric alteration process of biotite, amphibole, pyroxene or other mafic minerals, Nesse (2004).

The occurrence of nimite and willemseite suggest a very close genetic relationship, an indication of contemporaneous formation.

Serpentine

The serpentine formed from the alteration of olivine rich ultramafic rocks (peridotites) through hydration processes. This is envisaged to also represent the early phase of the alteration of primary orthopyroxenes which also resulted in talc formation. According to Fruh-Green et al (2004), serpentinisation of peridotites in the ocean (Fig 5.4) is dominated by progressive alteration of olivine to lizardite and/or chrysotile bearing assemblages that form characteristic mesh textured pseudomorphs. Serpentine usually occurs as acicular fibers mainly embedded within the willemseite, this relationship is vital as it illustrates one of the end products of the primary liebenbergite. Primary liebenbergite was altered to népouite, and népouite was altered to form willemseite which occurs intergrown with nimite in multiple processes of formation.

Talc

The talc is the most abundant mineral in most of the samples. The BA host rocks are enriched in the magnesium-rich, talc end member but depleted in nickel. The close association of talc and chlorite is an indication that they formed together as a result of heat and chemically active fluids that altered the highly Mg rich rocks (such as peridotites, Fig 5.4) during a hydrothermal phase and further substantiated by evidence of formation from weathering of ferromagnesian minerals (olivine, amphibole and pyroxene) rich rocks. The alteration of the

ferromagnesian mineral rich magmatic rocks first occurred through hydration by influx of water which resulted in the formation of serpentine (serpentinisation). This, was then followed by the alteration of the serpentine into negligible magnesite through the addition of CO_2.

The willemseite found confined to the BA oxide samples underwent multiple stages of formation: including alteration of magmatic magnesium rich rocks at elevated temperatures, which resulted in the formation of minor bunsenite which was later replace by xenomorphic trevorite.

Liebenbergite

Only relic liebenbergite grains are present in the matrix of nepouite, since most of the liebenbergite has been replaced by népouite, nimite and likely willemseite. In some cases the népouite is in the interstices between the trevorite grains. The relic liebenbergite within the népouite is an indication that népouite is a secondary phase formed after the liebenbergite. The large amounts of willemseite observed in these once magnesium-rich rocks make it possible to also assume that liebenbergite was at some stage directly altered to form the willemseite in the BA oxide samples.

Trevorite

Metasomatism through the interaction of serpentinised peridotite with nickel rich fluids resulted in the formation of trevorite and alteration of liebenbergite formed xenomorphic trevorite grains. Initially these serpentinised peridotites formed ferroan magnetite, however with time some of the iron was replaced through interaction with nickel rich fluids. The trevorite appears to have also formed through the alteration of bunsenite to form xenomorphic trevorite.

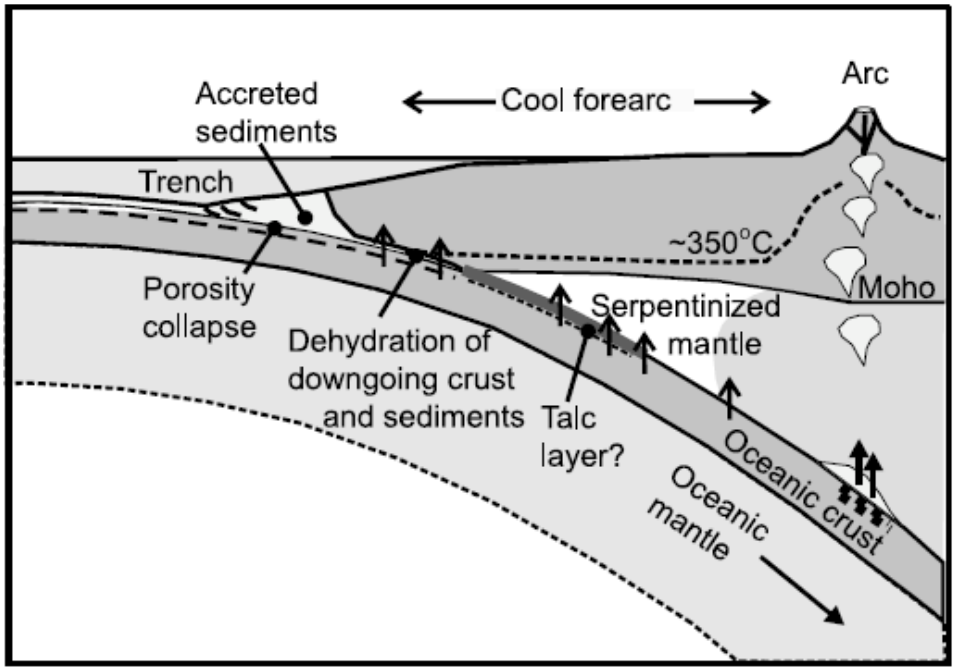

Figure 5.4. Schematic cross section illustrating fluid expulsion from subducting oceanic crust and sediments and serpentinisation of the overlying forarc mantle. (Adapted after Hyndman et al, 2003).

The close association of the ferroan magnetite and trevorite is further support of a secondary genetic relationship between the two mineral species. Trevorite is the second dominant phase after willemseite in the BA oxide samples and is largely characterised by a cubic crystal symmetry.

Hematite

Hematite formed from the alteration of mafic and spinel minerals. In most of the sections it occurs in veins running across the entire thin section, cross cutting the dominant phases.

Magnetite

The magnetite formed through serpentinisation of peridotites and dunites in a relatively low temperature and pressure environment (close to the surface). However, the magnetite confined to the BA host samples formed from the precipitation grains (equation 1) from magma together with some ilmenite grains.

Ilmenite

The bulk of ilmenite formed as discrete grains with some magnetite in solid solution and through weathering processes of Fe-Ti rich phases. Accessory leucoxene formed from the alteration of ilmenite.

Sulphides

The nature and morphology of the minute sulphide grains in the BA oxide deposit represent a late stage fluid activity (ocean crust hydration) which happened during an obduction event possibly associated with subduction zone related processes (Fig 5.4).

Goethite

Goethite occurs in most cases genetically associated with hematite, thus providing further support for formation of goethite through weathering and/or hydrothermal alteration of other Fe-bearing minerals particularly the oxides and sulphides.

5.3. Rare earth elements (REE) geochemistry

The REE data for the BA oxide body and its immediate host rocks are plotted in Figs. 5.5 and 5.6. [Scotia Talc mine and Kraubath samples were not plotted on the REE abundance graphs since they were not analysed for REE.] The chondrite normalised REE plot (Fig 5.5) show distinct negative Eu patterns as result of Eu removal by a plagioclase phase as a residual phase. The encounter between crustal material and mafic-ultramafic magma resulted in slight LREE enrichment and in turn mafic material was lost to fractional crystallisation, a behaviour that has been described by Balaram et al (2013).

The host and BA oxide samples depict an almost linear trend in the distribution of the HREE patterns, whereas the REE in the ANL samples show very wide and slightly erratic behaviour as a result of enrichment at different times. However, one common factor is the general REE depletion with the exception of sample UFS 16c which is relatively enriched in LREE and UFS 39b which is slightly enriched in both LREE and HREE. The REE distribution patterns show evidence that the bulk of the BA host samples (NCA, NCD, NCE, NCF and NCG) and BA oxide sample (NCJ) have some commonalities. This relationship is deduced from the similar REE trends when plotted against chondrite and primitive mantle, albeit the concentrations are not necessarily the same. Quite obvious in all the rock suites is the apparent depletion in REE when compared to other crustal average abundances (Table 5.1).

The depletion in REE seen in the BA oxide and host rocks suggests a REE depleted source region, widely accepted as the mantle. The REE concentrations in the ANL samples show an erratic distribution, without any clearly distinguished distribution trend, however looking at the REE crustal abundances it is clear that the BA oxide and ANL specimens indicate similar concentrations (Table 5.1). Therefore the similar REE concentrations provide the only link and/or association between these rock suites. In contrast, when plotted on the spiderplot (Fig 5.5 and 5.6) only the HREE concentrations between the BA nickel oxide and ANL rock samples are similar in the chondrite normalised schematic (Fig. 5.5).

The REE patterns of the ANL samples observed in the primitive mantle normalised graph (Fig. 5.6) do not necessarily show any specific pattern but are very erratic in their distribution. The BA host and BA oxide samples are all relatively enriched in LREE and extremely depleted in Eu^{2+} as a result of plagioclase fractionation, which was later altered to form chlorite. The REEs abundance patterns in samples NCA, NCD, NCE, NCF, NCG and NCJ are indicative of relative enrichment in Ce and Nd followed by very flat patterns for the

other REE. Whereas in the ANL samples, only samples UFS 16b and UFS 39b show REE enrichment while the remaining ANL samples are depleted and show slight enrichment in Ce and variable distribution in Nd when compared to the other REE. The Ce patterns are consistent with its wide distribution in the earth's crust while the characteristic variability seen in the Nd is indicative of the typical minimum interaction of crustal processes with the melt.

Table 5.1 REEs crustal average abundances compared with Bon Accord oxide and host rock REE abundances (concentrations in ppm).

	Crust REE abundances from published research				Current research			Lodders 2003	Taylor and Mclennan 2001	Hofman 1988
	Taylor 1964	**Wedephol 1995**	**Lide 1997**	**McGill 1997**	**BA Host**	**BA Ni oxide**	**ANL**	**C1 chondrite**	**Archean bulk crust**	**PM**
La	30	30	39	5 to 18	1.81	1.49	1.77	0.232	15	0.61
Ce	60	60	66.5	20 to 46	4.07	3.48	4.07	0.621	31	1.6
Pr	8.2	6.7	9.2	3.5 to 5.5	0.55	0.43	0.54	0.0923	3.7	0.24
Nd	28	27	41.5	12 to 24	2.28	1.86	2.38	0.457	16	1.19
Sm	6	5.3	7.05	4.5 to 7	0.45	0.48	0.66	0.145	3.4	0.39
Eu	1.2	1.3	2	0.14 to 1.1	0.07	0.03	0.24	0.055	1.1	0.15
Gd	5.4	4	6.2	4.5 to 6.4	0.37	0.51	0.62	0.0198	3.2	0.51
Tb	0.9	0.65	1.2	0.7 to 1	0.05	0.09	0.1	0.036	0.59	0.09
Dy	3	3.8	5.2	4.5 to 7.5	0.33	0.63	0.65	0.238	3.6	0.64
Ho	1.2	0.8	1.3	0.7 to 1.2	0.07	0.14	0.13	0.056	0.77	0.14
Er	2.8	2.1	3.5	2.5 to 6.5	0.21	0.46	0.39	0.162	2.2	0.42
Tm	0.48	0.3	0.52	0.2 to 1	0.04	0.07	0.06	0.024	0.32	0.06
Yb	3	2	3.2	2.7 to 8	0.23	0.52	0.4	0.163	2.2	0.41
Lu	0.5	0.35	0.8	0.8 to 1.7	0.04	0.08	0.07	0.024	0.33	0.06

ANL = African Nickel Limited sulphide samples, PM = primitive mantle

From the C1 chondrite normalised spideplot (Fig 5.5) it is evident that samples NCB, NCH, and NCK all display an almost linear trend for both the LREE and HREE, illustrating distinct similarities between REE concentrations in these samples and C1 chondrite. Therefore, processes responsible for REE enrichment in C1 chondrites were possibly operating and/or similar processes were present during REE enrichment of samples NCB, NCH, NC-J and NCK. The remaining samples indicate a non-linear trend and relative enrichment in the

LREE as compared to the C1 chondrite, thus implying interaction with a fertile source (crust). All the studied samples with the exception of the ANL samples are highly depleted in Eu^{2+}. LREE enrichment is evident in most samples except, samples UFS 4CS2, UFS 38a, UFS 39a, and UFS 16a which are generally depleted in the whole range of REE (Fig 5.5). LREE enrichment in the BA oxide samples relative to the C1 chondrite occurred through crustal assimilation during the ascent of the proposed mode of transportation (thermal plume). While enrichment in LREE in BA host rock samples and samples UFS 16c and UFS 39b is characteristic of interaction with a fertile source mainly facilitated by the large heat influx that accompanied the envisaged plume, resulting in assimilation of fertile material and processes that followed after the emplacement event.

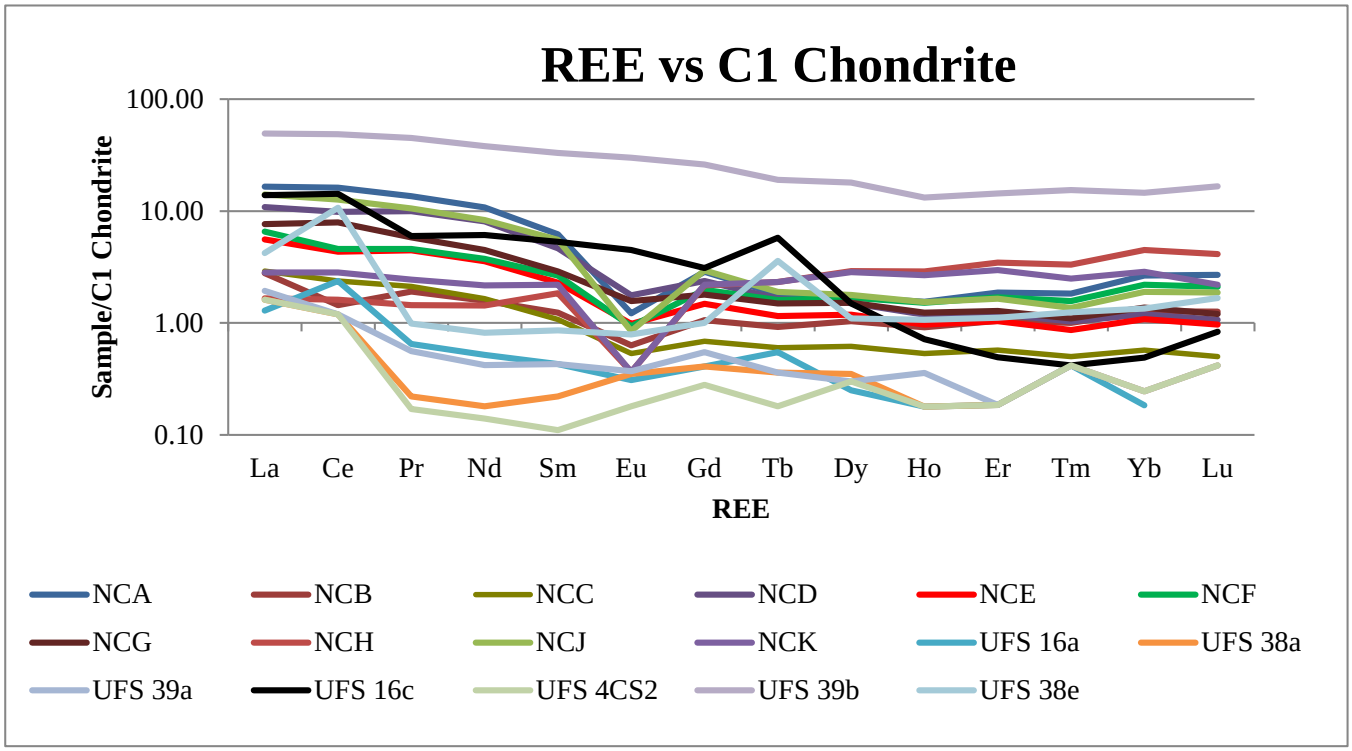

Figure 5.5. REE spiderplot against C1 chondrite illustrating the differences in elemental concentrations.

The resulting metamorphism alteration of the parent peridotite to form the metamorphic equivalent host rocks (serpentinites) as observed in the BA farm. Samples NCB, NCC, NCH

and NCK, all show an almost linear trend approximating 1 (one) with the exception only noted in Eu^{2+} depletion (Fig. 5.5), thus implying similar enrichment source and/or processes for these samples. Since refractory lithophile elements, such Ca, Al, Ti, REE, U and Th, occur in roughly constant proportions in different classes of chondrites and also in the solar photosphere (Lyubetskaya and Korenaga, 2007), it is reasonable to assume that the ratios of these elements in the bulk silicate earth should be (at least approximately) equal to those in chondritic meteorites. The Eu depletion trend in the BA oxide and host rock samples, can be attributed to occurrence over a range of oxygen fugacity conditions on earth as a result of its two oxidation states (+2 and +3). This phenomenon enabled Eu^{+2} to be easily incorporated into divalent cation sites, with the end result being, the easy substitution of Eu^{+2} for Ca similar to magmas that have experienced the crystallisation of plagioclase.

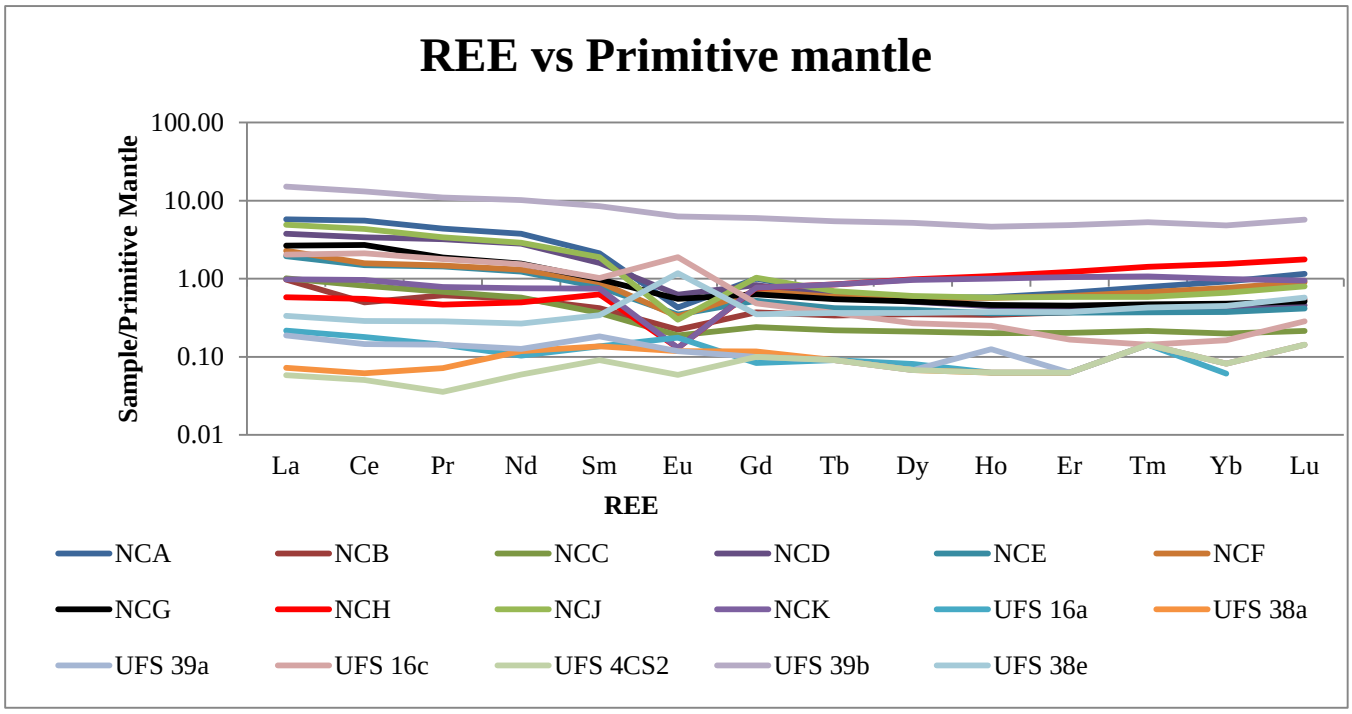

Figure 5.6. REE spiderplot against primitive mantle illustrating the differences in elemental concentrations.

The REE patterns (Fig. 5.6) are typical of patterns associated with partial melting, with variation from enriched LREEs patterns to flat HREEs and variable Eu anomalies. The variation in REE was partly caused by subduction related processes and/or processes associated with obduction of the crust, a phenomenon that has been proposed for the AB oxide deposit (an ophiolite). The HREE in the primitive mantle normalised graph (Fig. 5.6) indicate almost identical patterns as those in the primitive mantle data documented by Lyubetskaya and Korenaga (2007**),** it is therefore reasonable to assume that the LREE enrichment is indicative of a source composition that is not only the crust but a source region similar to the primitive mantle. The HREE linear trend (Fig 5.6) is as a result of compatibility differences between HREE and LREE associated with the decreased ionic radius of the HREE, a trend similar to the Al-undepleted komatiites. V, Co and Cu (with the exception of Bon Accord host samples) occur in abundance and also quite clear is the relative enrichment of ZnThe Eu was preferentially incorporated into plagioclase over other minerals thus resulting in a negative Eu anomaly, such that upon the extraction of the plagioclase into a solid phase the resultant magma would have been relatively depleted in Eu as compared to other REE.

5.4. PGE geochemistry of the African Nickel Limited samples

The work done by (Campbell and Barnes, 1984) illustrated that the concentrations of PGE in magmatic sulphide ores display a remarkable range of values and may vary by orders of magnitude from one deposit to the next. This is especially true when looking at the ANL samples and BA oxide deposit (Bon Accord oxide deposit PGE data is provided in Appendix C from the work conducted by Tredoux et al, (1989). The ANL samples are deficient in PGEs in contrast to the BA oxide samples, only sample UFS 16c shows minor PGE mineralisation, followed by UFS 39a and UFS 39b while the other samples are much more depleted in

comparison (Fig. 5.8). The trend suggests formation/origin in an environment that is sulphur enriched unlike the sulphur deficient environment of the BA oxide deposit. The presence of high MgO and higher PGE concentrations suggest that the magma responsible for the initial rock formation was derived from a PGE enriched fertile source. The high MgO, PGEs and variations in geochemical trends (Figs. 4.1 and 5.8) are indicative of interaction with a contamination source (Balaram et al, 2013) most likely upper mantle.

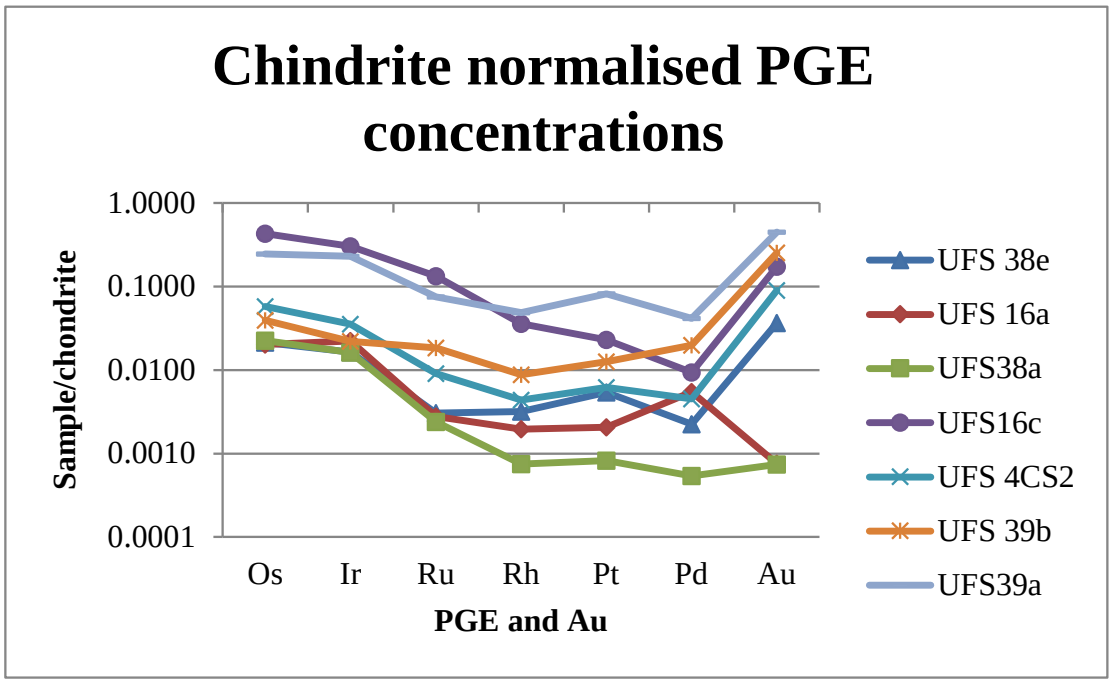

Figure 5.7. Chondrite normalised spiderplot of PGEs in the ANL samples. ***Normalised using PGE data from Lodders, 2003.***

Balaram et al, (2013) noted that enrichment of large ion lithophile element (LILEs) associated with LREE enrichment and negative Eu anomaly due to contamination and/or metasomatism will normally result in higher Cu and Pd concentrations due to the accommodation of IPGEs and Rh by mono-sulphide solid solutions (MSS), a conclusion that is in contrast to the high IPGE (Ir and Ru) mineralisation reported by Tredoux et al, (1989) in the nickel oxide deposit

The nickel oxide deposit is indicative of contrasting Cu behaviour when compared to the findings of Balaram et al, (2013) as a result of the inherent nature of Cu's ability to be readily mobile as a result of alteration and/or metamorphism especially in the vicinity of the nickel oxide deposit. The high PGE mineralisation in nickel oxide does not necessarily indicate accommodation by MSS, further illustrating the differences in PGE mineralisation between the ANL sulphide and BA oxide deposits.

The PGEs concentrations in BA oxide are high (Appendix C, PGEs) with characteristic LREE distributions caused by contamination and/or metasomatism processes but show no evidence of major interaction with sulphide (largely responsible for Cu mineralisation) except for the minor sulphide grains mainly embedded within the spinel phases. Therefore PGE mineralisation in the nickel oxide samples does not appear to have occurred in association with sulphide but rather as unique and probably confined to the farm of Bon Accord. The low PGE concentrations in the ANL samples are further quantified by the ratios plotted (Fig 5.9), the relatively flat PGE pattern with the exception of Pd (negative anomaly) and low Pd/Ir ratios (Appendix C) are similar to those observed in komatiites (Economou-Eliopoulos and Paraskevopoulos, 1989).

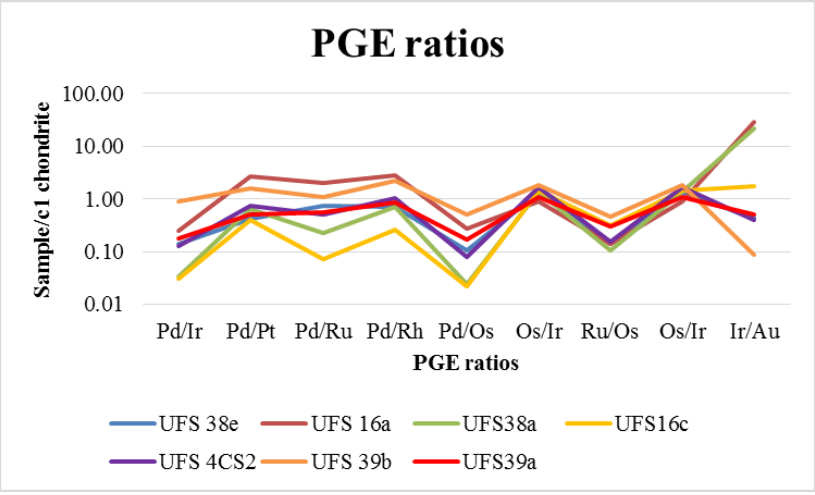

Figure 5.8. Platinum group element ratios of the ANL samples.

PGEs partition broadly evenly into segregating sulphides (Maier, 2003), the partitioning of the PGEs can be explained using partition coefficients however using partition coefficients causes problems, largely associated with the quantification of the distribution coefficient as well as the assumptions involved. However, Campbell and Barnes (1984) have shown that the problems of PGE partition-coefficients can be solved by using elemental ratios in sulphide samples. Thus through the investigations of Ni/Cu and Ni/Pd ratios and Pd, Pt and Ir (Fig. 5.10) it was possible to illustrate a fairly constant negative correlation trends between these elemental relationships which are mainly associated with normal cooling processes.

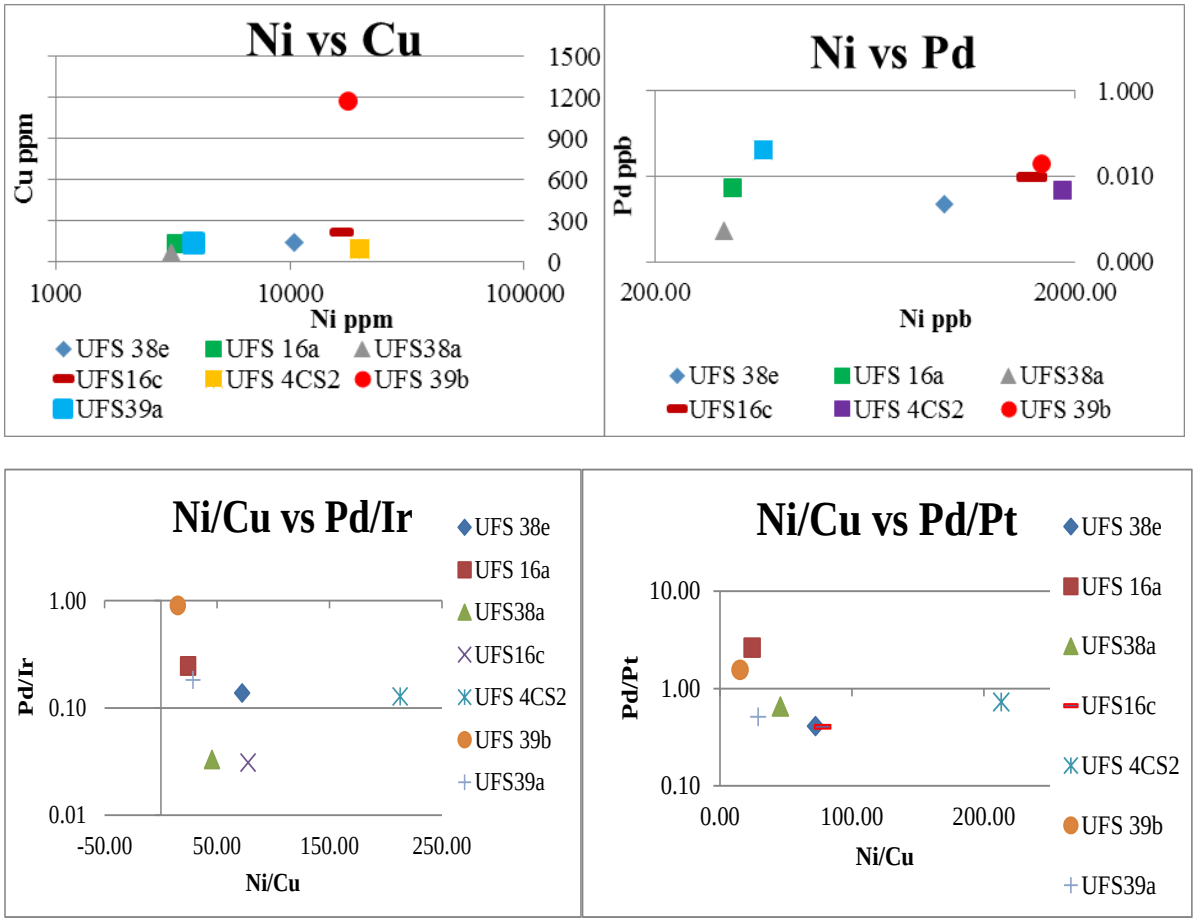

Figure 5.9. Chondrite normalised bivariate plots of (a). Ni vs Cu, (b). Ni vs Pd, (c). Ni vs Pt and (d). Ni/Cu vs Pd/Pt in the ANL samples.

According to Balaram et al (2013), high Ni/Cu, low Pd/Ir and Pd/Pt ratios and high concentrations of IPGEs are indicative of ultramafic rocks formed during a sulphur-unsaturated event. However, the relatively low Ni/Cu (<100 ppm on average) and Pd/Ir and relative enrichment in Pd/Pt (≈1 ppb) in the ANL samples (Fig. 5.10c and d), implies formation in an environment that contained some sulphur and/or sulphur phases that could have been replaced by late stage S-deficient processes such as low-temperature hydrothermal oxidation of the primary magmatic sulphide phases. Another possible explanation proposed by Maier (2003) is that sulphides could have remained in the source and retained the PGEs, and that the PGEs were fractionated during partial melting of the mantle, with the IPGE, Rh and Pt being hosted by more refractory mantle phases than Pd.

The BA oxide samples contain more PGE (Tredoux et al, 1989), when compared to the ANL samples, the only differences are noted in the ratios where the Pd/Pt ratio in the ANL samples is larger than the one in the BA oxide samples (Appendix C, PGEs). This occurrence is due to the propensity of IPGE and Rh to be largely accommodated by the MSS (Balaram et al, 2013) and Pd is hosted by interstitial Cu-rich sulphides (Maier, 2003). The conclusions made by Balaram et al (2013) and Maier et al (2003) are mainly true for the ANL samples but in contrast to the geochemistry of BA oxide samples. The BA nickel oxide deposit PGEs are concentrated in sulphide deficient rocks and have relative Cu enrichment compared to the ANL samples. Thus further supporting the unconventional PGE enrichment models and according to Zaccarini et al (2014), all the PGM inclusions (Pd-Sb, Pd-Cu-Sb, Pd-Sb-As, Ru-S, and Pt-As-S) and other Ni-Fe-Sb-As compounds, are present in the system when trevorite crystalises, thus more likely precipitated in equilibrium with the hydrothermal conditions that generated the trevorite-nepouite secondary assemblage. If the PGEs and alloys of BA oxide were indeed inside the nepouite matrix before liberation, then it is possible that the entire BA oxide mineralogy could have a common secondary origin associated with hydrothermal

reworking of the nickel oxide body, Zaccarini et al (2014). This model requires that Ni-PGE-Au form original components of the primary mineral assemblage of the nickel oxide precursor, with metasomatising fluids possibly contributing As, Sb, Bi, Te, and O, during near-surface evolution of the ore body, Zaccarini et al, (2014).

5.5. BA enrichment and plume activity model

The controversy associated with the origin of BA oxide deposit, has been a source of major debate and a lot of mechanisms have been proposed. In an attempt to further substantiate understanding of the BA nickel oxide deposit, this research will discuss the possible models that can be applied to support the enrichment of the studied samples together with data from komatiites, in order to delineate any similarities and/or differences.

The Fe enrichment in BA oxide can only be explained by a source region representing a Fe-Ni rich environment, while MgO depletion supports a source origin deficient in Mg (in contrast to Mg rich upper mantle) but enriched in Fe-Ni. The elemental compositions and their correlation trends (Fig. 4.1) tend to support a model that is line with limited chemical exchange between deep earth and mantle during core extraction in the early stages of differentiation. From, the high Fe concentration in BA nickel oxide deposit it can be inferred that, origin was from a region with an average Fe concentration enriched in an order of magnitude of atleast 1.2 times more compared to the Fe composition of the earth (≈31.9%, as reported by McDonough, 2001). The only region with Fe concentrations high enough to account for the Fe levels observed in BA nickel oxide deposit, is in the Fe-Ni core (McDonough, 2001). The marked distinction in the nickel geochemistry between BA oxide and the other rock suites is similarly indicative of multiple different mechanisms of formation at different times at their respective localities. The extent of NiO mineralisation in the BA

nickel oxide deposit has never been documented anywhere on earth except, in the Fe-Ni reservoir through simulation models (due to inability to access this part of the earth). Therefore in an effort to explain the Ni mineralisation, it is useful to consider the moderate volatility of Ni, which would act as a facilitator in ensuring easy incorporation of Ni into the fluid(s) originating from deep in the earth (possibly the D" layer) ascending towards the surface of the earth. The most likely and plausible mechanism with sufficient energy to carry such a deposit from the deep earth towards the surface could have been in the form of a thermal plume or associated with plume related processes. The clear distinction in concentration between Al and Mg (Fig 4.3), is typical behaviour for period 3 elements of the periodic table, where Mg is incorporated first during melting due to its relatively lower melting temperature when compared to the Al and subsequently crystallise Mg rich minerals (host rocks and UFS, 16a, UFS 38a and UFS 39a). The decrease in both Al_2O_3 and MgO appear to be controlled by an increasing SiO_2 content and therefore degree of differentiation, which in turn is an indication of the beginning of processes associated with talc formation. Talc is present as a major component in most of BA nickel oxide samples and its host rocks. While depletion in MgO indicates limited interaction if any, with processes that were operating within the mantle during the formation processes responsible for the other mineral phases. The erratic wide variation trends in SiO_2 (Fig. 4.4) are associated with the degree of melt extraction while the MgO trend of BA host rocks correlates with MgO values of primitive compositions ≈39% (Lyubetskaya and Korenaga, 2007). This relationship illustrates a relatively positive correlation, while the Si average (Appendix C) approximates that of the silicate earth ≈21% (McDonough, 2001).

The volatilisation and removal of Si from the mantle, Ringwood (1958) and Ringwood and Kesson (1977) resulted in relative depletion in Si in the BA oxide deposit (Appendix C). High Mg/Si ratios in the upper mantle are used to explain the low Mg/Si ratios in the lower

mantle Anderson (1977), as Mg is removed in the lower mantle and concentrated in the upper mantle therefore leaving behind a Mg depleted residual phase. Progressive increase in Al/Si ratio with an increasing Mg/Si ratio in the BA host rocks (positive correlation), is consistent with the tendency of Al and Mg to partition in the solid phase during melt extraction and crystallisation (Fig. 4.5).

The incompatibility nature of Si in the mantle, was a contributing factor to Si remaining in the liquid phase during melt extraction and crystallisation; however crustal assimilation processes played an important role in concentrating SiO_2 in the host rocks. The high depletion in both Mg/Ni and Al/Ni elemental ratios for the BA oxide deposit and sample UFS 4CS2 are due to a source environment deficient in Al and Mg. The erratic behaviour displayed by the ANL samples is due in part to their variance in elemental compositions and Mg/Ni and Al/Ni ratios in the Scotia Talc mine sample (NCL) are almost constant. Comparison between the two rock suites from ophiolites sequences (BA oxide and Kraubath samples) show that BA oxide samples were produced in a Ni enriched environment while BA host and Kraubath samples were formed in environments similar to the mantle (enriched in Mg but depleted in Ni) although Kraubath samples are much more depleted in Mg as a result of a variety of crystallisation processes such as Mg substituting for Ni.

In comparison, komatiites are thought to result from high degrees of over 30% mantle melting (Sun and Nesbitt, 1978; Herzberg, 1992), at great depths (down to 400 km; Herzberg, 1992), under conditions that, apart from one exception (the Cretaceous komatiites from Gorgona Island; Echeverria, 1980), have not existed since the Precambrian (Robin-Popieul et al, 2012). Komatiites are classified into three groups: (a) Al-depleted or Barberton-type komatiites with sub-chondritic Al_2O_3/TiO_2 ratios and depletion of the heavy rare earth elements (HREE); (b) Al-undepleted or Munro-type komatiites with near primitive-mantle

Al_2O_3/TiO_2 ratios of around ≈22 and flat HREE patterns; (c) Al-enriched komatiites with high Al_2O_3/TiO_2 ratios between ≈30 and ≈60 and enrichment of HREE (Robin-Popieul et al, 2012). All three komatiite types are present in the BGB and commonly occur within the same stratigraphic unit (Robin-Popieul et al, 2012). The dominant Barberton-type komatiites have an Al_2O_3/TiO_2 ratio of about ≈10.2 wt %, chondrites Al_2O_3/TiO_2 ≈20.4 ratio is double the Barberton type ratio, (Sun, 1984). Early Archaean komatiites tend to have different compositions from late Archaean komatiites, e.g. they are relatively depleted in Al_2O_3 and HREE (Maier et al, 2003).

The application of Al alone as a measure of differences and similarities between komatiites and the studied samples will not provide clear and unequivocal scientific correlations but through the application of different ratios and elemental compositions it is possible to compare these samples. Therefore based on the Al_2O_3/TiO_2 ratios, the BA oxide ratios show similar correlations with the chondritic ratios (group I early Archaean komatiites, Fig. 5.11). Looking at Fig. 5.11, it is very clear and evident that all three types of komatiites are represented either by one of the ratios or a combination thereof but less so for the group I and III komatiites (Fig 5.11).

Komatiites generally show high CaO/ Al_2O_3 ratios >1 which is not chondritic but differentiated Condie (1981), however the Similarities in CaO/Al_2O_3 ratio between BA oxide, BA host rock and group I komatiites are clear indications that at some stage the komatiites and magnesian type magmas did play a role no matter how insignificant their impact was on the final outcome of the BA oxide and its host rocks mineralogy and geochemistry. The Al_2O_3/TiO_2 ratio of sample NC-L is very similar to that seen in all the ANL samples (highly enriched) except in sample UFS 4CS2, it is however depleted in CaO/Al_2O_3 compared to

group I komatiites (Fig. 5.16). The CaO/Al_2O_3 ratio in BA oxide is very low <1, in some cases very little to no Ca was detected.

	Type 1 Al - depleted	**Type 2 Al - undepleted**	**Type 3 Al - enriched**
REE pattern	 La Yb HREE depleted	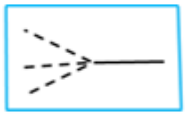 La Yb Flat HREE	 La Yb Enriched HREE
Chemistry	$(Gd/Yb)_N > 1$ $Al_2O_3/TiO_2 \approx 10$ $CaO/Al_2O_3 > 1$	$(Gd/Yb)_N \approx 1$ $Al_2O_3/TiO_2 \approx 20$ $CaO/Al_2O_3 \approx 1$	$(Gd/Yb)_N < 1$ $Al_2O_3/TiO_2 \approx 40$ $CaO/Al_2O_3 < 1$
Chondritic relation	Non chondritic	Chondritic	Non chondritic

Figure 5.10. Schematic illustrating the komatiites groups based on their Al_2O_3/TiO_2, CaO/Al_2O_3 and Gd/Yb ratios (interpreted and modified after, Rollinson 2007).

Komatiites and high magnesian basalts are generated by large degrees of partial melting in mantle diapirs, thus resulting in the removal of all the Al and Ca bearing phases (garnet and clinopyroxene etc.) from the residue and concentrate these elements into the melt, therefore resulting in poor partitioning in the solid phase. Alternatively, Sun (1987) noted that the chemical characteristics of Al-depleted komatiites accompanied by depletion in HREE, Sc and Y is as a result of garnet fractionation from komatiitic magmas or mechanical separation of dense garnet from a partially molten mantle diaper at depths ≥200 km under a higher temperature condition in the early Archaean mantle. This model accounts for the Al, Mg and Ca deficiency in BA oxide samples. The differences between the CaO/Al_2O_3 and Al_2O_3/TiO_2 ratios (Table 5.2) in the ANL, BA oxide and host rock samples further indicate their lack of relation and therefore lack of association.

Table 5.2. **Al_2O_3/TiO_2, CaO/Al_2O_3 and Gd/Yb ratios.**

Sample names	Gd/Yb	Al_2O_3/TiO_2	CaO/Al_2O_3
NCA	1.10	21.63	0.002
NCB	0.85	26.04	0.003
NCC	1.22	20.11	0.019
NCD	2.02	23.5	0.019
NCE	1.40	21.06	0.017
NCF	0.92	22.02	0.004
NCG	1.33	23.32	0.02
NCH	0.49	12.8	0.002
NCJ	1.58	20.61	-
NCK	0.78	18.25	-
NCL	NA	27.66	0.005
NCMA	NA	-	0.024
NCNA	NA	-	-
UFS 16a	1.37	22	1.77
UFS 38a	1.44	24	0.17
UFS 39a	2.24	26	0.04
UFS 16c	2.98	27.29	0.003
UFS 4CS2	1.23	43	0.15
UFS 39b	1.25	24.51	0.019
UFS 38e	0.79	29.22	0.005

Dashes indicate no data due to lack of CaO, Al_2O_3 and TiO_2 in those specific samples.

The BA host rocks are very high in silica (averaging ≈ 45 wt%) and magnesium (averaging ≈ 31 wt%), possibly representing siliceous magnesian basalt as a result of low pressure magma generation and/or assimilation of orthopyroxenes from the refractory peridotite in the mantle.

The low pressure magma generation is envisaged to have been modified by mantle metasomatism and/or subduction related processes which resulted in the depletion of Ti, Nb and Ta. The SEM data indicated the occurrence of Ca and Cl phase minerals in BA host rocks (NCD-NCG), an observation that is in direct contrast with the typical geochemistry expected in this type locality. However this has been attributed to the multiple stages of geological evolution and development events in the vicinity of the BA deposit.

The occurrence of serpentinites, schists and accessory mineral phases such as the apatite pseudomorph, calcite, tremolite etc., is a clear indication of weathering and metamorphic processes that took place associated with the mantle thermal plume processes responsible for the BA nickel oxide deposit. While the remnant amphibole and plagioclase phases are only observed in the host rocks, the Eu anomalies indicate the crystallisation and extraction of a plagioclase phase at some stage, thus indicating a source possibly associated with a spreading center and newly differentiated material from the upper mantle.

From the metamorphic mineral assemblage, it is clear that greenschist facies metamorphism was the dominant type of alteration that occurred to the initial mineral and rock assemblages. The occurrence of the normally sulphur-loving, enriched chalcophile elements (As and Sb) in sulphur deficient unknown phases further substantiates the theory of origin in a source environment devoid of sulphur. However the occurrence of As and Sb phases are only limited to very minute areas in the rock samples and are only observed in the BA nickel oxide samples, and mostly occur embedded in the spinel phases. Processes likened to those associated with early earth forming resulted in the formation of a Fe-Ni rich mass along with some Cr but were later replaced and resulted in Cr-rich magnetite and some silicates.

Mantle thermal plume activity was induced by either subduction of cold lithosphere or by lithosphere subduction in a back arc environment can be used as a precursor environment

with the crustal characteristics observed in the BA host rocks (i.e. low, Ti, Ni and high Pb), and it was responsible for the transportation of what would have been a metallic BA body from deep in the earth towards the surface. For material of the magnitude of the BA nickel oxide deposit (metallic - dense) to be transported by a thermal plume, the plume need to have been considerably large with sufficient energy to accommodate it and therefore played a major role in modifying the initial chemical and mineralogical characteristics of the BA oxide deposit. Chemical and isotopic characteristics of plume material can be modified by contributions from subduction zone related processes (e.g. sediment subduction for low P and Ti) or interaction with the continental crust which could have been modified by the same subduction zone process (McDonough and Sun, 1995). Therefore chemical depletion in the resultant ophiolite ultramafics can be attributed to heterogeneous melting regimes of the oceanic crest beneath the ridge crest following the plume and/or subduction related activities. MgO is relatively enriched compared to Cu in the BA host samples (Fig. 5.12), BA nickel oxide samples indicate the inverse as a result of a source region lacking Mg (possibly crust). Metasomatism of intercumulus liquids during the upwelling process of the envisaged mantle plume resulted in minor Cu concentration in the BA host rocks.

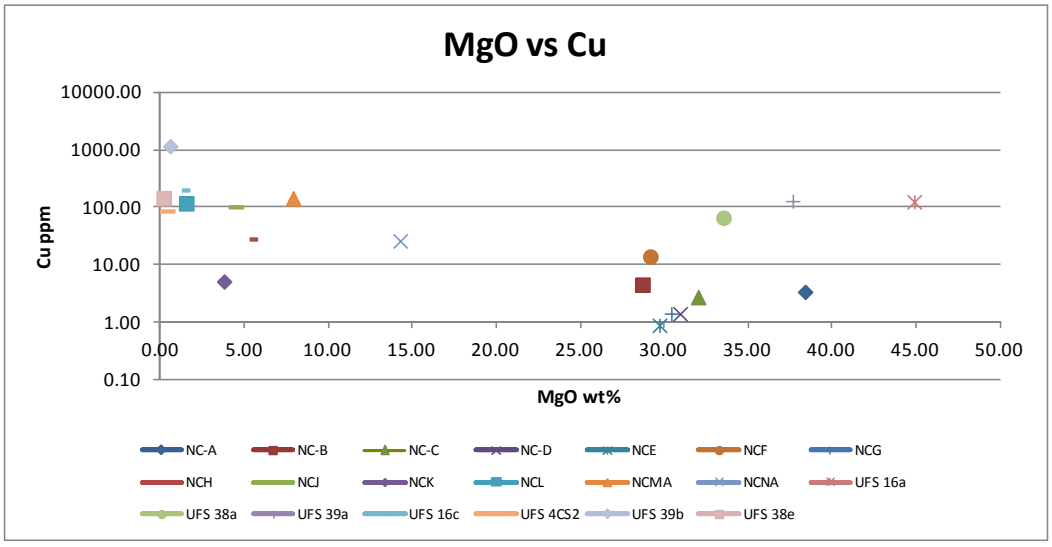

Figure 5.11. Harker diagram illustration between MgO vs Cu.

While the Cu concentrations in the ANL and NC-L samples appear to be associated with progressive fractionation where Cu is incompatible in silicates and oxides but highly compatible in sulphides such that the higher the sulphides the higher the potential to concentrate Cu. The mobility of Cu during alteration and/or metamorphism directly influenced the scattering patterns in the BA host rocks. In the BA nickel oxide samples Cu distribution does not show any specific trend or pattern, but visible is the apparent inverse relationship between Mg and Cu. Sample NC-NA did not plot because As was below the detection limit (Fig.5.13). The tendency for the original olivine to act as the main primary cumulus phase was responsible for the progressive decrease in As with increasing MgO content in the BA host (Fig 5.13). Such that, As acted as an incompatible species in silicates and oxides but strongly compatible in the sulphides therefore during progressive fractionation of olivine, As was incorporated into the melt phase resulting in As-poor olivine assemblages. However any remnants of olivine represent the pseudomorphous serpentine mineral phases.

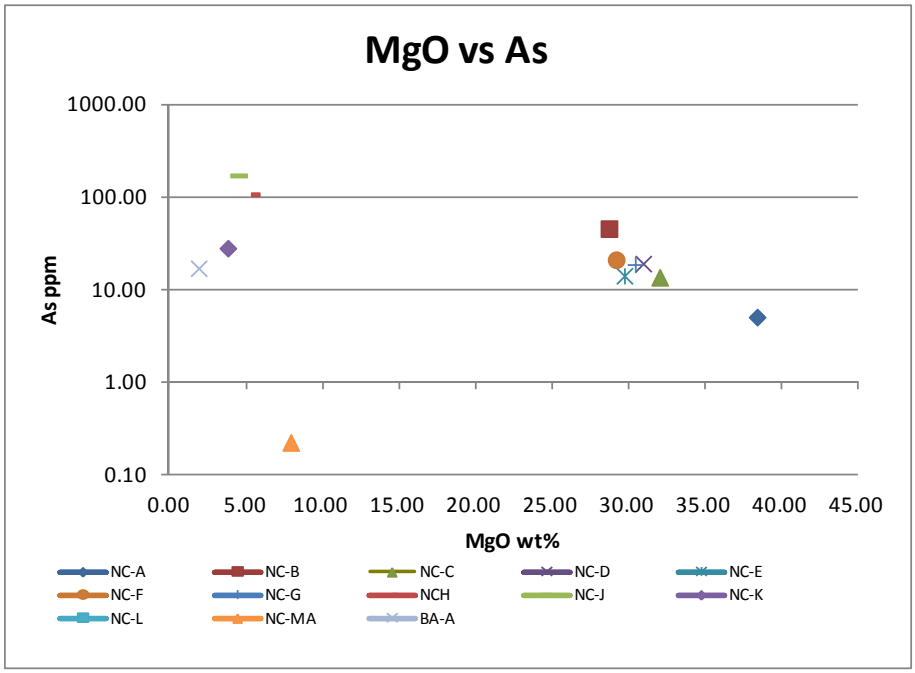

<u>Figure 5.12.</u> Harker diagram between MgO vs As. Sample NC-NA did not plot because As was below the detection limit.

The BA nickel oxide samples show relative increase in Ni/Cu with fixed MgO content (≈ 4%) due to the incompatibility nature of Cu during crystallisation. The high Ni/Cu ratio, serves as an indication of secondary sulphur saturation event in the BA nickel oxide deposit probably in the early stages of crystallisation. The Kraubath samples have very low Ni/Cu ratios indicating sulphur saturation had not yet occurred during their early crystallisation stage, while only remnants of sulphur can be seen in the BA nickel oxide samples. The BA host rocks occur clustered with the exception of NC-A, a trend characteristic of mineralisation during a sulphur saturation phase (Fig. 5.14).

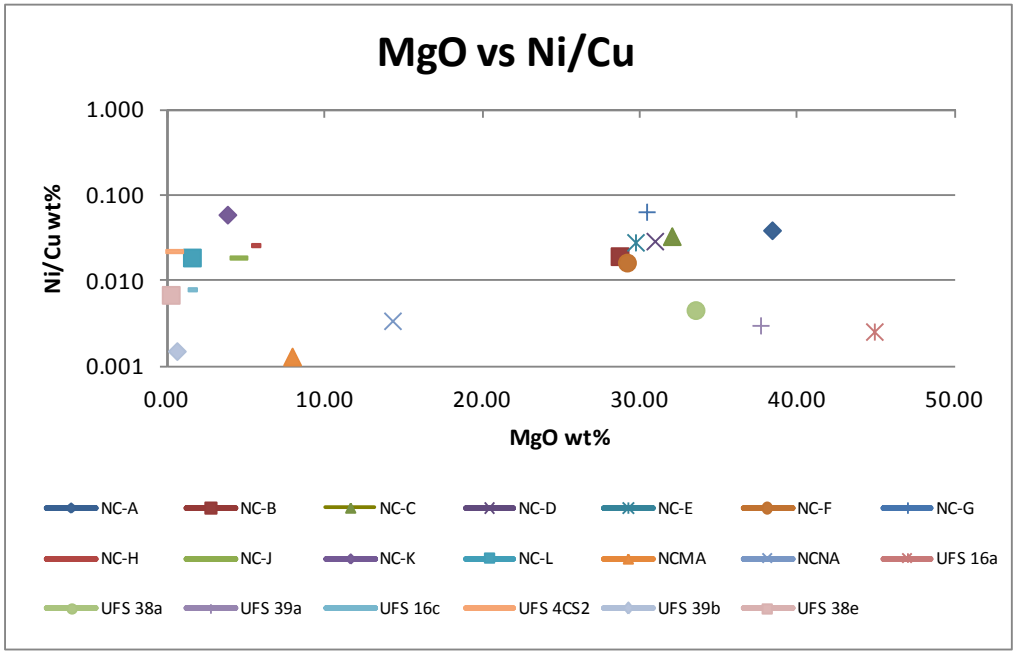

Figure 5.13. Harker diagram showing the relationship between Ni/Cu ratio and MgO during crystallisation.

5.6. Comparison between all the studied rock samples

The rare mineral assemblages together with the extreme NiO mineralisation are always going to be the most notable features when studying the BA oxide deposit. All the other studied samples comprise non exotic mineral assemblages and lack any evidence of NiO

mineralisation with the exception of ANL samples (albeit not enough to warrant exploitation). The Kraubath samples are thought to resemble an ophiolite (Melcher et al, 2004) similar to BA oxide as proposed by Tredoux et al (1989). The major element data of the Kraubath samples is completely different to the major element data of both BA oxide and its host rocks, i.e. SiO_2 of BA host is ≈45 wt% on average while Kraubath is ≈63 wt% and the ANL samples are ≈50 wt%. The MgO content of all four suites of rocks (Bon Accord oxide, host rocks, ANL and Kraubath samples) varies remarkably, where BA host is enriched, BA oxide and Kraubath are severely depleted together with the ANL samples with the exception of samples UFS 16a, UFS 38a and UFS 39a. Cr mineralisation was only documented in the Kraubath samples, while the other samples are severely depleted in Cr.

The origin of BA nickel oxide deposit has been compared to a variety of process (as previously mentioned) and as such this research will compare and contrast the BA nickel oxide deposit and komatiites to distinguish the presence or lack of relations between the two rock suites. When comparing komatiites and BA nickel oxide, it is very important to study the mechanisms and components associated with komatiite formation as provided by Arndt and Lesher (2004) below:

- Komatiites are formed from MgO rich melts.
- Mostly have spinifex texture.
- Sometime contain Ni-Cu-PGE mineralisation.

Using the guidelines as established by Arndt and Lesher (2004), elemental ratios and spiderplots (Figs. 5.5, 5.6, 5.10 and 5.14), it is quite obvious that BA oxide is MgO depleted with no evidence of spinifex texture. The only likely similarity between BA oxide and komatiites is the high Ni-PGE concentration even though the concentration proportions are

totally different and not in line with those expected in komatiites. Bon Accord oxide is Cu deficient, a characteristic not shared with komatiites. The nearly chondritic average $(Gd/Yb)_N$ ratio of ≈1, and the Al_2O_3/TiO_2 of ≈17 on average in the BA nickel oxide deposit represents a possible link in similarities between the two rock types (Bon Accord oxide samples and komatiites), while the only difference is noted in the CaO/Al_2O_3 ratio due to the lack of Ca. While the elemental $(Gd/Yb)_N$, CaO/Al_2O_3 and Al_2O_3/TiO_2 ratios of the ANL samples are similar to the ratios of the BA host rocks, only UFS 4CS2 is the only exception, comprising $(Gd/Yb)_N$ ≈1.50, CaO/Al_2O_3 ≈0.15 and Al_2O_3/TiO_2 ≈40 a characteristic of the group III komatiites.

The REE are also good delineators when comparing and contrasting rock suites, critically important in the case of BA nickel oxide samples and its host rocks is the differences in REE patterns and behaviour. Therefore the chondrite normalised data (Fig. 5.5) for the BA host rocks indicate slight enrichment in LREE and relatively flat HREE patterns in contrast to BA nickel oxide, which demonstrates an almost linear REE pattern with the exception of sample NC-J (slightly LREE enriched in comparison to the other two Bon Accord oxide samples). BA host rocks are slightly Eu enriched when compared to BA nickel oxide (Eu depleted), as a result of plagioclase fractionation in the source. While the ANL samples are variably enriched in LREE, except samples, UFS 4CS2, UFS 38a, UFS 39a, and UFS 16a which are generally depleted in the whole range of REE (Fig 5.5). Primitive mantle normalised data (Fig 5.6) shows LREE enrichment and flat HREE trend in BA host samples, while BA nickel oxide samples show an almost flat REE pattern in samples NCH and NCK, while NCJ is slightly LREE enriched with a flat HREE trend. The primitive mantle normalised data also shows that samples UFS 16c while UFS 39b are enriched in all the REE and the remaining ANL samples are depleted in the whole range of REE (UFS 16c and UFS 38e are slightly Eu enriched). Based on the high NiO mineralisation it is evident that processes responsible for

this remarkable and unique deposit were localised and confined to the geological context in which it occurred, since no other deposit similar to BA oxide has ever been documented anywhere in the Barberton region, and/or anywhere in the world. It is worth noting that studies conducted during this research could not completely rule out the influence of komatiite like processes in the final outcome of BA oxide deposit, particularly looking at the mineralogy and geochemistry.

5.7. Susceptibility measurements and mineral formation processes

5.7.1. Susceptibility measurements

The susceptibility measurements (Table. 5.3) were taken using a standard hand held susceptibility device. The susceptibility measurements observed in the BA host rocks indicate both diamagnetic and paramagnetic properties.

Table 5.3. Susceptibility measurements of BA and BA host rocks.

Sample name	Readings		Average	SD	Avg x 0.001
NC-A	7.17	7.12	7.145	0.04	0.0071
NC-B	124	100	112	16.97	0.1120
NC-C	1.21	1.32	1.265	0.08	0.0013
NC-D	24.8	22.4	23.6	1.7	0.0236
NC-E	31.2	39.6	35.4	5.94	0.0354
NC-F	94.4	69.4	81.9	17.68	0.0819
NC-G	15.2	16.1	15.65	0.64	0.0157
NC-H	2768	2231.2	2499.6	379.57	2.4996
NC-J	3686	2883	3284.5	567.81	3.2845
NC-K	7111	8506.3	7808.65	986.63	7.8087

Reading (x 10^{-3})

Paramagnetic susceptibilities are inversely proportional to the value of absolute temperature and the ferromagnetic materials (mainly BA oxide samples) show relatively large positive values and their susceptibility reading is in excess of 2000 (Fig 5.15). The BA host rocks susceptibility measurements read almost entirely below 100 with the exception of sample NC-B, a clear confirmation of their paramagnetic nature. BA oxide samples are characterised by a fairly fine-medium grained texture and the decrease in magnetisation potential is characterised by the fine grained nature of the BA host rocks.

The grain size dependencies of magnetic properties in the fine grained BA host rocks indicate a proportional relationship with magnetic susceptibility, therefore grain growth is indicative of increase in the magnetisation potential. Temperature, grain size and chemical composition were very critical in determining the susceptibility response in the samples, the magnetic properties of the BA oxide samples show very large magnetic susceptibility readings (due to their metallic nature), indicating very high temperatures which would be associated with upwelling plumes specifically in the case of BA oxide deposit.

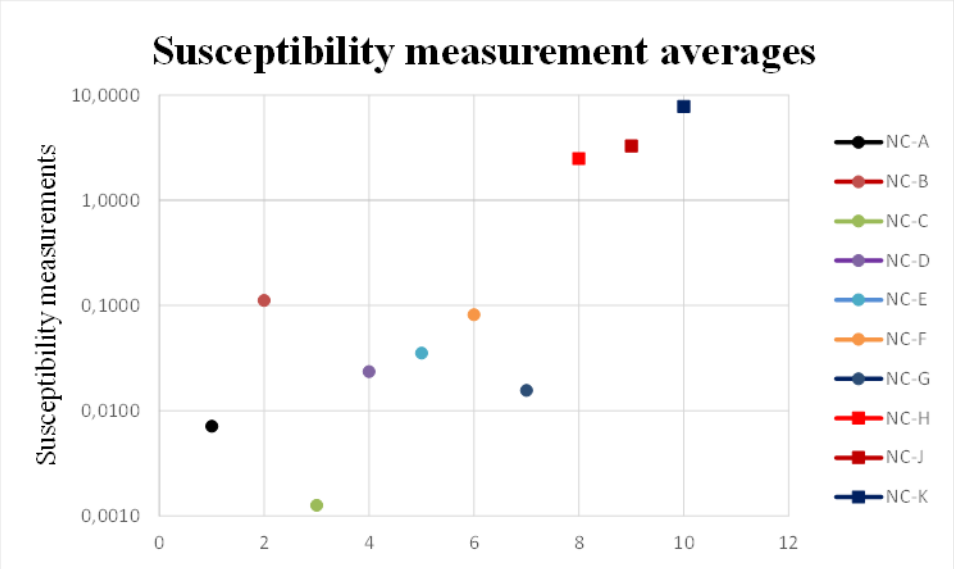

Figure 5.14. Susceptibility measurements from BA host and host rocks

The fine grained texture of the host rocks is associated with the metamorphic event related to the emplacement of the BA oxide ore body. The large occurrence of the greenschist facies minerals supports the cooling down of the plumes with increased height and decreased pressure. Plumes originating from the core-mantle boundary and with the potential to transport a deposit similar to BA oxide needs to be large and complimented by extensive temperatures to be able to transport such materials to the surface. The chemical composition of the BA host rocks influenced magnetisation to such an extent that only paramagnetic properties were recorded and preserved. While BA oxide samples are highly enriched in ferromagnesian-minerals and thus exhibit higher magnetic properties.

5.8. Evaluation of advances made in terms of the research questions

What is the relationship between the nickel-oxide rich BA oxide body and the surrounding low concentrated rare sulphide rocks?

The sulphides in BA nickel oxide deposit are always found in very minute amounts and embedded within the trevorite and magnetite phases, an indication of two separate unrelated mineralisation events that occurred at different times. The sulphides occur as disseminated grains averaging 3.1 wt% sulphur in the meta-peridotites, the nickel-ferroan trevorite assemblage formed as a result of crystallisation in a hydrothermal environment characterised by high nickel and low sulphur contents, where oxygen activity played a major role in the final concentration of sulphides. The unstable nature of nickel-iron sulphides relative to nickel-iron oxides as a result of oxygen activity, resulted in mineralisation of only small amounts of nickel sulphides and native nickel. The nickel sulphides and sulphosalts might have been present in the primary assemblages, but from textural evidence it appears more likely that they are of hydrothermal origin and formed prior to the xenomorphic trevorite or at

least at the same time (Wildau, 2012). Furthermore due to the presence of appreciable quantities of sulphur in hydrothermal fluids, and nickel in the primary mineral assemblage (liebenbergite), it is likely that the nickel sulphides are a by-product of the hydrothermal alteration of the primary minerals and the replacement of almost all primary minerals resulted in what is now sulphur deficient phases. The envisaged post-magmatic, low-temperature hydrothermal oxidation of the primary magmatic sulphide assemblages could have led to significant upgrading of the original Ni mineralisation and thus resulted in the associated sulphur loss.

What is the relationship between deep mantle originating body masses and Bon Accord oxide deposit?

The lower mantle, the region between the 660 km seismic discontinuity and the core-mantle boundary at 2900 km, is substantially less accessible to study than is the upper mantle. Therefore, understanding of the lower mantle beneath the 660 km seismic discontinuity is generally restricted to information derived from seismology, mineral physics and fluid experiments as explained by McDonough and Sun (1995). However even with no direct samples from this part of the earth, it is important to note that bodies originating from shallower depths, such as peridotite and komatiites, contain high MgO, relative concentrations of FeO, CaO, Al_2O_3 and REEs depleted, characteristics shared with the BA oxide deposit. The only exception noted is in the high Ni and Fe contents and unusually high MgO depletion in the BA nickel oxide deposit. Ita and Stixrude (1992) noted that thermal and chemical evolution of the earth depend critically on whether the transition zone is bounded by phase changes alone or by changes in phase and composition. The Bon Accord oxide transition zone appears to have been controlled by changes in both phase and composition, also important, is that these changes (sulphur deficiency and enrichment of Ni-rich mineral

assemblages) occurred once the BA oxide deposit was removed from its point of origin (source environment).

The MgO depletion in BA oxide deposit is further evidence of none to very little (short lived) interaction between BA oxide and mantle together with any mantle related processes. Therefore, BA oxide does not seem to have any direct relationship with the conventional mantle originating masses nor does BA oxide seem to have any association with crustal masses as evidenced by the complete contrast in mineralogy and geochemistry. The contrasting distribution and behaviour of REE and apparent lack of similarities between BA oxide, crust and mantle points to environments that have nothing in common. In the chondrite normalised plot (Fig 5.5), BA nickel oxide, demonstrates an almost linear REE pattern with the exception of sample NC-J (slightly LREE enriched in comparison to the other two BA oxide samples). Primitive mantle normalised data (Fig 5.6) BA nickel oxide samples show an almost flat REE pattern in samples NCH and NCK, while NCJ is slightly LREE enriched with a flat HREE trend. BA oxide lacks the MgO rich melts responsible for the formation of komatiites and the characteristic spinifex textures associated with komatiites, similarities noted include, the high Ni-PGE concentration albeit the concentration proportions are totally different and not in line with those expected in komatiites. The nearly chondritic average $(Gd/Yb)_N$ ratio of ≈1, and the Al_2O_3/TiO_2 of ≈17 on average in the BA nickel oxide deposit represents a possible link in similarities between Bon Accord oxide and komatiites. The Cu deficiency in BA oxide is a characteristic not shared with komatiites, REE distribution of BA oxide can be related to those observed in the Al-depleted or Barberton-type: sub-chondritic Al_2O_3/TiO_2 ratios and depletion of the heavy rare earth elements (HREE), an indication of interaction with processes similar to those responsible for the formation of Barberton type komatiites.

How can the previously proposed models be compared to current data?

Thermal plumes initially originate at the D" layer, and if this holds true, then plumes need to be able to rise nearly 3000 km as narrow conduits without fading away in the mantle (Albers and Christensen, 1996). Hauri et al (1994) and Olson et al (1993), found that thermal diffusion and entrainment of ambient mantle can be responsible for the rise of plumes with sufficient energy through the mantle without significantly fading away. As mentioned previously, komatiite-like processes played some kind of a role during the deposition of BA oxide deposit and komatiites are thought to be generated in mantle plumes by moderate to high partial melting processes of dry garnet peridotite at depths of 150 to 350 km, and temperatures in the order of 1600–1900 °C (Furnes et al, 2013). Thus, using the thermal plume model, it is reasonable to suggest that the responsible formation processes for the BA oxide deposit must have had temperatures ranging between 1800-2200°C, since the excess temperature of mantle plumes inferred from petrological studies, is 200-300°C (Farnetani, 1997). These temperatures would have needed to be sufficient enough to maintain and continue carrying the Ni-Fe rich mass towards the surface of the earth, as the plume continued to rise through the mantle, flow resistance would have caused the head to rise more slowly than the material in the tail, consequently, resulting in the enlargement of the plume head as it is fed by material flowing up through the long narrow tail and the rising plume head will inflate like a balloon (Hamblin and Christiansen, 2003). Accordingly, the now inflated plume head will result in engulfing of the cooler plume surrounding material (which is assumed to bring additional energy) into the plume which would have also contributed to the enlargement of the plume head as it continued with its ascent. Therefore the thermal processes could have resulted in a komatiite type reactions with engulfed material from the mantle which in turn resulted in the komatiite like signatures seen in the BA nickel oxide samples.

The plume mechanisms and functions proposed by Hauri et al (1994) and Olson et al (1993), (Furnes et al, 2013), (Farnetani, 1997) and (Hamblin and Christiansen, 2003) could be applied to support the model proposed by this research for the transportation of the BA oxide mass from a Ni – Fe reservoir that interacted with mantle material that resulted in a komatiitic type reaction and subsequently komatiitic type REE concentrations and distribution patterns. The envisaged later metamorphism and/or weathering of the host rocks close to the surface resulted in highly altered meta-peridotitic material enriched in equivalents of the exotic minerals found in BA nickel oxide deposit. Therefore, based on current findings the C1 chondrite normalised REE plots with the exception of Eu (BA oxide) show linear patterns, a favourable indication of similar enrichment processes. The rare and unusual mineralogy and chemistry of BA oxide is equivalent to none and their formation is largely associated with high temperature processes, the kind that has only been reported and associated with mantle plumes. The current research has found evidence of similar Al_2O_3/TiO_2 chondritic ratio correlations between BA oxide and group I early Archaean komatiites (Fig. 5.11). It was established that there is, clear evidence of all three types of komatiites being represented either by one of the ratios or a combination thereof though not to the same extent (Fig 5.11), the Similarities in CaO/Al_2O_3 ratio between BA oxide, BA host rock and group I komatiites are clear indications that magnesian komatiitic type magmas did play role in the final outcome of the BA oxide deposit at some stage.

The data obtained for BA oxide does not show any evidence of ever interacting with processes that could be associated with the oxidised iron rich meteorite model. Data from mmajor and trace element concentrations are very different, in that iron meteorites are depleted in these elements when compared to BA oxide. The proposed alteration of the iron meteorite would have needed to be extensive such that it became highly enriched in Ni while

losing significant amounts of PGEs and Fe, a phenomenon not currently seen in BA nickel oxide.

Therefore, from all the evidence presented above, it is not possible to conclusively support any of the proposed mechanisms of formation, however it is worth noting that the BA oxide deposit appear to have been already concentrated into a metallic phase prior to emplacement.

How can the evaluation of full set of major elements found in BA oxide using modern methods and the full implication of these analyses/methods be used to determine and/or establish the probable origin of Ni-mineralisation in BA?

The current morphology of both BA nickel oxide and its host rocks is as a result of a variety of process, from mantle thermal plume activities possibly induced by either subduction of cold lithosphere or by lithosphere subduction in a back arc environment. Where nickel mineralisation could have been influenced by its moderate volatility, which would have acted as a facilitator in ensuring that it would be easily incorporated into the fluid(s) associated with these thermal plume activities. A mechanism that is envisaged to have lasted until the dense BA body was emplaced beneath the lithosphere where volatilisation continued to play a pivotal role in the removal of Si from the mantle thus resulting in relative depletion of Si in the BA oxide deposit. Other processes such as mantle melting processes associated with formation of komatiite type magmas and their relevant mineralogical and chemical signatures, provide consistent similarities between the Al_2O_3/TiO_2 ratios of BA oxide and chondrite.

The relatively high Ni/Cu, low Pd/Ir and Pd/Pt ratios and high concentrations of IPGEs in the BA oxide deposit are indicative of ultramafic rocks that formed during a sulphur-unsaturated event while the depletion in HREE, Sc and Y as a result of fractionation from komatiitic

magmas from a partially molten mantle diaper under higher temperature conditions in the early Archaean mantle also resulted in Al, Mg and Ca deficiency in BA oxide samples. The diversity of BA oxide is further amplified by the relative increase in Ni/Cu with fixed MgO content (≈ 4%) as a result of Cu's incompatible nature during crystallisation and effectively the relatively high Ni/Cu ratio, serves as an indication of secondary sulphur saturation event probably in the early stages of crystallisation

Processes responsible for formation and enrichment of BA oxide can be summarised as follows: with continued ascent from the deep earth, a boudinage effect ensued caused by entrapment of surrounding ambient material which resulted in the formation of small "concentrated blobs with some surrounding material" along the trail of the upwelling plumes and as a result. As transportation continued and the resulting reduction of excess temperature with height, some of concentrated blobs in the weaker part of the plume were left behind, in a process akin to the boudinage effect and resulted in the apparent rootless nature of BA nickel oxide deposit. Therefore as the plume head continued to rise and flatten, the cooler entrained mantle edge of the plume started to melt due to the low pressures at shallow depths. Upon reaching, BA oxide mass was emplaced beneath the lithosphere where no further melting occurred as a result of energy reduction caused by "colder" ambient material. As a result plume head melting occurred as a result of adiabatic decompression, a phenomenon also reported by Jones et al (2002), where melting of the plume began at the hot leading edge of the top of the plume, and produced high MgO magmas (normally associated with komatiites) and since BA oxide already differentiated only minor reactions occurred and BA oxide mass was then exposed on the surface during magma extrusion. The subsequent uplift associated with upwelling and emplacement resulted in brittle deformation which could have formed conduits used as migration paths for secondary enrichment.

What could be the cause/s of the low sulphide grade in the high Bon Accord oxide compared to the relatively enriched areas in the vicinity of Bon Accord?

The difference is mainly expressed as a result of different environments of origin and mineralisation. The oxide rich phases originated in a Ni – Fe reservoir and were later altered and/or replaced and further mineralised by hydrothermally induced processes to result in what was BA nickel oxide deposit, while the sulphides were mainly enriched in the upper mantle and possibly the lower crust during ascent and emplacement of the deposit, as evidenced by the relative LREE and MgO enrichment. However considerable replacement of interstitial sulphides by the spinel minerals together with the presence of millerite and remnant violarite bearing, pyrrhotite-free sulphide phases could be indicative of significant post-magmatic, low-temperature hydrothermal oxidation of the primary magmatic sulphide (pyrrhotite-pentlandite-chalcopyrite) assemblages and the associated sulphur loss that could have led to significant upgrading of the original nickel mineralisation.

A second possibility suggested would have needed to have the fluids associated with the envisaged plume event be highly deficient in sulphides and their mineral equivalents such that only minor amounts of sulphides and/or the sulphur that was contained was melted with minor amounts remaining due to its low melting point. But as geological processes continued the sulphides were eventually later replaced by trevorite and magnetite during a hydrothermal oxidation driven event.

The close relationship between the unknown mineral phases with the trevorite are only related through a secondary phase of enrichment, an event that could have been characterised by enough sulphides to concentrate these unknown phases enriched in As, Pt and minor Sb.

Chapter 6 - Conclusions

The mineralogy and geochemistry documented in the BA oxide deposit indicate that, it is the only rock of its type ever found and reported anywhere in the world. The petrographic studies established that the mineral talc (willemseite) occurs as the main abundant constituent of both BA oxide and its host samples followed by trevorite and népouite. The dominant willemseite and its associated nimite formed as a result of heat and chemically active fluids acting to alter highly Mg rich rocks (such as peridotites): The Kraubath samples are dominated by the minerals olivine (specifically, Mg rich end member forsterite), pyroxene and amphibole, while the ANL samples are mainly dominated by pyroxene, olivine, and are sulphide rich.

Metasomatism through the interaction of serpentinised peridotite with nickel rich fluids resulted in the formation of trevorite and the alteration of bunsenite resulted in the formation of xenomorphic trevorite. The intricate association of the liebenbergite- népouite -willemseite assemblage is due to the alteration of primary liebenbergite to form népouite which in turn altered to form willemseite. The closely interwoven nimite and willemseite are an indication of their contemporaneous formation. The onset of formation of the oxide minerals particularly in the BA nickel oxide deposit is characterised by serpentinisation of ultramafic-mafic rocks while the sulphides represent processes associated with ocean crust hydration. The mineralogy and chemistry of BA host rocks was significantly influenced by late metamorphism and subsequent weathering. Characteristically BA host is dominated by talc which is a secondary product formed after alteration of high Mg rich rocks by heat and chemically active fluids during a hydrothermal phase.

The chemical and geochemical outcome of BA nickel oxide deposit together with its host rocks was largely dependent on the compositions of the source and residue, pressure, temperature and degree of melting, the nature and degree of crustal contamination (however

most of the evidence appears to have been removed) and the degree of remobilisation of elements through hydrothermal alteration, metamorphism and metsomatism. The REE patterns are typically associated with partial melting (mainly true for BA oxide and host rock samples), with variation from relatively enriched LREEs patterns (indicative of source region that is not depleted mantle) to flat HREEs and with variable Eu anomalies in both chondrite and primitive mantle normalised plots (Fig 5.5 and 5.6). The HREE correlations between chondrite and primitive mantle normalised plots are similar therefore substantiating the suggestion of BA oxide samples being concentrated by processes similar to early earth forming processes. The main variation in REE is partly caused by subduction and/or processes associated with obduction of the crust, which acted as an additional source component that was added to the mantle melts. The depletion in the moderately incompatible elements (HREEs, Ti, Eu, Gd, Dy) suggest moderate to high degrees of partial melting (30-60%), depending on the composition of the source and the degree of prior melt extraction (Sproule et al, 2003).

The high MgO concentrations (29-38%) of BA host rocks was sourced from a mantle source (possibly olivine rich rock) which probably left behind a lherzolite or harzburgite residue. The ANL samples represents mainly variably altered ultramafic rocks, which are sulphur rich in certain instances, and are not in any way related to either the BA oxide deposit or its host rocks. The investigations of this research did not indicate any relationship(s) to a reworked palaeometeorite parental mass as previously suggested by de Waal (1978). However what was evident and thoroughly corroborated was the possible association of the BA oxide samples with processes that originate in a Ni – Fe rich environment as well as associations to magnesian komatiitic type magma processes even though the extent of this association could not be established.

The only similarities between BA nickel oxide and komatiites deposits were noted in the high Ni-PGE concentration and some elemental ratios such as the nearly chondritic average ratio of $(Gd/Yb)_N \approx 1$, and the Al_2O_3/TiO_2 ratio of ≈17 on average. The ANL and BA host rocks have similar $(Gd/Yb)_N$, CaO/Al_2O_3 and Al_2O_3/TiO_2 ratios, with only sample UFS 4CS2 showing $(Gd/Yb)_N$, CaO/Al_2O_3 and Al_2O_3/TiO_2 ratios characteristic of the Al-enriched komatiites.

The PGE enrichment in the BA oxide deposit (as reported by Tredoux et al, 1989), point to magma responsible for the initial rock formation being derived from a PGE enriched fertile source, a suggestion also supported by the once MgO rich mineral relics of liebenbergite. The PGE patterns in the ANL samples (Fig 5.5 and 5.6) are similar to those seen in komatiites, characterised by relatively flat PGE patterns with the exception of Pd (negative anomaly) and low Pd/Ir ratios. The relatively low in Ni/Cu (<100 ppm on average) and Pd/Ir and relatively enriched Pd/Pt (≈1 ppb) in the ANL samples is an indication of formation in an environment that contained some sulphur and/or sulphur phases that could have been replaced later. The low grade sulphides could also be associated with considerable replacement of interstitial sulphides by spinel minerals together with the presence of millerite and remnant violarite bearing, pyrrhotite-free sulphide phases which could serve as indicators of post-magmatic, low-temperature hydrothermal oxidation of primary magmatic sulphide assemblages. The associated sulphur loss that could have accompanied these processes is suggested to have been a contributor by significantly upgrading the original nickel mineralisation.

SEM studies indicated the occurrence of silicate with apatite characteristics (probably ellestadite), however the high SiO_2 (maximum of 77.34 wt%), CaO (maximum of 21.94 wt%) and Cl (maximum of 18.74 wt%) meant that it was unlikely to be apatite unless remarkable SiO_2 substitution took place and has therefore been referred to as unknown #11. Also, very

important was the occurrence of another unknown mineral species marked unknown #12, which seems to be a remnant of plagioclase of some kind but the higher than normal SiO_2 content and slightly high MgO with low K_2O and CaO as well as lack of any visible or relic plagioclase in thin section possibly due to deformation makes it almost impossible to accurately confirm plagioclase as its precursor. Electron microprobe analyses indicated the occurrence of high concentrations of trace elements, Sb, As and Pt in minerals unknown #4, unknown #5 and unknown #9 respectively, however no further investigations were carried out nor were these phases identified since their investigation did not form the scope of this research.

Recommendations

- Complete study of the processes responsible for komatiites deposits in the Onverwacht Group and any association to the Bon Accord oxide samples and its host rocks

- The complete elemental comparison of the sulphide layer data (ANL samples) with Bon Accord oxide sample information to distinguish any similarities and/or differences through sulphide mineralisation studies.

- To further ascertain the true geological properties of the Bon Accord oxide samples, further isotope analysis is required for better understanding of the Bon Accord oxide samples. Sulphur and oxygen isotopes analysis can be used to assess the origin of sulphur and metal carrying fluids.

- Geochemical and mineralogical analyses of the phases identified as unknown in this research which might assist to better understand, delineate and distinguish the Bon Accord oxide samples.

Acknowledgements

This research was made possible through the funding of Inkaba ye Afrika. I am therefore very grateful to Inkaba ye Afrika for affording me the chance to pursue my dream of completing a Masters Degree in Science. Without their support this dream would not have been possible.

I would like to say thank you to my supervisor Professor Marian Tredoux for her constant support, encouragement and confidence in me throughout this research. I am dearly indebted to Professor Marian Tredoux for her helpful discussions and constructive comments during the preparation of this thesis.

I would like to say special thank you to Dr. Freddie Roelofse for his comments and questions which were beneficial in my completion of this research. I am also grateful to Exxaro Resources Ltd for giving me time off whenever I needed to go and attend to the needs of this research to make it a success.

To all my friends, who always encouraged me to thrive on even when times seemed difficult and against my cause, I say plenty thank you.

To everyone else who had a hand in my completing my Masters Degree I say thank you very much for believing in me and supporting my dreams. Special thanks to Mr. Andries Felix for providing the final versions of several figures and for assisting with the final collation of the document.

Finally I thank God for giving me the strength and courage to continue even when situations were tough and light seem to be dimming a little, God always made way and shone his light even brighter. Thank you Lord!

References:

Albers, M and Christensen, U.R. (1996). The excess temperature of plumes rising from the core-mantle boundary, Geophysical Research Letters, 23, no. 24, pp. 3567-3570.

Anderson, D.L. (1977). Composition of the mantle and core, Annual Review of Earth and Planet Sciences, 5, pp. 179-202.

Arndt, N and Lesher, C. M. (2004). Komatiite. Encyclopedia of Geology, Elsevier, pp. 260-268.

Balaram, V., Singh, S. P., Satyanarayanan, M. and Anjaiah, K. V. (2013). Platinum group elements geochemistry of ultramafic and associated rocks from Pindar in Madawara Igneous Complex, Bundelkhand massif, central India, Journal of Earth System Science, 122, pp. 79-91.

Bastin, E.S. (1957). Interpretation of ore textures, New Yrok: Geological Society of America.

Brandl, G., Cloete, M. And Anhaeusser, C.R. (2006). Archaean Greenstone Belts, in Johanson, M.R., Anhaeusser C.R. and Thomas., R.J. (eds.) The geology of South Africa, Johannesburg: Geological Society of South Africa.

Campbell, I.H and Barnes, S.J. (1984). A model for the geochemistry of the platinum-group elements in magmatic sulfide deposits, Canadian Mineralogist, 22, pp. 151-160.

Chadima, M. (2011). Application of magnetic susceptibility as a function of temperature, field and frequency, Latinmag letters, special issue, 1, Proceedings tandil, Argentina.

Condie, K.C. (1981). Developments in PreCambrian geology: Archean Greenstone Belts, Amsterdam-Oxford-New York, Elsevier scientific publishing company.

De Waal, S.A. (1969). Nickel minerals from Barberton, South Africa: I. ferroan trevorite, the American mineralogist, 54, July-August, pp. 1204-1208.

De Waal, S.A. (1970a). Nickel minerals from Barberton, South Africa: II. Nimite, a nickel rich chlorite, the American mineralogist, 55, January – February, pp. 18-30.

De Waal, S.A. and Calk, L.C. (1973). Nickel minerals from Barberton, South Africa: VI. Liebenbergite, a nickel olivine, the American mineralogist, 58, April, pp. 733-735.

De Waal, S.A. (1978). The Nickel deposit at Bon Accord, Barberton, South Africa-A proposed palaeometeorite: Mineralization in metamorphic terranes, geological society of South Africa, special publication, 4, pp. 87-98.

De Wit, M. J. (1991). Archaean greenstone belt tectonism and basin development: Some insights from the Barberton and Pietersburg greenstone belts, Kaapvaal Craton, South Africa, Journal of African Earth Sciences, 13, pp. 45-63.

De Wit, M.J, Hart, R.A. and Hart, R.J. (1987). The Jamestown Ophiolite Complex, Barberton mountain belt: a section through 3.5 Ga oceanic crust, Journal of African Earth Sciences, 6, pp. 681-730.

De Wit, M. J., and Tredoux, M. (1988). PGE in the 3.5 Ga Jamestownite Ophiolite Complex, Barberton Greenstone Belt, with implications for the PGE distribution in simatic lithosphere, in Prichard, H. H., Potts, P. J., Bowles, J. F. W., and Cribb, S.J. (eds.) Geo-Platinum, Elsevier publishers, 87, pp. 319 – 341.

De Wit, M.J., Furnes, H. and Robins, B. (2011). Geology and tectonostratigraphy of the Onverwacht Suite, Barberton Grenstone Belt, South Africa. Pre-Cambrian Research, in press, pp. 1-26.

Dick, H.J.B. (1974). Terrestrial nickel-iron from the Josephine peridotite, its geologic occurrence, associations and origins, Earth Planet. Sci. let, 24, pp. 291-298.

Echeverria, L. M. (1980). Tertiary or Mesozoic komatiites from Gorgona Island, Colombia: Field relations and geochemistry, Contributions to Mineralogy and Petrology, 73, pp. 253-266.

Economou-Eliopoulos, M., and Paraskevopoulos, G.M. (1989). Platinum-group elements and gold in komatiitic rocks from the Agrilia Formation, Othrys ophiolite complex, Greece, Chemical Geology, 77, pp. 149-158.

Eggins, S.M., Rudnick, R.L. and McDonough, W.F. (1998). The composition of peridotites and their minerals: a laser-ablation ICP–MS study, Earth and Planetary Science Letters, 154, pp. 53-71.

Evans, C. A and Girardeau, Jacques. (1988). Galicia margin peridotites: undepleted abyssal peridotites from the north Atlantic, Proceedings of the Ocean Drilling Program, Scientific Results, 103, pp. 195-207.

Farnetani, C. G. (1997). Excess temperature of chemical stratification mantle plumes: The role of across D", Geophysical Research Letters, 24, pp. 583-1586.

Fruh-Green, G.L., Connolly, J.A.D., Plas, A. (2004). Serpentinisation of oceanic peridotites: Implications for geochemical cycles and biological activity, Geophysical Monography Series, 144, pp. 119-136.

Furnes, H., de Wit, M. and Robins, B (2013). A review of new interpretations of the tectonostratigraphy, geochemistry and evolution of the Onverwacht Suite, Barberton Greenstone Belt, South Africa, Gondwana Research, 23, pp. 403-428.

Hamblin, W.K. and Christiansen, E.H. (2003). Earth's dynamic systems, 10th edition, Prentice Hall, pp. 816.

Hauri, E.H., Whitehead, J.A. and Hart, S.R. (1994). Fluid dynamic and geochemical aspects of entrainment in mantle plumes, Journal of Geophysical Research, 99, pp. 24275-24300.

Herzberg, C. (1992). Depth and degree of melting of komatiites, Journal of Geophysical Research, 97, pp. 4521-4540.

Hofmann, A. W. (1988). Chemical differentiation of the Earth: the relationship between mantle, continental crust, and oceanic crust, Earth and Planetary Science, 90, pp. 297 – 314

Holmes, A. (1930). Petrographic methods and calculations, Indiana University, Thomas Murby & Company.

Hyndman, R.D. and Peacock, S.M. (2003). Serpentinization of the forearc mantle, Earth and Planetary Sciences Letters, 212, pp. 417-432.

Ita, J. and Stixrude, L. (1992). Petrology, elasticity and composition of the mantle transition zone, Journal of Geophysics, 97, pp. 6849-6866.

Jagoutz, E., Palme, H., Baddenhausen, H., Blum, K, Cendales, M., Dreibus, G., Spettel, B., Lorenz, V. and Wank, H. (1979). The abundance of major, minor and trace elements in the earth's mantle as derived from primitive ultramafic nodules, 10th Lunar and Planetary Science Conference, pp. 2031-2050.

Jones, A.P., Price, G.D., Price, N.J., DeCarli, P.S and Clegg, R.A. (2002). Impact induced melting and the development of large igneous provinces, Earth and Planetary Sciences, Letters, 202, pp. 551-561.

Keenan, J. (1986). The Bon Accord nickel sulphide deposit, Barberton greenstone belt, Geological Society of South Africa, I, pp. 281-285.

Knoche, R., Angel, R.J., Seifert, F. and Fliervoet, T.F. (1998) Complete substitution of Si for Ti in titanite Ca(TiSi)SiO5, American Mineralogist, 83, pp. 1168–1175.

Lide, D.R. (1997). Abundance of elements in the Earth's crust and sea. In: CRC handbook of physics and chemistry, 78th edition: Boca Raton, Florida, CRC Press, pp. 14.

Lodders, K. (2003). Solar system abundances and condensation temperatures of the elements, The Astronomical Journal, 591, pp. 1220-1247.

Lyubetskaya, T and Korenaga, J. (2007). Chemical composition of earth's primitive mantle and its variance: 1. Method and results, Journal of Geophysical Research, 112, pp. 1-21.

Maier, W.D., Roelofse, F. and Barnes, S.J. (2003). The Concentration of the Platinum-Group Elements in South African Komatiites: Implications for mantle sources, melting regime and PGE fractionation during crystallization, Journal of Petrology, 44, pp. 1787-1804.

Malitch, K.N., Thalhammer, O.A.E., Knauf, V.V. and Melcher, F (2003). Diversity of platinum-group mineral assemblages in banded and podiform chromitite from the Kraubath ultramafic massif, Austria: evidence for an ophiolitic transition zone. Mineralium Deposita, 38, pp. 282–297.

McDonough, W.F. and Sun, S.S. (1995). The composition of the earth, Chemical Geology, 120, pp. 223-253.

McDonough, W.F. (2001). The composition of the earth. In R. Teisseyre and E. Majewski (eds) Earthquake thermodynamics and phase transformations in the earth's interior. Academic Press. San Diego, pp. 3-23.

McGill, I. (1997). Rare earth metals, In: F, Habashi (ed) Handbook of extractive metallurgy, Weinheim, Wiley-VCH. New York, 3, pp. 1695 – 1741.

Melcher, F and Meisel, T. (2004). A metamorphosed early cambrian crust– mantle transition in the Eastern Alps, Austria, Journal of Petrology, 45, pp. 1689–1723.

Nesse, W.D. (2004). Introduction to optical mineralogy, Oxford University Press.

Olson, P., Schubert, G and Anderson, C. (1993). Structure of axisymmetric mantle plumes, Journal of Geophysical Research, 98, pp. 6829-6844.

Pereira, M.D., Peinado, M., Blanco, J.A. and Yenes, M. (2008). Geochemical characterisation of serpentinites at cabo ortegal, Northwestern Spain, The Canadian Mineralogist, 46, pp. 317-327.

Rathore, J.S. and Heinz, H. (1980). The application of magnetic susceptibility anisotropy analyses to the study of tectonic events on the periadriatic line, 10, pp. 275-295.

Reed, S.J.B. (2005). Electron microprobe analysis and scanning electron microscopy in geology, 2nd edition. Cambridge university press.

Ringwood, A.E. (1958). The constitution of the mantle-III. Consequences of the olivine-spinel transition, Geochimica et Cosmochimica Acta, 15, pp. 195-212.

Ringwood, A.E and Kesson, S.E. (1977). Basaltic magmatism and the bulk composition of the moon II, siderophile and volatile elements in moon, earth and chondrites: implications for lunar origin, the moon, 16, pp. 425-464.

Rollinson, H. R. (1993). Using geochemical data: evaluation, presentation, interpretation, New Jersey, Pearson education, prentice hall.

Rollinson, R. H. (2007). Early Earth Systems: A Geochemical Approach, first edition, Wiley-Blackwell publishing.

Robin-Popieul, C. C. M., Arndt, N. T., C. Chauvel., G. R. Byerly., A. V. Sobolev. and Wilson, A. (2012). A new model for Barberton komatiites: Deep critical melting with high melt retention, Journal of Petrology, 53, pp. 2191-2229.

Sack, R. O. and Ghiorso, M.S (1991). Chromian spinels as petrogenetic indicators: Thermodynamics and petrological applications, American Mineralogist, 76, pp. 827-847.

Sproule, R.A., Lesher, C.M., Ayer, J.A. and Thurston, P.C. (2003). Geochemistry and metallogenesis of komatiitic rocks in the Abitibi greenstone belt, Ontario; Ontario Geological Survey, Open file Report 6073, pp. 119.

Sun, S. S. and Nesbitt, R.W. (1978). Petrogenesis of Archaean ultrabasic and basic volcanics: Evidence from rare earth elements, Contributions to Mineralogy and Petrology, 65, pp. 301-325.

Sun, S.-S. (1984). Geochemical characteristics of Archean ultramafic and mafic volcanic rocks: Implications for mantle composition and evolution, in A. KrÖner, G. N. Hanson, and A. M. Goodwin. (eds.) Archaean Geochemistry, Springer-Verlag, New York, pp. 25 -47.

Sun, S.S. (1987). Chemical composition of Archean komatiites" implications for early history of the earth and mantle evolution, Journal of Volcanology and Geothermal Research, Elsevier Science Publishers B.V, Amsterdam, 32, pp. 67-82.

Taylor, S. R and McLennan, S. M. (2008). Chemical composition and element distribution in the Earth's crust. In: Encyclopedia of Physical Sciences and Technology, Academic Press, 2, pp. 697-719.

Tredoux, M., De Wit, M.J., Hart, R.J. and Armstrong, R.A. (1989). Platinum group elements in a 3.5 Ga Nickel-Iron occurrence: possible evidence of a deep mantle origin, Journal of geophysical research, 94, pp. 795-813.

Tredoux, M., Chabangu, N., Wildau, A., Miller, D.E., Zaccarini F., Garuti, G and Madala, F. (2010). Jamestownite: a new PGE-rich rock type from the Barberton greenstone belt, South Africa, 20th general meeting of the International Mineralogical Association,6, pp. 266.

Truswell, J.F. (1977). The geological evolution of South Africa, the University of California, Purnell.

Tyrrell, G.W. (1975). The principles of petrology: An introduction to the science of rocks, London, Chapman & Hall.

Wedepohl, K.H. (1995). The composition of the continental crust. Geochim Cosmochim Acta, 59, pp. 1217-1232.

Wildau, A. (2012). An investigation of microscopic phases in the Bon Accord Ni-Oxide body, Barberton region, South Africa. Bloemfontein: University of the Free State (MSc-thesis).

Zaccarini, F., Tredoux, M., Miller, D.E., Garuti1, G., Aiglsperger, T and Proenza, J.A. (2014). The occurrence of platinum-group element and gold minerals in the Bon Accord Ni-oxide body, South Africa, American Mineralogist, 99, pp. 1774-1782.

Connexions. (2010). ICP-MS for trace metal analysis, (Online), Available: http://cnx.org/content/m34666/latest/ (04 November 2012).

United States geological survey. (2005) Search-what is ICP-MS, (Online), Available http://minerals.cr.usgs.gov/icpms/What_is_ICPMS.pdf (10 April 2013).

Appendices

Appendix A

Analytical methods description

1. Thin section preparation

Thin section preparation was carried out by a simple process of grinding a chip of rock until the desired thickness (30μm) was obtained.

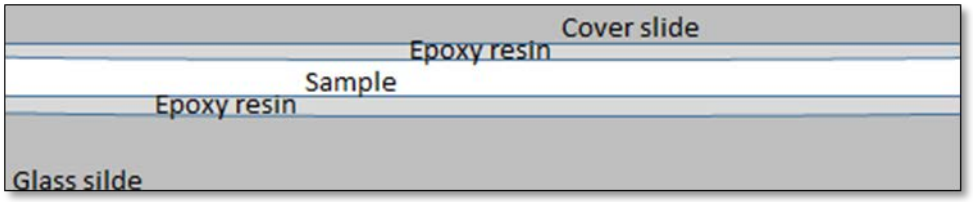

Figure 1. Preparation of thin sections.

The sample was grinded onto a flat surface using distilled water. The distilled water was used to avoid any chemical reactions that might occur. Upon completion of grinding, the sample was firstly dried, once dried the grinded surface was then mounted onto a glass slide using a 400 mesh diamond plate. An epoxy resin was then prepared together with a hardener, once the preparation of the epoxy resin was done, it was then laid onto the glass slide and the sample was added to the glass slide.

The glass slide and sample were then pressed together by hand (Fig. 1). When pressing was completed the slide was placed in a sample box to let it cure. Using distilled water the sample was mounted on the glass grinded using diamond impregnated metal wheel. It was grinded until the thickness of the sample was approximately the same as that of the glass slide. To check the desired thickness a petrographic microscope was used.

2. Microscopic analysis

2.1. Optical Microscope

Figure 2. An Olympus BX 51 microscope at the Geology Department, University of the Free State.

The Olympus BX 51 optical microscope at the Geology Department, University of the Free State (Fig. 2) was used to magnify images which were far too small to be seen by the naked eye. The optical microscope fulfils three requirements:

(a) Generate a magnified image of the object or specimen being examined

(b) Distinguish details in the magnified image

(c) Make details visible

The optical microscope gathers light from a tiny area of a thin well illuminated specimen and due to the small and spherical objective lens the microscope has a shorter focal length on either side. The image being viewed is brought to focus at a short distance within the microscope tube. The image is then magnified by a second lens called the ocular lens as it is brought to the eye. Changes in the magnification of a microscope are achieved by varying the

shape of the objective lens. A relatively flat objective lens is used in low magnification applications, while a higher magnification is achieved through the use of a more spherical objective lens.

The optical microscope uses light waves which are bent as they travel through glass, here the focus is to bend diverging light into a parallel path, then bend that parallel-path into a small focus at the eye.

3. Scanning electron microscope (SEM)

The SEM (Fig. 3) uses electron beams, to track over an object and create an exact image of the original object on a monitor. As the electron beam traces over the object it will interact with the surface object and dislodge secondary electrons from the surface of the specimen in unique patterns. The SEM forms a 3D image on a cathode-ray tube (CRT) by moving a beam of focused electrons across a sample and reads both the electrons scattered by the sample and the secondary electrons produced by the sample. The secondary electrons are then attracted by a secondary electron detector and depending on the number of electrons that reach the secondary detector, the secondary electrons will register different levels of brightness on a monitor.

SEMs have coils which are used to create a magnetic field using fluctuating voltage to manipulate the electron beam. The scanning coils are able to move the beam precisely back and forth over a defined section of an object. The SEM allows for a large amount of sample to be in focus at one time because of its large depth of field. Due to the high resolution images produced by the SEM, closely packed features can be examined at a high

magnification. Sample preparation is easy because most SEMs require that the sample be conductive.

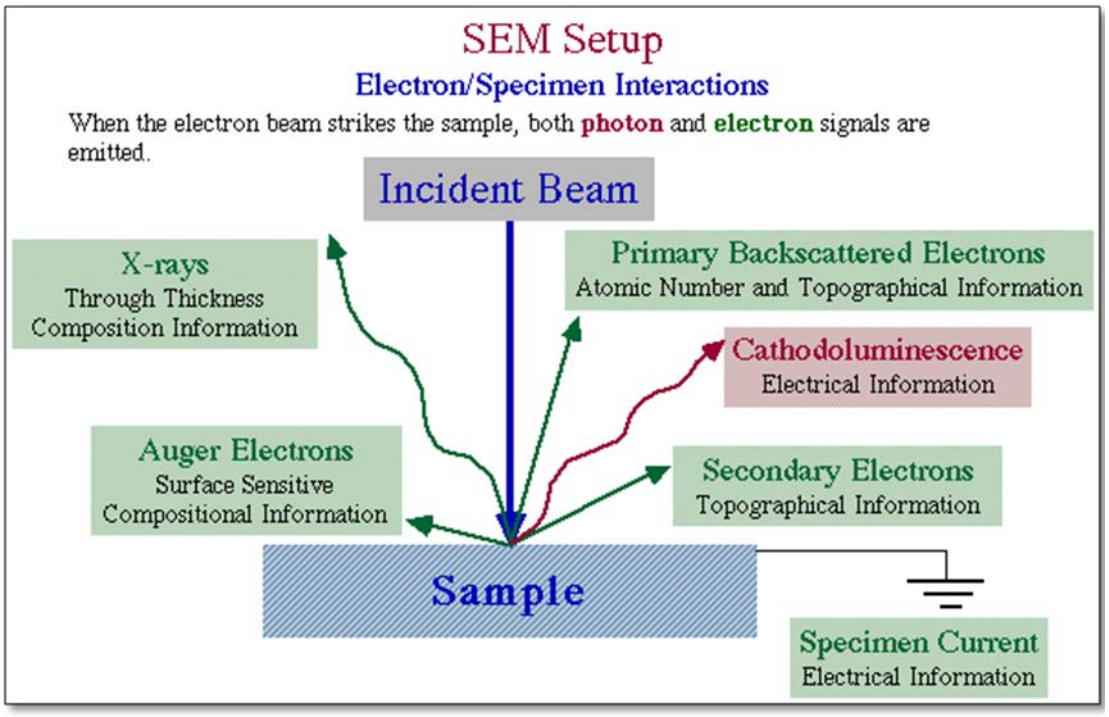

Figure 3. Shows how a SEM is set-up.

Semi-quantitative results were obtained for the BA host rock, NCL and Kraubath samples with results cumulating to 100% while the BA oxide samples were measured using the nickel standard: Nickel Silicide and results cumulating to 100%. The SEM was used as an aid in the identification of rare mineral phases and it was preferred due to its application of non-destructive analyses on solid surfaces, therefore preserving the sample.

The non-destructive method creates an electron beam in an electron source: a hot cathode containing a tungsten filament will be heated and in the process emit electrons, which will become accelerated in an electrical field of 20kV (electrical field of the SEM in the Geology department at the UFS). The electron beam is scanned over an object and creates an exact image of the original object on the screen for viewing purposes.

4. Electron microprobe analysis (EMPA)

An electron microprobe (Fig. 4) analyses material by bombarding it with an accelerated and focused electron beam. The incident beam has sufficient energy to liberate both, atoms and energy from the sample. These electron sample interactions will mainly liberate heat, but they also yield both derivative electrons and x-rays. X-ray generation is produced by inelastic collision of the incident electrons with electrons in the inner shells of atoms in the sample. When an inner shell electron is ejected from its orbit, it leaves a vacancy and shed some energy in doing so. Therefore the x-rays produced are characteristic of a specific element. This technique is used for chemically analysing small selected areas of solid samples, in which the x-rays are excited by a focused electron beam (Reed 2005).

Figure 4. Joel JSM 5410 EMPA at the Geology Department at the University of Johannesburg.

Quantitative analysis are then obtained by identifying the lines from their wavelengths because the x-ray spectrum contains lines characteristic of the elements present. The concentrations of the elements are determined through a quantitative measure by comparing the intensities of the elements present in the x-ray spectrum with those emitted from the standard samples.

5. Whole rock geochemistry

5.1. Fusion discs

To produce fusion discs, the weathering on samples was removed by a scrapper and rock grinder. Once weathering was removed, the rock samples were then crushed and milled to produce a homogenised powder to eliminate texture effects. The milled powder was weighed using a Precisa BJ 6100D balance and then dried in an oven furnace at temperatures of 110ºC for 24 hours. After 24 hours it was weighed again to determine the adhesive water lost. It was then roasted for a further 4 hours at 1000ºC and weighed again to determine the loss on ignition (LOI). From the roasted powder fusion discs were produced for the analysis of major elements. The unusual chemistry of BA oxide made the production of fusion discs to deviate from the normal method used for fusion discs for major element analysis by XRF. Fusion discs were produced from a mixture of 1.5g Li-metaborate and Li-tetraborate (fluxes) together with 0.21g of milled sample plus 0.7 SiO2 and 0.02g of sodium nitrate which added up to 2.43g in total.

5.2. Pellets

Pellets for trace element analysis were produced using methods similar to those employed in the preparation of fusion discs. From the homogenised powder, pellets were pressed from 8g of crushed and milled sample mixed with 3g of Hoechst wax and this mixture was then shaken in the Griffin flask shaker for ±5 minutes which allowed the mixture to thoroughly mix for the production of reliable pellets for the analysis of trace elements.

6. X-Ray Fluorescence (XRF)

The XRF was used for the analysis of major and trace elements. The use of XRF is made possible by the behaviour of atoms when they interact with radiation. This technique is used for chemically analysing small selected areas of solid samples, in which the x-rays are excited by a focused electron beam (Reed, 2005). Quantitative analyses were obtained by identifying the lines from the wavelengths of the solid samples since the x-ray spectrum contains lines characteristic of the elements present. The concentrations of the elements are determined through a quantitative measure by comparing the intensities of the elements present in the x-ray spectrum with those emitted from the standard solid samples (field samples).

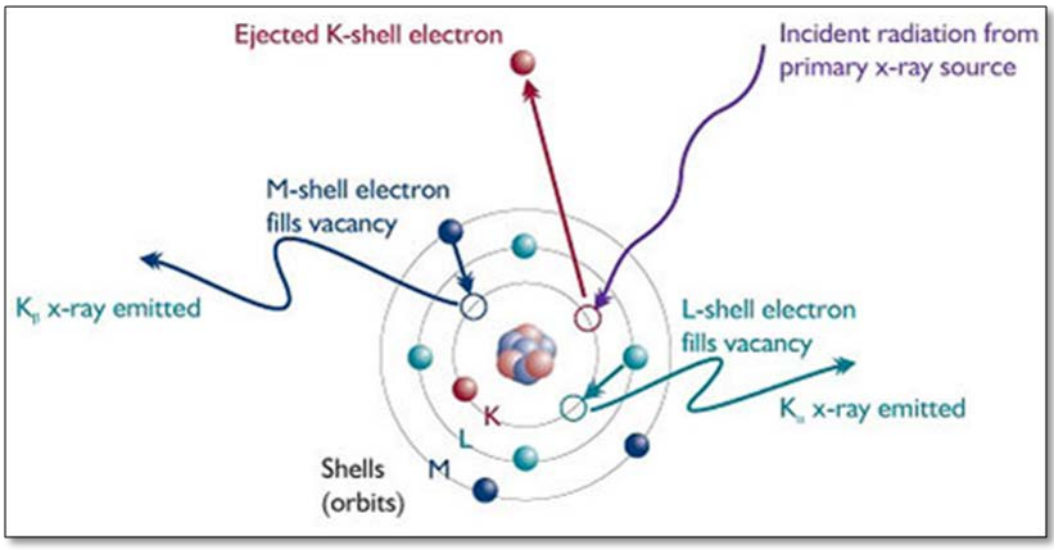

Figure 5. Principles of X-Ray fluorescence.

The principles of XRF are based mainly on the understanding of the structure of an atom. The nucleus of an atom is made up of both positively charged particles called protons and electrically neutral particles called neutrons and orbiting around the nucleus are negatively charged electrons. Electrons can have different orbits, called shells, which are appropriately

labelled starting with K, L, M, etc. (Fig. 5). When a sample is illuminated by an intense x-ray beam (Fig. 6 and Fig. 7), known as the incident beam, some of the energy is scattered and some energy is absorbed within the sample depending on the chemistry of that sample. During the illumination of the sample by the primary incident x-ray beam, the sample is said to be excited. Therefore the excited sample, in turn emits x-rays along a spectrum of wavelengths characteristic of the types of atoms present in the sample.

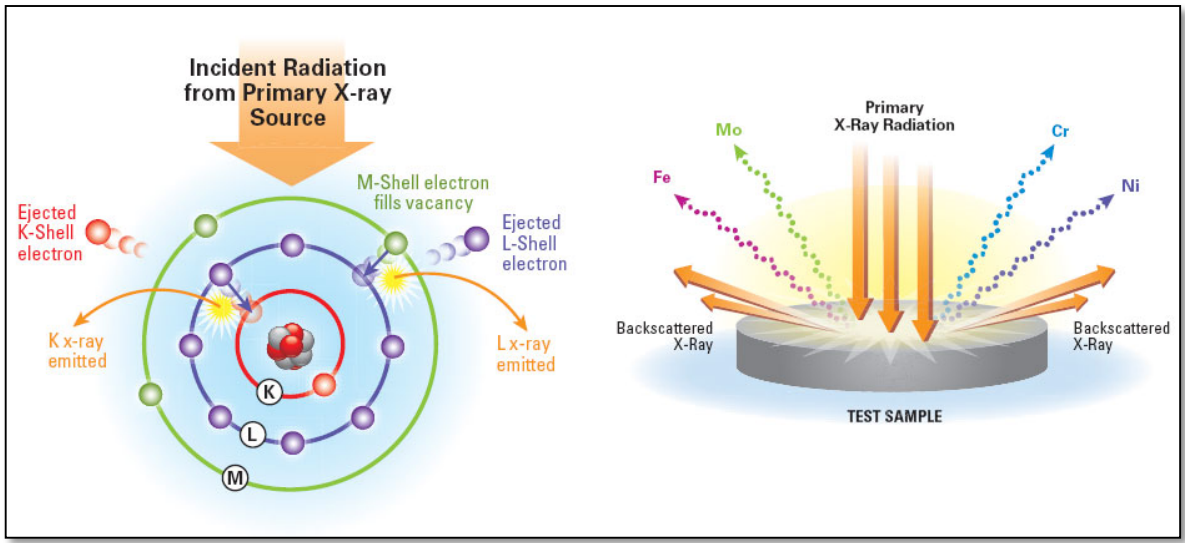

Figure 6. Complex functions of X-Ray fluorescence.

The atoms in the sample absorb x-ray energy by ionising higher electrons from the lower (usually K and L) energy levels. The ejected electrons are replaced by electrons from an outer higher energy orbital. When this occurs, the energy is released due to the decreased binding energy of the inner electron orbital compared to the outer one. This energy release is in the form of emission characteristic of x-rays indicating the type of an atom present. Various detectors are used to measure the intensity of the emitted beam. The flow counter is usually utilised for measuring long wavelength x-rays that are typical of the K spectra from elements lighter than Zn. The scintillation detector is used to analyse shorter wavelengths in x-ray

spectra (K spectra of elements from Nb to I; L spectra of elements Th and U). X-rays of intermediate wavelength (K spectra produced from Zn to Zr and L spectra from Ba and REE) are generally measured by using both detectors in tandem. The intensity of the energy measured by these detectors is proportional to the abundance of the element in the sample. Because the energy of the emitted photon is characteristic of a transition between specific electron orbitals in a particular element, the resulting fluorescent x-rays can be used to detect the abundances of elements that are present in the samples.

7. Inductively coupled plasma- mass spectrometry (ICP-MS)

The ICP-MS (Fig. 7) uses a flame technique, with flame temperatures in the range 6000-10000 K (Rollinson 1993). ICP-MS is also a solution technique and standard silicate methods are employed. The solution is introduced into the ICP-MS as an aerosol by aspirating a liquid sample into a nebuliser. Once the sample aerosol is introduced into the ICP torch, it is completely desolvated and the elements in the aerosol are converted first into gaseous atoms and then ionised towards the end of the plasma (USGS).

The inductively coupled plasma is a stream or argon atoms heated by the inductive heating of a radio frequency coil and ignited by a high frequency tesla spark (Rollinson, 1993). The sample will dissociate in the argon plasma and a large number of atomic and ionic spectral lines are excited. A range of photomultipliers will detect these spectral lines and compare them with the calibration lines and convert their intensities into concentrations.

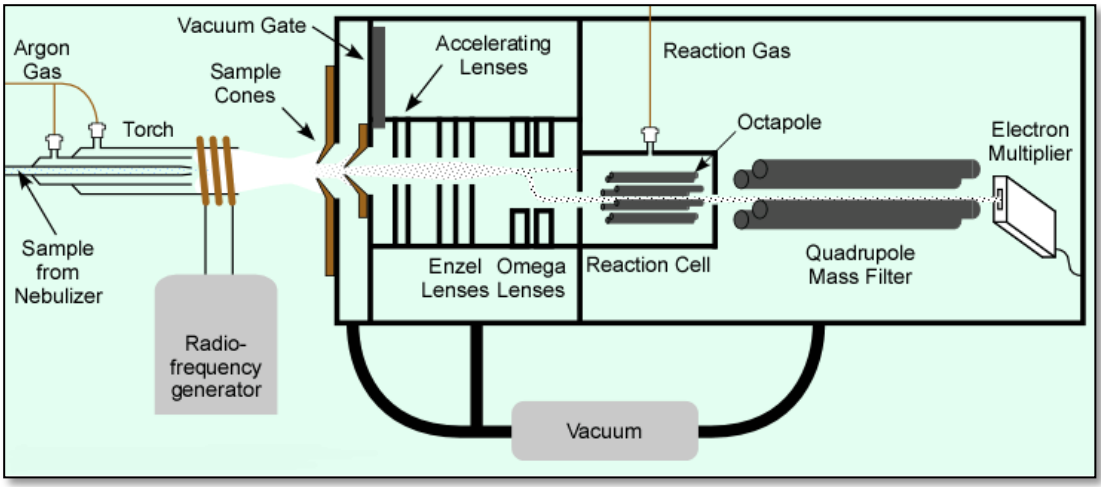

Figure 7. Sketch illustrating an ICP-MS with its components.

Once the elements in the sample have been converted into ions, they are brought into the mass spectrometer via the interface cones (Fig. 8).

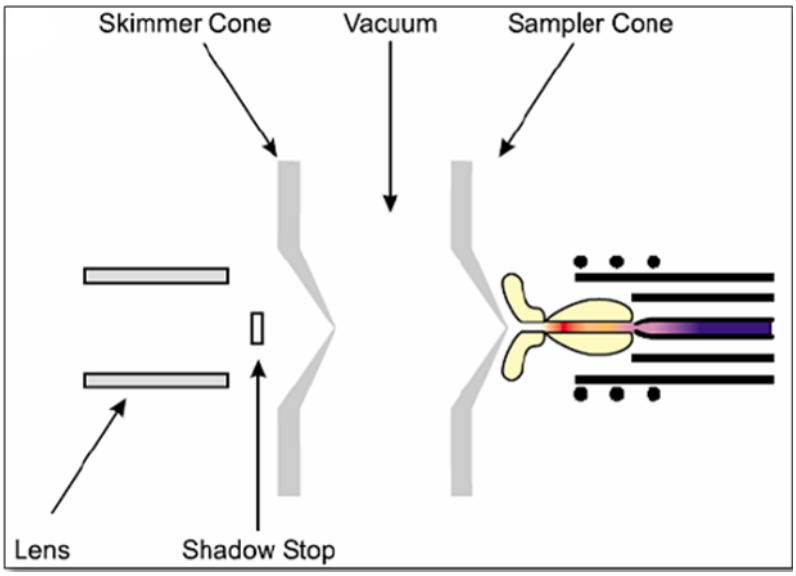

Figure 8. The interface region of the ICP-MS (from USGS).

The interface region in the ICP-MS transmits the ions travelling in the argon sample stream at atmospheric pressure (1-2 torr) into the low pressure region of the mass spectrometer (<1 x 10-5 torr). This is done through the intermediate vacuum region created by the interface

cones, sampler and skimmer. The sampler and skimmer cones were created for the purpose of sampling the center portion of the ion beam coming from the ICP torch. A small component sometimes referred to as a shadow stop in-between the two lenses blocks the photons coming from the ICP torch. The ions from the ICP source are then focused by the electrostatic lenses in the system. Due to its positive charge, the electrostatic lens, it collimates the ion beam and focuses it into the entrance aperture or slit of the mass spectrometer.

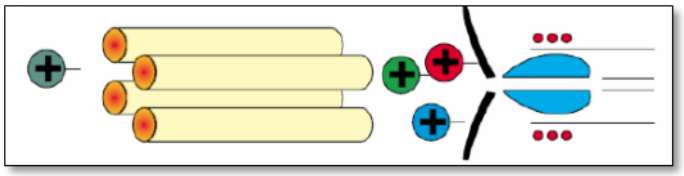

Figure 9. Quadruple mass filter (from USGS)

Once the ions have entered the spectrometer they are then separated by their mass-to-charge ratio. This is done using the quadruple mass filter (Fig. 9), basically, in the quadruple mass filter alternating AC and DC voltages are applied to opposite pairs of the rods, these voltages are then rapidly switched along with an RF-field. This results in the establishment of an electrostatic filter which will allow ions of single mass-to-charge ratio (m/e) to pass through the rods to the detector at a given instant time.

8. Susceptibility measurements

The magnetic susceptibility was measured using the hand held KT-6 magnetic susceptibility meter with an effective resolution of 1 x 10^{-5} SI units, the KT-6 meter obtains measurement by using an LC oscillator of 10 KHz which comprises a flat measuring coil located in the active face of the susceptibility meter. The intrinsic magnetic susceptibility of material is computed using the following formula χ,=J/H, where χ, is the magnetic susceptibility, J is the

magnetisation and H is the applied magnetic field strength (Rathore and Heinz, 1980). This is a second rank tensor (H) that depends only on the intrinsic properties of the magnetic material (Rathore and Heinz, 1980), such as chemical composition, grain size distribution and P/T conditions of formation. Magnetic susceptibility is a very sensitive indicator of magnetic minerals in rock or environmental samples because any slight variation in magnetic mineralogy is usually reflected by a profound change of susceptibility (Chadima, 2011).

To get measurements the hand held KT-6 susceptibility measurement meter was placed on the flat face of the sample to be measured, once the meter was removed true magnetic susceptibility measurements of the sample were displayed on the screen in SI units.

The inherent susceptibility properties were classified in three different ways ranging from diamagnetic, paramagnetic to ferromagnetic. The application of this classification is based largely on the magnetisation response of measured material to an external applied magnetic field. As a result diamagnetic materials are characterised by constant, small negative susceptibilities and are slightly affected by changes in temperature. Paramagnetic materials are characterised by constant, small positive susceptibilities, usually less than 1/1000 at room temperatures. Therefore the magnetism within the material is relatively small when compared to the external applied magnetic field.

Appendix B

Hand specimen detailed descriptions and microscopic characteristics

NC-A

Table 1. Hand specimen and petrographic table of sample NC-A

Hand specimen	***Optical microscopy descriptions***			
Fine grained	***Texture***	***Minerals***	***Modal %***	***Rock type***
	Hypidiomorphic texture	Serpentine Talc Chlorite Opaques Quartz	5 35 10 40 10	Talc schist

NC-A is greenish-grey in colour with evidence of possibly undergoing oxidation processes, supported by the rusty orange colours and it is very fine grained with an aphanitic texture with a soapy feel.

NC-B

Table 2. Hand specimen and petrographic table of sample NC-B

Hand specimen	***Optical microscopy descriptions***			
Fine - medium grained	***Texture***	***Minerals***	***Modal %***	***Rock type***
	Subhedral prismatic and almost tabular form	Serpentine Opaques Quartz Talc	10 65 5 20	Serpentinised talc schist

This is a highly oxidised weathered sample characterised by rusty yellowish - orange and greyish-red colours. It is fine - medium grained characterised by subhedral grains in parts with an aphanitic texture.


NC-B

NC-C

Table 3. Hand specimen and petrographic table of sample NC-C

Hand specimen	***Optical microscopy descriptions***			
Fine grained 	***Texture***	***Minerals***	***Modal %***	***Rock type***
	Aphanitic	Quartz Serpentine Opaques Chlorite Talc	15 5 45 10 25	Quartz talc schist

NC-C is slightly oxidised and characteristic of oxidation processes visible from rusted reddish-orange colours. It is fine crystalline and the grains are subhedral at places with an aphanitic texture.


NC-C

NC-D

Table 4. Hand specimen and petrographic table of sample NC-D

Hand specimen	***Optical microscopy descriptions***			
Medium grained	***Texture***	***Minerals***	***Modal %***	***Rock type***
	Skeletal texture	Chlorite Quartz Serpentine Talc Opaques	6 8 6 40 40	Talc schist

The extreme oxidation and weathering nature of this sample directly influenced the colours (orange, reddish and grey) observed. The texture is medium crystalline with distinct porphyritic texture. The serpentines, chlorites, talc and clay minerals have resulted in the soapy feel of the sample.


NC-D

NC-E

Table 5. Hand specimen and petrographic table of sample NC-E

Hand specimen	***Optical microscopy descriptions***			
Fine – medium grained	***Texture***	***Minerals***	***Modal %***	***Rock type***
	Porphyritic texture	Opaques Talc Chlorite Serpentine	30 45 10 15	Serpentinised talc schist

NC-E, is highly oxidised and weathered, very similar to sample NC-D. It is characterised by reddish, grey and orange oxidation and weathering colours. It is fine to medium grained, with a soapy feel due to serpentines, clay minerals, chlorites and talc within the sample.


NC-E

NC-F

Table 6. Hand specimen and petrographic table of sample NC-F

Hand specimen	***Optical microscopy descriptions***			
Fine grained	***Texture***	***Minerals***	***Modal %***	***Rock type***
	Hypidiomorphic texture	Talc Opaques Chlorite Serpentine Pyroxene	35 47 7 8 3	Serpentinised talc schist

NC-F is characterised by rusting associated with oxidation processes. It is enriched in talc, clay minerals, chlorites and serpentines and dominated by aphanitic texture.


NC-F

NC-G

Table 7. Hand specimen and petrographic table of sample NC-G

Hand specimen	***Optical microscopy descriptions***			
Coarse grained	***Texture***	***Minerals***	***Modal %***	***Rock type***
	Allotriomorphic - porphyritic	Serpentine Quartz Talc Opaques Chlorite	10 10 30 40 10	Serpentinised quartz talc schist

This sample is highly weathered and oxidised with a coarse grained texture. Like all the samples above, it feels very soapy due to the chlorite, talc, serpentines and clay minerals


NC-G

NC-H

Table 8. Hand specimen and petrographic table of sample NC-H

Hand specimen	***Optical microscopy descriptions***			
Fine - medium grained	***Texture***	***Minerals***	***Modal %***	***Rock type***
	Poikilitic texture	Liebenbergite Népouite Nimite Willemseite Opaques	2 8 15 40 35	Ultramafic rock

It is greenish-grey (dark) in its physical appearance with weathering reddish-orange colours with medium – coarse grained texture. The greenish-grey colours are as a result of the spinel/oxides, chlorite, serpentines and talc in the sample.

The soapy feel of the sample, is due to the chlorite and talc in the sample. It is highly magnetic especially in places where the opaque grains (spinel/oxides) are in abundance.

NC-J

Table 9. Hand specimen and petrographic table of sample NC-J

Hand specimen	***Optical microscopy descriptions***			
Fine - medium grained	***Texture***	***Minerals***	***Modal %***	***Rock type***
	Porphyritic - poikilitic texture	Opaques Nimite Willemseite Népouite	45 20 25 10	Ultramafic rock

The sample is greenish-grey and brownish-red in its physical appearance. The texture is Fine - medium grained. The reddish-brown colours represent oxidation reaction processes. The greenish-grey colours represent the mineral assemblages found in the sample. The sample is highly magnetic especially in places where the dark grains (spinel oxides) are in abundance.


NC-J

NC-K

Table 10. Hand specimen and petrographic table of sample NC-K

Hand specimen	***Optical microscopy descriptions***			
Medium-coarse grained	***Texture***	***Minerals***	***Modal %***	***Rock type***
	Allotriomorphic texture	Nimite Nepouite Willemseite Opaques	5 10 5 75	Ultramafic rock

NC-K is greenish-grey in its physical appearance with a medium-coarse grained texture. The greenish-grey colour is from the serpentine, talc and chlorite mineral phases found in this rock sample. The grains observed are mostly subhedral in their appearance. NC-K is highly magnetic, especially in places where the dark grains (spinel/oxides) are in abundance.


NC-K

Table 11. Hand specimen and petrographic table of sample NC-L

NC-L

Hand specimen	***Optical microscopy descriptions***			
Medium grained 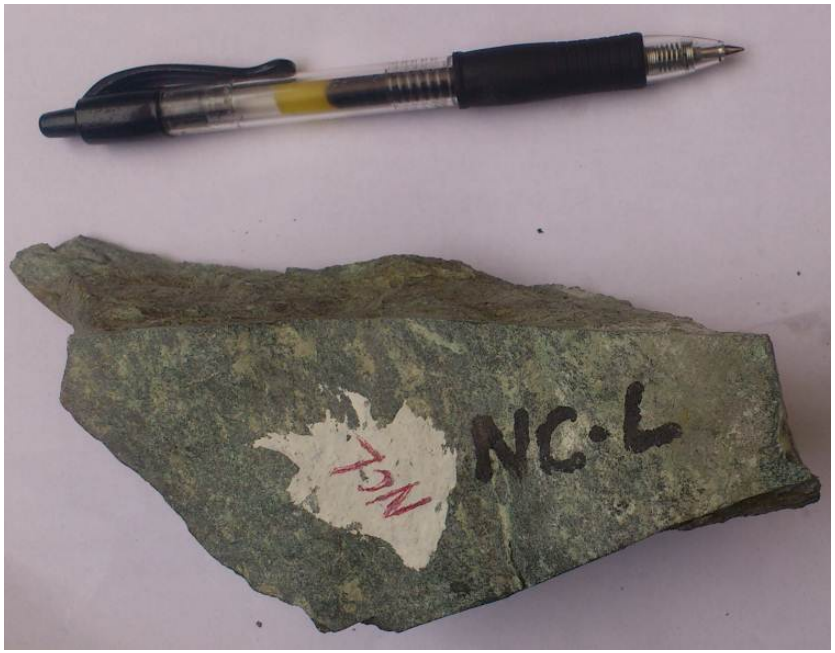	***Texture***	***Minerals***	***Modal %***	***Rock type***
	Porphyritic texture	Quartz Chlorite Talc Opaques	25 5 15 55	Quartz chlorite schist

It is greenish-grey in its physical appearance and it is largely surrounded by brass yellow and gold sulphides (pyrite) and in some places it is oxidised. It is fine to medium grained and shows an aphanitic to porphyritic texture. The soapy feel of the sample is attributed to the talc and chlorite minerals found in the sample.


NC-L

NC-MA

Table 12. Hand specimen and petrography table of sample NC-MA

Hand specimen	***Optical microscopy descriptions***			
Fine grained	***Texture***	***Minerals***	***Modal %***	***Rock type***
	Cumulate texture	Olivine Chlorite Pyroxene Opaques	65 5 <10 20	Olivine-rich ultramafic rock

The physical appearance of NC-MA is greyish in nature and it is fine grained. It is characterised by the dominant phenocrysts of olivine. Fractured olivine phenocrysts with alteration along the fracture planes together with cumulate textures are very characteristic in the thin section. The pyroxene phase occurs as the second dominant phase.


NC-MA

.

NC-NA

Table 13. Hand specimen and petrography table of sample NC-NA

Hand specimen	***Optical microscopy descriptions***			
Medium-coarse grained 	***Texture***	***Minerals***	***Modal %***	***Rock type***
	Cumulate texture	Olivine Quartz Amphibole Pyroxene Chlorite	5 20 50 15 10	Amphibolite

It is brownish grey in its physical appearance and medium-coarse grained. It is characterised by long prismatic and fibrous crystals and generally shows two directions of cleavage in the hand specimen. It is largely dominated by the amphiboles (hornblende). Quartz occurs as vein infillings.


NC-NA

UFS 38a

Sample is fresh and grey to olive green in colour, the colour is due to the serpentine minerals present in the sample, it is characterised by a medium crystalline texture.

Table 14. Hand specimen and petrography table of sample UFS 38a

Hand specimen	***Optical microscopy descriptions***			
Fine grained	***Texture***	***Minerals***	***Modal %***	***Rock type***
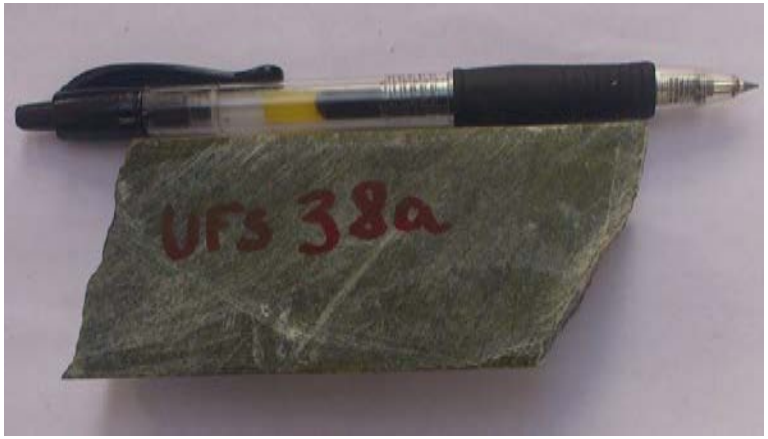				Serpentinite

No optical studies were conducted on the sample due to the unavailability of thin sections in the archives

UFS 4CS2

Table 15. Hand specimen and petrography table of sample UFS 4CS2

Hand specimen	***Optical microscopy descriptions***			
Fine – medium grained 	***Texture***	***Minerals***	***Modal %***	***Rock type***
	Cumulate texture	Opaques Quartz Pyroxene	35 55 10	Mineralised chert (sulphide chert zone)

This is a fresh sample with minimum weathering and dark grey in colour, however it does show rusty "orangish" brown colours normally characteristic of oxidation processes. It is fine – medium grained and sulphide rich such that these are visible to the naked eye, these sulphides normally occur clustered in one area of the sample.


UFS 4CS2

UFS 39a

Table 16. Hand specimen and petrography table of sample UFS 39a

Hand specimen	***Optical microscopy descriptions***			
Fine grained 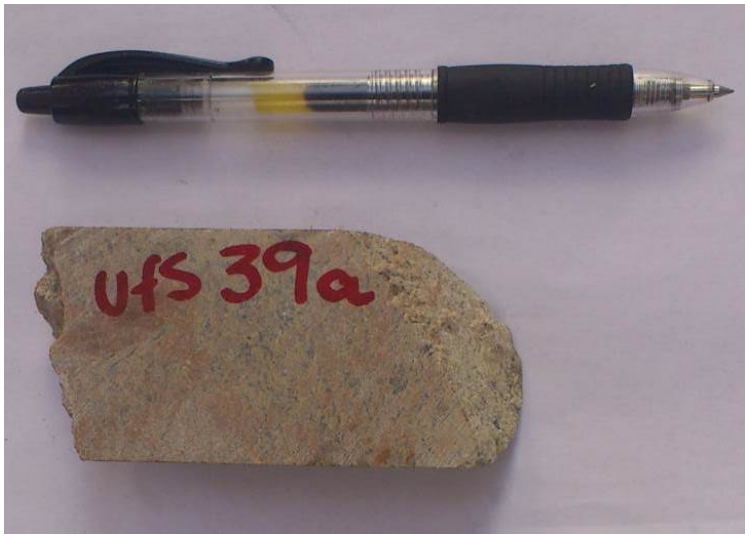	***Texture***	***Minerals***	***Modal %***	***Rock type***
	Hypidiomorphic texture	Olivine Plagioclase Pyroxene Chlorite Opaque Micas	20 15 38 2 15 10	Pyroxene schist

Relatively fresh Schistosed sample, with minor weathering with whitish - light brown to pink colours and it exhibits a fine to medium crystalline texture.


UFS 39a

UFS 16a

Table 17. Petrography table of sample UFS 16a

Hand specimen	*Texture*	*Minerals*	*Modal %*	*Rock type*
				Serpentinite

This is a relatively whitish to light green fresh sample, characterised by a medium to coarse crystalline texture. The green physical appearance of the sample is attributed to the serpentine and chlorite mineral phases present. Quartz and some minor feldspars are visible to the naked eye.

No optical studies were conducted on the sample due to the unavailability of thin sections in the archives

UFS 16c

Table 18. Hand specimen and petrography table of sample UFS 16c

Hand specimen	***Optical microscopy descriptions***			
Fine grained 	***Texture***	***Minerals***	***Modal %***	***Rock type***
	Porphyritic	Quartz Chlorite Opaque Micas	40 30 15 5	Quartz chlorite schist

Grey in its physical appearance with moderate weathering, and quartz and sulphide rich. Greenish colours are attributed to the chlorite minerals present while the sulphides appear to be mainly confined to the veins, there is also minor micas visible in the sample. The schistose foliation is characteristic of the sub-parallel to parallel orientation of platy minerals chlorite and micas present within the sample.


UFS 16c

UFS 39b

Table 19. Hand specimen and petrography table of sample UFS 39b

Hand specimen	***Optical microscopy descriptions***			
Fine grained 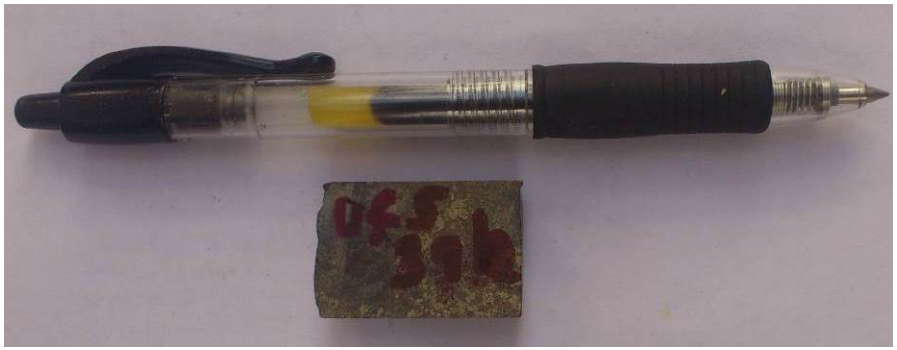	***Texture***	***Minerals***	***Modal %***	***Rock type***
	Hypidiomorphic to allotriomorphic	Pyroxene Chlorite Opaque Micas	18 20 40 2	Pyroxene chlorite schist

Grey in colour and characterised by moderate weathering, and rusty brownish and yellow oxidation colours at places. Also visible are voids together with visible sulphide grains.


UFS 39b

UFS 38e

Table 20. Petrography table of sample UFS 38e

Hand specimen	***Optical microscopy descriptions***			
Medium to coarse grained 	***Texture***	***Minerals***	***Modal %***	***Rock type***
	Porphyritic	Opaque Pyroxene Feldspar Quartz	35 45 10 10	Pyroxene quartzo-feldsphatic schist

This is a whitish to light green sample and relatively fresh, characterised by a medium to coarse grained texture. The green physical appearance of the sample is attributed to the serpentine and chlorite mineral phases present. Minor quartz and some minor feldspars are visible to the naked eye.


UFS 38e

Optical photomicrographs and descriptions of all studied thin sections

1. Bon Accord Host Rocks

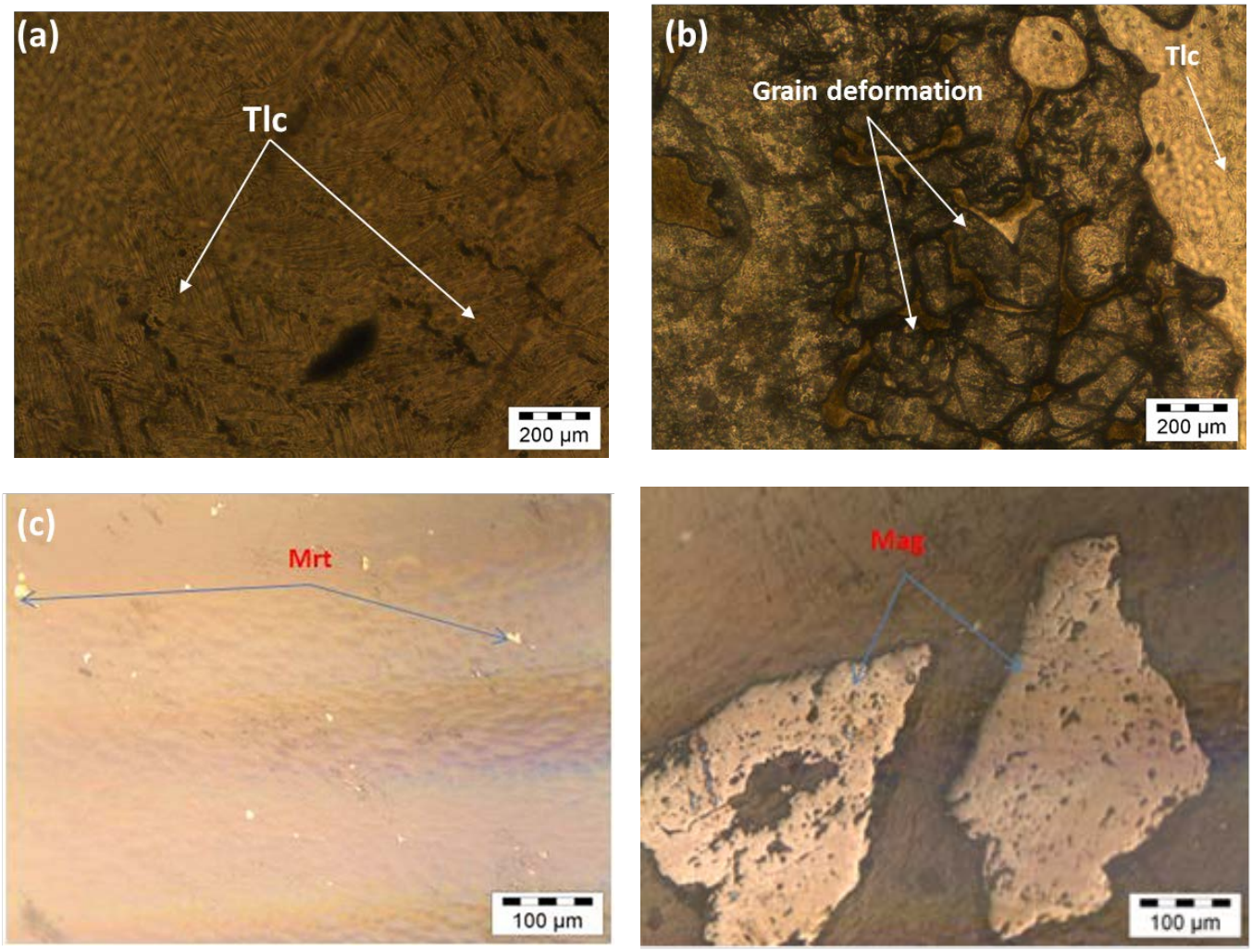

Figure 1. Photomicrograph of sample NC-A (a) Talc showing kinking texture under plane polarised light, (b) homogenous (large) deformed opaque minerals under plane polarised light, (c) Sulphide grains with characteristic bright colours under transmitted light and (d) Large granular magnetite grains characterised by an equant texture.

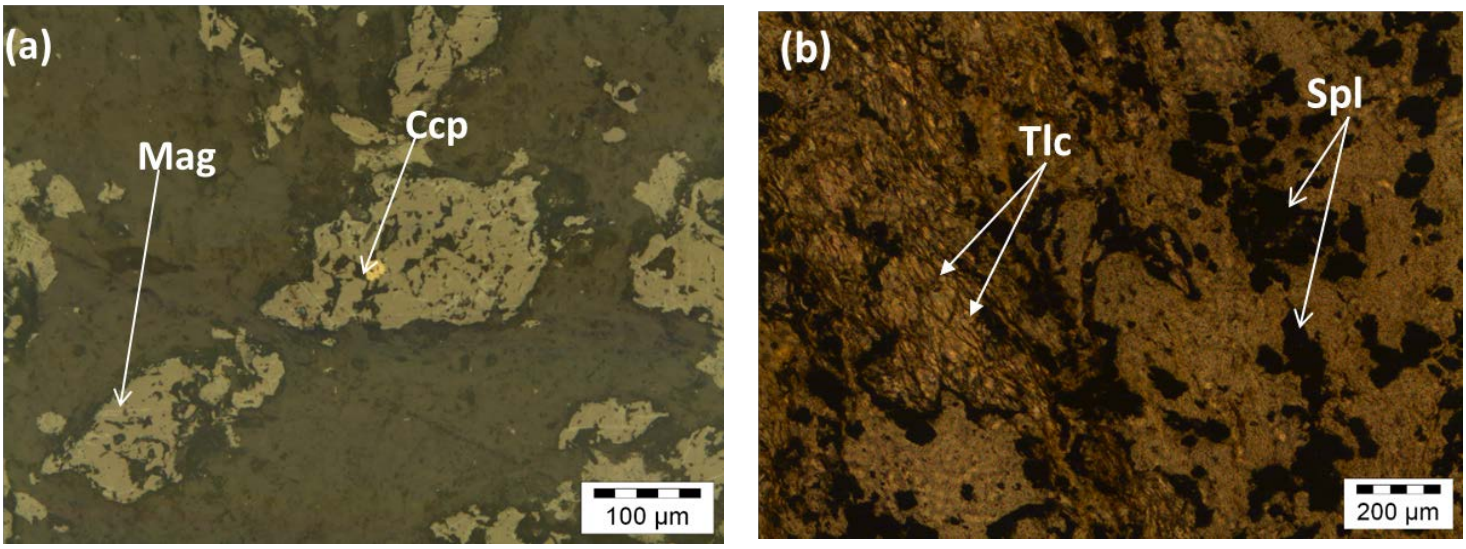

Figure 2. Photomicrographs from sample NC-B. (a) Chalcopyrite embedded in the spinel (magnetite) minerals with a porphyritic texture, observed in reflected light and (b) Irregular orientated flakes of talc, surrounded by spinel minerals, under plane polarised light, all

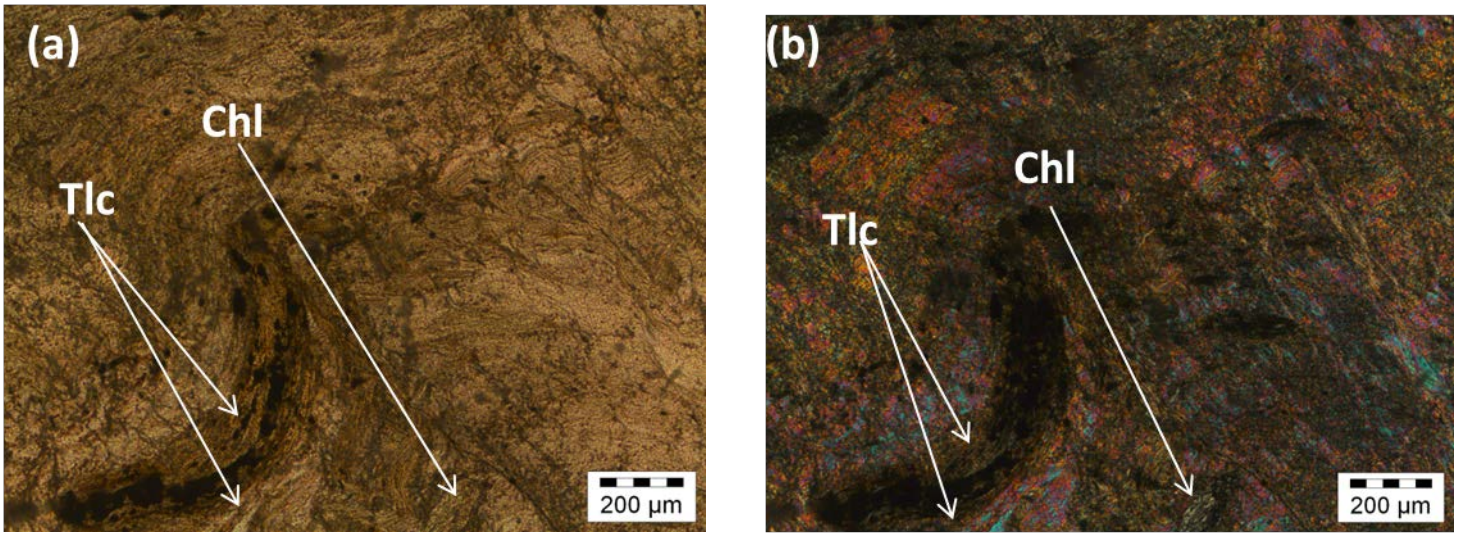

Figure 3. Photomicrographs all from sample NC-C. (a) Moderately altered talc with opaques inside exhibiting a flowing texture and (b) Crossed nicols showing chlorite in close association with the talc, observed in plane polarised light and under crossed nicols respectively.

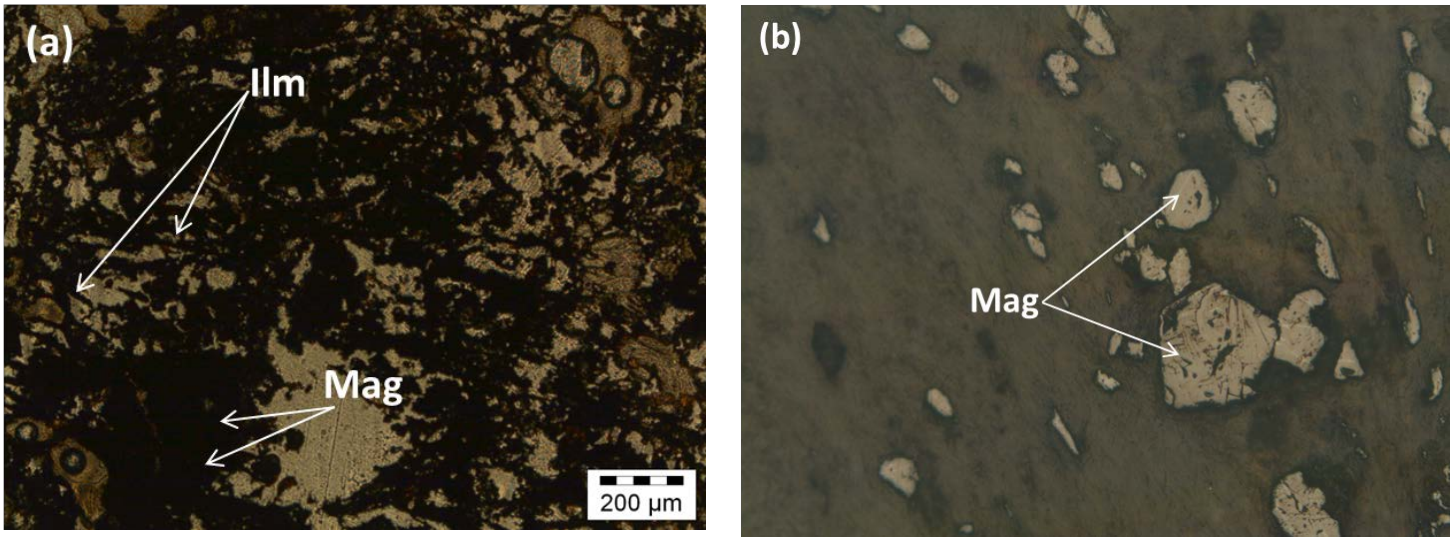

Figure 4. Photomicrographs from sample NC-D. (a) Anhedral grains of the spinel group minerals in a groundmass of talc altering to ilmenite with embedded serpentine fibers. Characterised by the skeletal texture of ilmenite and (b) Inequigranular magnetite grains in a groundmass of talc, observed in plane polarised light and reflected light respectively.

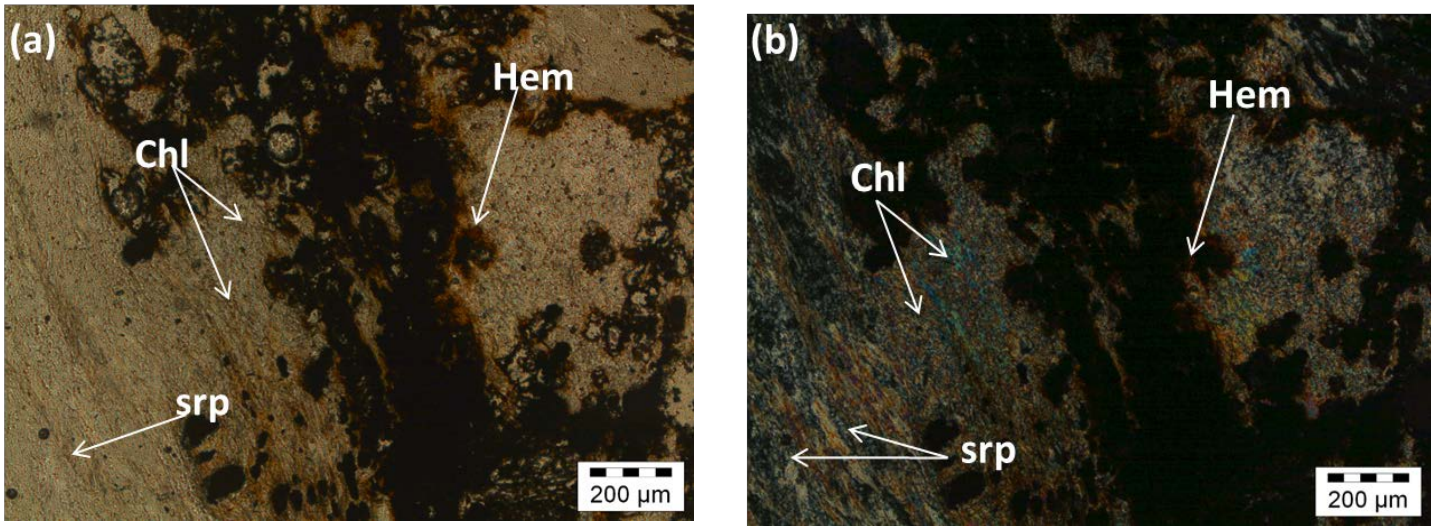

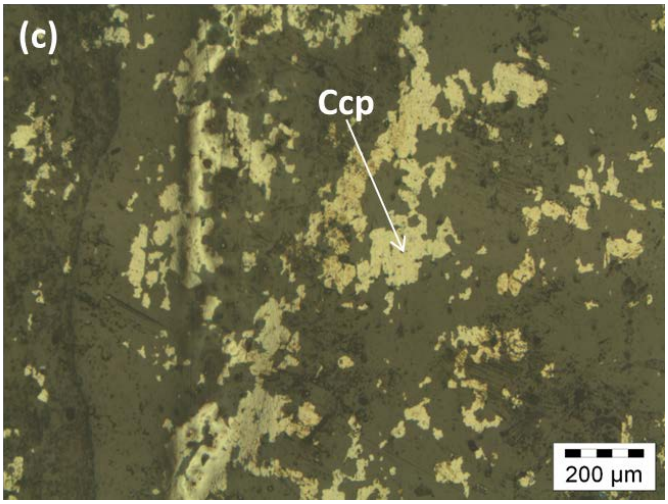

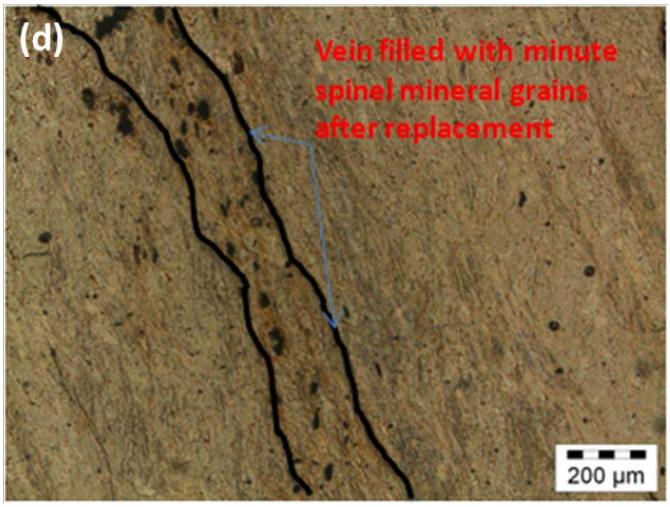

Figure 5. All photomicrographs from sample NC-E. (a) Replacement of the magnetite to goethite and hematite starting from the rim to the core in the dominant talc groundmass, also visible minute serpentine as well as chlorite, observed in plane polarised light (b) photomicrograph of (a) observed under crossed nicols, (c) Irregular anhedral chalcopyrite mineral grains under reflected light and (d) Vein filled with tiny opaque grains after replacement.

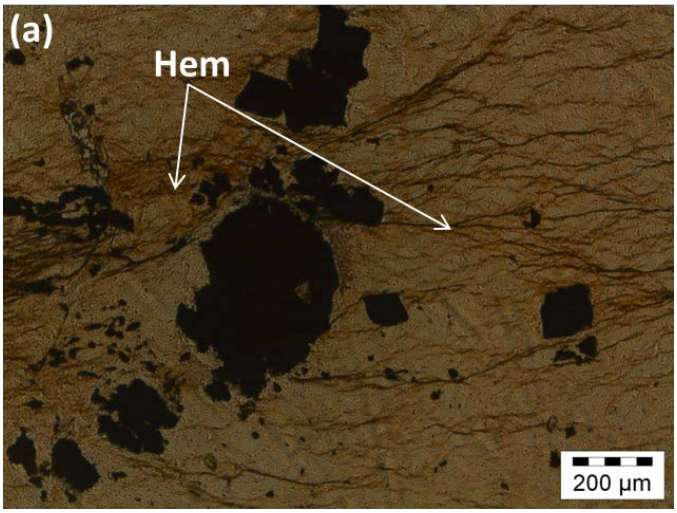

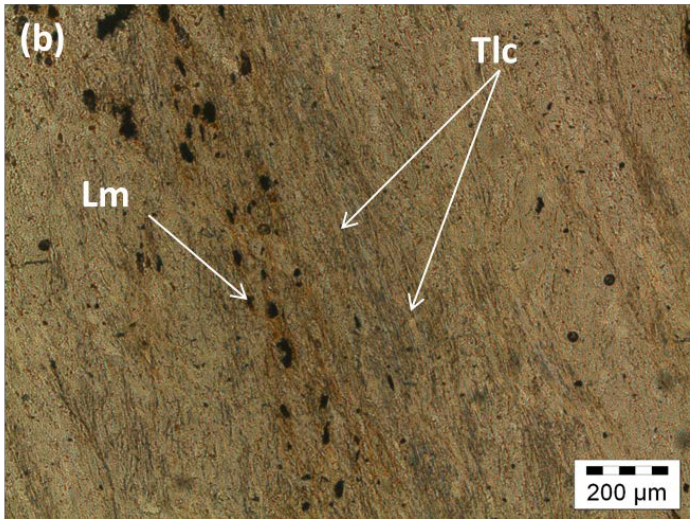

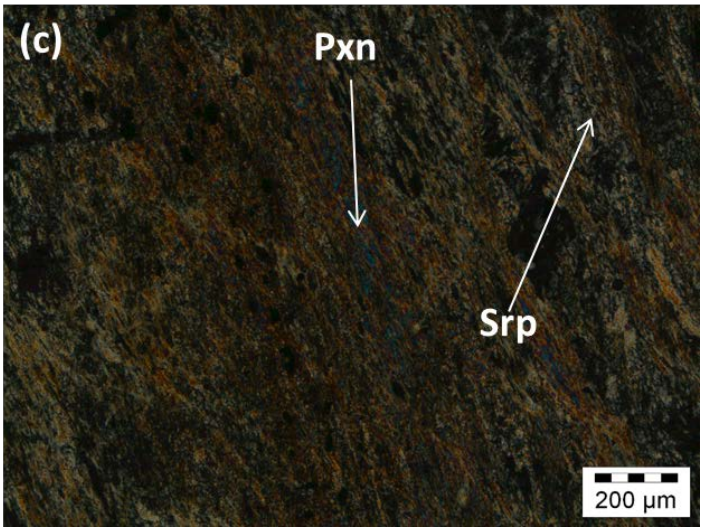

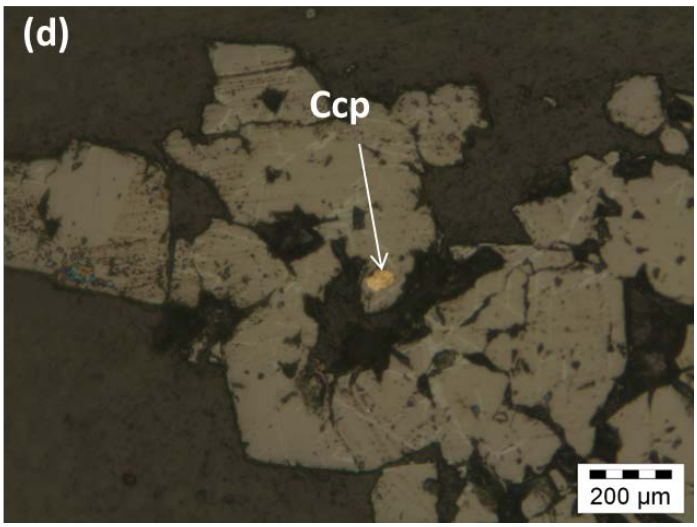

Figure 6. All photomicrographs from sample NC-F. (a) Multiple veins filled with hematite and minor goethite, an indication of late stage hematite and goethite enrichment, under plane polarised light, (b) Talc seen here as elongated grains and limonite appears to be filling cracks and altering to form magnetite, view in plane polarised light, (c) Remnant pyroxene, which is now altering to form chlorite minerals, also visible in this section is the serpentine mineral grains characterised by their very low first order interference colours, under crossed nicols and (d) Single chalcopyrite grain embedded within the irregular oxide mineral (magnetite) grains in reflected light.

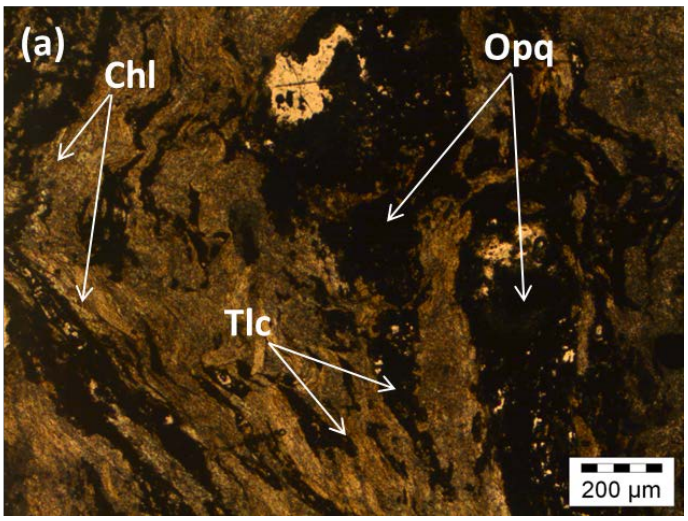

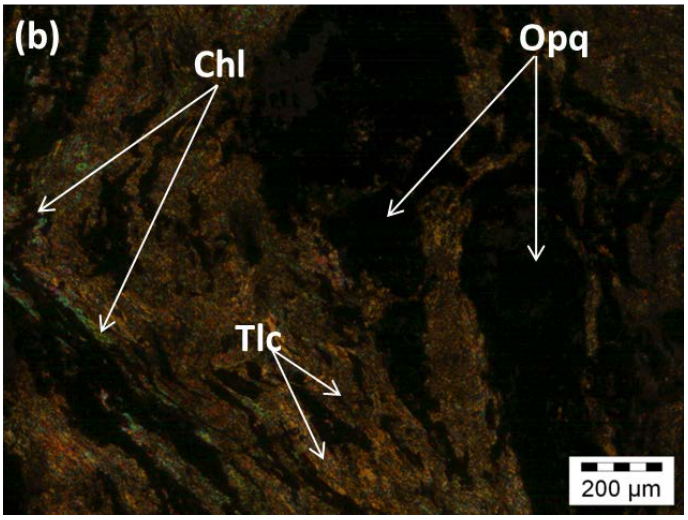

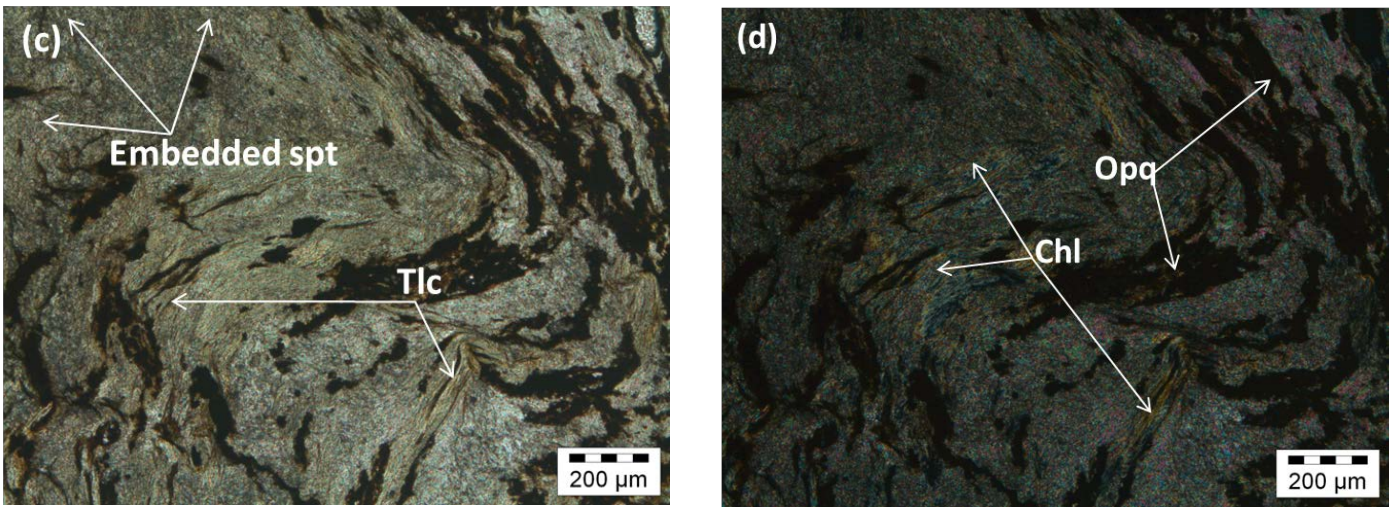

Figure 7. Photomicrographs from sample NC-G. (a) Highly altered matrix of talc, chlorite and spinel minerals. Chlorite visibility is limited by the intense alteration, view in plane polarised light and (b) Talc, chlorite and spinel mineral assemblage, viewed under crossed nicols. (c) Characterised by flowing texture of talc with spinel minerals probably indicating simultaneous growth and (d) The chevron pattern is mainly visible on the opaque minerals, view under crossed nicols, the flow pattern/texture could be an indication of micro-folding.

2. Bon Accord Oxide

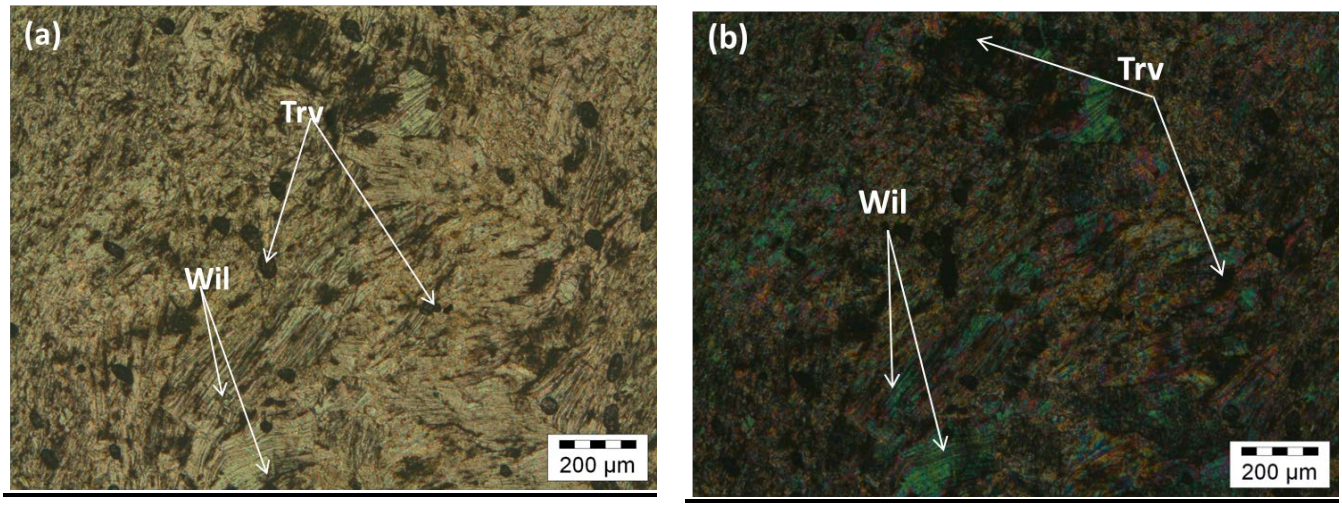

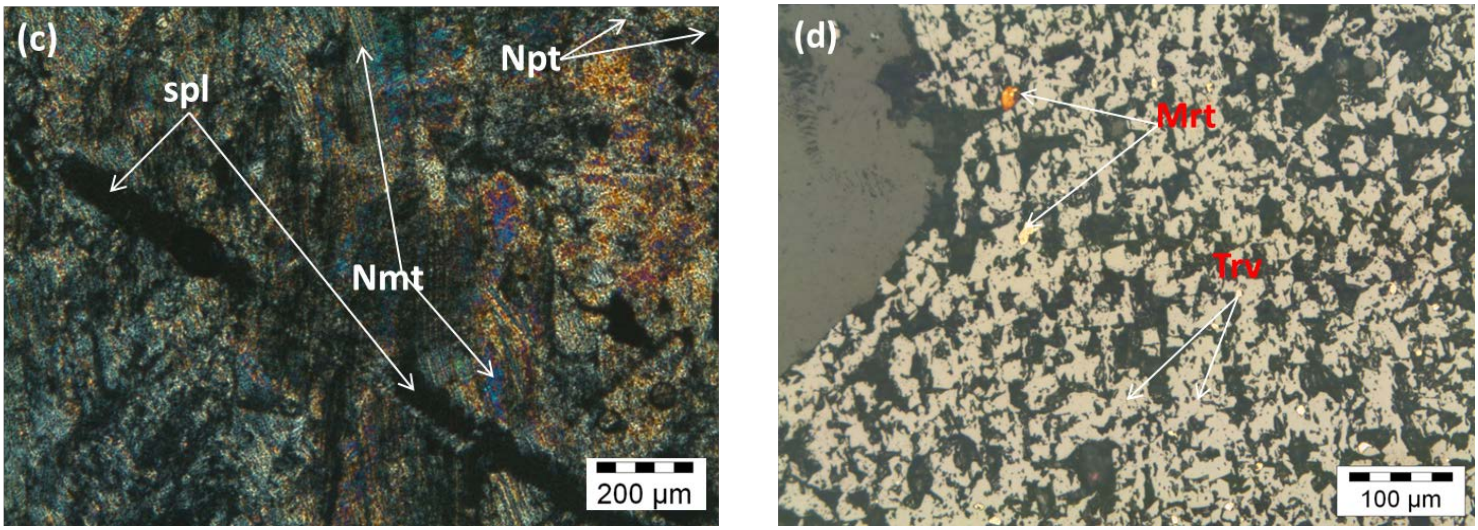

Figure 8. Photomicrographs from sample NC-H. (a) Small chlorite crystals embedded in flaky talc minerals and (b) Subhedral crystals of talc with close association of chlorite, observed under plane polarised light and crossed nicols respectively, (c) Opaque- nimite and népouite mineral assemblages, under crossed nicols and (d) Spinel minerals enclosing subhedral-anhedral sulphide grains under reflected light.

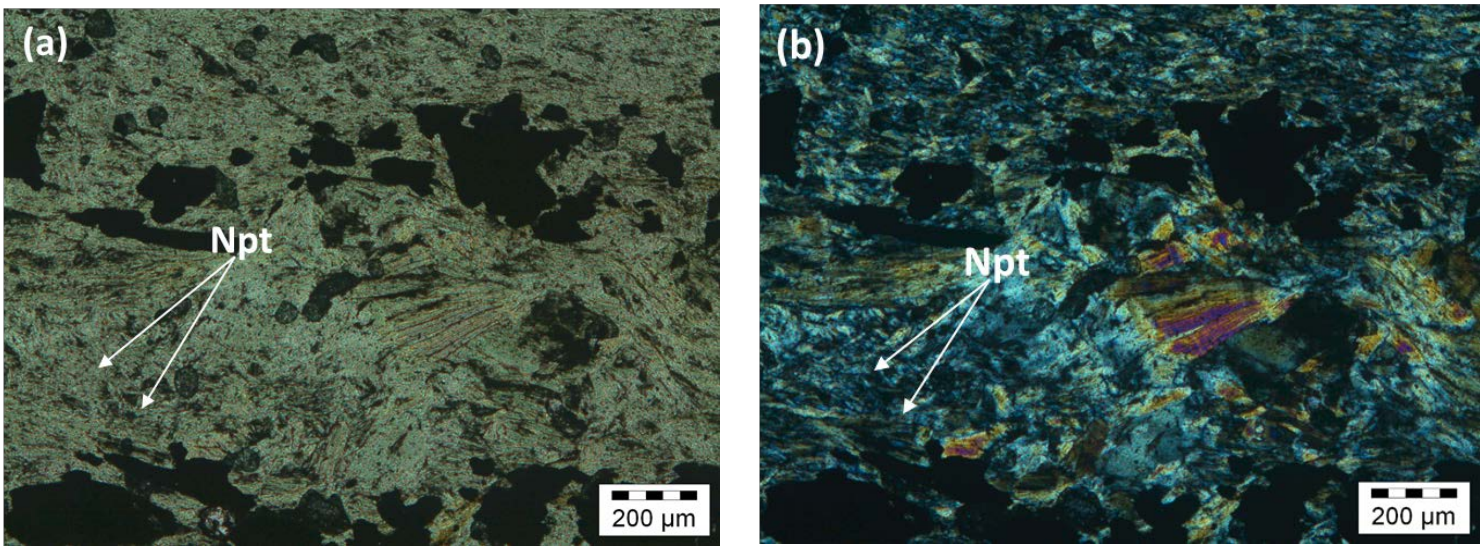

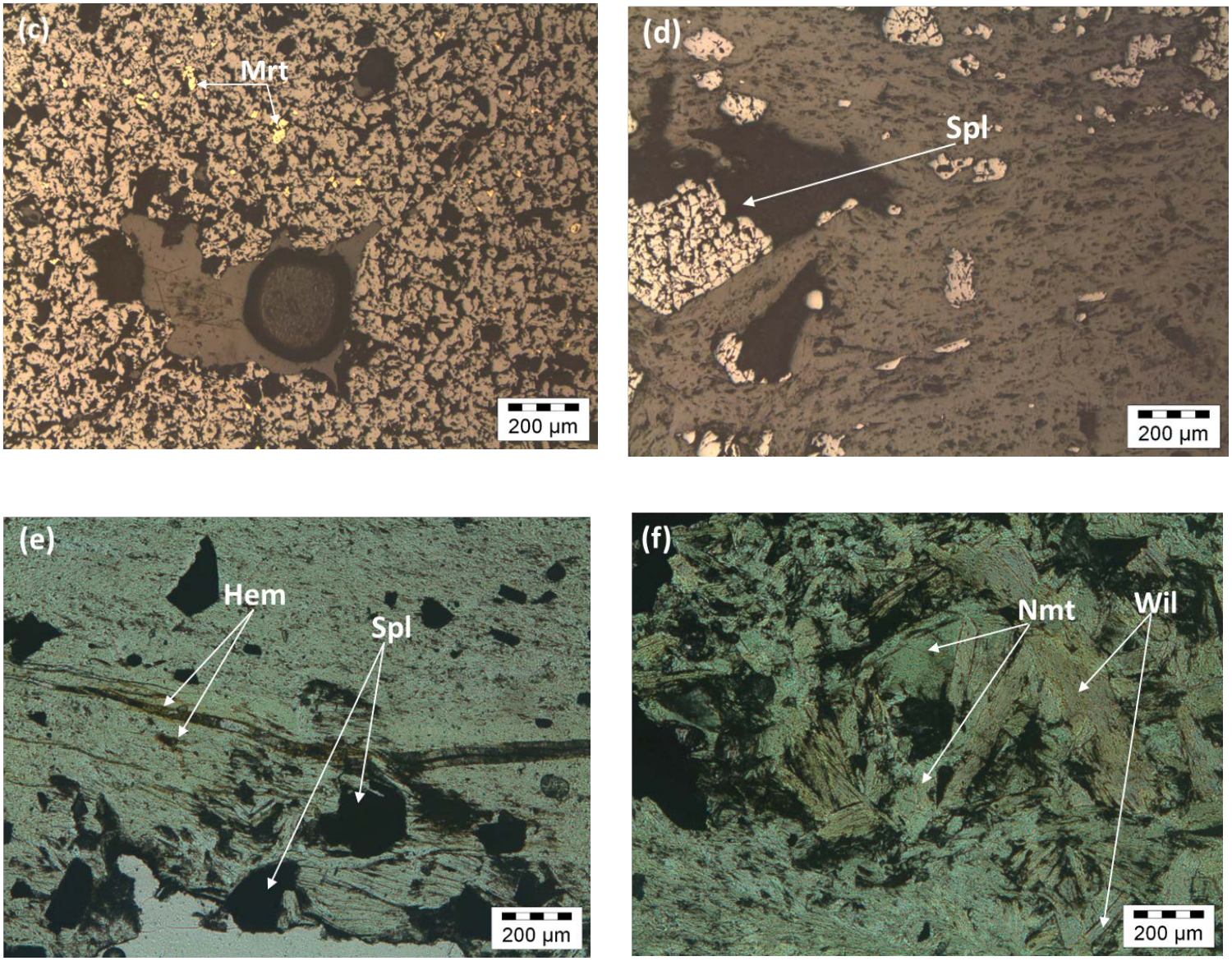

Figure 9. Photomicrographs from sample NC-J. (a) Minute népouite grains enclosed within the talc groundmass, in plane polarised light (b) Népouite showing low order colours while the talc shows high birefringent colours, under crossed nicols. (c) Inclusion of sulphide (millerite) grains inside the irregular to columnar spinel minerals, under reflected light, (d) Irregularly shaped spinel minerals characterised by replacement textures in reflected light, (e) Hematite filling pathways across the section and spinel minerals occurring as scattered irregular grains, in plane polarised light and (f) Nimite characterised by greenish colours and flaky willemseite representing a nimite-willemseite-spinel mineral assemblage.

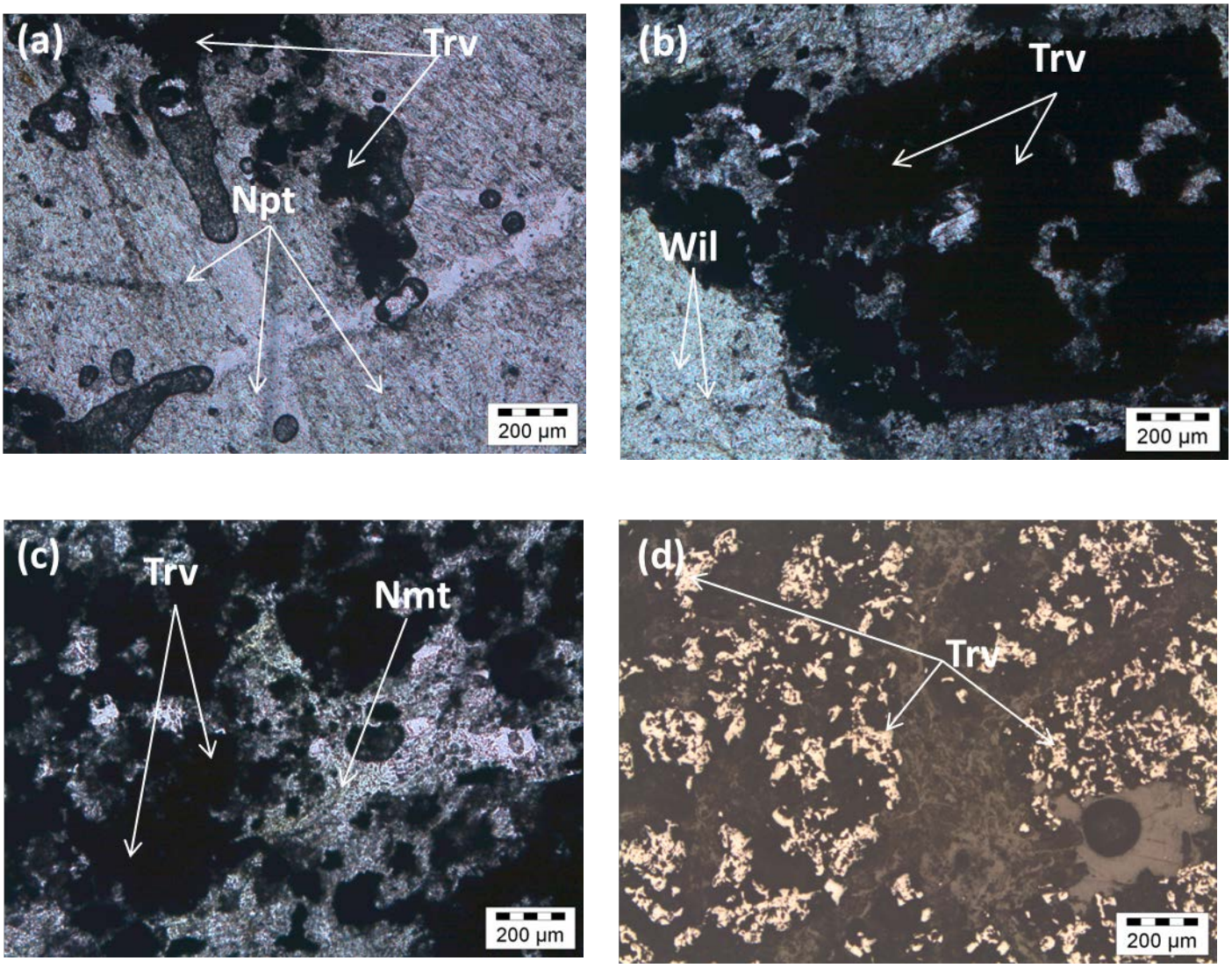

Figure 10. Photomicrographs from sample NC-K. (a) Népouite characterised by minute low order colour grains and irregular grains of willemseite with a characteristic replacement texture under crossed nicols, (b) Irregularly shaped nimite exhibiting characteristic greenish colours in plane polarised light, (c) Intense deformation of the spinel minerals under crossed nicols (d) Irregularly arranged spinel minerals, variable in size distribution.

3. Scotia Talc Mine

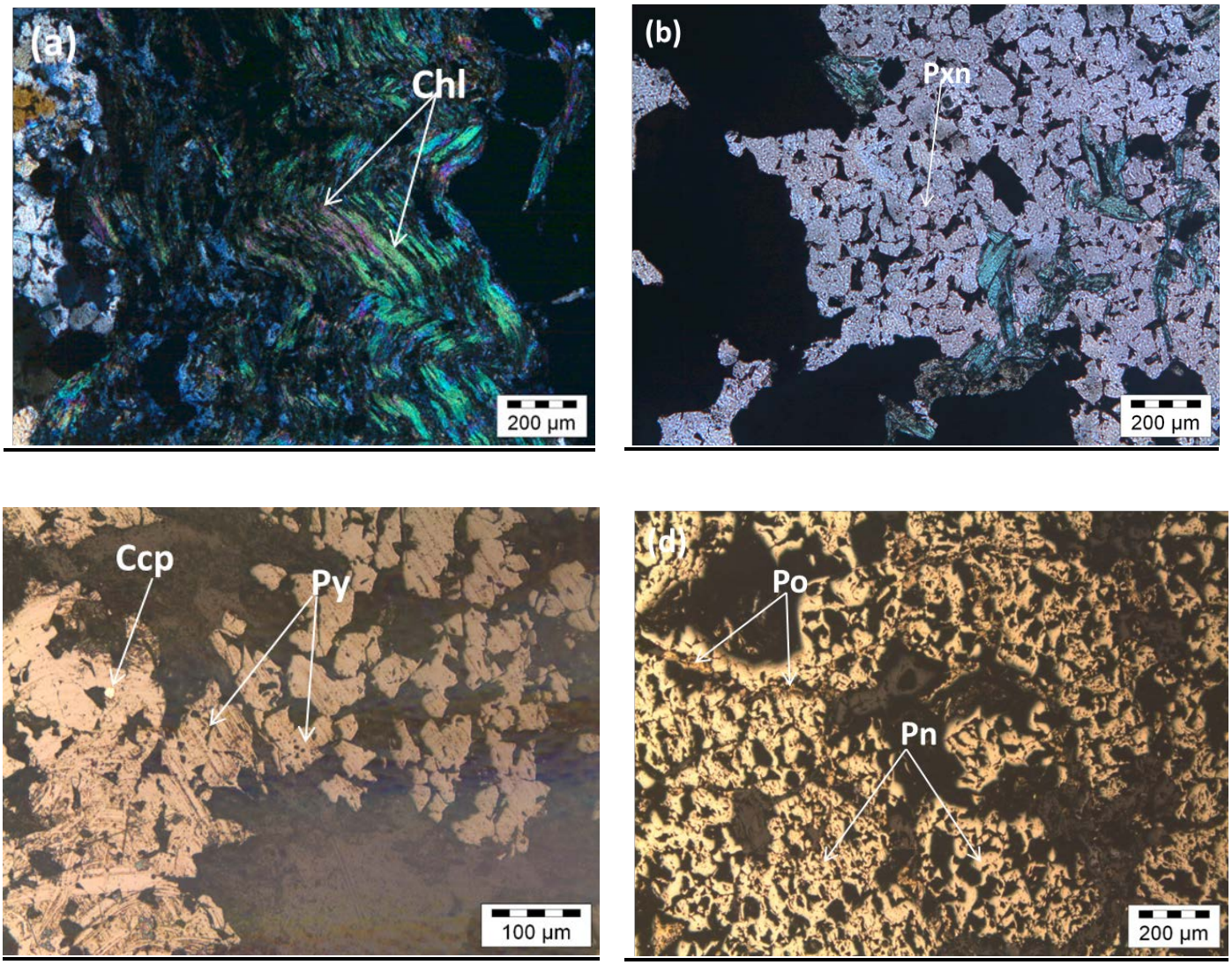

Figure 11. Photomicrographs from sample NC-L. (a) Chlorite characterised by a flow pattern (possible indication of micro-folding) under crossed nicols, (b) Groundmass of pyroxene in close association with the chlorite (almost flaky) exhibiting characteristic greenish blue colours in plane polarised light, (c) Chalcopyrite and pyrite assemblage in reflected light and (d) Pentlandite and pyrrhotite minerals, viewed in reflected light.

4. Kraubath Samples

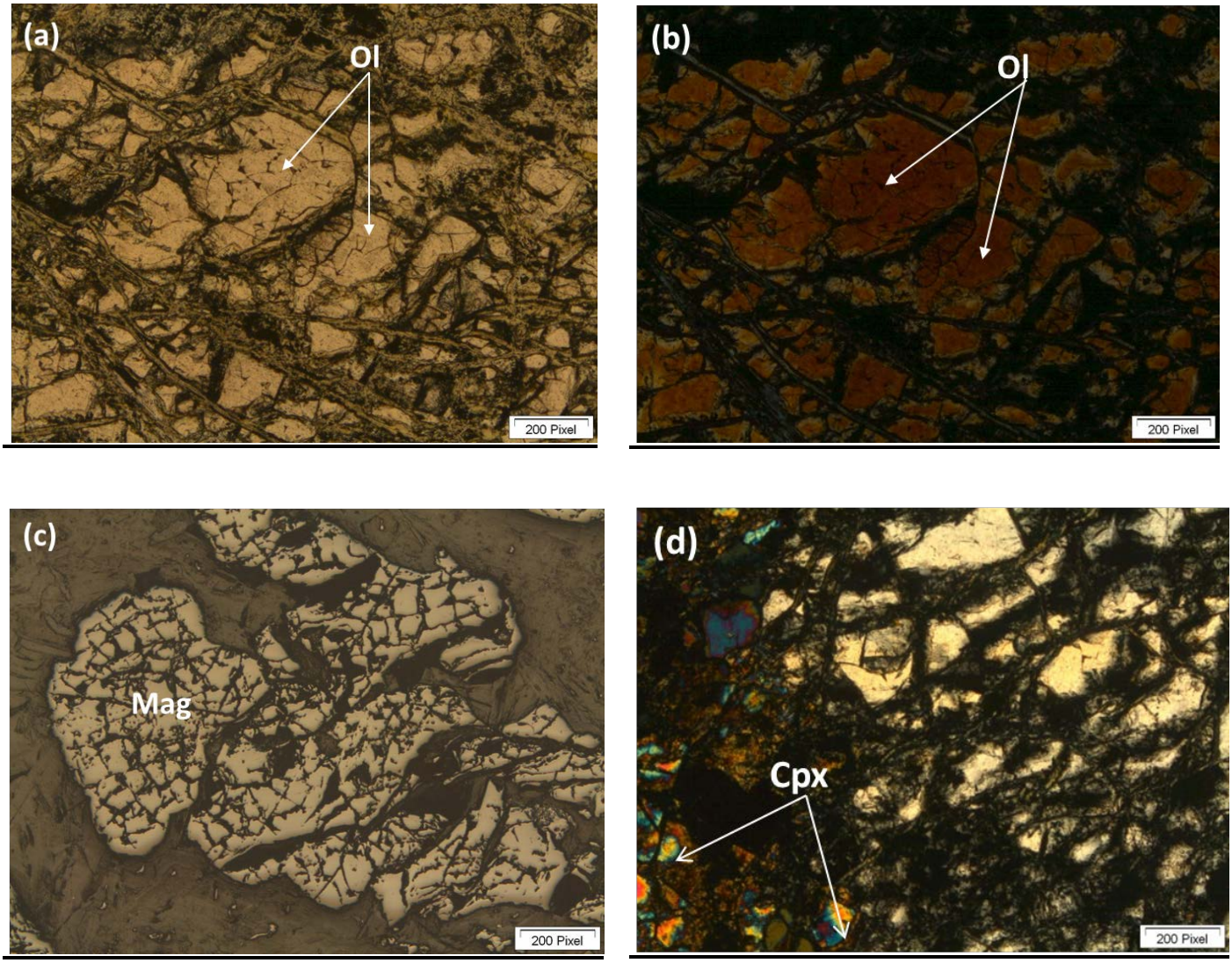

Figure 12. Photomicrographs from sample NC-MA. (a) Fractured olivine phenocrysts, with alteration along the fracture planes in plane polarised light, (b) Fractured olivine phenocrysts, with alteration along the fracture planes in crossed nicols, (c) Magnetite showing some form of alteration under reflected light and (d) Clinopyroxene characterised by its high interference colours under crossed nicols.

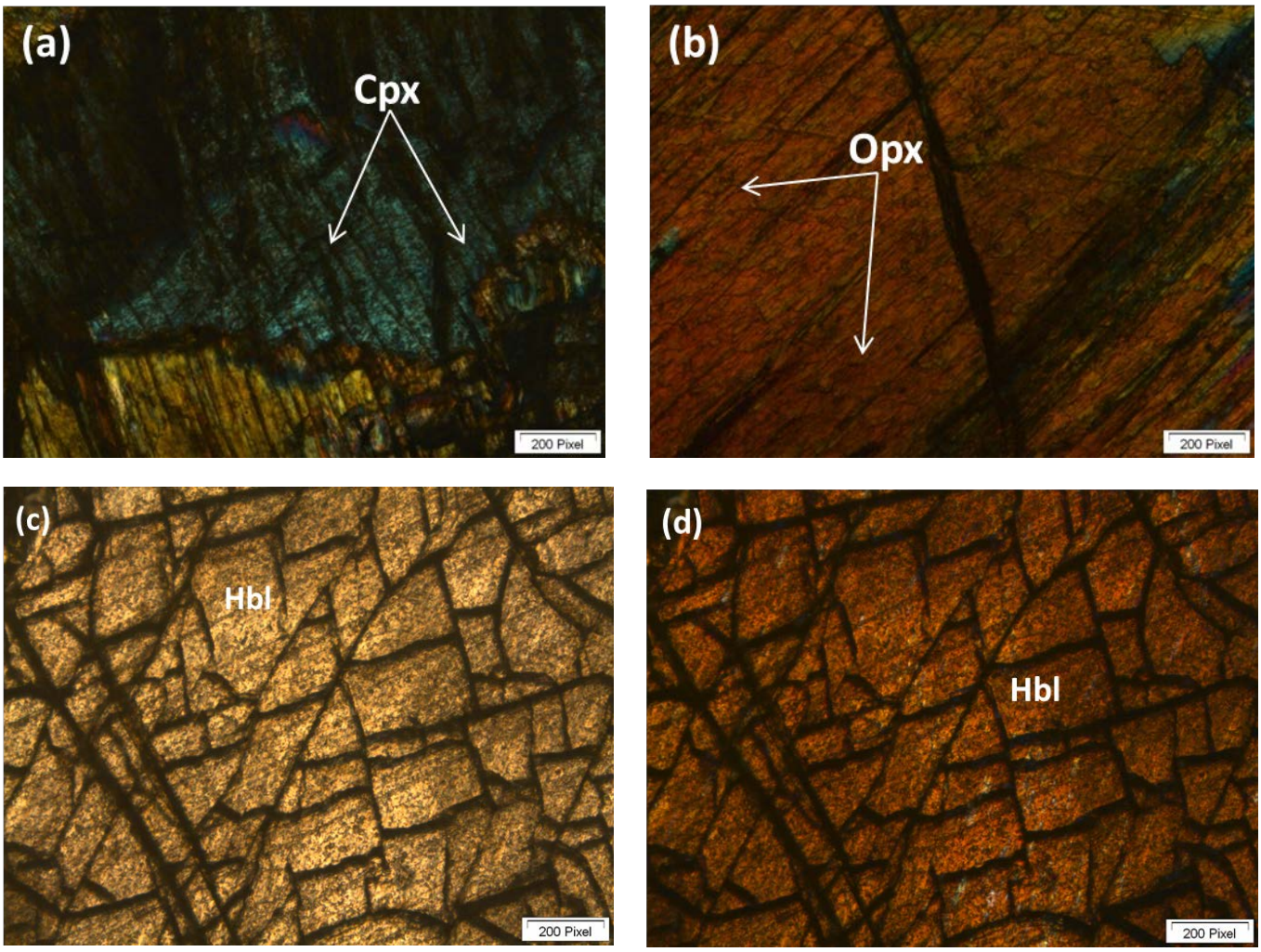

Figure 13. Photomicrographs from sample NC-NA. (a) Elongated flaky clinopyroxene under crossed nicols, showing moderate interference colours, (b) Orthpyroxene with characteristic cleavage intersecting at 90 degrees, viewed under crossed nicols, (c) Hornblende characterised by its distinct cleavage at 56 and 124 degrees which forms a distinctive diamond shape in cross section, viewed in plane polarised light and (d) Disticnt cleavage on the hornblende viewed under crossed nicols.

5. African Nickel Limited Samples

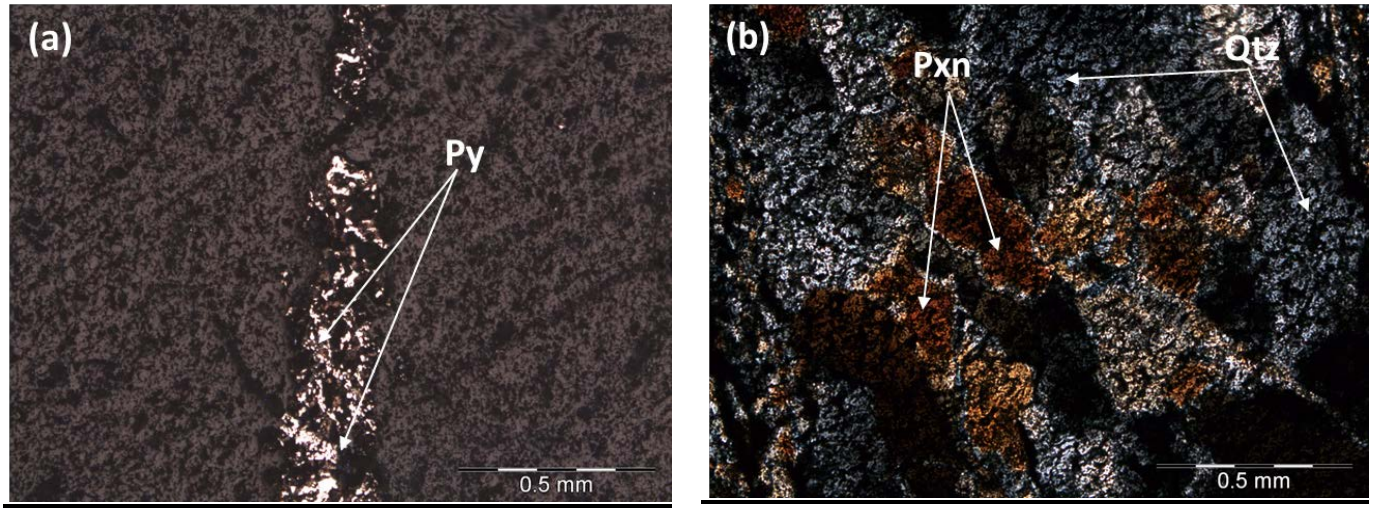

Figure 14. Photomicrographs from sample UFS 4CS2. (a) Irregular pyrite grains with deformation textures and largely restricted to interstitial areas, viewed in reflected light and (b) Highly distinct large pyroxene minerals characterised by alteration processes and poorly developed exsolution lamellae, while dominant quartz grains appear to be closely associated with the pyroxene, view in plane polarised light.

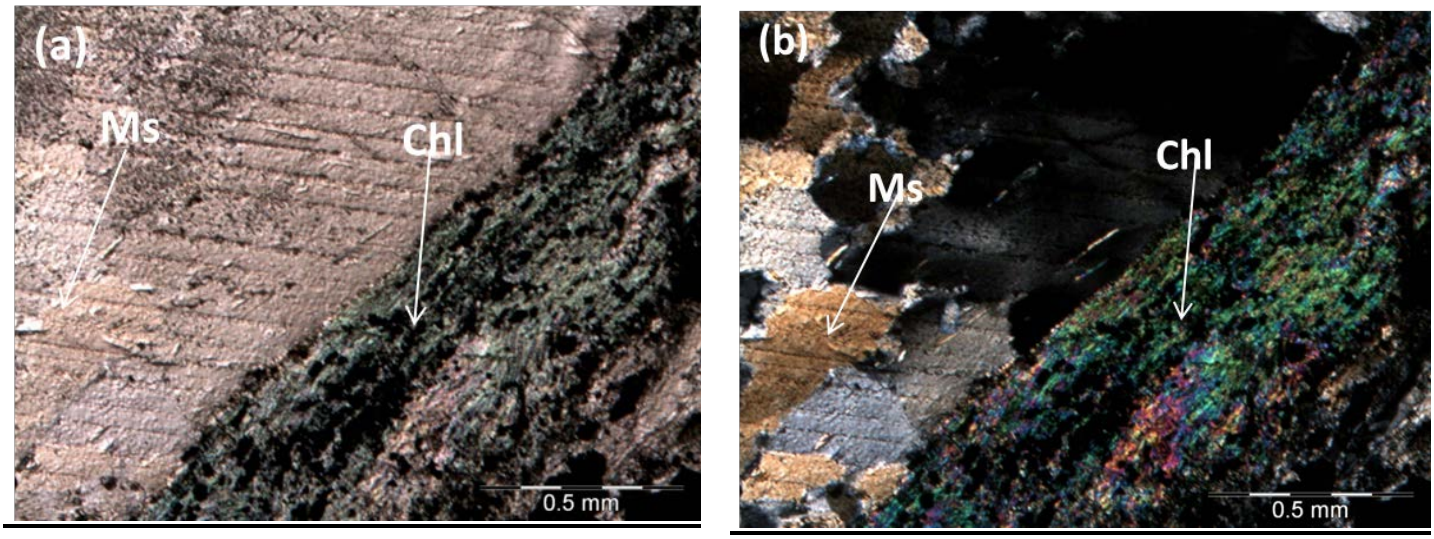

Figure 15. Photomicrographs from sample UFS16c. (a) Muscovite-chlorite mineral assemblage, also appears to be an indication of calcite occurring in close association with the

muscovite, viewed in plane polarised light and (b) Muscovite and chlorite, the high interference colours of the chlorite could be associated with remnant pyroxene minerals, viewed under crossed nicols.

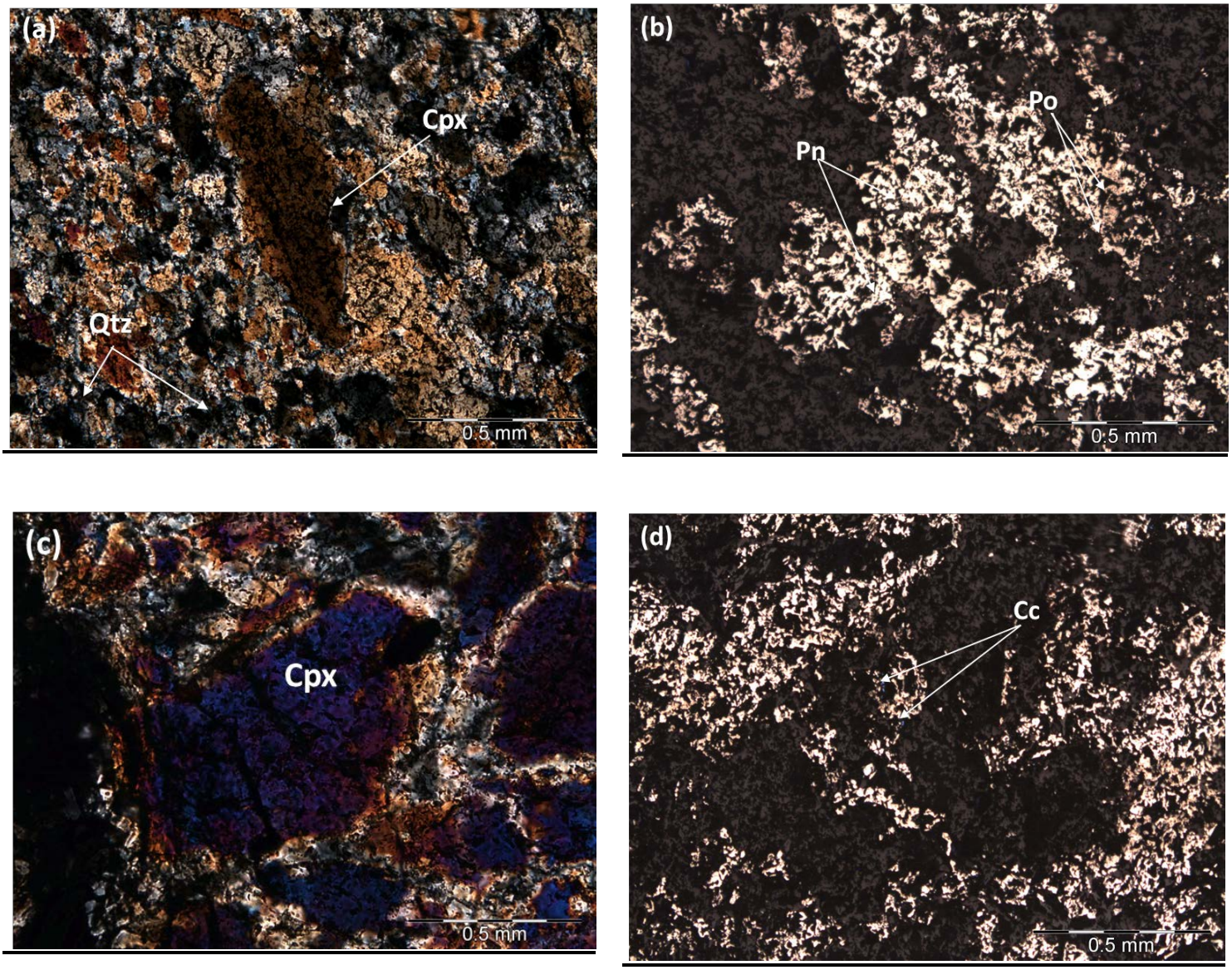

Figure 16. Photomicrographs from sample UFS38e. (a) Clinopyroxene and quartz mineral assemblage, viewed under crossed nicols and (b) Close association of pentlandite and pyrrhotite minerals as a result of exsolution occurring after magmatic segregation, view in reflected light, (c) Clinopyroxene characterised by high interference colours and surrounded

by quartz grains, viewed under crossed nicols and (d) Minute chalcocite grains characterised by their bluish colour, view in reflected light.

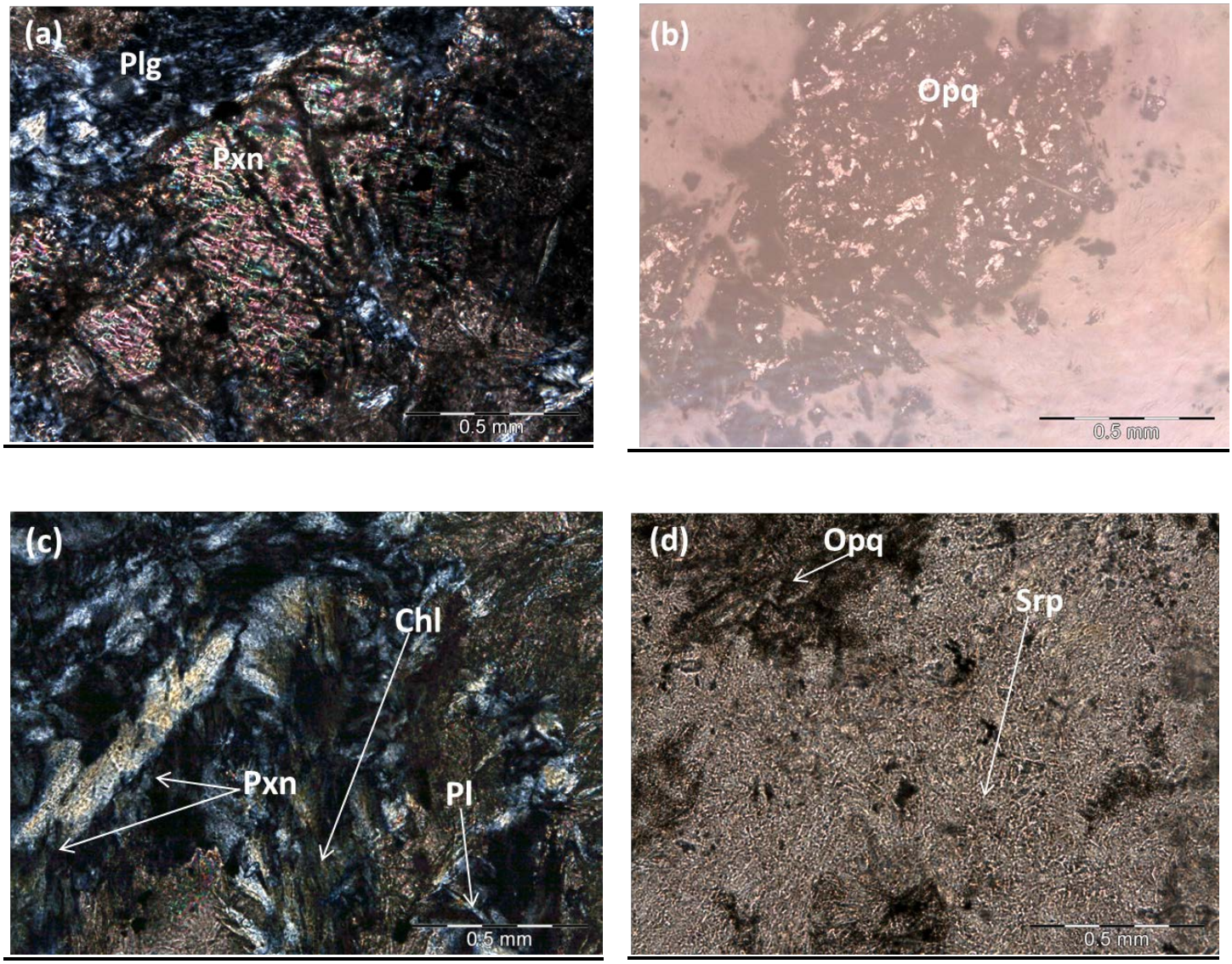

Figure 17. Photomicrographs from sample UFS39a. (a) Pyroxene and plagioclase mineral assemblage, the pyroxene appears to be deforming to form serpentines (serpentinisation), viewed under crossed nicols and (b) Highly deformed opaque minerals, viewed in reflected light, (c) Only minute and little amounts of plagioclase remain and relics of pyroxene are also seen in the chlorite and serpentine products, view under crossed nicols and (d) Abundant minute serpentine in association with the deformed opaque minerals.

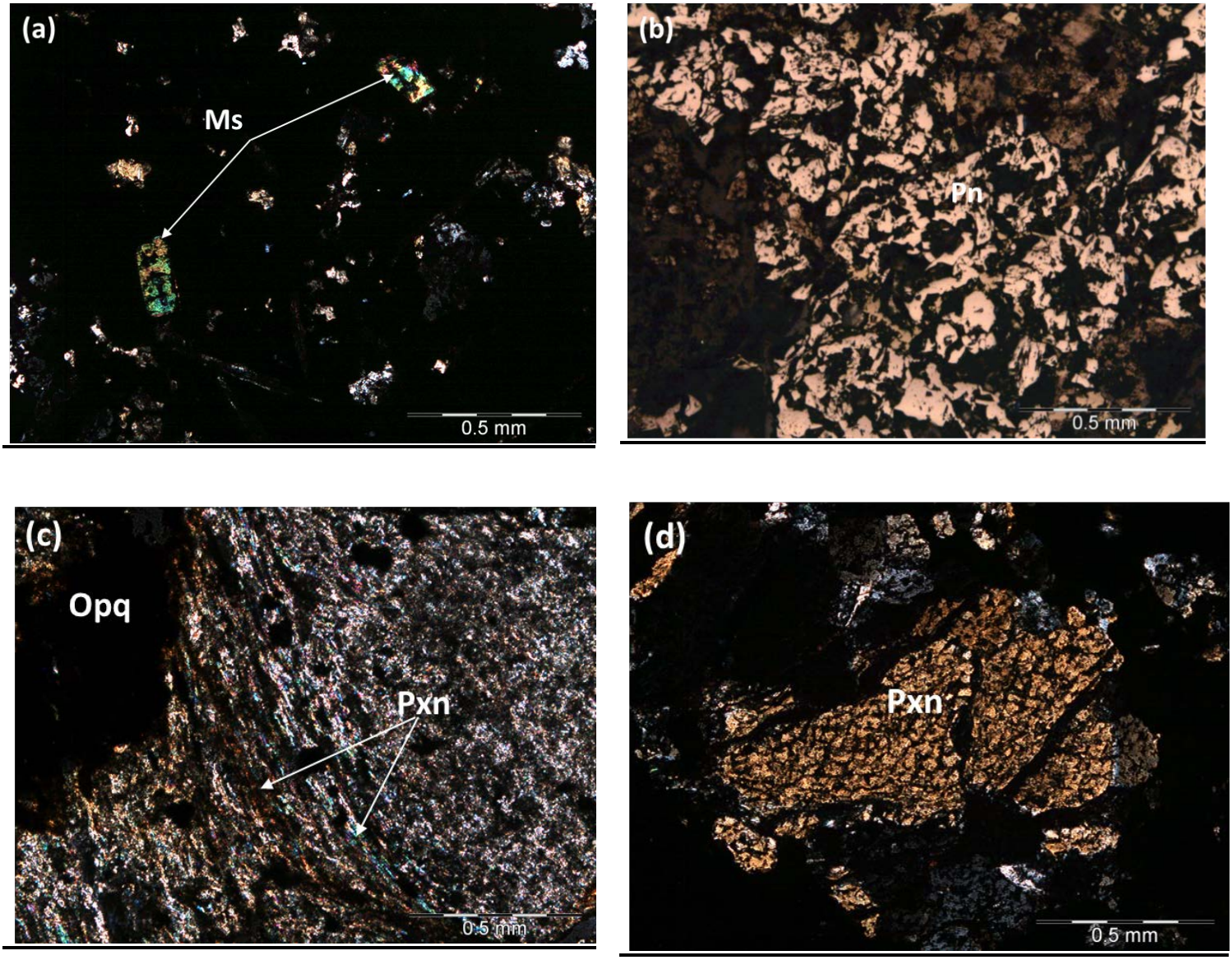

Figure 18. Photomicrographs from sample UFS39b. (a) Muscovite grains characterised by high interference colours in an altered matrix of pyroxenes, viewed under crossed nicols, (b) Pentlandite occurring as large irregular grains, viewed in reflected light, (c) Opaque-pyroxene mineral assemblage, the pyroxene deformation to form chlorite is not clearly visible due to the intense nature of the deformation, view under crossed nicols and (d) Irregular pyroxene grains characterised by the occurrence of quartz on the rims, viewed under crossed nicols.

Appendix C

See the CD in the pocket inside the back cover.